INVESTIGATION OF PHASE TRANSITION BEHAVIORS AND TRANSITION MECHANISMS OF NAT-TOPOLOGY ZEOLITES IN T-P_{H_2O} SPACE

Hsiu-Wen Wang

Submitted to the faculty of the University Graduate School
in partial fulfillment of the requirements
for the degree
Doctor of Philosophy
in the Department of Geological Sciences,
Indiana University
May, 2011

Accepted by the Graduate Faculty, Indiana University, in partial fulfillment of the requirements for the degree of Doctor of Philosophy.

Doctoral Committee

_____

David Bish, Ph.D.

_____

Bogdan Dragnea

_____

James Brophy

_____

Robert Wintsch

Date of Dissertation Defense - April 26, 2011

To my parents and sister

Acknowledgments

When I first became a student of Prof. David Bish, my adviser, six years ago, I knew nothing about zeolites and spoke only a little English. He defined the problem, raised funds to support me financially, gave me continuous encouragement, and provided invaluable criticism through this entire research period. He is also my best English teacher, from correcting my oral errors on a daily basis to even minor mistakes in my dissertation. I have benefited so greatly from his kindness that the brief mention here is hardly adequate to express my gratitude to him. I would like to extend my heartiest thanks to Karen Bish. She is like my second mother and has been giving me parental care during my studies in the US.

I am thankful to my doctoral committee, Profs. James Brophy, Robert Wintsch, and Bogdan Dragnea, for their continuous support and advice in every moment of my doctoral work. I extend my sincerest thanks to Prof. Michael Carpenter from University of Cambridge, UK, who provided me invaluable help during my thesis defense year and changed my aspects of physical properties and thermodynamic behaviors in minerals. I am grateful to Prof. Wei-Teh Jiang, my undergraduate advisor in National Cheng Kung University, Taiwan, who brought me into the field of mineralogy and gave me a solid and fundamental knowledge of minerals. I also wish to thank him and Prof. Huai-Jen Yang for their constant encouragement during my studies at National Cheng Kung University and Indiana University.

My sincere thanks must go to every one who has supported me during my doctoral work. I thank Michael Cheshire, Hongwei Ma, Sasha Wilson, Kevin Robertson, Hongji Yuan, Tingting Liu, Rebecca Stokes, Polly Root, and Ray Chuang, who have provided much help in my daily life and shared all the frustrations and excitements of the research in the past six years. I also wish to thank all the faculty members and staff of the Department of Geological Sciences at Indiana University who helped me in various ways and for their patience in helping me. I cannot forget En-Jui Lee and all my friends in Taiwan who shared many happy memories and who gave me many pleasurable moments to take with me to the US.

Hsiu-Wen Wang
May, 2011

Hsiu-Wen Wang

INVESTIGATION OF PHASE TRANSITION BEHAVIORS AND TRANSITION MECHANISMS OF NAT-TOPOLOGY ZEOLITES IN T-P_{H_2O} SPACE

NAT-topology zeolites, namely natrolite (Na-bearing), mesolite (Na/Ca-bearing), and scolecite (Ca-bearing), consist of a three-dimensional host framework of $(Al_2Si_3)O_{10}$ chains, with structural "pores" that contain reactive guest cations and H_2O molecules. The nature of structural interactions between a host framework and guest cations and H_2O molecules defines the character of phase transitions, which depend on the chemistry of the guests and rely on the symmetry (topology) of the host framework. X-ray diffraction and synchrotron X-ray total scattering experiments coupled with appropriate modeling methods showed the existence of different dehydration (heating)/phase transition behaviors under high- and low-P_{H_2O} conditions in these zeolites. Infrared spectroscopic studies of the dynamic interactions among the guest cation-H_2O complexes and host frameworks allowed characterization of host-guest interactions as a function of T and P_{H_2O}. Structural analyses reconciled these data and showed that different structural evolutions result from the cooperative processes in which the thermal behaviors of cations-H_2O complexes are coupled with the framework symmetry constraints through direct bonding interactions. These results showed for the first time that the extent of coupling under specific T and P_{H_2O} conditions influences the flexibility of the structure and ultimately drives structural changes. The determined bulk thermodynamic behaviors in the NAT system were consistent with the observed structural behaviors. The computed *apparent* enthalpies of dehydration in these zeolites reflect strong dependence not only on guest cation chemistry but also on the local hydrogen bonding configurations.

Table of Contents

List of Tables

List of Figures

INTRODUCTION

Since the dawn of mineralogy, mineralogists have strived to understand how crystal structures are formed and modified in given physical and chemical environments. A tradition of studying phase transformation process in mineral structures has evolved from the need to understand the physical and thermodynamic properties of minerals and to elucidate the fundamental factors determining their stability in the Earth and at its surface. This significant goal has been one of the primary objectives of crystallographic and mineralogical research and has not yet to be fully attained. As noted by Dove (1997),

> *Many advances in our understanding of phase transitions originally developed in the fields of solid-state physics and chemistry have recently begun to have a significant impact in mineralogy and mineral physics, even though there are very few minerals that show no influence of transition processes in the critical range of pressures and temperatures relevant to the Earth.*

Studies of the phase transition behaviors of the nanoporous solids such as zeolites are particularly challenging because their guest cations and H_2O molecules can directly communicate and exchange with the external environment, making the structure of zeolites not only sensitivity to chemistry of guest components but also very responsive to temperature (T), pressure (P), partial pressure of water (P_{H_2O} or also known as relative humidity, RH), and other thermodynamic variables. Natural zeolites are low-density silicates that occur near the Earth surface and are often found as late-stage crystallization or alteration products. Common chemical features associated with zeolite formation are the availability of SiO_2 and Al_2O_3 and a $(Ca^{2+} + Na^{+} + K^{+}) / H^{+}$ activity ratio greater than that in which a phyllosilicate would be

formed. Zeolites have crystal structures consisting of aluminosilicate frameworks that create a system of uniform linked channels and cavities (Gottardi and Galli 1985; Coombs *et al.* 1998; Ambruster and Gunter 2001). A characteristic of zeolites is that they exhibit a range of composition with respect to both the aluminosilicate framework (host) and to the extraframework cations and H_2O molecules (guests). In addition, many framework configurations can occur, and these play important roles not only in defining the structural symmetry but also in determining physical and chemical properties. Driven partly by a myriad of industrial uses of zeolites, the exploitation of host-guest interactions is extremely important. The corner-linked, rigid polyhedral frameworks in zeolites are very flexible and are very interactive to changes in guest cation chemistry and hydration state. They show a certain range of tolerance in their framework deformations (strains in the structure) and yield a range of group-subgroup geometric topology relations arising from structural accommodations around the local guest complexes. In addition to guest chemistry, which exerts strong influence on crystal structure, the compressibility and expansibility of a framework system are also influenced by increasing pressure (compression) or increasing temperature (expansion), and vice versa. Unfortunately, the evaluation of structural change mechanisms is not as simple as changing an individual variable. Phenomena observed with increasing pressure will be different from those seen on decreasing temperature or changing guests to a smaller cation or molecule. Even though these variables (i.e., T, P, P_{H_2O}, and guest chemistry) can be investigated separately, no specific "critical geometry" of the transition in the framework can be independently determined. As natural zeolites are hydrous minerals, particular attentions must be paid to the combined temperature and P_{H_2O} effects on thermally

and P_{H_2O}-induced dehydration reactions and accompanying structural changes[1]. In hydrous mineral systems, these two environmental parameters, i.e., temperature and P_{H_2O}, are coupled and do not operate independently of one another. Increasing P_{H_2O} will expand the stability field of the low-temperature hydrous phase, whereas decreasing P_{H_2O} will expand the stability fields of the high-temperature anhydrous phase(s). However, most previous studies focused on dehydration-induced structural transitions in zeolites by heating samples under partially saturated to dry conditions, where the P_{H_2O} conditions were seldom monitored or controlled (e.g., Artioli 1997). Simply observing structural changes as a function of temperature without control of P_{H_2O} will likely result in an incomplete picture of the reaction and phase transition behavior in zeolites. Such combined information is important, as much of the interest in zeolites comes from their industrial applications as catalysts at high temperatures and as adsorbents at lower temperatures, usually in environments in which H_2O can potentially participate in reactions. Several lines of evidence emphasize the impact of investigation of combined temperature and P_{H_2O} effects in zeolite thermal reactions and accompanying phase transitions. First, zeolites are hydrous minerals, and interactions between H_2O molecules, extraframework cations, and framework oxygens are very important

[1] The different types of structural changes found in minerals are similar in many respects to the phase transitions observed in ionic, metallic, and molecular crystals, and they include reconstructive phase transitions, displacive phase transitions, and cation order-disorder transitions. Displacive phase transitions involve no breaking of bonds (at least first-coordination bonds) and only small migrations of atoms, which result in changes of atom positions, bond angles, and symmetry of original crystal structure. These should not be confused with order-disorder transitions that involve ordering of cations between discrete crystallographic sites. Displacive phase transitions include 1st- and 2nd-order phase transitions (Buerger 1951, 1972). Strictly speaking, phase transition phenomena caused by dehydration reaction in zeolites are not an isochemical process (i.e., they are a chemical reaction). Therefore they cannot be treated solely by the standard Buerger theory of phase transition. However, in zeolites (and other tectosilicates), the (Al, SiO_4)-tetrahedra are much stiffer than the forces involved in rotating two tetrahedra around a shared oxygen vertex, which allows the deformation of the network of tetrahedra without the tetrahedra themselves distorting. The resulting framework deformations, involving no breaking of Si(Al)-O bonds and occurring rapidly and sometimes reversibly, are similar to the descriptions of Buerger's displacive phase transition. Moreover, in many studied cases the framework symmetry of the dehydrated phase is a subgroup of that of the hydrous phase and their thermodynamic properties also obey Buerger's descriptions.

in determining their structural stability. Furthermore, as mentioned before, the nature of guest cation-H_2O complexes and their ability to induce deformations in a zeolite framework must also be considered. Thus, the dynamic motions of guest cation-H_2O complexes with temperature have a great influence on zeolite thermal behaviors. Second, as the H_2O molecules occupy much of the volume of the channel system and are ion-dipole attracted to the extraframework cations, a gain or loss of H_2O molecules has a direct effect on the bonding configurations of the extraframework cations and framework geometry. Third, both thermally induced (i.e., the response of framework deformation and guest cation migration to temperature, generally occurring as a result of dehydration reactions) and dehydration-induced structural transformation usually occur together. Because it is a challenge to separate these two effects, it is desirable to consider both effects together.

This research encompasses an investigation of the structural, chemical, temperature-, and P_{H_2O}-dependences of NAT-topology (fibrous) zeolites, namely natrolite ($Na_{16}Al_{16}Si_{24}O_{80} \bullet 16H_2O$), mesolite ($Na_{16}Ca_{16}Al_{48}Si_{72}O_{240} \bullet 64H_2O$), and scolecite ($Ca_8Al_{16}Si_{24}O_{80} \bullet 24H_2O$). These zeolites were chosen for their relatively simple structures (in comparison with most other zeolites) and their thoroughly investigated crystal chemistry (see reviews in Armbruster and Gunter 2001; Passaglia and Sheppard 2001). The main goal of this study is to explore the atomic factors controlling zeolite structural properties and phase transitions behaviors, and to enhance the knowledge to predict their structural stabilities under given physical or chemical environments. This is important because minerals' macroscopic behaviors, and ultimately rocks, can be obtained from a detailed knowledge of their microscopic or atomistic nature and are related to their thermodynamic properties.

A short reader's guide

This research consists of a multi-faceted approach to explore the combined temperature and P_{H_2O} effects into the mechanisms of phase transitions in NAT-topology zeolites. Experimental methods applied to this study include: (i) static structure probes of varied length scales, including laboratory powder X-ray diffraction (XRD Cu Kα; to study the average structure) and synchrotron X-ray pair distribution function analysis of total scattering analysis (PDF; to examine local host-guest geometry). The resulting data were analyzed with appropriate modeling methods. Results can quantify different interaction length scales and clarify short-range host-guest configurations and long-range accommodation of the framework structures as a function of temperature and P_{H_2O}; (ii) a dynamic probe with infrared (IR) spectroscopy in the frequency range of 650-4000 cm^{-1}. This IR frequency range is sensitive to H_2O vibrational motions and dynamic interactions among guest cations, H_2O molecules, and host aluminosilicate frameworks. The characteristic evolution of a phase transition from suitable IR-active vibrational modes can be obtained; and (iii) thermogravimetric (TG) analyses applied to the characterization of macroscopic bulk behaviors during simple dehydration and rehydration processes. Qualitative features of hysteresis behaviors and related thermodynamic descriptions can be formulated from thermal analyses results.

Chapters in this thesis are presented based on the analysis methodologies. Detailed background information on individual experimental techniques is not included in this thesis but can be found in many standard textbooks. Chapters 1, 2, and 3 constitute the XRD and/or PDF structural phase transition studies of natrolite, scolecite, and mesolite, respectively. A portion of the XRD and PDF results has been published in several journals, including

American Mineralogist (for natrolite and mesolite)[2], *European Journal of Mineralogy* (for natrolite)[3], and *Philosophical Magazine* (for all three zeolites but mainly focused on natrolite)[4]. Chapter 4 presents the study of dehydration and accompanying phase transitions using IR spectroscopy for NAT-topology zeolites. Chapter 5 discusses hysteretic behaviors based on TG analyses. The thermodynamic descriptions of the dehydration and rehydration behaviors in NAT-topology zeolites are also included in this chapter. Finally, Chapter 6 provides summaries of the results, with major conclusions, and discusses future research directions in this studying field. With the exception of Chapter 5, each chapter can be read independently without further understanding of the materials presented in the other chapters.

[2] Natrolite-Wang and Bish 2008; Mesolite-Wang *et al.* 2010.
[3] Wang and Bish 2010.
[4] Bish and Wang 2010.

CHAPTER 1

Temperature- and P_{H_2O}-dependent structural phase transitions in the zeolite natrolite

Natrolite ($Na_2Al_2Si_3O_{10} \bullet 2H_2O$; Z = 8) consists of a three-dimensional network of $(Al_2Si_3)O_{10}$ chains, with oxygen atoms shared between (Al,SiO_4)-tetrahedra, yielding a negatively charged framework and elliptical channels occupied by H_2O molecules and charge-balancing Na^+ cations. The basic building blocks of natrolite are so-called T_5O_{10} chains of (Al,SiO_4)-tetrahedra running parallel to the *c* axis (see Fig. 1.1a or Figs. 0.2B and 1.1A in Gottardi and Galli 1985). Each T_5O_{10} chain is linked to a neighboring chain at 2/8 *c* higher or lower, and the NAT-topology framework[5] can therefore be described as being formed by a single chain at four levels (Fig. 1.1b). The completely ordered (Al,Si) distribution in the natrolite framework results in orthorhombic *Fdd*2 symmetry. The essential structural features of natrolite were first formulated by Pauling (1930), a detailed description was given by Taylor *et al.* (1933), and the first structure refinement was made by Meier (1960) using diffraction data measured at room temperature. In the natrolite channels, the Na^+ cation is coordinated by four framework oxygens (O), one H_2O (Ow) from above and one H_2O (Ow) below the framework O plane, in the form of a distorted octahedron (Fig. 1.1c). Each H_2O (Ow) is ion-dipole attracted to two Na^+ cations forming zigzagging -Ow-Na-Ow-Na-Ow- chains along the *c* direction, with two Na^+ cations and two H_2O (Ow)

[5] Structure code NAT represents a fibrous topology and was originally named for the topological symmetry of the zeolite natrolite. Mesolite and scolecite are the other two natural zeolites belonging to the NAT group and they have the same aluminosilicate framework configuration as in natrolite.

Natrolite ($Na_{16}Al_{16}Si_{24}O_{80} \cdot 16H_2O$)

Space group = *Fdd*2, *a* = 18.2915(3) Å, *b* = 18.6324(3) Å, *c* = 6.5856(1) Å, *V* = 2244.5(1) Å^3

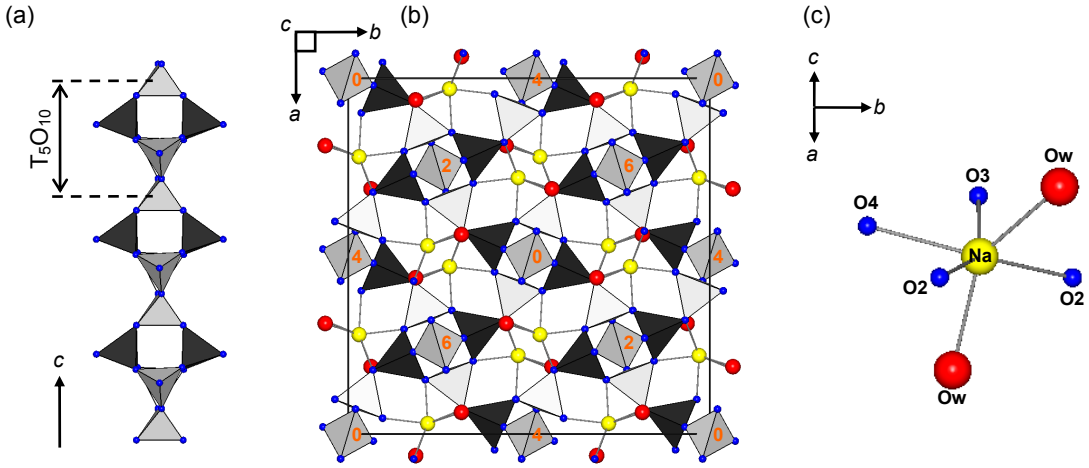

Figure 1.1. Refined crystal structure of natrolite at 23 ºC. **(a)** Basic T_5O_{10} chain viewed along the *c* axis. **(b)** NAT framework viewed down the cross-linked chains. Numbers in the central tetrahedra indicate the height above the (001) plane as multiples of *c*/8. **(c)** Local view of coordination of Na^+ cations in the natrolite channel system. Si tetrahedra = gray; Al tetrahedra = black; oxygen atoms = blue spheres; Na^+ cations = yellow spheres; H_2O molecules = red spheres; Bonds = solid gray lines.

molecules per unit cell. The crystallographic sites occupied by Na^+ cations and H_2O molecules obey *Fdd*2 symmetry.

In the 122 years since Rinne (1890) studied natrolite dehydration, various authors (van Reeuwijk 1974; Alberti and Vezzalini 1983; Belitsky *et al.* 1992; Joswig and Baur 1995; Baur and Joswig 1996; Wang and Bish 2008, 2010) have shown that the framework of natrolite is collapsible. Upon heating, the natrolite framework shrinks through rotations of tetrahedra and shows a displacive phase transition[6] to a dehydrated phase, α-metanatrolite ($Na_{16}Al_{16}Si_{24}O_{80}$; the name α-metanatrolite was first used by van Reeuwijk 1974). During this process, natrolite evolves all H_2O molecules (Ow), and the extraframework Na^+ cations migrate to new channel sites, recoordinating to framework oxygens in order to maintain their charge compensation. The transition and the resulting dehydrated phase occurred at various temperatures from 160 to 400 °C. The wide range in transition temperature is a reflection of the strong dependence on the surrounding P_{H_2O} during the measurements (i.e., comparatively moist environments employed on heating caused the initial dehydration temperatures to increase; a parallel example is the effect of CO_2 partial pressure on $CaCO_3$ decomposition). On exposure to moist air, α-metanatrolite adsorbs H_2O and reconverts to natrolite. Belitsky *et al.* (1992) suggested that a new phase, "x-metanatrolite," coexists simultaneously with α-metanatrolite as an intermediate metahydrated phase during slow linear heating under vacuum (10^{-2} torr), but they did not provide any structural model or further discussion about the nature of this intermediate phase. We recently (Wang and Bish 2008, 2010) confirmed Belitsky *et al.*'s suggestion of a second phase coexisting with α-metanatrolite and we also discovered that natrolite undergoes two very different phase transitions to two distinct

[6] Displacive phase transitions are based on the phenomena that the soft behavior of the zeolite channels and the more rigid behavior of their tetrahedral frameworks lead to easy rotation of any two adjacent tetrahedra around an oxygen hinge, resulting in a so-called displacive transformation (i.e., no breaking of bonds).

dehydrated phases under controlled-P_{H_2O} conditions, with α1-metanatrolite occurring at elevated P_{H_2O} and α2-metanatrolite appearing at low-P_{H_2O}, which later transforms to α1-metanatrolite at higher temperatures (for clarity, we renamed the previously known α-metanatrolite phase to α1-metanatrolite). The newly discovered α2-metanatrolite phase has unit-cell parameters similar to those for Belitsky *et al.*'s "x-metanatrolite" (see Wang and Bish 2008). The discovery of α2-metanatrolite underscores the importance of the combined effects of temperature and P_{H_2O} on zeolite phase transitions and shows that we previously had only an incomplete picture of the phase transition behavior in natrolite. This chapter is aimed at providing a comprehensive representation of temperature- and P_{H_2O}-dependent structural phase transitions during natrolite dehydration and rehydration, emphasizing the important results that have been observed in my research. For a detailed description of the structure determination of α1- and α2-metanatrolite phases and Rietveld refinement analyses with X-ray diffraction data, refer to Wang and Bish (2008, 2010).

1.1 Samples and experimental methods

The natrolite sample used in this study is from San Benito County, California, USA ($Na_{14.72}Al_{15.52}Si_{24.80}O_{80} \bullet 16.32H_2O$). The crystal chemistry of San Benito natrolite was characterized by electron microprobe analysis of crystals in several thin sections and its averaged chemical composition is very close to the ideal end-member stoichiometric formula. The sample was crushed into a fine powder (<38 μm) using a Retsch Micro-Rapid mill with agate mortar and pestle and was studied using an Anton-Paar TTK-450 heating stage on a Bruker D8 diffractometer (Cu Kα radiation; equipped with a Vantec position-sensitive detector). The diffractometer was calibrated using NIST SRM 660a LaB_6. The TTK

450 stage provides the opportunity for measuring data as a function of temperature, up to 450 ºC, and the sample environment humidity was controlled via gas flow into and out of the sample chamber using an automated V-Gen dew point/*RH* generator (InstruQuest Inc.). *In-situ* X-ray diffraction (XRD) measurements with sample powders prepared as thin-layer slurry mounts were performed in controlled-temperature and -P_{H_2O} environments. Thermogravimetric (TG) analyses conducted under ambient *RH* conditions were made to characterize the bulk dehydration phenomena, and these results will be combined with the structural data obtained with XRD measurements.

1.1.1 Laboratory X-ray powder diffraction analysis

Diffraction data were collected under controlled-P_{H_2O} conditions ranging from ~0.3-27 mbar (corresponding to ~1-90% *RH* at 23 ± 1 °C and 1 bar) to ~ $10^{-0.8}$-$10^{-3.1}$ mbar (roughing pump vacuum condition, $10^{-3.8}$ bar) at sample temperatures up to 400 °C. The lower limit of P_{H_2O} ($10^{-3.1}$ mbar) under vacuum conditions was estimated based on the ambient *RH* at the time of measurement (i.e., ~20% *RH* at 23 °C; scaled by a factor of $10^{-3.8}$). On the other hand, the upper limit of P_{H_2O} ($10^{-0.8}$ mbar) under vacuum conditions was estimated based on the assumption that all residual gas remaining in the cell was H_2O vapor. Measurements were made from 12º to 33º 2θ, counting for 0.66 sec at each 0.017º 2θ step, equivalent to a count time of 613.3 sec/step. Dehydration (heating) and rehydration (cooling) behaviors were monitored through *in-situ* XRD measurements using a thin slurry-mounted specimen with a stepwise heating/cooling procedure under a fixed P_{H_2O} value for each temperature ramp. Sample temperature was increased to the set-point temperature in 25 ºC increments from room temperature to 100 ºC and in 10 ºC increments from 100 to 400 ºC, and it was reversed (decreasing temperature) in the same manner. Attempts were made to

establish equilibrium by applying the sample powder to a set temperature for 60 min prior to each data collection (under fixed P_{H_2O} value). This equilibration time was determined by measuring XRD data until no further structural changes occurred.

1.1.2 Thermogravimetric analysis

TG experiments were performed using a TA Instruments 2960 TG analyzer. Analyses made in this study were conventional isobaric experiments at 1 bar (no vacuum TG analyses). The dynamic method (i.e., heating the sample powder continually at a constant rate while recording the weight loss) was performed with a 1 °C/min heating rate. The sample environment was under ambient humidity conditions, and humidity (~40-50% *RH*, corresponding to ~11-13 mbar P_{H_2O} at 22 ± 1 ºC) was recorded before and after the measurement. The experiments were designed to measure the H_2O content of natrolite as a function of temperature. About 11.5(2) mg of natrolite powder was evenly distributed onto an alumina sample pan. The total weight change of the sample was monitored while heating to 950 °C under ambient atmospheric conditions. The emphasis here is that the results from dynamic TG measurements are only qualitatively comparable with static XRD measurements. If the rate of the dehydration reaction is much faster than the heating rate (i.e., 1 °C/min), there should be no significant overshoot of the dehydration temperature. In addition, the P_{H_2O} (or *RH*) conditions applied during TG measurements were not well controlled, and the much larger sample mass (than the XRD slurry mount) placed in the sample cup may enhance the opportunity of build-up of P_{H_2O} in intercrystallite pore spaces. All of these kinetic effects may inhibit the dehydration reaction, raise the dehydration temperature, and create discrepancies with the XRD data (see section 5.1 for a detailed description of the importance of kinetic effects).

1.2 Results and discussions

1.2.1 Natrolite phase transitions in P_{H_2O} and temperature spaces

Figure 1.2 illustrates natrolite dehydration and phase transition behaviors (the original natrolite phase is labeled with square symbols and the two dehydrated phases, α1- and α2-metanatrolite are labeled with circle and star symbols, respectively). Upon heating, the structural transition in natrolite is triggered by the dehydration reaction, manifested as a discontinuous change in the XRD reflection peaks. The observed transition temperatures (Fig. 1.2; black dashed lines) gradually increase as the environments move from low- to high-P_{H_2O} conditions. For instance, the transition from natrolite-to-α1/α2-metanatrolite occurred at 160 °C when P_{H_2O} was ~$10^{-0.8}$-$10^{-3.1}$ mbar, it increased to 220 °C when P_{H_2O} was 0.3(1) mbar (controlled at ~1.1 ± 0.2% *RH*, 23 ± 1 °C, and 1 bar), and it increased to 290 °C when P_{H_2O} was 14.8(2) mbar (controlled at 50.2 ± 0.5% *RH*, 23 ± 1 °C, and 1 bar). Similarly, the transition from natrolite-to-α1-metanatrolite began at 300 °C when P_{H_2O} was 20.9(5) mbar (controlled at 69.8 ± 0.5% *RH*, 23 ± 1 °C, and 1 bar) and increased to 310 °C when P_{H_2O} was 26.9(8) mbar (controlled at ~91.3 ± 0.8% *RH*, 23 ± 1 °C, and 1 bar). In addition, a single-stage weight loss in the TG curve measured under ~40-50% *RH* (equivalent to ~11-13 mbar P_{H_2O}) yielded an inflection temperature (the maximum rate of weight change) of 285 ºC (Fig. 1.3). This inflection temperature is approximately comparable with XRD measurements made under similar *RH* (P_{H_2O}) conditions (i.e., Figs. 1.2j-k), which also supports idea that the phase transition in natrolite is caused by dehydration (as in many other zeolites). The total weight loss up to 300 ºC determined from the TG curve is 9.8(2) wt.%, which is in close agreement with the results of the H_2O content determined by microprobe analysis, i.e., 9.7(1) wt.%, and is also near the ideal stoichiometric H_2O content of natrolite (9.5 wt.%). The

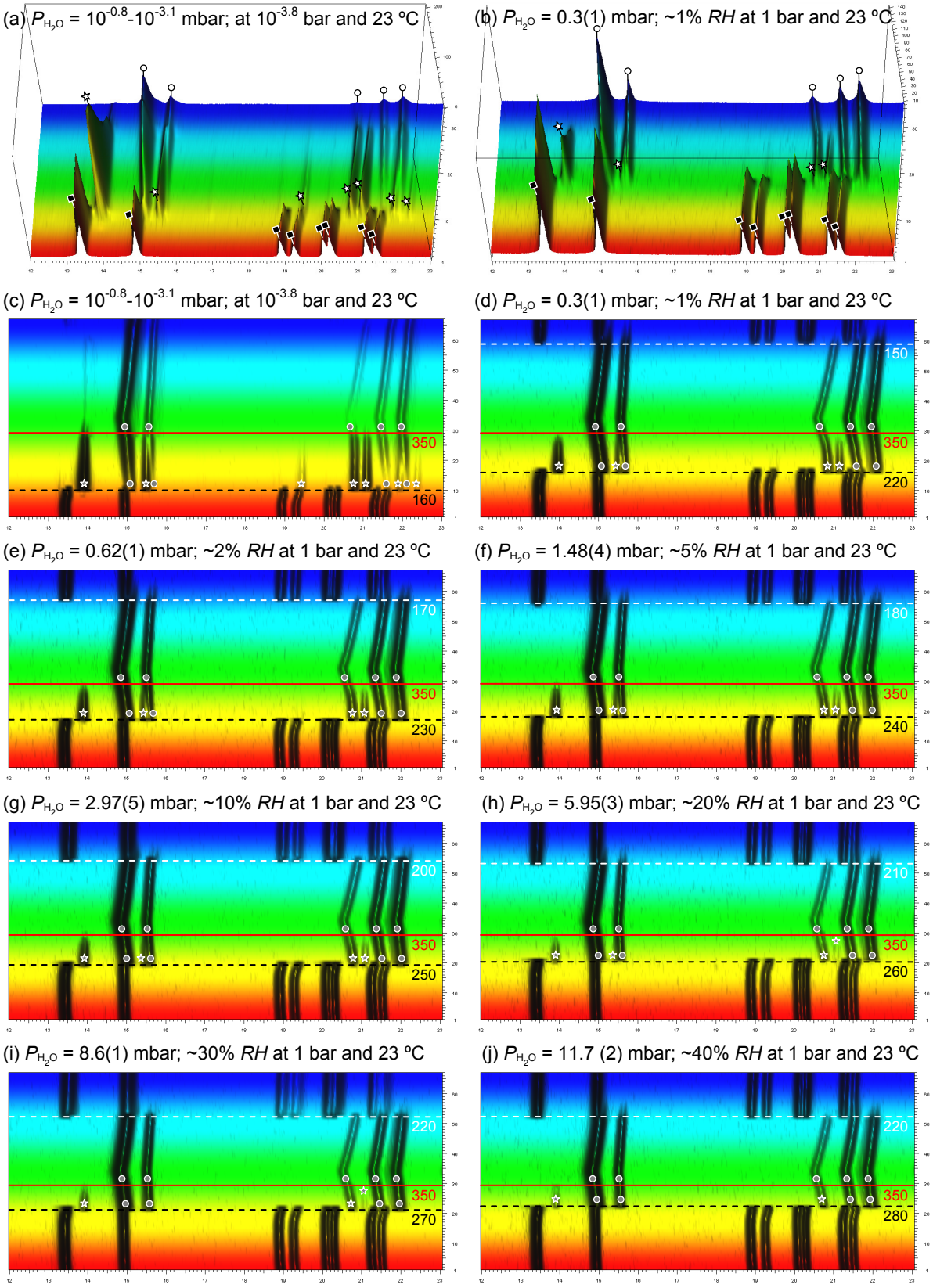

Figure 1.2. Continued on next page.

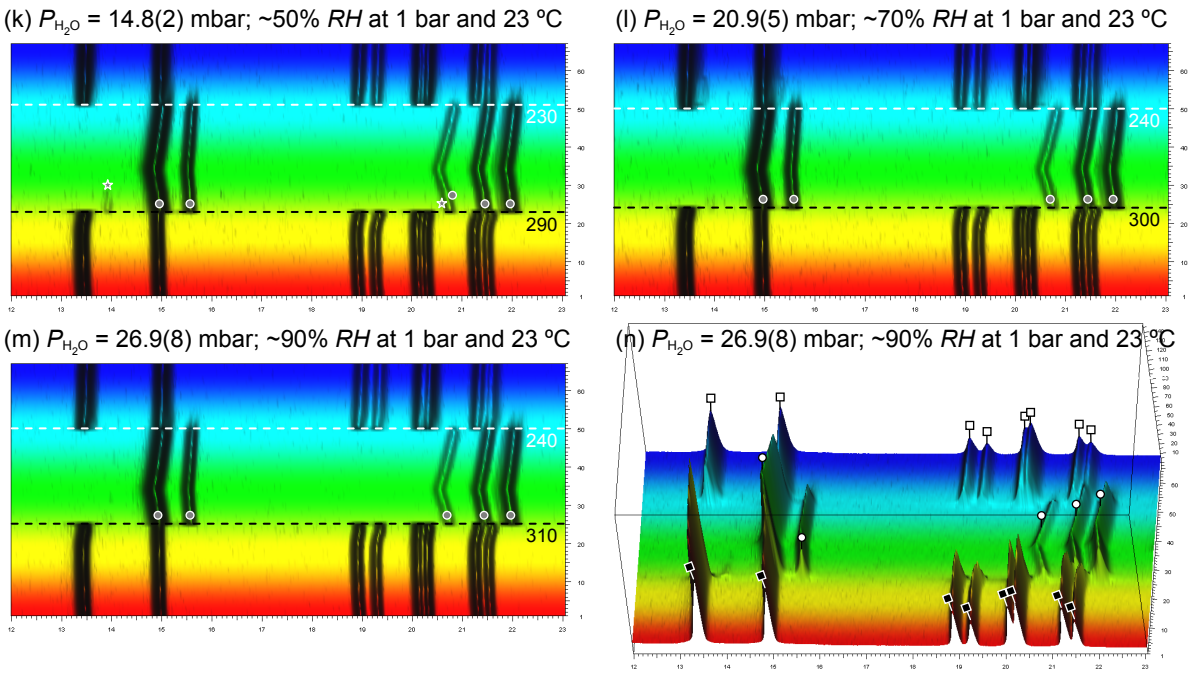

Figure 1.2. Temperature-resolved 3D-XRD patterns for natrolite measured under different P_{H_2O} conditions, illustrating the distinct changes as a function of temperature: *x*, *y* and *z* axes represent 12-23º 2θ, intensity (cps), and temperature (#1-67, in sequence of 23, 50, 75, 100, 110, 120, 130, 140, 150, 160, 170, 180, 190, 200, 210, 220, 230, 240, 250, 260, 270, 280, 290, 300, 310, 320, 330, 340, 350, 360, 370, 380, 390, 400, 390, 380, 370, 360, 350, 340, 330, 320, 310, 300, 290, 280, 270, 260, 250, 240, 230, 220, 210, 200, 190, 180, 170, 160, 150, 140, 130, 120, 110, 100, 75, 50, and 23 ºC), respectively. The square, star, and circle symbols represent diffraction peaks of natrolite, α2-, and α1-metanatrolite, respectively. The black dashed line represents either the natrolite-to-α1/α2-metanatrolite reaction **(c-k)** or the natrolite-to-α1-metanatrolite reaction **(l-m)**. The red solid line represents the α2-metanatrolite-to-α1-metanatrolite reaction, which occurred at 350 ºC and was not dependent on P_{H_2O} conditions. At temperatures >350 ºC, the α2-metanatrolite diffraction peaks (stars) disappeared and only α1-metanatrolite (circles) remained. The white-dashed line represents the α1-metanatrolite-to-natrolite reaction, which occurred during rehydration. Plots **(a)**, **(b)** and **(n)** are orthogonal views; Plots **(c)** to **(m)** are viewed down the *y* axis. Diffraction peaks that have no labels belong to natrolite.

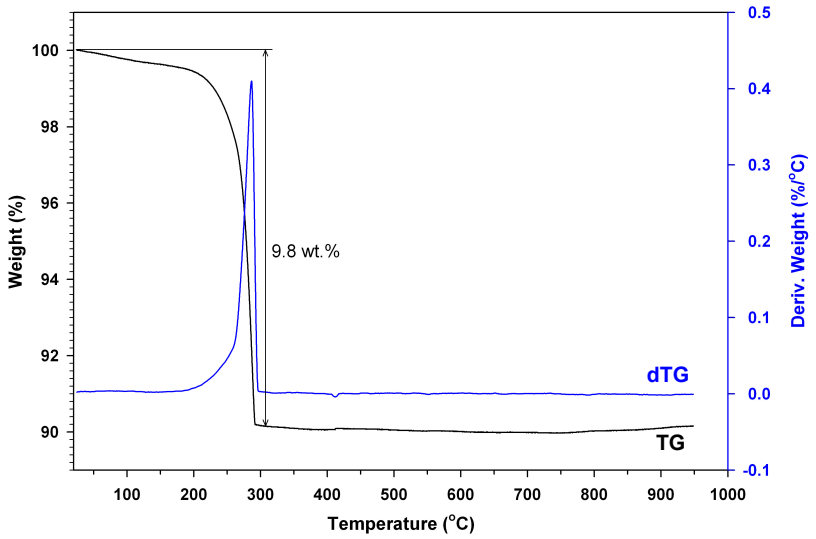

Figure 1.3. TG data for natrolite measured during dehydration (black curve). Sample mass was 11.5(2) mg. Measurement was made at ambient *RH* conditions (~40-50% *RH*) with 1 ºC/min heating rate. The first derivative of the black TG curve is given by the blue curve labeled dTG. The inflection temperature (i.e., the maximum rate of weight change, representing a peak in the dTG plot) is at ~285 ºC.

existence of different transformation paths is apparent. When measurements were made under low-P_{H_2O} conditions (i.e., below ~15 mbar P_{H_2O}; Figs. 1.2a-k), a transition from natrolite-to-α1/α2-metanatrolite occurred, whereas when measurements were made under high-P_{H_2O} conditions (i.e., above ~20 mbar P_{H_2O}; Figs. 1.2l-n), a direct transition from natrolite-to-α1-metanatrolite was observed. Both phase transitions are 1st-order in character with a discontinuous change in the unit-cell parameters and structures (i.e., the natrolite structure "snaps" into the α1- and/or α2-metanatrolite structures above transition temperatures). Both α1- and α2-metanatrolite are completely dehydrated phases, and α2-metanatrolite transforms to α1-metanatrolite (via a 1st-order transition) on further heating, irrespective of the P_{H_2O} of the environment. Above 350 ºC, all α2-metanatrolite reflections are absent (Figs. 1.2c-j; red solid lines). It is noteworthy that this "hidden" natrolite-to-α1/α2-metanatrolite phase transition can only be observed when P_{H_2O} is lower than ~15 mbar (corresponding to ~50% *RH* at ambient conditions). At high-P_{H_2O}, the hydrous natrolite phase is stabilized to higher temperatures at which the α2-metanatrolite phase field no longer exists, and natrolite transforms directly to α1-metanatrolite without passing through α2-metanatrolite. Kinetically, this result demonstrates that P_{H_2O} affects not only the temperature but also the nature of structural phase transitions in natrolite. Understanding the bonding interactions among H_2O molecules, Na^+ cations, and framework oxygens in the natrolite channel system during dehydration is key to pinpointing the phase-transition mechanism(s) and to clarifying why and how the response of natrolite structure is a function of P_{H_2O} and temperature.

During rehydration (cooling), α1-metanatrolite transforms back to natrolite at temperatures ~60 °C lower than the transition temperatures during dehydration (Figs.1.2d-m;

white dashed lines). The temperature gap between dehydration and rehydration represents hysteretic behavior, which is likely due to the great modifications of the natrolite framework system upon dehydration. (The hysteresis phenomenon will be discussed in Chapter 5). There is no evidence of recurrence of α2-metanatrolite during rehydration, suggesting that α2-metanatrolite is a metastable phase, and it further transforms to the thermodynamically stable phase, α1-metanatrolite, at elevated temperatures. Thus, at low-P_{H_2O}, natrolite fails to transform to the thermodynamically stable state and partially undergoes a structurally easier transformation to α2-metanatrolite. This reaction occurs only at lower temperatures, probably because the structural configuration of α2-metanatrolite is kinetically more accessible than α1-metanatrolite. The "lifetime" of α2- metanatrolite depends on the detailed temperature and P_{H_2O} conditions, and it remains for a finite period before irreversibly transforming to α1-metanatrolite. Higher temperature and P_{H_2O} decrease the "lifetime" of α2-metanatrolite and increase the probability for natrolite to overcome the energy barriers on the path to α1-metanatrolite. Thus, one can visualize that with increasing temperature and P_{H_2O}, α2-metanatrolite leaves the zone of reversibility and relaxes irreversibly to a thermodynamically favored phase, α1-metanatrolite. According to XRD results, the maximum temperature and P_{H_2O} conditions for the occurrence of α2-metanatrolite during dehydration are 350 °C and ~15 mbar P_{H_2O}.

1.2.2 Structural details of α1- and α2-metanatrolite and their relationships to natrolite

From a crystal structural point of view, α1- and α2-metanatrolite have different distortions of their tetrahedral framework around the shared oxygen vertex, coupled with different Na^+ cation positions (Fig. 1.4). α1-metanatrolite has *F*112 symmetry (or the standard space group setting *C*121) which is a subgroup of *Fdd*2 symmetry. The two d-glide

reflections are missing upon dehydration and the rotation angle (ψ, after Pauling 1930) of the T_5O_{10} chain around the *c* axis in α1-metanatrolite is 34.7°. In comparison with natrolite (ψ = 24.1º), the two adjacent T_5O_{10} chains rotate in opposite directions by ~10.6º in α1-metanatrolite (Fig. 1.4a). α2-metanatrolite remains in *Fdd*2 symmetry upon dehydration. The angle ψ in α2-metanatrolite is 28.2º, meaning that the T_5O_{10} chain in α2-metanatrolite rotates only 4.1º (Fig. 1.4b). The larger amount of chain rotation around the O2 hinges in α1-metanatrolite leads to a greater contraction in the *a* and *b* unit-cell parameters. It also causes the smaller Si-O2-Al angles and the smaller channel size than those found in α2-metanatrolite (Fig. 1.4; Si-O2-Al angles are outlined in red). This rotation mechanism, driven by decreasing *a* and *b* unit-cell parameters as the rotation angle (ψ) increases, was originally postulated by Pauling (1930) and Hey (1932). Furthermore, small T-O-T angles (T = Al or Si) are energetically unfavorable in tectosilicates. Of 548 Si-O-Si angles measured in silicates and SiO_2 polymorphs, only 31 (i.e., 5.7%) are smaller than 130° (Baur 1980). On occasion Si-O-Al angles have been observed to be smaller than Si-O-Si angles, but even in these cases, values below 125° are relatively rare (Joswig and Baur 1995). Thus, the small Si-O2-Al angles in α1-metanatrolite are energetically unfavorable. These small angles must be stabilized by strong additional interactions of O2 with the extraframework Na^+ cations (Fig. 1.4a), as discussed by Baur and Joswig (1995). Reduction in the minimum energetically feasible T-O-T angles by increasing the coordination of bridging oxygens with other cations (such as Na^+, K^+, Ca^{2+}, or H^+) has also been discussed in feldspars (Geisinger *et al.* 1985). For α2-metanatrolite, however, a different mechanism operates. The α2-metanatrolite framework has a larger channel size (i.e., the framework does not contract as much as in α1-metanatrolite), with its guest Na^+ cations positionally disordered between two distinct sites

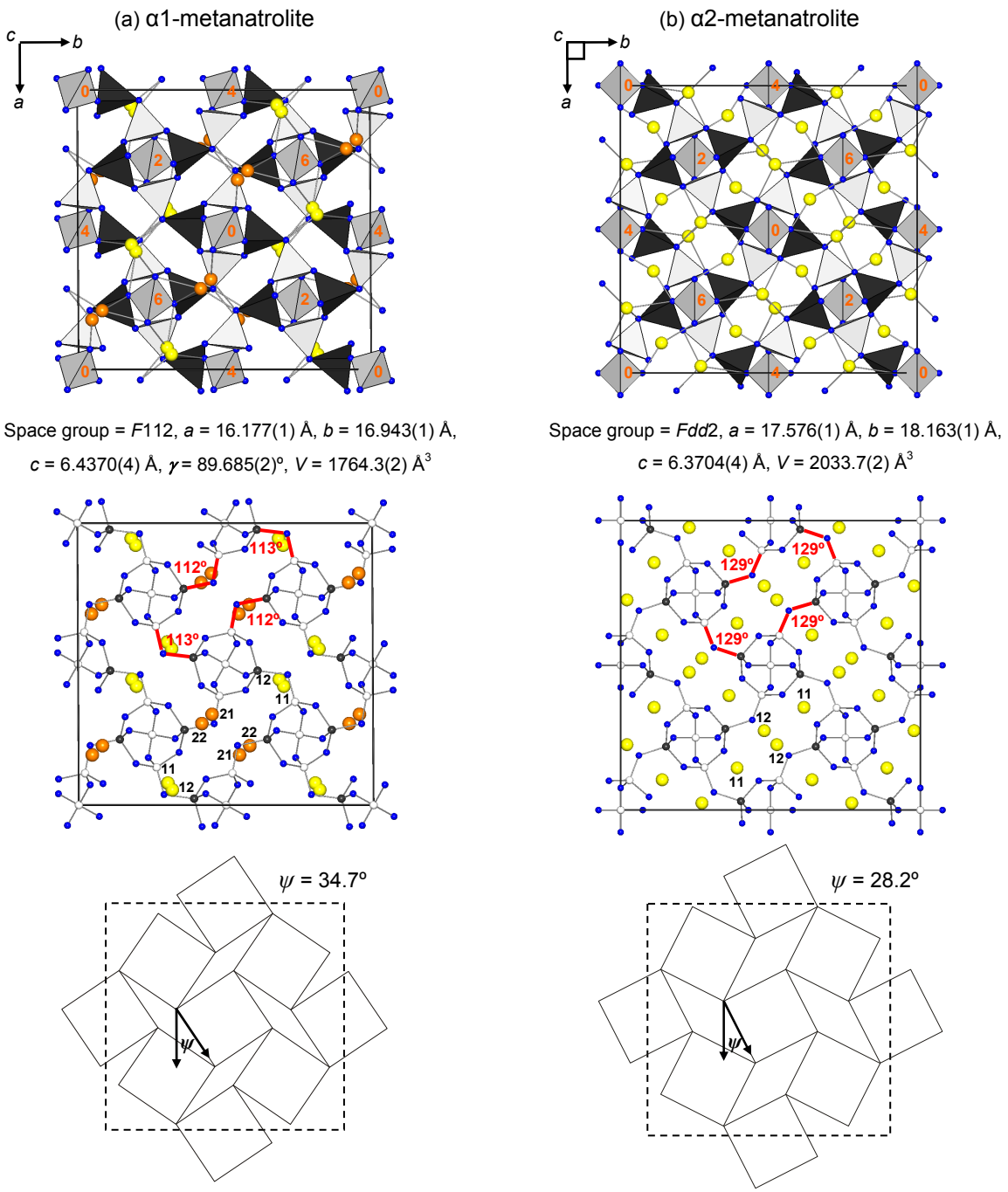

Figure 1.4. Refined crystal structures of **(a)** α1-metanatrolite and **(b)** α2-metanatrolite, viewed down the cross-linked chains. In α1-metanatrolite, Na^+ cations are yellow (Na11 and Na12) and orange (Na21 and Na22) spheres. Site occupancies for Na(11), Na(12), Na(21) and Na(22) are 0.49(2), 0.51(2), 0.27(1), and 0.73(1), respectively. In α2-metanatrolite, Na^+ cations are yellow spheres (Na11 and Na12). Site occupancies for Na(11) and Na(12) are 0.57(2) and 0.43(2), respectively. The Si-O2-Al angles are outlined in red. The chain rotation angles (ψ) are shown in the schematic drawing. Note that the Si-O2-Al angle and the size of unit-cell decrease as the chain rotates. Other symbols are the same as in Figure 1.1.

close to the center of the channels (Fig. 1.4b). The Si-O2-Al angle of α2-metanatrolite is 129º, near the minimum possible values of pure Si-O-Al hinge angles (125º) for a stable configuration without strong bonds to other cations such as Na^+. This contrast with α1-metanatrolite implies that when natrolite collapses to α2-metanatrolite, the host framework retains a tendency not to form Si-O-Al angles less than the 125º minimum angle if the extraframework Na^+ cations have not yet migrated closer to framework oxygens. α2-metanatrolite appears to be a metastable structural configuration between the two global minima of the low- and high-temperature phases, natrolite and α1-metanatrolite, respectively.

Tetrahedral twisting within the T_5O_{10} chain occurs in both α1- and α2-metanatrolite. As the tetrahedra cannot be compressed significantly along the chain direction in NAT-topology zeolites, twisting of the tetrahedra around the oxygen vertex is an alternative way to shorten the *c* axis (Alberti and Vezzalini 1983). Based on the *c* unit-cell parameter of α1- and α2-metanatrolite (Fig. 1.4), the amount of chain twisting in α2-metanatrolite is slightly larger than in α1-metanatrolite. This perhaps also represents an energy minimization strategy in the natrolite framework and indicates a cooperation between the framework and its extraframework Na^+ cations.

1.3 Chapter summary

The crystal structures of natrolite and its dehydrated high-temperature phases (α1- and α2-metanatrolite) have been determined from powder X-ray diffraction measurements. The response of the natrolite crystal structure to dehydration and rehydration shows two different phase transition paths, depending on the P_{H_2O}, with only α1-metanatrolite occurring at elevated P_{H_2O}, and a new phase, α2-metanatrolite occurring at low-P_{H_2O}. A low-P_{H_2O}

atmosphere allowed access to a phase space that was not accessible at higher P_{H_2O} because dehydration at higher P_{H_2O} was suppressed to higher temperatures, thereby stabilizing hydrated natrolite to higher temperatures. Both phase transitions are 1st-order in character. Reaction from natrolite-to-α1-metanatrolite-natrolite is reversible but is strongly hysteretic. Reaction from natrolite-to-α1/α2-metanatrolite-to-α1-metanatrolite-natrolite is also reversible and hysteretic. However, once α2-metanatrolite leaves the zone of reversibility, it does not recur during rehydration, indicating that α2-metanatrolite is a metastable phase. The appearance of α2-metanatrolite directly reflects the manner in which the aluminosilicate framework of natrolite responds to the migration of its extraframework Na^+ cations. A different way to think of this phenomenon is by considering the manner in which host-guest interactions drive phase transitions. Here, the host is the aluminosilicate framework of natrolite and the guests are Na^+ cations and H_2O molecules. The strength of host-guest interactions is a function of temperature and P_{H_2O}, and interactions are likely coupled (cooperative) with framework symmetry constraints through direct bonding interactions. The extent of coupling influences the range of energetically feasible T-O-T angles and the flexibility of the framework, and it thus determines the phase transition behaviors upon dehydration. Accordingly, other zeolites, especially zeolites having strong interactions between their H_2O molecules and extraframework cations (usually zeolites having extraframework cations at fixed positions and low-entropy H_2O molecules in the channel system) should exhibit similar temperature- and P_{H_2O}-dependent phenomena. A clear understanding of the interplay between the host structure and the guest cation-H_2O complexes and their behaviors as a function of temperature and P_{H_2O} is central to understanding many of the fundamental themes in zeolite science.

CHAPTER 2

Temperature- and P_{H_2O}-dependent structural phase transitions in the zeolite scolecite

Scolecite ($CaAl_2Si_3O_{10} \bullet 3H_2O$; Z = 4 or 8), a calcium zeolite, has the same aluminosilicate framework configuration and ordered (Al,Si) distribution as in natrolite. Scolecite belongs to the NAT group, and the NAT-topology framework consists of the so-called T_5O_{10} building chains of (Al,SiO_4)-tetrahedra running parallel to the *a* axis (base-centered setting) or the *c* axis (face-centered setting, see Fig. 1.1a or Figs. 0.2B and 1.1A in Gottardi and Galli 1985). In the *C*1*c*1 space group setting (Z = 4), each T_5O_{10} chain is connected to a neighboring chain at the same height or at height differing by 1/2 *a*, forming a three-dimensional network and elliptical channels occupied by charge-balancing Ca^{2+} cations and H_2O molecules (Fig. 2.1a). In comparison with natrolite (*Fdd*2), scolecite possesses a lower symmetry (*F*1*d*1 with Z = 8 or in the standard space group setting *C*1*c*1 with Z = 4). The reduction in symmetry from orthorhombic (*Fdd*2) to monoclinic (*F*1*d*1 or *C*1*c*1) is due to the arrangements of extraframework Ca^{2+} cations and H_2O molecules in the channel system. To maintain charge balance in the scolecite framework, the two Na^+ cations in natrolite channel have been replaced by one Ca^{2+} cation with additional H_2O (Ow3) occupying the position similar to the missing Na site in natrolite, i.e., $Na_2(H_2O)_2 \leftrightarrow Ca(H_2O)_3$. The 2-fold screw axes (2_1) operating on the Na^+ cations in natrolite do not occur in scolecite because there is only one Ca^{2+} cation per unit-length along the *c* axis. However, the local Ca coordination is still similar to that of Na in the natrolite channel with Ow3 H_2O in the framework O plane, forming a pentagonal bipyramid (Fig. 2.1b). Three H_2O molecules

Scolecite ($Ca_4Al_8Si_{12}O_{40} \cdot 12H_2O$)

Space group = *C*1*c*1, *a* = 6.5262(1) Å, *b* = 18.9708(2) Å, *c* = 9.8449(2) Å, β = 109.974(1)°, *V* = 1145.55(4) Å^3

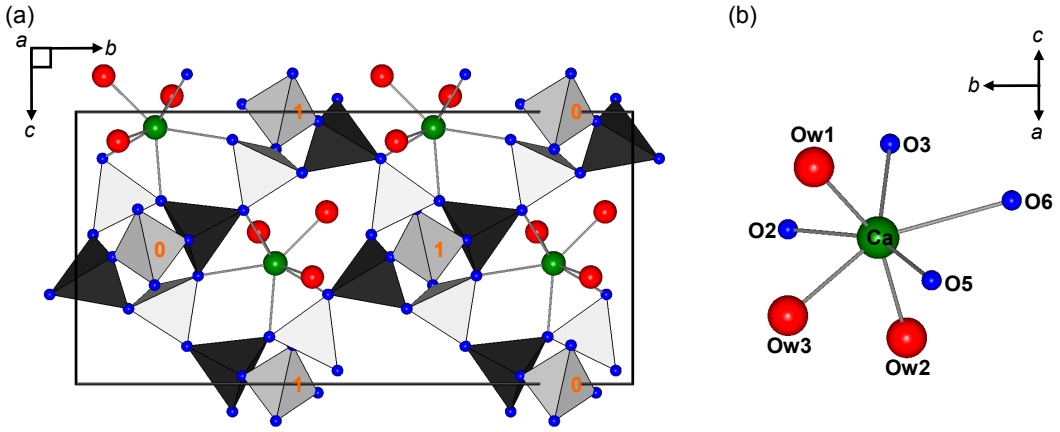

Figure 2.1. Refined crystal structure of scolecite at 23 ºC. **(a)** NAT framework viewed down the cross-linked chains. Numbers in the central tetrahedra indicate the height above (001) as multiples of *a*/2. **(b)** Local view of coordination of Ca^{2+} cations in the scolecite channel system. Si tetrahedra = gray; Al tetrahedra = black; oxygen atoms = blue spheres; Ca^{2+} cations = green spheres; H_2O molecules = red spheres; Bonds = solid gray lines.

(Ow1, Ow2 and Ow3) are ion-dipole attracted to one Ca^{2+} cation only, thereby each Ca polyhedron is isolated by a vacancy site along the *c* direction (i.e., in the form of -Ow1-Ca-Ow2-□-Ow1-). The crystal structure of scolecite was refined by Adiwidjaja (1972) and later by Fälth and Hansen (1979), Joswig *et al.* (1984), Kvick and Ståhl (1985), Stuckenschmidt *et al.* (1997), Kuntzinger *et al.* (1998), and Comodi *et al.* (2002).

Studies on scolecite dehydration and accompanying structural changes were first described by Rinne (1923), and the structure of the partially dehydrated phase named metascolecite ($CaAl_2Si_3O_{10} \bullet 2H_2O$; Z = 4 or 8) was later determined by Adiwidjaja (1972). More detailed studies on the dehydration behaviors were made by van Reeuwijk (1974) and Ståhl and Hanson (1994). The dehydration of scolecite occurs in two steps. As described by Ståhl and Hanson (1994), the first dehydration begins at ~137 °C with a gradual expulsion of Ow3 H_2O molecules. When the Ow3 occupancy decreases to ~0.5, the framework of scolecite undergoes a displacive phase transition to the metascolecite structure and the crystal symmetry changes from *F*1*d*1 (*C*1*c*1) to *Fd*11 (*Cc*11). The migration of extraframework Ca^{2+} cations to new coordination spheres occurs simultaneously with framework modification, and both the framework modifications and extraframework cation migrations occur as a result of dehydration (i.e., loss of Ow3 H_2O molecules). The original seven-coordinated Ca polyhedron drops to a six-coordinated configuration after the loss of the Ow3 H_2O molecule, and each Ca^{2+} cation is coordinated by four framework oxygens (O) and two remaining H_2O molecules (Ow1 and Ow2), in the form of a distorted octahedron. After the first dehydration reaction to metascolecite, this phase is stabilized during continued heating and does not show a significant reduction in H_2O content until the second step of dehydration is approached. The second dehydration occurs at ~325 °C and is accompanied by a large reduction in the

remaining H_2O molecules, which reduces the Ca coordination sphere to below six and the metascolecite structure is destroyed, creating an X-ray amorphous phase (I refer to this phase as the amorphous T_5O_{10} phase). It has been suggested by Artioli (1999a, 1999b) and Cruciani *et al.* (2003) that the lower limit in the Ca coordination number for several Ca-bearing zeolites appears to be six and phase transitions to an amorphous phase are triggered when the Ca coordination sphere drops below six due to dehydration. The thermogravimetric analysis made by van Reeuwijk (1974) also showed two steps of dehydration with virtually no weight loss between the two main dehydration steps, consistent with results of Ståhl and Hanson (1994).

As emphasized in the introduction chapter, the structures of zeolites are known to be very responsive to changes in temperature, pressure, and the partial pressure of H_2O (i.e., P_{H_2O} or relative humidity, *RH*), because their extraframework cations and H_2O molecules can directly communicate and exchange with the external environments. However, the combined effects of temperature and P_{H_2O} on scolecite dehydration have not been previously studied. P_{H_2O} conditions of previous studies were not controlled and inconsistent dehydration/ structural transition temperatures are typically found in the literature, reflecting the dependence on the surrounding P_{H_2O} during the measurements (a parallel example is the effect of CO_2 partial pressure on $CaCO_3$ decomposition). In addition, a recent successful study on temperature- and P_{H_2O}-dependent structural phase transitions in natrolite showed a remarkable result indicating that the evolution of the crystal structure of natrolite as a function of temperature showed two different phase transition paths, depending on P_{H_2O}, with only α1-metanatrolite occurring when heating at elevated P_{H_2O} and α2-metanatrolite occurring at low-P_{H_2O} (see Wang and Bish 2008, 2010 or Chapter 1). A low-P_{H_2O} allows

natrolite to undergo a "hidden phase transition" that does not occur at higher P_{H_2O}. This natrolite study demonstrated that using P_{H_2O} (or *RH*) control to promote or suppress dehydration can open a window to new energy minimization processes, providing the possibility to observe previously unseen structural phase transitions. Accordingly, scolecite should exhibit similar temperature- and P_{H_2O}-dependent phenomena. The primary purpose of this chapter is to discuss whether or not a combined temperature and P_{H_2O} effect influences the phase transition behaviors in scolecite. New results on scolecite phase transition behaviors during dehydration and rehydration are presented in this chapter. This original work has not been published and hence descriptions of the structural modeling methods are discussed in this chapter.

2.1 Samples and experimental methods

The scolecite specimen used in this study is from Maharashtra, India, with a composition of $Ca_{7.81}Al_{15.62}Si_{24.30}O_{80} \bullet 24.51.H_2O$ (or with half Z), an average of electron microprobe analyses of crystals in several thin sections. The sample was crushed into a fine powder (<38 μm) using a Retsch Micro-Rapid mill with agate motor and pestle under acetone. Two types of measurements were made in order to investigate the possible dependence of the phase transition behaviors in temperature and P_{H_2O} spaces and to characterize the local structure of the amorphous T_5O_{10} phase formed at temperatures >325 °C (the structure of this phase has not been previously described). The first studies employed laboratory X-ray powder diffraction (XRD) measurements with *in-situ* controlled-temperature and -P_{H_2O} to monitor structural changes as a function of changing environmental parameters (i.e., temperature and P_{H_2O}). The second type of study employed synchrotron X-

ray total scattering measurements with pair distribution function (PDF) analysis, used as a local probe to characterize the local structure of the amorphous T_5O_{10} phase. In addition to the above two measurements, thermogravimetric (TG) analyses conducted under ambient *RH* conditions were made to characterize the bulk dehydration phenomena, and these results were combined with the structural data obtained with XRD measurements.

2.1.1 Laboratory X-ray powder diffraction analysis

Laboratory XRD data were measured using a Bruker D8 Advance X-ray diffractometer (Cu Kα radiation), equipped with a Vantec position-sensitive detector, an Anton-Paar TTK 450 heating stage, and a sample environmental chamber. The TTK 450 stage provides the opportunity for measuring data as a function of temperature up to 450 ºC, and the sample environment humidity was controlled via gas flow into and out of the sample chamber using an automated V-Gen dew point/*RH* generator (InstruQuest Inc.). Measurements were made under controlled-P_{H_2O} conditions ranging from ~0.1-23 mbar (corresponding to ~0.5-82% *RH* at 23 ± 1 °C and 1 bar) down to ~$10^{-0.8}$-$10^{-2.7}$ mbar (roughing pump vacuum condition, $10^{-3.8}$ bar), at sample temperatures up to 450 °C, measuring in 25 ºC increments from room temperature to 100 ºC and in 10 ºC increments from 100 to 450 °C. The lower limit of P_{H_2O} ($10^{-2.7}$ mbar) under vacuum conditions was estimated based on the ambient *RH* at the time of measurement (i.e., ~48% *RH* at 22 °C; scaled by a factor of $10^{-3.8}$). On the other hand, the upper limit of P_{H_2O} ($10^{-0.8}$ mbar) under vacuum conditions was estimated based on the assumption that all the residual gas remaining in the cell was H_2O vapor. Samples were mounted in one of two ways, as a thin-layer slurry mount and in a 0.2-mm depth cavity mount, and the different mounting methods influenced reaction kinetics. The much larger sample mass (~20-30 mg) and thicker sample used in a cavity mount

increased the opportunity for the P_{H_2O} to increase in intercrystallite pore spaces, which inhibited the temperature at which phase transitions began and resulted in longer times required for completion of dehydration. An equilibrium method was applied for both mounting methods which involved exposing a specimen to a controlled-P_{H_2O} environment and heating to a given temperature, waiting, and measuring until no further structural changes occurred, and then heating to successively higher temperatures (at a fixed P_{H_2O} value) in the same manner. Data obtained with thin-layer slurry mounts (11º to 33º 2θ) using the same heating procedure but under different P_{H_2O} conditions were compared qualitatively, because the thin-layer slurry mounts minimized build-up of P_{H_2O} in intercrystallite pore spaces, thereby providing a more accurate picture of the phase transition behaviors. Data measured using cavity mounts (11º to 100º 2θ) were used for structural determination and subsequent Rietveld refinements, due to the more accurate intensity information obtained from the cavity mounts. This approach allowed the determination of the phase transition behaviors of scolecite under specific environmental conditions, and subsequent structural analyses gave information on the average crystal structure as a function of temperature and P_{H_2O}. The software package TOPAS-Academic v.4.1 (Coelho 2007) was used for all structural analyses.

2.1.2 Synchrotron X-ray total scattering

Data for X-ray PDF analysis were obtained using the RA-PDF technique (Chupas *et al.* 2003), utilizing a monochromatic high-energy (0.2127 Å, 58.3 keV) X-ray beam selected from a Si (311) Laue monochromator crystal at beamline 11-ID-B at the Advanced Photon Source, Argonne National Laboratory. Scolecite powder was loaded into a glass capillary (1 mm inner diameter and 1.1 mm outer diameter) under room conditions. The sample capillary

was placed in a sample-environment cell mounted directly on the goniometer (Chupas *et al.* 2008). The entire sample assembly was heated under ambient humidity conditions (31 ± 1% *RH* at 24 ± 1 °C and 1 bar; corresponding to ~9-10 mbar P_{H_2O}), and temperature was ramped continuously from 25 to 450 °C with 1 ºC/min heating rate. Scattering data were collected with 1 min exposure times, repeated 425 times in a manner to synchronize with the temperature ramp. After 450 °C, the sample temperature was quickly raised to 500 °C, waiting for 10 min, and then measured with a 1 min exposure time. An amorphous silicon flat-panel detector (allows many images to be efficiently averaged with little overhead, to improve counting statistics) was positioned at 156.4(1) mm from the sample and this small sample-to-detector distance ensured that data could be accumulated over a wide 2θ or Q range (Chupas *et al.* 2003). Parasitic scattering from the atmosphere and capillary were measured using the same temperature ramp, duplicating the assembly without a sample. This ensured measurement of data that were rigorously normalized with an accurate background subtraction. The program Fit2D (Hammersley *et al.* 1996) was used to integrate the raw scattering images and data were then converted into intensity versus Q plot ($\boldsymbol{Q}$ is momentum transfer vector, $Q = |\boldsymbol{Q}| = 4\pi sin\theta/\lambda$). The program PDFgetX2 (Qiu *et al.* 2004) was used for data treatment. The total scattered intensity, $I(Q)$, was corrected for background, Compton scattering, and absorption, and was then converted to normalized total scattering structure function, $S(Q)$. The data were then terminated at $Q_{max} = 17$ Å^{-1} to obtain the corresponding real-space reduced pair distribution function, $G(r)$. The program PDFgui (Farrow *et al.* 2007) was used for quantitative structural refinement of the reduced pair distribution function.

2.1.3 Thermogravimetric analysis

TG experiments were performed using a TA Instruments 2960 TG analyzer. Analyses made in this study were conventional isobaric experiments at 1 bar (no vacuum TG analyses). The dynamic method (i.e., heating the sample powder continually at a constant rate while recording the weight loss) was performed with a 1 °C/min temperature heating rate. The sample environment was under ambient humidity conditions, and the humidity (~15-20% *RH*, corresponding to ~4-6 mbar P_{H_2O} at 22 ± 1 ºC) was recorded before and after measurements. Experiments were designed to measure the H_2O content of scolecite as a function of temperature. About 11.5(2) mg of scolecite powder was evenly distributed onto a alumina sample pan. The total weight change of the sample was monitored while heating to 950 °C under ambient *RH* conditions.

2.2 Results and discussions

2.2.1 Scolecite phase transitions in P_{H_2O} and temperature spaces

Figure 2.2 illustrates scolecite dehydration and accompanying phase transition behaviors. The existence of distinct different transition paths was apparent especially when scolecite was heated under low-P_{H_2O} conditions (the scolecite and metamesolite phases are labeled with square and star symbols; the newly observed phases, namely x2- and x1-metamesolite, are labeled with x2 and x1 symbols). When measurements were made under high-P_{H_2O} conditions (Figs. 2.2h-n), the structural transitions in scolecite occurred in two steps and the transition temperatures gradually increased with increasing P_{H_2O}, indicating that these structural changes corresponded with dehydration reactions. Similar to previous studies (van Reeuwijk 1974; Ståhl and Hanson 1994), the first transformation was a scolecite-to-

metascolecite displacive phase transition (Figs. 2.2h-l; black dashed lines). It occurred at 180 °C when P_{H_2O} was 3.88(7) mbar (controlled at 15.1 ± 0.1% *RH*, 23 ± 1 °C, and 1 bar), it increased to 190 °C when P_{H_2O} was 5.2(1) mbar (controlled at ~20.0 ± 0.1% *RH*, 23 ± 1 °C, and 1 bar), and it continuously increased to 220 °C when P_{H_2O} was 22.5(5) mbar (controlled at 81.7 ± 0.1% *RH*, 23 ± 1 °C, and 1 bar). The transformation of scolecite-to-metascolecite is 1st-order in character with discontinuous shifts in the XRD peaks, attributed to changes in the scolecite structure and unit-cell parameters upon dehydration. Upon further heating to higher temperatures, the second phase transition to the amorphous T_5O_{10} phase occurred (Figs. 2.2h-l; white dashed lines). This second transformation also showed dependence on P_{H_2O}, and not all the metascolecite reflections disappeared upon transformation. Some residual reflections were still seen, especially under a high-P_{H_2O} environment (e.g., Figs. 2.2k-n). This may be due to the higher hydration energy of Ca^{2+} cations, and H_2O molecules may be strongly held by both Ca^{2+} cations and the metascolecite frameworks after the first step of dehydration. The corresponding TG weight loss curve (Fig. 2.3) measured under ~15-20% *RH* shows two steps of dehydration, with the primary and secondary inflection temperatures (the maximum rate of weight change) at 188 and 356 ºC, respectively, comparing well with XRD observations made under ~20% *RH* conditions (Fig. 2.2i). These results also support the idea that the structural phase transitions in scolecite are trigged by dehydration reactions. The weight loss based on TG measurement was 4.6 wt.% at ~220 °C, corresponding to the loss of 4 out of 12 H_2O molecules, and was 10.7 wt.% at ~400 °C, corresponding to the loss of 10 out of 12 H_2O molecules (Fig. 2.3). Above 400 °C, continued weight loss occurred, probably indicating the loss of relic-OH groups that formed upon or after the transformations to amorphous T_5O_{10} (OH group formation in the dehydration of scolecite has been studied by

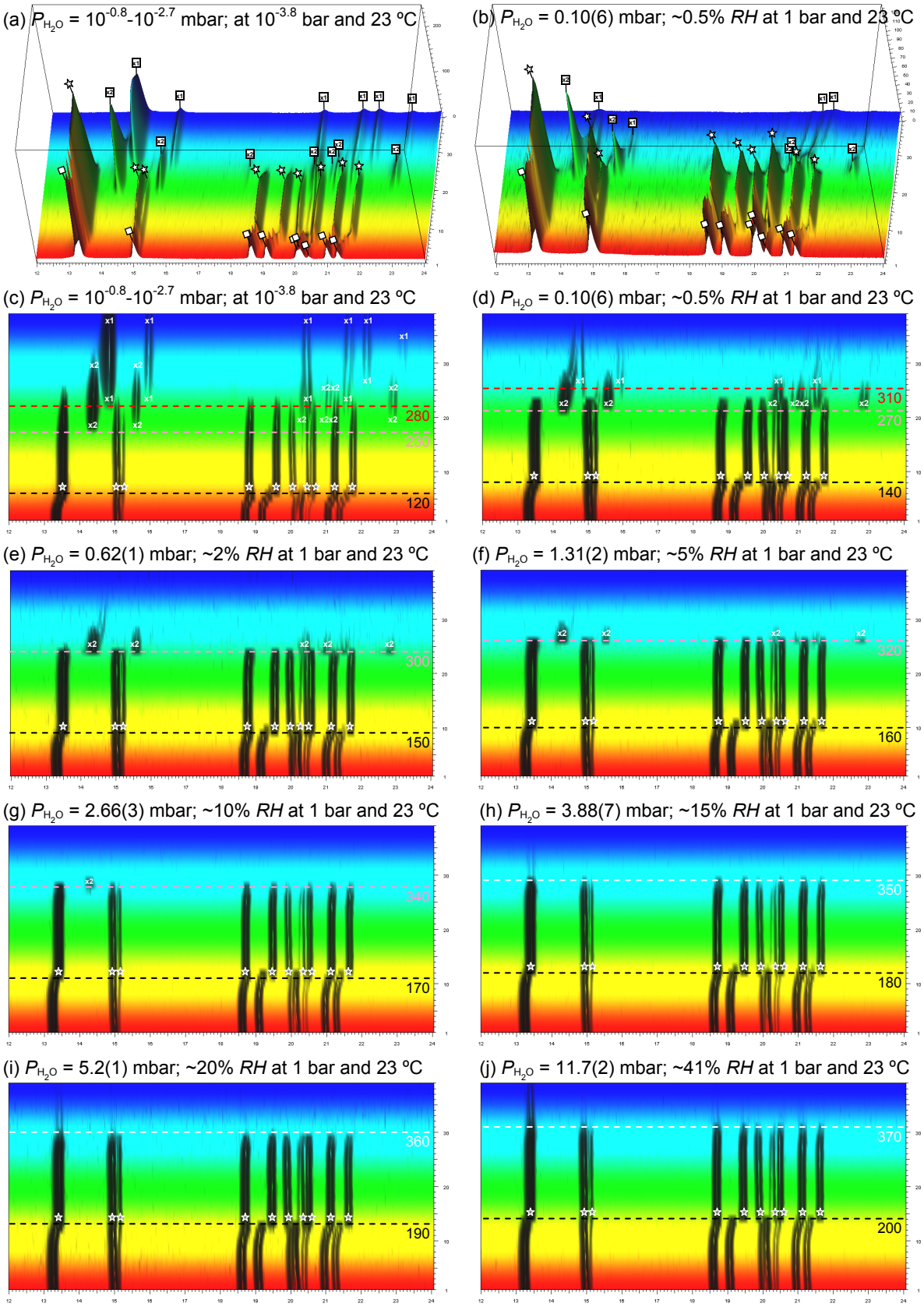

Figure 2.2. Continued on next page.

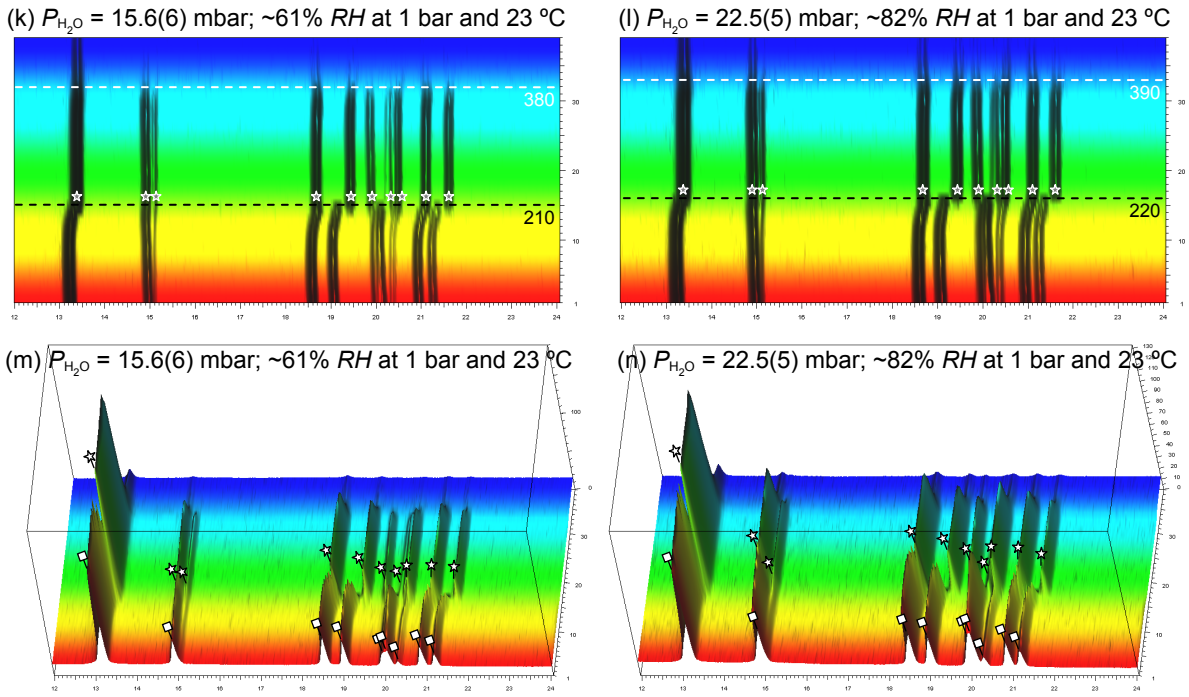

Figure 2.2. Temperature-resolved 3D-XRD patterns for scolecite measured under different P_{H_2O} conditions, illustrating the distinct changes as a function of temperature: *x*, *y* and *z* axes represent 12-24º *2θ*, intensity (cps), and temperature (#1-39, in sequence of 23, 50, 75, 100, 110, 120, 130, 140, 150, 160, 170, 180, 190, 200, 210, 220, 230, 240, 250, 260, 270, 280, 290, 300, 310, 320, 330, 340, 350, 360, 370, 380, 390, 400, 410, 420, 430, 440, and 450 ºC), respectively. The square, star, x1, and x2 symbols represent diffraction peaks of scolecite, metascolecite, x1-, and x2-metascolecite, respectively. The black dashed line represents the scolecite-to-metascolecite reaction **(c-l)**. The pink dashed line represents the metascolecite-to-x2-metascolecite reaction **(c-g)**. The red dashed line represents the x2-metascolecite-to-x1-metanatrolite/amorphous T_5O_{10} reaction **(c** and **d)**, which only occurred under low-P_{H_2O} conditions. The white dashed line represents the reaction going directly from metascolecite-to-amorphous T_5O_{10} **(h-l)**. Plots **(a)**, **(b)**, **(m)** and **(n)** are orthogonal views; Plots **(c)** to **(l)** are viewed down the *y* axis. Diffraction peaks that have no labels in the low-temperature region belong to scolecite. Note the increased background in plots **(m)** and **(n)**, which indicates formation of the amorphous T_5O_{10} phase upon dehydration.

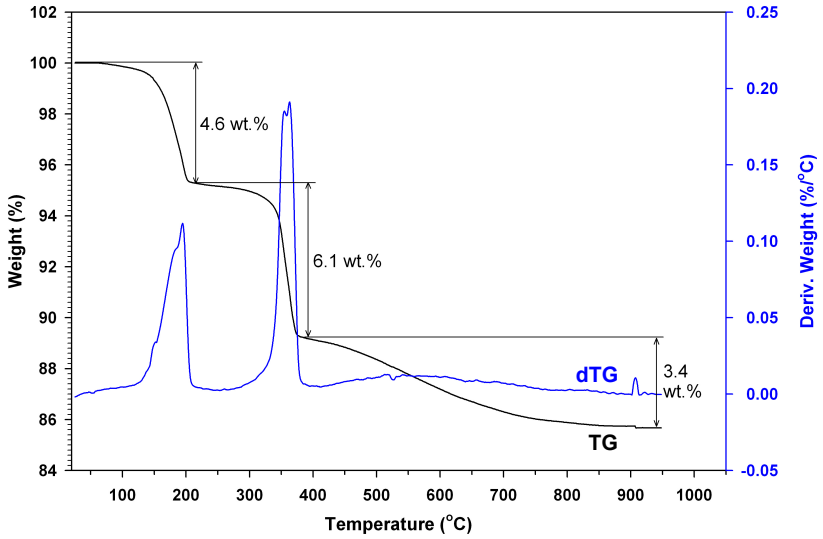

Figure 2.3. TG data for scolecite measured during dehydration (black curve). Sample mass was 11.5(2) mg. Measurement was made under ambient *RH* conditions (~15-20% *RH*) with 1 ºC/min heating rate. The first derivative of the black TG curve is given by the blue curve labeled dTG. The primary and secondary inflection temperatures (i.e., the maximum rate of weight change, representing a peak in the dTG plot) are at ~188 and ~356 ºC, respectively.

Mirzai 1985 and Mirzai *et al.* 1989). The total weight loss up to 950 ºC was 14.1(4) wt.%, in close agreement with the results of H_2O content determined by microprobe analysis, i.e., 13.8(2) wt.%.

Surprisingly, heating scolecite under low-P_{H_2O} conditions yielded different phase transitions (Figs. 2.2a-g). The first was still the 1st-order displacive phase transition to a metascolecite phase, which is the same as that observed under high-P_{H_2O} conditions but it occurred at lower temperatures (Figs. 2.2c-g; black dashed lines). Continued heating to higher temperatures caused metascolecite to undergo another 1st-order displacive phase transition with a discontinuous change in unit-cell parameters to a new unknown-structure phase (Figs. 2-2c-g; pink dashed lines). The structure of metascolecite "snapped" into this unknown structure beginning at 230 °C when P_{H_2O} was ~$10^{-0.8}$-$10^{-2.7}$ mbar, increasing to 340 °C when P_{H_2O} was 2.66(3) mbar (controlled at 10.1 ± 0.1% *RH*, 23 ± 1 °C, and 1 bar). This unknown phase (termed x2-metascolecite by us) was clearly observed under low-P_{H_2O} conditions (e.g., Figs. 2.2a-e) and coexisted with metascolecite phase over a small temperature interval. The diffraction intensities of the x2-metascolecite phase reached a maximum and the intensities of the metascolecite phase dropped to zero at ~20 °C above the transformation temperature. Upon continuous heating to higher temperatures, diffraction intensities of the x2-metasclecite phase gradually decreased and a third 1st-order displacive phase transition to another unknown phase (termed x1-metascolecite by us, see Figs. 2.2c-d; red dashed lines) occurred. Diffraction peaks were broadened during this third transformation, together with an increase in the background (i.e., at this stage the diffraction pattern is composed of a mixture of two phases, x1-metascolecite and the amorphous T_5O_{10} phase). The temperature at which the reflections of x2-metascolecite began to disappear

depend on the P_{H_2O}, indicating that x2-metascolecite is an intermediate partially dehydrated phase. Moreover, depending on the P_{H_2O}, the structure of x2-metascolecite may collapse into the amorphous phase before the transformation to x1-metascolecite (Figs. 2.2a-g).

During rehydration (data are not shown), the flexibility of the scolecite framework makes the scolecite-to-metascolecite reaction reversible, but the reaction is accompanied by noticeable transformation-induced lattice strains and/or strain-induced mosaicity reflected in the diffraction peak widths and intensities. The structures of x2- and x1-metascolecite are only partially reversible probably, in part, due to the formation of OH groups during the dehydration of scolecite. In addition, once the amorphous T_5O_{10} phase was formed (no matter whether at high- or low-P_{H_2O}), scolecite lost its rehydration ability and never transformed back to the original structure.

2.2.2 Phase transitions in scolecite analyzed by X-ray PDF

Based on qualitative inspection, the temperature-resolved PDFs of scolecite (Fig. 2.4) measured under ambient *RH* conditions (31 ± 1% *RH*) showed clear $G(r)$ changes at ~200 °C. Continued heating to ~375 °C caused a gradual decrease in the PDF $G(r)$ signals, and at 500 °C, $G(r)$ signals were damped at about r >8 Å (Fig. 2.4). These $G(r)$ variations provided clear evidence of the phase transitions of scolecite-to-metascolecite (at ~200 °C) and metascolecite-to-amorphous T_5O_{10} (at ~375 °C). These transformation temperatures are comparable to XRD observations made under similar *RH* conditions (e.g., Figs. 2.2i-j). In addition, from 375 to 450 °C, some residual metascolecite $G(r)$ signals were present along with amorphous T_5O_{10}, which yielded relatively weak and broad $G(r)$ intensities in the high-r region. At 500 °C, the PDF $G(r)$ signals suggested the disappearance of long-range order in

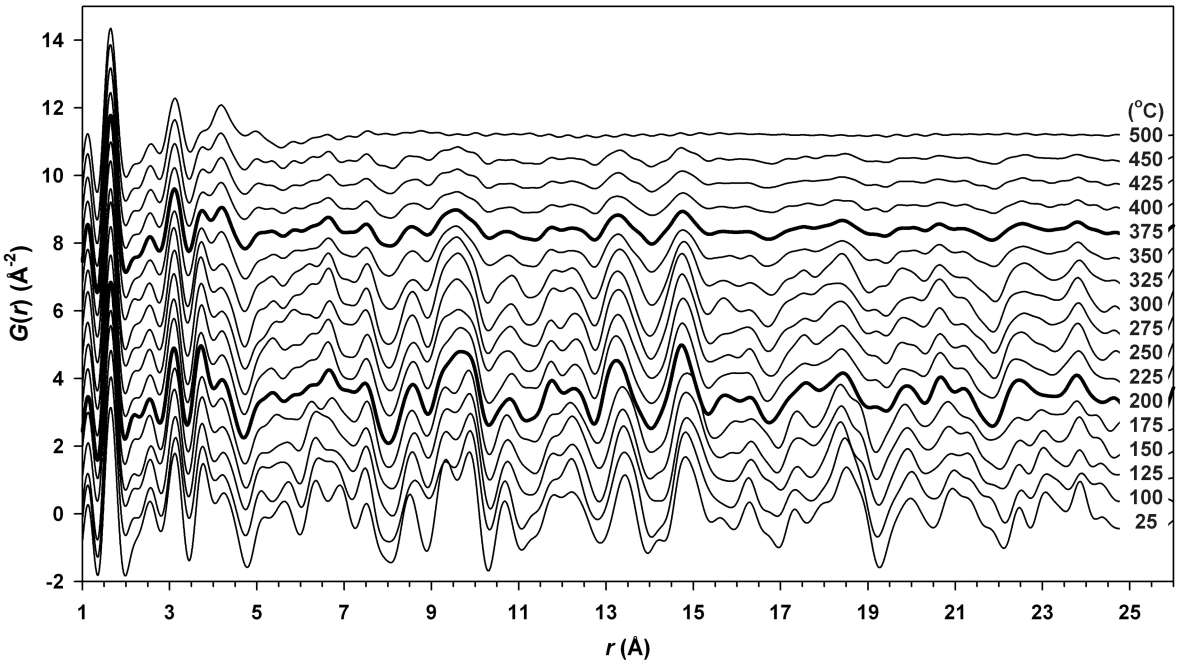

Figure 2.4. The reduced pair distribution functions, $G(r)$, obtained through direct Fourier transformation of the observed structure functions, $S(Q)$, are plotted and stacked in order of increasing temperature. The two bold $G(r)$ curves represent the scolecite-to-metascolecite (at 200 ºC) and the metascolecite-to-amorphous T_5O_{10} (at 375 ºC) transformations, respectively.

the structure and the remaining metascolecite phase completely transformed to an amorphous state.

As the PDF $G(r)$ represents the probability of finding an atom at a distance r from any reference atom and is defined as the sum over all atomic pairs within the model crystal, the first $G(r)$ peak centered at 1.65 Å represents the Si(Al)-O distances, the second peak in the r range of 2.3-2.8 Å represents a combination of the Ca-O, Ca-Ow, and O-O distances, and the third peak at 3.1 Å is from the Ca-Si(Al) distances and the first shell of the Si-Si(Al) distances (Fig. 2.4). Peaks below 1.4 Å and centered at 2.15 Å (Fig. 2.4) are termination ripples from the Fourier transform at a value of Q_{max} = 17 Å^{-1} (these termination ripples shifted when Q_{max} was dropped to 12 Å^{-1}). In the high-r region, the PDF $G(r)$ was difficult to interpret due to the complexity of the material. For example, the fourth peak at 3.75 Å is composed of the second shell of Si-Si, Si(Al)-O, Ca-Si(Al), Ca-O distances and the first shell of Al-Al distances. Therefore, extracting structural information directly from PDF $G(r)$ without a fitted structure model is somewhat limited for complex materials. Some qualitative observations are described here, and PDF real-space refinements using fitted structure models are presented in the next section. The Si(Al)-O peaks (at 1.65 Å) and Ca-Si(Al)/Si-Si(Al) peaks (at 3.1 Å) were broadened as temperature was increased. The intensity of the peak centered at ~3.75 Å gradually decreased and a group of peaks ranging from ~4.8-8 Å showed distinct changes before and after phase transformation steps. Peaks in the high-r region (>8 Å) were broadened with increasing temperatures and showed distinct variations corresponding to the phase transition processes.

2.3 Refinements

2.3.1 X-ray Rietveld refinements

XRD data (Fig. 2.5) used for Rietveld refinements were measured using cavity-mounted specimens heated in a stepwise manner from 23 to 450 °C (in 25 ºC increments) under a P_{H_2O} of ~$10^{-0.8}$-$10^{-2.9}$ mbar (roughing pump vacuum condition at pressure of $10^{-3.8}$ bar). Specimens were equilibrated at least 120 min prior to each data collection. Measurement 2θ range was from 11º to 100º, counting for 0.66 sec at each 0.017º 2θ step using a position-sensitive detector, equivalent to a count time of 613.3 sec/step. Rietveld refinements were performed using the fundamental parameters approach implemented in the TOPAS-Academic v.4.1 software package. Fundamental parameters for Rietveld refinements were determined from instrumental parameters and by measuring reference materials (LaB_6) and refining associated parameters, which were then fixed based on the instrumental descriptions. The structure model for scolecite at 23 °C was adopted from Comodi *et al.* (2002) in the standard space group $C1c1$ setting. The refined structure at 23 °C was used as the starting model for subsequent refinements of the scolecite structure at 100, 150, and 175 °C. The structure model for metascolecite was determined by the charge-flipping method using XRD data measured at 225 °C and the TOPAS-Academic v.4.1 software package[7]. The

[7] Charge flipping (Oszlanyi and Suto 2004, 2005) is one of the latest tools whereby the phase problem is solved by an iterative procedure involving both real- and reciprocal-space perturbations instead of statistical phase relations. It is a dual-space method that switches back and forth between real and reciprocal space. The first application of charge flipping to the solution of crystal structures from powder diffraction data were presented by Wu *et al.* (2006). Both real- and reciprocal-space perturbations were applied to determine the structure of metascolecite in the present study. Perturbations in reciprocal space included setting data resolution to 1.0 Å. Observed reflections below 1.0 Å were regenerated based on the given space group and unit-cell parameters and treated as weak reflections. There are 594 unique reflections over the Ewald sphere (with $d \leq 1.0$ Å). Of these 594 reflections, 372 were set to weak. During each iteration (of switching between real and reciprocal space), amplitudes of the weak reflections were maintained while a $\pi/2$ phase shift was randomly added to 1/5 of the weak reflection. In real space, electron density was modified (flipped) if the density pixels were below the given threshold value, according to the "flip_regime_3" formula (which introduces relatively little electron density perturbations while reducing the occurrence of over-consistent solutions). In addition, an inexact but sufficiently strong symmetry restraint was applied to the flipped electron density pixels so that they followed

structure model obtained from charge flipping was then evaluated and refined using Rietveld approaches. The determined structure for metascolecite is in *C*1*c*1 space group and is structurally similar to Ståhl and Hanson (1994)'s metascolecite model but with a better defined relation to the original scolecite structure. Structural validation of the determined metascolecite model was made through calculated bond valance sums for unique atoms (except H_2O) in the unit cell. The bond valance sums are Si1 4.03, Si2 3.89, Si3 4.06, Al1 2.90, Al2 3.01, O1 1.73, O2 1.98, O3 2.03, O4 1.74, O5 2.01, O6 1.99, O7 1.99, O8 1.71, O9 2.02, O10 1.74, and Ca 1.83, in agreement with the expected oxidation states of these ions in the structure. The determined metascolecite structure at 225 °C was then used as the starting model for refinements of the metascolecite structure at 175, 275 and 325 °C. The background was modeled by a fourth-order Chebychev polynomial. Unit-cell parameters, scale factors, specimen displacement, and specimen-related profile parameters were initially refined, with the positions of all atoms fixed. Sources of peak broadening as a function of temperature through the phase transition were analyzed by interpreting the Lorentzian coefficients refined in TOPAS-Academic v.4.1, considering only microstrain broadening, because the analyses suggested that microstrain makes a considerable contribution to the observed XRD peak breaths, with much less contribution coming from finite crystallite size. Preferred orientation was modeled using a spherical harmonics correction up to eighth order. After initial refinements, atomic coordinates and isotropic displacement factors (B_{iso}; $B_{iso} = 8\pi^2 U_{iso}$) were refined for all atoms of the tetrahedral framework and the extraframework Ca^{2+} cations and H_2O molecules. In some cases, refined isotropic displacement factors were negative for Ca^{2+}

---

the space group symmetry. The charge-flipping loop was interrupted if the *R* factor did not decrease for 100 consecutive iterations, and then random phases in the range of (-π, π) were given to the structure factor amplitudes to begin a new cycle. The solution was found with $R = 0.508$ after 1593 iterations within 20 sec. The *R* factor contrast is ~0.1, a value sufficient for determining the structure solution. All independent non-hydrogen atoms and their equivalents were located.

cations and some framework oxygen atoms. In these cases, displacement factors were constrained to be equal for all atoms of the same type. Soft constraints were applied to the Si-O and Al-O bond distances using 1.61(3) Å and 1.76(3) Å for the Si-O and Al-O bond distances, respectively (Alberti and Gottardi 1988) The tetrahedral O-T-O angles (T = Si or Al) were also constrained to 109(3)°, close to perfect tetrahedral geometry. Occupancies of the H_2O sites in scolecite (Ow1, Ow2 and Ow3 sites) and in metascolecite (Ow1 and Ow2 sites) were refined. Simultaneous refinement of H_2O site occupancies and isotropic displacement factors was successful only when constraining the isotropic displacement factor for all H_2O molecules to be equal.

The structures of scolecite at 23, 100, 150, and 175 °C and of metascolecite at 175, 225, 275, and 325 °C were then used as starting models for subsequent Rietveld refinements wherein only unit-cell parameters and H_2O occupancies were varied. The 23 °C structure was used for refinements of unit-cell parameters and H_2O occupancies at 50 and 75 °C. The 100 °C structure was used for refinements of unit-cell parameters and H_2O occupancies at 125 °C. The 225 °C structure was used for refinements of unit-cell parameters and H_2O occupancies at 200 and 250 °C. The 275 °C structure was used for refinements of unit-cell parameters and H_2O occupancies at 300 °C. The 325 °C structure was used for refinements of unit-cell parameters and H_2O occupancies from 350 to 425 °C. Figure 2.6 depicts a selected 2θ range from Rietveld refinements using XRD data measured at 23, 150, 175, 225, and 425 ºC on dehydration. Refinement summaries are given in Table 2-1.The refined scolecite and metascolecite structures at 23 and 225 °C are presented in Table 2-2 and in Figures 2.1 and 2.7, respectively.

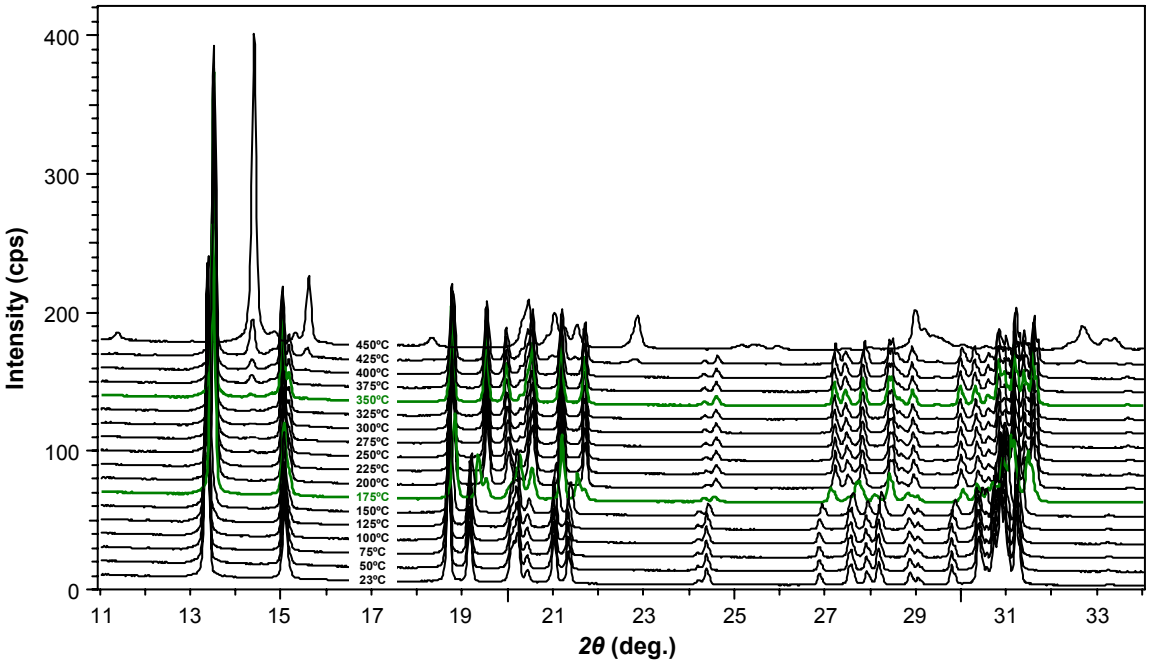

Figure 2.5. Extended view of temperature-resolved 2D-XRD pattern measured with a cavity mount under a P_{H_2O} of $10^{-0.8}$-$10^{-2.9}$ mbar (roughing pump vacuum condition at a pressure of $10^{-3.8}$ bar), illustrating the scolecite-to-metascolecite (at 175 ºC) and the metascolecite-to-x2-metascolecite (beginning at ≥350 ºC) transformations. The XRD pattern measured at 450 ºC consists of the x2-metascolecite phase, but a small amount of x1-metascolecite may also coexist. These XRD data were used for Rietveld refinements shown in Figure 2.6.

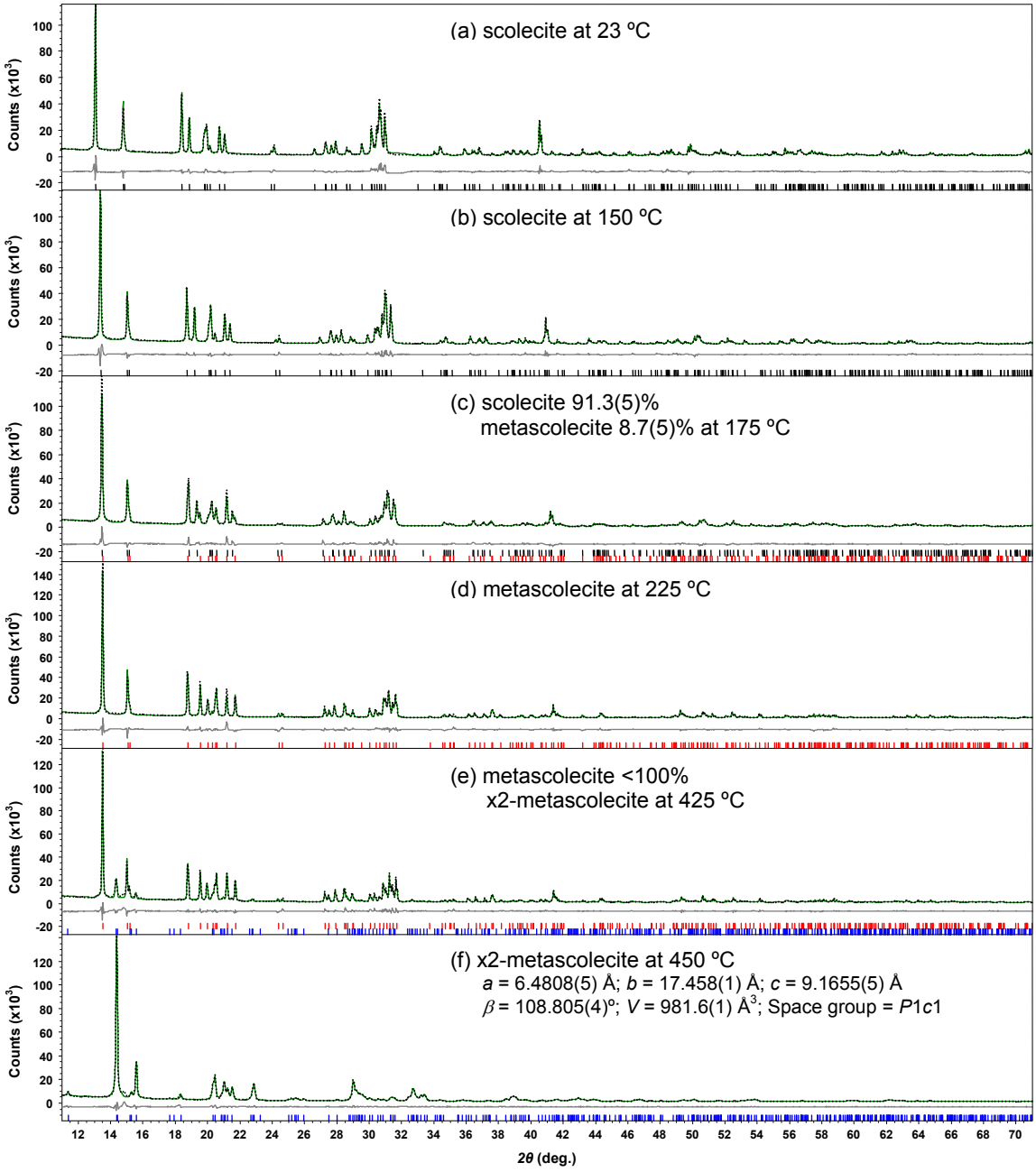

Figure 2.6. Observed XRD patterns (dotted line) measured with a cavity mount under a P_{H_2O} of $10^{-0.8}$-$10^{-2.9}$ mbar (roughing pump vacuum condition at pressure of $10^{-3.8}$ bar) for scolecite, metascolecite, and x2-metascolecite. Calculated (green line) and difference plots (gray line) are from Rietveld refinements for scolecite and metascolecite, and a Le Bail fit for x2-metascolecite. Short vertical lines mark the positions of Bragg reflections (Kα1 and Kα2) for scolecite (black), metascolecite (red), and x2-metascolecite (blue).

Table 2-1. Scolecite and metascolecite XRD Rietveld refinement summary (e.s.d. values in parentheses)

Temperature (ºC)	**23**	**100**	**150**	**175**	**225**	**275**	**325**
Scolecite (%)	100(0)	100(0)	100(0)	91.3(5)	--	--	--
a (Å)	6.5262(1)	6.5292(1)	6.5326(1)	6.5393(3)	--	--	--
b (Å)	18.9708(2)	18.9717(2)	18.9174(2)	18.8123(4)	--	--	--
c (Å)	9.8449(2)	9.8504(1)	9.8289(1)	9.7649(3)	--	--	--
β (º)	109.974(1)	110.016(1)	110.151(1)	110.336(3)	--	--	--
V (Å^3)	1145.55(4)	1146.47(3)	1140.30(3)	1126.41(6)	--	--	--
Ow1 occupancy	0.98(3)	0.95(2)	0.94(3)	0.93(3)	--	--	--
Ow2 occupancy	0.99(3)	0.96(2)	0.93(3)	0.93(3)	--	--	--
Ow3 occupancy	0.99(3)	0.93(2)	0.79(3)	0.42(4)	--	--	--
Metascolecite (%)	--	--	--	8.7(5)	100(0)	100(0)	100(0)
a (Å)	--	--	--	6.5403(5)	6.5417(2)	6.5433(2)	6.5446(2)
b (Å)	--	--	--	18.1447(7)	18.1295(3)	18.1313(3)	18.1331(3)
c (Å)	--	--	--	10.0224(5)	10.0294(2)	10.0339(2)	10.0366(1)
β (º)	--	--	--	109.734(5)	109.833(2)	109.891(1)	109.934(1)
V (Å^3)	--	--	--	1119.5(1)	1118.91(4)	1119.40(4)	1119.72(4)
Ow1 occupancy	--	--	--	0.93(3)	0.95(2)	0.93(3)	0.92(3)
Ow2 occupancy	--	--	--	0.93(3)	0.91(2)	0.91(2)	0.91(2)
Ow3 occupancy	--	--	--	0.00(0)	0.00(0)	0.00(0)	0.00(0)
strain (%)	2.4(3)	2.2(2)	5.0(2)	9.5(2)	5.4(2)	6.3(4)	6.2(4)
R_{wp}*	0.1097	0.0914	0.0920	0.1032	0.0979	0.1002	0.1037
R_p†	0.0940	0.0702	0.0697	0.0813	0.0815	0.0819	0.0854
R_B‡	0.0502	0.0451	0.0355	0.0628	0.0526	0.0509	0.0518
GOF§	6.71	4.73	4.78	5.19	5.64	5.78	5.95
# of variables	106	106	106	176	102	102	102
# of observations	5290	5290	5290	5290	5290	5290	5290
# of reflections	1243	1243	1243	2467	1224	1224	1224

* R_{wp} = *R*-weighted pattern;

$$R_{wp} = \sqrt{\frac{\sum w_m (I_{o,m} - I_{c,m})^2}{\sum w_m I_{o,m}^2}}$$

† R_p = *R* pattern;

$$R_p = \frac{\sum |I_{o,m} - I_{c,m}|}{\sum I_{o,m}}$$

‡ R_B = *R* Bragg;

$$R_B = \frac{\sum |I_{o,k} - I_{c,k}|}{\sum I_{o,k}}$$

§ *GOF* = Goodness of fit ;

$$GOF = \chi^2 = \frac{R_{wp}}{R_{\exp}} = \sqrt{\frac{\sum w_m (I_{o,m} - I_{c,m})^2}{N_{data} - N_{\text{var}}}}$$

$I_{o,m}$ & $I_{c,m}$ = observed and calculated intensities at a given 2θ point
$I_{o,k}$ & $I_{c,k}$ = observed and calculated intensities of the k^{th} reflection
w_m = the weighting given to data point *m*

Table 2-2a. Structure of scolecite ($Ca_4Al_8Si_{12}O_{40} \bullet 12H_2O$) at 23 ºC (Rietveld refinement)

Atom	*x*	*y*	*z*	U_{iso} (Å^2)	Occupancy
Si1	0.5000(0)	0.3705(1)	0.0000(0)	0.012(1)	1.0
Si2	0.2365(2)	0.3369(1)	0.2048(3)	0.012(1)	1.0
Si3	0.5459(3)	0.0851(1)	0.3272(2)	0.012(1)	1.0
Al1	0.9417(3)	0.4641(2)	0.0945(3)	0.012(1)	1.0
Al2	0.3537(2)	0.2180(1)	0.4384(2)	0.012(1)	1.0
O1	0.5397(4)	0.0304(1)	0.4509(3)	0.017(1)	1.0
O2	0.4532(3)	0.0474(1)	0.1709(2)	0.017(1)	1.0
O3	0.3951(2)	0.1528(2)	0.3266(2)	0.017(1)	1.0
O4	0.1120(4)	0.2013(2)	0.4706(2)	0.017(2)	1.0
O5	0.3482(4)	0.3008(1)	0.3609(3)	0.017(2)	1.0
O6	0.0702(3)	0.2808(2)	0.1017(3)	0.017(2)	1.0
O7	0.4194(2)	0.3590(1)	0.1363(2)	0.017(2)	1.0
O8	0.1030(2)	0.4059(2)	0.2234(3)	0.017(2)	1.0
O9	0.7935(3)	0.1109(1)	0.3576(2)	0.017(2)	1.0
O10	0.6735(4)	0.4343(1)	0.0324(2)	0.017(2)	1.0
Ca	0.1655(3)	0.1421(2)	0.0564(3)	0.030(4)	1.0
Ow1	0.8996(3)	0.0755(3)	0.1067(4)	0.025(4)	0.98(3)
Ow2	0.9196(3)	0.3278(3)	0.4410(4)	0.025(4)	0.99(3)
Ow3	0.5818(4)	0.4504(3)	0.3670(4)	0.025(4)	0.99(3)

Note: Space group = *C*1*c*1, monoclinic, a = 6.5262(1) Å, b = 18.9708(2) Å, c = 9.8449(2) Å, β = 109.974(1)º, V = 1145.55(4) Å^3 (e.s.d. values in parentheses).

Table 2-2b. Structure of metascolecite ($Ca_4Al_8Si_{12}O_{40} \bullet 8H_2O$) at 225 ºC (Rietveld refinement)

Atom	*x*	*y*	*z*	U_{iso} (Å^2)	Occupancy
Si1	0.5000(0)	0.6313(1)	0.5000(0)	0.017(1)	1.0
Si2	0.2384(2)	0.6666(2)	0.7016(2)	0.017(1)	1.0
Si3	0.5383(3)	0.9136(1)	0.8213(3)	0.017(1)	1.0
Al1	0.9325(2)	0.5316(1)	0.5812(2)	0.017(1)	1.0
Al2	0.8522(2)	0.2780(1)	0.9358(2)	0.017(1)	1.0
O1	0.5188(3)	0.0259(2)	0.4346(2)	0.022(1)	1.0
O2	0.9553(2)	0.4461(2)	0.6614(3)	0.022(1)	1.0
O3	0.8830(3)	0.3438(2)	0.8205(3)	0.022(1)	1.0
O4	0.6174(2)	0.2940(2)	0.9739(3)	0.022(2)	1.0
O5	0.8575(2)	0.8088(2)	0.3671(2)	0.022(2)	1.0
O6	0.5784(2)	0.2245(2)	0.5885(2)	0.022(2)	1.0
O7	0.9278(2)	0.1425(2)	0.6384(3)	0.022(2)	1.0
O8	0.5964(2)	0.9067(2)	0.2044(2)	0.022(2)	1.0
O9	0.2872(3)	0.6143(3)	0.3630(3)	0.022(2)	1.0
O10	0.1646(3)	0.0618(2)	0.5268(3)	0.022(2)	1.0
Ca	0.1556(4)	0.1465(3)	0.0678(4)	0.032(4)	1.0
Ow1	0.8824(3)	0.0752(4)	0.1078(4)	0.043(4)	0.95(2)
Ow2	0.8172(3)	0.3678(3)	0.3969(3)	0.043(4)	0.91(2)

Note: Space group = *C*1*c*1, monoclinic, a = 6.5417(2) Å, b = 18.1295(3) Å, c = 10.0294(2) Å, β = 109.833(2)º, V = 1118.91(4) Å^3 (e.s.d. values in parentheses).

Metascolecite ($Ca_4Al_8Si_{12}O_{40} \cdot 8H_2O$)

Space group = *C*1*c*1, *a* = 6.5417(2) Å, *b* = 18.1295(3) Å, *c* = 10.0294(2) Å, β = 109.833(2)°, *V* = 1118.91(4) Å^3

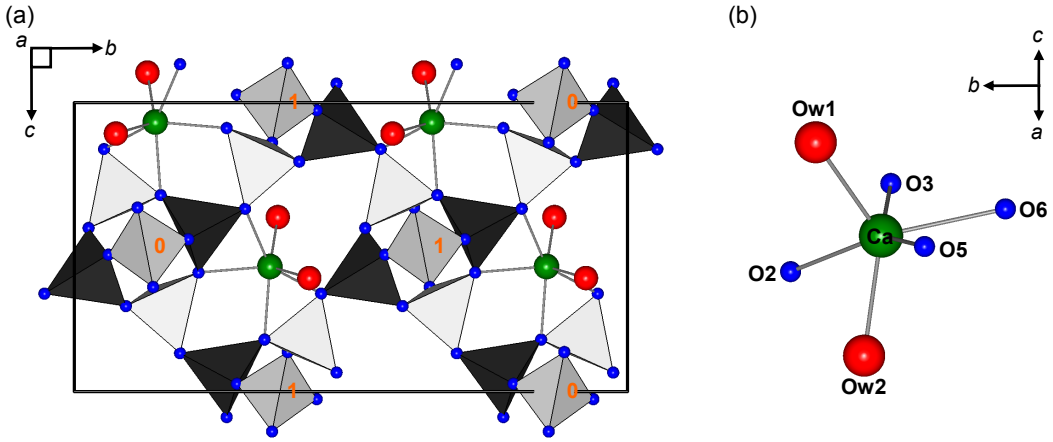

Figure 2.7. Refined crystal structure of metascolecite at 225 ºC. **(a)** NAT framework viewed down the cross-linked chains. Numbers in the central tetrahedra indicate the height above (001) as multiples of *a*/2. **(b)** Local view of coordination of Ca^{2+} cations in the metascolecite channel system. All symbols are the same as in Figure 2.1.

The x2-metascolecite phase appeared at temperatures ≥350 °C and coexisted with the metascolecite phase at temperatures from 350 to 450 °C (Fig. 2.5). To begin solution of the structure of x2-metascolecite, the 450 °C XRD pattern was used for the determination of possible space groups and unit-cell parameters. The indexing solution was evaluated graphically using the Le Bail profile-fitting algorithm (Le Bail *et al.* 1988). Indexing and Le Bail fitting yielded unit-cell parameters of a = 6.4808(5) Å, b = 17.458(1) Å, c = 9.1655(5) Å, β = 108.805(4)º, V = 981.6(1) Å^3, and $P1c1$space group, which fits all diffraction peaks with the exception of a peak at ~14.9º 2θ (Fig. 2.6f). This ~14.9º 2θ diffraction peak may be due to the x1-metascolecite phase, which formed from x2-metascolecite on further heating. Successful pattern indexing requires knowledge of whether the unknown material is a single phase or a mixture. At this stage, the determined space group and unit-cell parameters for x2-metascolecite were valid only if the ~14.9º 2θ diffraction peak truly belonged to the x1-metascolecite phase. The proto-framework model based on $P1c1$ space group setting is illustrated in Figure 2.8. This initial model was determined through distance-least squares methods where strong bond constrains were applied to each individual tetrahedron and allowed a free rotation of any two adjacent tetrahedra around a shared oxygen vertex. The determined proto-framework shows two Si-O-Al bridging angles less than 125º (see red markers in Fig. 2.8b). Oxygen bridging angles <125º are energetically unfavorable in the framework configurations of tectosilicates unless they are stabilized by strong additional interactions of the bridging oxygens with the extraframework Ca^{2+} cations or hydrogen atoms. Hence, the Ca^{2+} cations, residual H_2O molecules, and/or relic-OH groups are most likely located in the proximity of the framework oxygens with small bridging angles.

Complete determination of the atomic positions of x2-metascolecite and determination of a structural model of x1-metascolecite are ongoing.

Refined unit-cell parameters, unit-cell volumes, and H_2O contents for scolecite and its dehydrated phases as a function of temperature are illustrated in Figure 2.9. The dehydration process began with a gradual expulsion of Ow3, the Ca^{2+} cation-coordinated H_2O molecules (Fig. 2.1b). Ow3 is the H_2O molecule that substitutes in place of one Na^+ cation in the natrolite-type channel but it occupies a completely different site in the channel (than Na^+ in natrolite). In contrast, the other H_2O molecules, Ow1 and Ow2, are only slightly displaced from their corresponding positions in natrolite. The channel site where Ow3 H_2O molecules are located is responsible for weaker hydrogen bonding environments, and hence Ow3 is the first H_2O molecule to be expelled during heating. Changes in the unit-cell are associated primarily with changes in the occupancy of H_2O molecules. During scolecite dehydration (at temperatures <175 °C), the gradual decrease in *b* and *c* and increase in *a* and β unit-cell parameters corresponded to the steady decrease in occupancy of the Ow3 site and the minor decrease in occupancies of the other Ow sites (i.e., Ow1 and Ow2) (Fig. 2.9). The partial loss of Ow3 H_2O molecules associated with the minor decrease in occupancies in Ow1 and Ow2 sites and the steady increase in the *a* and β unit-cell parameters likely facilitate the thermal migration and rearrangement of extraframework Ca^{2+}. At 175 °C, the Ow3 site occupancy in scolecite decreased to 0.42(4) and the metascolecite phase formed (see Figs. 2.5 and 2.9f). At 175 °C, a sudden contraction in *b*, β, and unit-cell volume and a sudden expansion in *a* and *c* were associated with the formation of the metascolecite phase (the Ow3 site occupancy is zero in metascolecite). From 175 to 350 °C, a steady increase in all unit-cell parameters and unit-cell volume in the metascolecite structure is primarily due to thermal expansion and

x2-metascolecite ($Ca_4Al_8Si_{12}O_{40}$ • nH_2O; n ≤2)

Space group = *P*1*c*1, *a* = 6.4808(5) Å, *b* = 17.458(1) Å, *c* = 9.1655(5) Å, *β* = 108.805(4)º, *V* = 981.6(1) Å^3

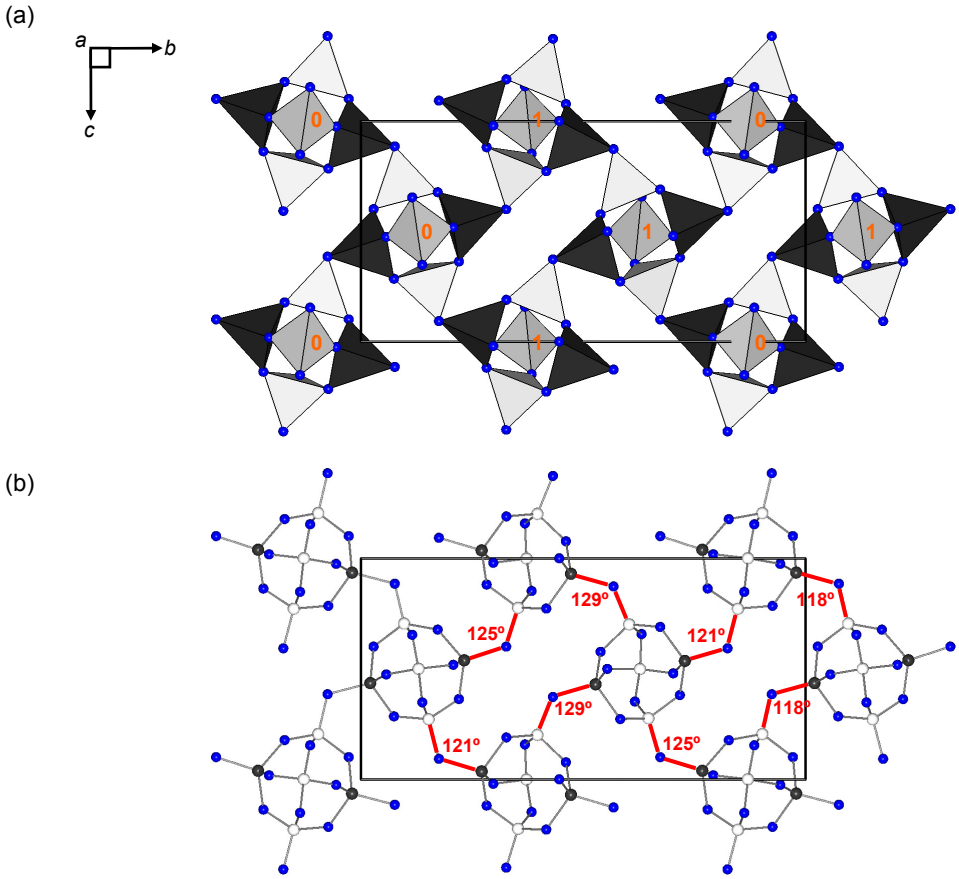

Figure 2.8. The proto-framework model of x2-metascolecite determined at 450 ºC. **(a)** NAT framework viewed down the cross-linked chains. Numbers in the central tetrahedra indicate the height above (001) as multiples of *a*/2. **(b)** Ball-and-stick view of the framework. Si-O-Al angles less than 130º are outlined in red. Ca^{2+} cations, H_2O molecules, and/or relic-OH groups were not located in this proto-structure model. All other symbols are the same as in Figure 2.1.

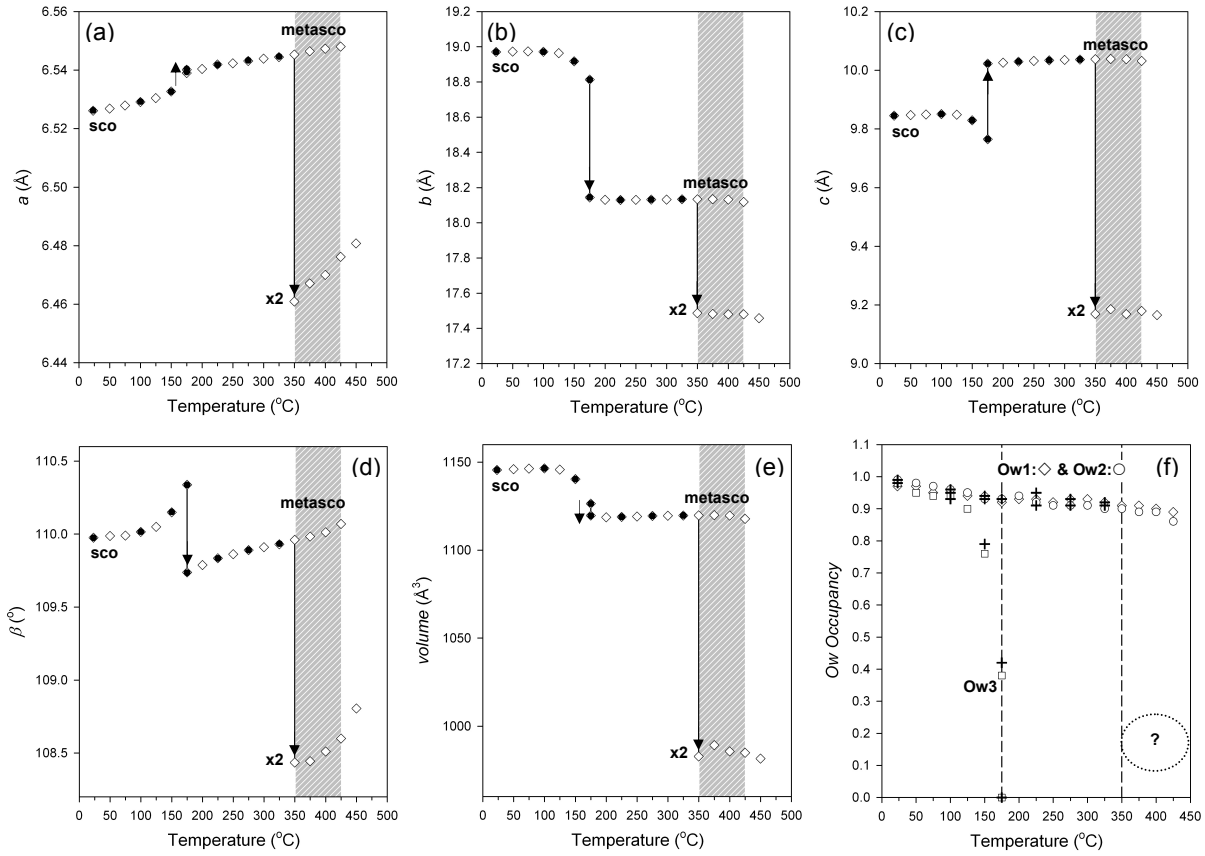

Figure 2.9. Changes in unit-cell parameters **(a-e)** and H_2O content **(f)** of scolecite, metascolecite, and x2-metascolecite as a function of temperature. Arrows indicate the occurrence of metascolecite (≥175 ºC) and x2-metascolecite (≥350 ºC). The gray diagonal-hatched area marks regions of the coexistence of metascolecite and x2-metascolecite phases during dehydration. Open diamonds, open circles, and open squares represent refinements with only unit-cell parameters and H_2O occupancies refined. Black circles and pluses represent data from Rietveld refinements using XRD data obtained during dehydration. Unit-cell parameters for x2-metascolecite were determined from a Le Bail fit. The H_2O content in x2-metascolecite was not determined using Rietveld analyses due to its incomplete structural model. The estimated H_2O occupancy in x2-metascolecite is ~0.25-0.1 based on the TG weight loss curve. Errors for each data point are smaller than the symbols.

minor structural modifications in response to the minor loss of H_2O occurring over this temperature range (Fig. 2.9). At 350 °C, the x2-metascolecite phase formed and coexisted with the metascolecite phase at temperatures between 350 and 425 °C (see Figs. 2.5 and 2.9). The site occupancies of Ow1 and Ow2 in metascolecite are 0.89(3) and 0.86(3) at 425 °C (Fig. 2.9f). It was not possible to determine the H_2O site occupancy in x2-metascolecite with Rietveld analyses due to incomplete structural information. However, the estimated H_2O occupancy is ~0.25-0.1 in x2-metascolecite based on the TG weight loss curve. These simple XRD measurements made over different ranges of temperature and P_{H_2O} spaces showed that the drop in Ca coordination below six is not the factor driving the phase transition as proposed previously. When scolecite was heated under low-P_{H_2O} conditions, the aluminosilicate framework of metascolecite did not become amorphous and instead underwent a displacive phase transition to x2- and x1-metascolecite phases.

2.3.2 X-ray PDF real-space refinements

During structure refinement with the program PDFgui (Farrow *et al.* 2007), starting models for the structure at different temperatures were obtained based on a model of the average crystal structure from XRD Rietveld refinements at each corresponding temperature. The symmetry of the starting models was constrained to *C*1*c*1 for both scolecite at 25 °C and metascolecite at 275 °C. No soft constraints can be applied in PDFgui, as the bond-length distribution is naturally reflected in the PDF $G(r)$ function. In general, the parameters that can be refined with PDFgui include scale factor, resolution of the instrument (only the parameter Q_{damp} was considered which was fixed to 0.04 $Å^{-1}$ according to refined results using a standard CeO_2 crystal), and structural parameters, including unit-cell parameters, atomic positions, displacement parameters ($U_{ij\ (ij=11,22,33)}$), occupancy factors, and parameters

for contribution of peak sharpening in the low-*r* range due to correlated motion (only δ_2 and *low-r α ratio*). The refinement procedure is described in the PDFgui program user manual (Farrow *et al.* 2009). The mathematical theory and background of PDF analysis can be found in Egami and Billinge (2003). Several recent studies have successfully applied the PDF method to probe short- to medium-range structures in materials as complex as zeolites (Martínez-Iñesta *et al.* 2005; Martínez-Iñesta and Lobo 2005, 2007).

Figures 2.10a and c show the fitted PDF $G(r)$ profiles for 25 and 275 °C data using the average structure models of scolecite and metascolecite, respectively. Only scale factor and two peak-width related parameters, δ_2 and *low-r α ratio*, were refined, and the starting average structure models gave sufficient matches with the exception of the low-*r* range (i.e., the difference curves were large at r <14.3 Å for the 25 °C PDF and at r <11.3 Å for the 275 °C PDF). Subsequent refinements varying unit-cell parameters, atomic positions, displacement parameters ($U_{ij\ (ij=11,22,33)}$), and occupancy factors for H_2O molecules gave significantly improved fits for both PDFs (Figs. 2.10b and d). Considering the complexity of the scolecite structure and the nature of real-space refinements, the final R_{wp} value of ~0.23 can be considered a reasonable result (many published PDF refinements have R_{wp} values varying from 0.1 to 0.4). Refinement summaries for scolecite and metascolecite are given in Table 2-3, and the corresponding atomic positions are summarized in Table 2-4. The precisions of refined unit-cell parameters and atomic positions of both mesolite and disordered metamesolite are approximately one order of magnitude lower than those obtained with XRD Rietveld analysis. As bond distances and angles were not constrained during the PDF refinements, the resulting models should provide better representations of the short- to medium-range structural features. For example, the refined atomic displacement parameters

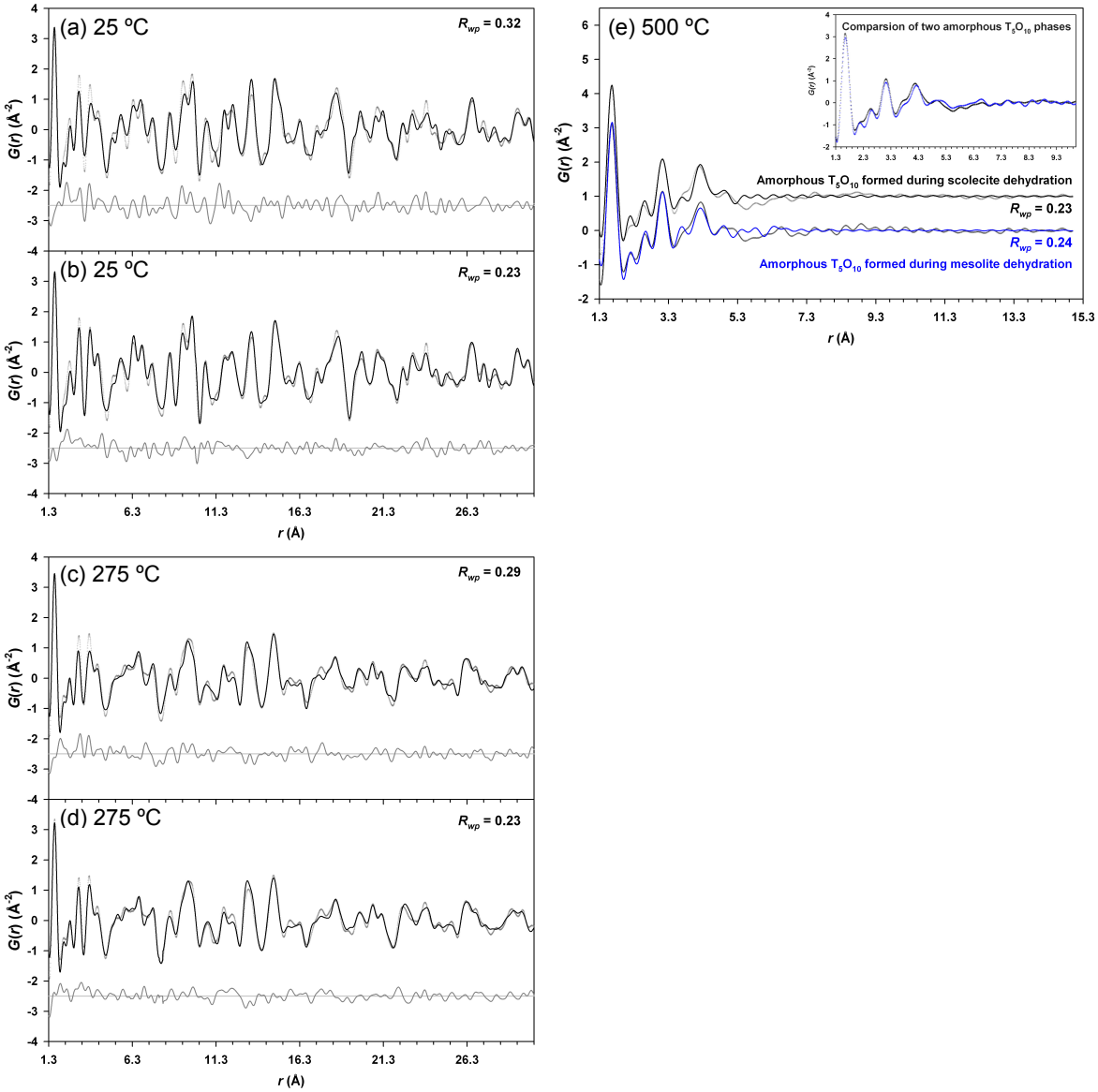

Figure 2.10. PDF refinements for scolecite **(a** and **b)**, metascolecite **(c** and **d)**, and amorphous T_5O_{10} **(e)**. In plots **(a)** and **(c),** fits were obtained by constraining to the average structure models obtained with Rietveld refinements (this study), allowing only scale factor, δ_2, and *low-r α ratio* to vary. In plots **(b)** and **(d)**, fits were obtained by allowing scale factor, δ_2, *low-r α ratio*, unit-cell parameters, atomic positions, isotropic displacements, and occupancy factors to vary. In plot **(e)**, the local structure of the amorphous T_5O_{10} phase was modeled by allowing the additional parameter, *spdiameter*, to vary. The amorphous T_5O_{10} phase formed during scolecite dehydration (black fit) has a local structure similar to the amorphous T_5O_{10} phase formed during mesolite dehydration (blue fit), and their comparison is shown in the insert. For all plots, the observed PDF $G(r)$ function is shown with crosses and the calculated PDF $G(r)$ function is shown as a black (or blue) solid line. The difference plot is shown as a gray solid line.

Table 2-3. Scolecite, metascolecite, and amorphous T_5O_{10} PDF refinement summary (e.s.d. values in parentheses)

Phase type	**Scolecite**	**Metascolecite**	**Amorphous T_5O_{10}**
Temperature (ºC)	25	275	500
Space group	*C*1*c*1	*C*1*c*1	--
a (Å)	6.5094(6)	6.5339(1)	--
b (Å)	18.922(1)	18.122(2)	--
c (Å)	9.817(1)	10.031(2)	--
β (º)	109.68(1)	110.07(1)	--
V (Å^3)	1138.7(1)	1115.5(1)	--
U_{iso} (Si, Al)	0.008(1)	0.012(1)	0.025(5)
U_{iso} (O)	0.013(2)	0.020(3)	0.040(5)
U_{iso} (Ca)	0.025(3)	0.028(4)	0.072(6)
U_{iso} (Ow)	0.020(4)	0.032(5)	--
R_{wp}*	0.23	0.23	0.23
δ_2 (Å^2)	2.46(2)	2.42(4)	2.47(2)
Low-r σ ratio	0.60(3)	0.51(3)	0.32(2)
Scale factor	0.97(1)	0.87(1)	0.99(1)

Note: The parameter r_{cut} was fixed to 3.2 Å and Q_{damp} was fixed to 0.04 Å^{-1} for all refinements. Atomic coordinates for scolecite and metamesolite phases are given in Table 2-4. The PDF shape damping parameter, *spdiameter*, was refined for the amorphous T_5O_{10} phase, and the final domain (particle) diameter is 7.5(1) Å.

* R_{wp} = *R*-weighted pattern; $R_{wp} = \sqrt{\frac{\sum w(r_i) \times [G_o(r_i) - G_c(r_i)]^2}{\sum w(r_i) \times G_o^2(r_i)}}$

$G_o(r_i)$ = observed reduced pair distribution function at point r_i
$G_c(r_i)$ = calculated reduced pair distribution function at point r_i
$w(r_i)$ = the weight for each data point r_i

Table 2-4a. Structure of scolecite ($Ca_4Al_8Si_{12}O_{40} \bullet 12H_2O$) at 25 ºC (PDF refinement)

Atom	*x*	*y*	*z*	U_{iso} (Å^2)	Occupancy
Si1	0.504(3)	0.369(1)	0.000(0)	0.008(1)	1.0
Si2	0.235(3)	0.329(1)	0.208(1)	0.008(1)	1.0
Si3	0.558(3)	0.085(1)	0.321(1)	0.008(1)	1.0
Al1	0.945(3)	0.465(1)	0.097(1)	0.008(1)	1.0
Al2	0.360(3)	0.218(1)	0.437(1)	0.008(1)	1.0
O1	0.552(2)	0.034(1)	0.452(1)	0.008(1)	1.0
O2	0.416(3)	0.049(1)	0.169(1)	0.008(1)	1.0
O3	0.390(2)	0.152(1)	0.320(2)	0.008(1)	1.0
O4	0.111(3)	0.203(1)	0.471(1)	0.013(2)	1.0
O5	0.372(2)	0.301(1)	0.370(2)	0.013(2)	1.0
O6	0.068(2)	0.274(2)	0.109(1)	0.013(2)	1.0
O7	0.411(2)	0.361(1)	0.129(3)	0.013(2)	1.0
O8	0.098(3)	0.404(1)	0.222(1)	0.013(2)	1.0
O9	0.806(3)	0.116(1)	0.352(2)	0.013(2)	1.0
O10	0.672(3)	0.434(2)	0.025(2)	0.013(2)	1.0
Ca	0.169(2)	0.144(2)	0.061(2)	0.025(3)	1.0
Ow1	0.899(5)	0.076(3)	0.105(3)	0.020(4)	1.1(2)
Ow2	0.973(4)	0.339(2)	0.437(4)	0.020(4)	0.9(1)
Ow3	0.564(5)	0.4821(3)	0.370(5)	0.020(4)	0.9(2)

Note: Space group = *C*1*c*1, monoclinic, a = 6.5094(6) Å, b = 18.922(1) Å, c = 9.817(1) Å, β = 109.68(1)º, V = 1138.7(1) Å^3 (e.s.d. values in parentheses).

Table 2-4b. Structure of metascolecite ($Ca_4Al_8Si_{12}O_{40} \bullet 8H_2O$) at 275 ºC (PDF refinement)

Atom	*x*	*y*	*z*	U_{iso} (Å^2)	Occupancy
Si1	0.512(2)	0.631(2)	0.500(0)	0.012(1)	1.0
Si2	0.239(2)	0.665(2)	0.708(3)	0.012(1)	1.0
Si3	0.538(1)	0.914(2)	0.821(2)	0.012(1)	1.0
Al1	0.933(2)	0.532(2)	0.581(2)	0.012(1)	1.0
Al2	0.853(2)	0.280(2)	0.939(2)	0.012(1)	1.0
O1	0.519(2)	0.026(2)	0.435(3)	0.020(3)	1.0
O2	0.955(2)	0.446(2)	0.661(3)	0.020(3)	1.0
O3	0.943(1)	0.330(2)	0.821(3)	0.020(3)	1.0
O4	0.615(2)	0.289(1)	0.975(2)	0.020(3)	1.0
O5	0.858(2)	0.810(2)	0.367(3)	0.020(3)	1.0
O6	0.554(1)	0.225(1)	0.606(2)	0.020(3)	1.0
O7	0.928(2)	0.143(1)	0.638(3)	0.020(3)	1.0
O8	0.595(1)	0.907(2)	0.204(3)	0.020(3)	1.0
O9	0.294(2)	0.606(1)	0.368(3)	0.020(3)	1.0
O10	0.163(2)	0.059(1)	0.539(3)	0.020(3)	1.0
Ca	0.150(3)	0.146(3)	0.063(3)	0.028(4)	1.0
Ow1	0.882(5)	0.075(4)	0.108(4)	0.032(5)	0.8(3)
Ow2	0.859(5)	0.369(4)	0.411(5)	0.032(5)	0.9(3)

Note: Space group = *C*1*c*1, monoclinic, a = 6.5339(5) Å, b = 18.122(2) Å, c = 10.031(2) Å, β = 110.07(1)º, V = 1115.5(1) Å^3 (e.s.d. values in parentheses).

Table 2-5. Selected bond distances for all refined models (e.s.d. values in parentheses)

Structure	Source	<Si-O> Å	Range (Å)	<Al-O> Å	Range (Å)	R_{wp}
Scolecite	XRD	1.615(3)	1.609(1)-1.618(1)	1.741(2)	1.738(1)-1.743(1)	0.10
	PDF	1.62(4)	1.592(2)-1.691(2)	1.76(3)	1.717(2)-1.791(2)	0.23
Metascolecite	XRD	1.624(4)	1.613(1)-1.642(1)	1.732(4)	1.718(1)-1.752(1)	0.10
	PDF	1.63(2)	1.602(2)-1.670(2)	1.74(2)	1.718(3)-1.784(2)	0.23
Amorphous T_5O_{10}	PDF	1.64(3)	1.598(3)-1.689(3)	1.74(3)	1.703(3)-1.743(3)	0.23

($U_{ij\ (ij=11,22,33)}$) were smaller in PDF (Table 2-4) refinements and refined Si(Al)-O bond lengths showed a larger range of distributions (Table 2-5). The distributions of bond distances likely arise from lattice deformations and contribute to the microstrain effects observed in XRD profiles. However, it is difficult to tabulate the distributions of all bond lengths and angles, and perhaps the best way to compare local (PDF) and average (XRD) structure models is to plot the two structure models using the data in Tables 2-2 and 2-4. Figure 2.11 shows comparisons between the average (XRD) and local (PDF) structure models for scolecite and metascolecite.

The disordered nature of the amorphous T_5O_{10} phase does not lend itself to classical elastic powder diffraction methods, as the material does not give rise to Bragg diffraction peaks. However, the corresponding PDF $G(r)$ elucidates the residual local structure in the low-r region. The Si(Al)-O bonds (centered at ~1.65 Å) and the first coordination shell of Si-Si(Al) (centered at ~3.1 Å) were preserved, suggesting that the original long-range ordered aluminosilicate framework has broken into randomly oriented domains. Domain sizes are roughly 7 Å, as indicated by sharp $G(r)$ features, suggesting that the intra-domain Si, Al, and O bonding correlations are preserved (Fig. 2.10e). The initial model for the amorphous T_5O_{10} domain structure was derived from the structure models of α2-metanatrolite (Wang and Bish 2010). As discussed in Wang and Bish (2008, 2010), α2-metanatrolite is one of the dehydrated phases of natrolite and has slightly twisted T_5O_{10} chains after natrolite loses all its H_2O molecules. The PDFgui modeling program provides a shape damping parameter, *spdiameter*, allowing the model of the finite domain size using a spherical form factor. The initial value of *spdiameter* was set to 7 Å (the initial estimate for domain diameter) and was allowed to refine. After several refinement cycles, a suitable local structural picture was

obtained from the initial α2-metanatrolite model. The refinement process was terminated when no more improvements were observed, after ensuring that the resulting model was crystal chemically reasonable. The fitted PDF $G(r)$ function is shown in Figure 2.10e, and refinement results are summarized in Table 2-3. The final *spdiameter* value of 7.5(1) Å is slightly larger than expected, as the dimensions (LWH) of an untwisted single T_5O_{10} chain are approximately 7 × 7 × 6.5 Å (Alberti and Vezzalini 1981). Twisted chains will have roughly the same length and width but a smaller height, depending on the degrees of the twisting (Alberti and Vezzalini 1983). Final refinement results showed a twisted T_5O_{10} chain with dimensions (LWH) of about 6.9 × 7.3 × 6.5 Å (Fig. 2.11c), suggesting that each domain is composed of a single twisted nano-fiber formed from the breakage of the aluminosilicate framework. Hence, the amorphous T_5O_{10} phase can be described as a collection of nano-fibers randomly oriented with respect to each other. The slightly larger domain diameter (i.e., *spdiameter* = 7.5 ± 0.1 Å) suggests the attachment of Ca^{2+} cations (and possibly hydroxyl groups) to the nano-fibers. The average number of cations attached to a single nano-fiber is one, suggesting that each nano-fiber has at least zero or one cation attached to it. Figure 2.11c shows a representation of the attachment of one cation to a chain. Moreover, the PDF $G(r)$ in the r-range between 5.3 to 8 Å did not fit very well, because a spherical form factor was used as a damping parameter. The nano-fibers are not spherical in shape and fiber-fiber correlations are weak, adding to the difficulties in obtaining a good PDF fit in this region (Fig. 2.10e). In addition, the observed PDF $G(r)$ for the amorphous T_5O_{10} phase formed during scolecite dehydration has local structural features very similar (by inspection) to the other amorphous T_5O_{10} phase found during mesolite dehydration (Fig. 2.10e). This is not a surprising result because both scolecite and mesolite share the same aluminosilicate

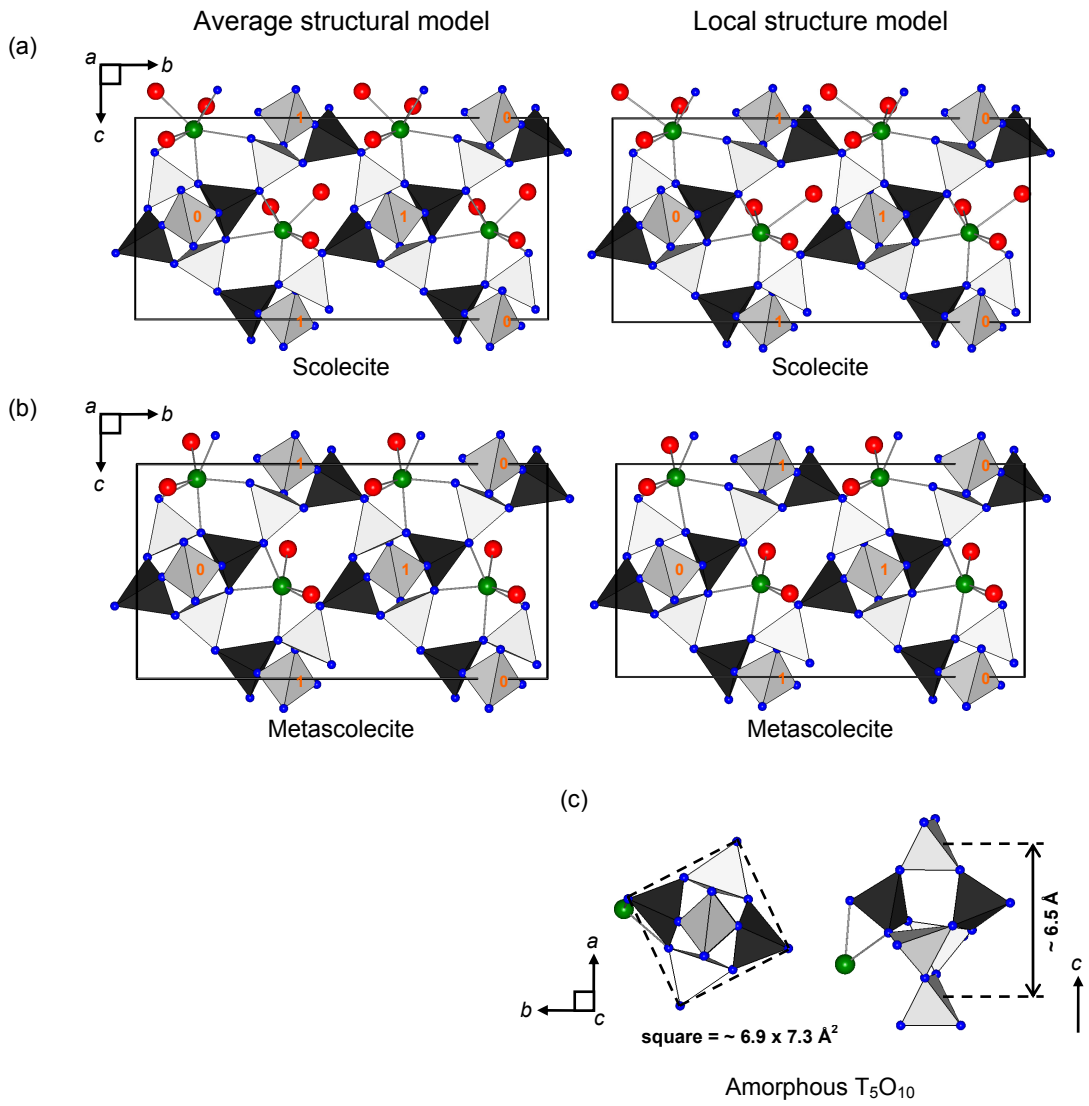

Figure 2.11. Average vs. local view of structure of scolecite **(a)** and metascolecite **(b)**. The average crystal structure was determined from XRD Rietveld refinements, whereas the local structure was determined from PDF refinements. **(c)** Local structure of amorphous T_5O_{10}. This phase has a twisted T_5O_{10} chain with dimensions (LWH) of ~6.9 x 7.3 x 6.5 Å. Amorphous T_5O_{10} comprises a collection of many of these twisted chains randomly oriented with respect to each other. Ca^{2+} cations (green spheres) and/or relic-OH groups are attached close to Al tetrahedra (black tetrahedra). All symbols are the same as in Figure 2.1.

framework configurations, and hence they exhibit similar dehydration behaviors. Discussions on the amorphous T_5O_{10} phase formed during mesolite dehydration can be found in Chapter 3 or in Wang *et al.* 2010.

2.4 Chapter summary

The crystal structures of scolecite and its dehydrated high-temperature phases (metascolecite, x1-, x2-metascolecite, and amorphous T_5O_{10}) have been characterized using powder X-ray diffraction and synchrotron X-ray pair distribution function analyses. The response of the scolecite crystal structure to dehydration shows two main steps, the first of which is the scolecite-to-metascolecite displacive phase transition, which is 1st-order in character. During this reaction, Ow3 H_2O molecules are lost and the scolecite framework contracts along the *b* axis and the β angle decreases. Controlled-temperature and -P_{H_2O} XRD measurements showed that the transition temperature to metascolecite depends on the P_{H_2O} conditions. A comparatively moist environment employed on heating caused the initial dehydration temperature to increase. The flexibility of the scolecite framework makes the scolecite-to-metascolecite reaction reversible, although a certain amount of the transformation-induced lattice strains and strain-induced mosaicity is not reversible. The second dehydration step, the high-temperature phase transition, is also 1st-order in character and not only showed a P_{H_2O}-dependent transition temperature but also two different phase transition paths, namely displacive phase transitions from metascolecite-to-x2-metascolecite-to-x1-metamesolite/amorphous T_5O_{10} (occurring at P_{H_2O} below ~2.7 mbar) and a phase transition from metascolecite-to-amorphous T_5O_{10} (occurring at P_{H_2O} above ~3.7 mbar). These different structural changes are clearly seen with discontinuous changes in the XRD

pattern (as marked by changes in the unit-cell dimensions) or by disappearance of long-range ordering in the XRD and PDF data. The total amounts of H_2O lost during the dehydration reaction are also shown in TG data, with two sharp weight losses in the TG dehydration curve, and not all H_2O molecules were removed by 400 ºC. The TG curve exhibits additional weight loss at temperatures above 400 ºC, probably indicating the evolution of relic-OH groups. The hydroxyl groups gradually evolved during further heating. Thus, the temperature of dehydration affects the nature of structural phase transitions in scolecite, and evidence for separate phase fields under low- and high-P_{H_2O} conditions was found. When scolecite was heated under high-P_{H_2O} conditions, the newly observed x1-/x2-metamesolite phase field was bypassed due to the enhanced stability of the hydrous phase, and scolecite transformed directly to metascolecite and then to the amorphous T_5O_{10} phase. Lower P_{H_2O} conditions destabilized the hydrous phase at comparatively lower temperatures. Under these conditions, the aluminosilicate framework of metascolecite remained intact and the structure then underwent a displacive phase transition to the x1-/x2-metamesolite structures. Hence, under low-P_{H_2O} conditions one sees the "hidden phase transition" to x1-/x2-metamesolite that cannot be observed at higher P_{H_2O}. The structure of the amorphous T_5O_{10} phase determined from PDF refinements showed that it is composed of a collection of randomly oriented nano-fibers, each with a twisted T_5O_{10} structure with zero or one Ca^{2+} cation (and possibly relic-OH groups) attached to it. The determined unit-cell parameters and space group for x2-metascolecite provide a clue that the framework structures of x2-metamesolite (and perhaps x1-metascolecite) should be very similar to that of α1- or α2-metanatrolite.

This study demonstrated the important conclusion that the combined effects of temperature and P_{H_2O} influence not only the temperature but the nature of structure phase

transitions in the zeolite scolecite. Understanding the bonding interactions of the guest Ca^{2+} cations and H_2O molecules with the host aluminosilicate frameworks upon dehydration is key to pinpointing the phase transition mechanism(s) in scolecite. The observation of x1- and x2-metascolecite phases reflects the manner in which the host structure of scolecite responds to the thermal motions of its guest Ca-H_2O complexes. The drop of the Ca coordination sphere to below six is apparently not the only triggering mechanism causing scolecite to undergo a structural transformation. Similar to natrolite, the host structure of scolecite likely has a tendency not to form Si-O-Al angles less than 125º unless there are additional bonds from guest Ca^{2+} cations or hydrogen atoms to stabilize the small bridging oxygen angles. If this criterion cannot be achieved upon dehydration, the framework structure of metascolecite will collapse into the amorphous state as observed under the high-P_{H_2O} heating measurements. When measurements were made under low-P_{H_2O} conditions, the observation of different phase transition paths elucidated the subtle host-guest interactions that influence the energetically feasible Si-O-Al angles and the flexibility of the host frameworks. As the guest cations in scolecite are Ca^{2+}, only half the number of cations are needed to balance the negatively charged aluminosilicate framework. This makes the transition to the amorphous phase in scolecite comparatively easier because there are insufficient cations in the channel sites to mate with the framework. Compared with natrolite (which has twice the amount of guest cations (Na^{+}) in its channel systems and does not become amorphous upon dehydration), maintenance of host structure rigidity during scolecite dehydration most likely requires formation of OH group in the dehydrated scolecite framework. The occurrence of relic-OH groups is likely responsible for the partially irreversible structural changes in x1- and x2-metascolecite.

CHAPTER 3

Temperature- and P_{H_2O}-dependent structural phase transitions in the zeolite mesolite

Mesolite ($Na_2Ca_2Al_6Si_9O_{30} \bullet 8H_2O$; Z = 8) under room conditions possesses the same framework topology (NAT) and space group (*Fdd2*) as natrolite. The basic building blocks of the NAT-type framework are T_5O_{10} chains of (Al,SiO_4)-tetrahedra running parallel to the *c* axis (see Fig. 1.1a or Figs. 0.2B and 1.1A in Gottardi and Galli 1985). Each T_5O_{10} chain is linked to a neighboring chain at 2/8 *c* higher or lower, and the NAT framework can be described as being formed by single chain at four levels (Fig. 3.1a). Mesolite has two distinct channel types, one with two Na^+ cations and two H_2O molecules (the two Na^+ cations and H_2O molecules (Ow1) are crystallographic equivalent), and the other containing one Ca^{2+} cation and three H_2O molecules (Ow2, Ow3, and Ow4). In the first channel type, the Na^+ cation is coordinated by four framework oxygens (O), one H_2O (Ow1) from above and one H_2O (Ow1) below the framework O plane, in the form of a distorted octahedron (Fig. 3.1b). Each H_2O (Ow1) is ion-dipole attracted to two Na^+ cations in zigzagging -Ow1-Na-Ow1-Na-Ow1- chains along the *c* axis, with two Na^+ cations and two Ow1 molecules per unit-length along the *c* direction. The local Na^+ cation coordination is similar to that found in the channels in natrolite. In the second channel type, the bonding configuration of Ca^{2+} cations is similar to that of Na^+ cations in the first channel type, but with additional H_2O (Ow4) in the framework O plane, forming a pentagonal bipyramid (Fig. 3.1c). Each H_2O (Ow2, Ow3 and Ow4) is coordinated to one Ca^{2+} cation only, in the form of an isolated pentagonal bipyramid separated by a vacancy site along the *c* axis (i.e., -Ow2-Ca-Ow3-□-Ow2-). The local Ca

Mesolite ($Na_{16}Ca_{16}Al_{48}Si_{72}O_{240} \cdot 64H_2O$)

Space group = *Fdd*2, *a* = 18.4207(4) Å, *b* = 56.689(1) Å, *c* = 6.5494(2) Å, *V* = 6839.3(3) Å^3

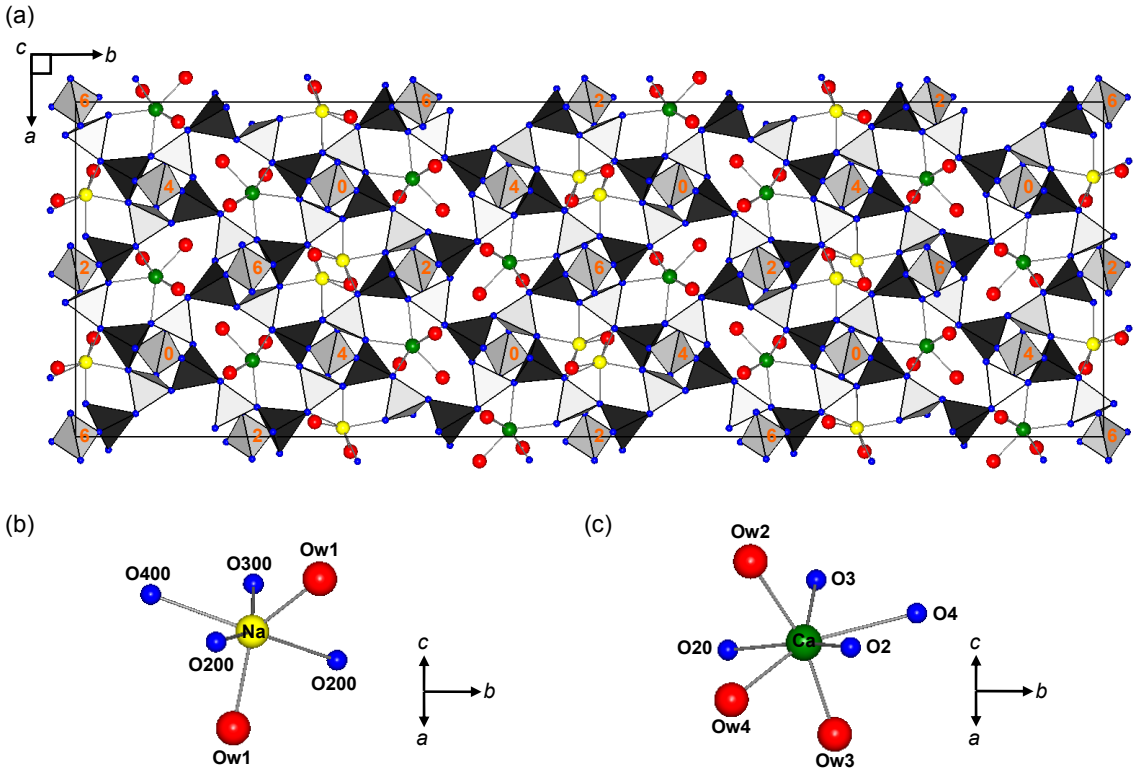

Figure 3.1. Refined crystal structure of mesolite at 23 ºC. **(a)** NAT framework viewed down the cross-linked chains. Numbers in the central tetrahedra indicate the height above the (001) plane as multiples of *c*/8. **(b)** and **(c)** Local view of coordination of Na^+ and Ca^{2+} cations in the mesolite channel system. Si tetrahedra = gray; Al tetrahedra = black; oxygen atoms = blue spheres; Na^+ cations = yellow spheres; Ca^{2+} cations = green spheres; H_2O molecules = red spheres; Bonds = solid gray lines.

configuration is similar to that found in the channels in scolecite. The mesolite structure can therefore be described as one plane of Na channels alternating with two planes of Ca channels parallel to (010), resulting in *a* and *c* unit-cell parameters similar to natrolite, with a tripled *b* unit-cell length.

Early studies on structural phase transitions in mesolite during dehydration and rehydration (Ståhl and Thomasson 1994; Ståhl and Hanson 1994) showed that mesolite undergoes an extraframework cation order-disorder phase transition on heating at temperatures >200 °C and another phase transition to an amorphous phase at temperature >325 °C. The extraframework cation order-disorder phase transition (in short, order-disorder phase transition) is thought to be triggered by the partial loss of Ow4 (one of the H_2O molecules coordinated to Ca^{2+} cation) beginning below 200 °C. The decreased coordination of the Ca^{2+} cations (from seven to six) with an increase in temperature causes the remaining Ow4 molecules to be expelled and allows the migration of extraframework cations to different channel sites. The resulting structure, namely extraframework cation-disordered metamesolite (we refer to this phase as Na/Ca-disordered metamesolite, see Wang *et al.* 2010), is similar to natrolite's structure but has a random distribution of Na^+, Ca^{2+}, and vacancies in the natrolite Na site. Thus, the structure of Na/Ca-disordered metamesolite maintains F*dd2* symmetry. Above the order-disorder transition temperature, remaining H_2O molecules (Ow1, Ow2, and Ow3) occupy positions similar to the natrolite H_2O site and these three can be considered as equivalent to the natrolite H_2O site (Ow'). On further heating, the H_2O (Ow') occupancy continuously decreases from 1 (i.e., equivalent to a fully occupied natrolite H_2O site) to ~0.66. When the Ow' occupancy is less than ~0.66, the local Ca configuration statistically can no longer maintain a coordination number of six. As described

by Artioli (1999a, 1999b) and Cruciani *et al.* (2003) for several Ca-bearing zeolites, phase transitions to an amorphous phase are triggered when the Ca coordination sphere drops below six. At temperatures >325 °C, the Ow' occupancy decreases to <0.66, the crystal structure is destroyed, and mesolite becomes X-ray amorphous (we refer to this phase as amorphous T_5O_{10}, see Wang *et al.* 2010).

These phases and the sequence of structural transformations are well demonstrated by the results of Rietveld analyses using data measured by conventional and synchrotron X-ray powder diffraction methods from Ståhl and Thomasson (1994; *ex-situ* measurements with pre-dehydrated/sealed samples) and Ståhl and Hanson (1994; *in-situ* measurements). In both experiments, *ex-situ* and *in-situ* heating to a given temperature gave rise to identical phase transition phenomena. However, P_{H_2O} conditions during both heating experiments were not controlled, and, as a consequence, it is not possible to know the possible dependence of the phase transition behavior on P_{H_2O}. Accordingly, we recently (Wang *et al.* 2010) published the results of a study of structural phase transition behaviors in mesolite under controlled-temperature and -P_{H_2O} conditions. As expected from the natrolite phase transition behavior, mesolite also exhibits similar temperature- and P_{H_2O}-dependent phenomena. At 425 ºC under low-P_{H_2O} conditions, dehydrated mesolite preserved the long-range ordered aluminosilicate framework structure, which was observed by us for the first time. This newly observed high-temperature dehydrated phase, x-metamesolite, has a crystal structure similar to those of other dehydrated natrolite phases (either α1- or α2-metanatrolite). Conversely, under high-P_{H_2O} conditions, dehydrated mesolite became amorphous (but remained T_5O_{10} local structural configuration). These two distinct high-temperature P_{H_2O}-dependent phase transition paths illustrate the importance of considering the combined effects of temperature and P_{H_2O} in

mesolite. This chapter provides a comprehensive representation of the temperature- and P_{H_2O}-dependent structural phase transitions observed during mesolite dehydration and rehydration, emphasizing the important results that have been observed in my research. For a detailed description of modeling methods, including structure determination, X-ray Rietveld analyses and synchrotron X-ray pair distribution function analysis, refer to Wang *et al.* (2010).

3.1 Samples and experimental methods

The mesolite specimen used in this study is from Berufjőrdur, Iceland, with a composition of $Na_{15.76}Ca_{16.18}Al_{48.28}Si_{71.76}O_{240} \bullet 63.50H_2O$, an average of electron microprobe analyses of crystals in several thin sections. The sample was crushed into a fine powder (<38 μm) using a Retsch Micro-Rapid mill with agate mortar and pestle under acetone. In order to investigate mesolite structural behaviors under controlled-temperature and -P_{H_2O} conditions and to characterize the local structure of the amorphous T_5O_{10} phase, two types of measurements were made: (i) X-ray power diffraction (XRD) with *in-situ* controlled-temperature and -P_{H_2O} in order to monitor structural changes as a function of environmental parameters (i.e., temperature and P_{H_2O}); (ii) synchrotron X-ray total scattering measurements with pair distribution function (PDF) analysis as a local probe to investigate possible short-range Na/Ca ordering in the Na/Ca-disordered metamesolite phase and to obtain local structure information for the amorphous T_5O_{10} phase. In addition to the above two measurements, thermogravimetric (TG) analyses conducted under ambient *RH* conditions were made to characterize the bulk dehydration phenomena, and these results were combined with structural data obtained with XRD measurements.

3.1.1 Laboratory X-ray powder diffraction analysis

Laboratory XRD data were measured using a Bruker D8 Advance X-ray diffractometer (Cu Kα radiation), equipped with a Vantec position-sensitive detector, an Anton-Paar TTK 450 heating stage, and a sample environmental chamber. The TTK 450 stage provides the opportunity to measure data as a function of temperature, up to 450 ºC, and the sample environment humidity was controlled via gas flow into and out of the sample chamber using an automated V-Gen dew point/*RH* generator (InstruQuest Inc.). Measurements were made under controlled-P_{H_2O} conditions ranging from ~0.6-24 mbar (corresponding to ~2-90% *RH* at 23 ± 1 °C and 1 bar) down to ~$10^{-0.8}$-$10^{-2.9}$ mbar (roughing pump vacuum condition, $10^{-3.8}$ bar), at sample temperatures up to 430 °C, measuring in 25 ºC increments from room temperature to 100 ºC and in 10 ºC increments from 100 to 430 °C. The lower limit of P_{H_2O} ($10^{-2.9}$ mbar) under vacuum conditions was estimated based on the ambient *RH* at the time of measurement (i.e., ~30% *RH* at 22 °C; scaled by a factor of $10^{-3.8}$). On the other hand, the upper limit of P_{H_2O} ($10^{-0.8}$ mbar) under vacuum conditions was estimated based on the assumption that all the residual gas remaining in the cell was H_2O vapor. Samples were mounted as thin-layer slurry mounts and were measured from 11º to 33º *2θ*, counting for 0.66 sec at each 0.017º *2θ* step, equivalent to a count time of 613.3 sec/step. An equilibrium method was applied which involved exposing a specimen to a controlled-P_{H_2O} environment and heating to a given temperature, waiting for 60 min, and measuring until no further structural changes occurred, and then heating to successively higher temperatures (at a fixed P_{H_2O} value) in the same manner. Data obtained with thin-layer slurry mounts using the same heating procedure but under different P_{H_2O} conditions were compared qualitatively, because the thin-layer slurry mounts minimized build-up of P_{H_2O} in

intercrystallite pore spaces, thereby providing a more accurate picture of the phase transition behaviors. This approach allowed the determination of mesolite phase transition behaviors under specific environmental conditions.

3.1.2 Synchrotron X-ray total scattering

Data for X-ray PDF analysis were obtained using the RA-PDF technique (Chupas *et al.* 2003), utilizing a monochromatic high-energy (0.1372 Å, 90.4 keV) X-ray beam selected from a Si (111) Laue monochromator at beamline 11-ID-B at the Advanced Photon Source, Argonne National Laboratory. Mesolite powder was loaded into a glass capillary (1 mm inner diameter and 1.1 mm outer diameter) under room conditions. The sample capillary was placed in a sample-environment cell mounted directly on the goniometer (Chupas *et al.* 2008). The entire sample assembly was heated under dry air flow (the predicted P_{H_2O} is ~1.5 mbar, equivalent to ~5% *RH* at 23 ± 1 °C and 1 bar), and temperature was ramped from 25 to 400 °C (in 50 °C increments) with 30 min equilibrium times before each data collection. Scattering data were collected ten times every 6.7 min at a set temperature, using a MAR345 imaging plate detector positioned 187.72(2) mm from the sample. Parasitic scattering from the atmosphere and capillary were collected using the same temperature ramp, duplicating the assembly without a sample. The program Fit2D (Hammersley *et al.* 1996) was used to integrate the raw images, summing the ten repeated scattering signals for each temperature set (to improve counting statistics), and then generating plots of intensity versus Q ($\boldsymbol{Q}$ is momentum transfer vector, $Q = |\boldsymbol{Q}| = 4\pi sin\theta/\lambda$). The program PDFgetX2 (Qiu *et al.* 2004) was used for data treatment. The total scattered intensity, $I(Q)$, was corrected for background, Compton scattering, and absorption, and was then converted to normalized total scattering structure function, $S(Q)$. The data were then terminated at $Q_{max} = 24$ Å^{-1} to obtain the

corresponding real-space reduced pair distribution function, $G(r)$. The program PDFgui (Farrow *et al.* 2007) was used for quantitative structure refinement of the reduced pair distribution function.

3.1.3 Thermogravimetric analysis

TG measurements were performed using a TA Instruments 2960 TG analyzer. Analyses made in this study were conventional isobaric experiments at 1 bar (no vacuum TG analyses). The dynamic method (i.e., heating the sample powder continually at a constant rate while recording the weight loss) was performed with a 1 °C/min temperature rate. The sample environment was under ambient humidity conditions, and the humidity (~20-30% *RH*, corresponding to ~6-8 mbar P_{H_2O} at 22 ± 1 ºC) was recorded before and after the measurement. The experiments were designed to measure the H_2O content of mesolite as a function of temperature. About 11.5(2) mg of mesolite powder was evenly distributed onto a alumina sample pan. The total weight change of the sample was monitored while heating to 950 °C under ambient *RH* conditions.

3.2 Results and discussions

3.2.1 Mesolite phase transitions in P_{H_2O} and temperature spaces

Figure 3.2 illustrates mesolite's phase transition behavior and shows the existence of different transition paths when mesolite was heated under different P_{H_2O} conditions (mesolite, Na/Ca-disordered metamesolite, and x-metamesolite phases are labeled with square, star and x symbols, respectively). The first phase transition, an extraframework cation order-disorder phase transition, to Na/Ca-disordered metamesolite occurred at 110 °C when P_{H_2O} was ~$10^{-0.8}$-$10^{-2.9}$ mbar, it increased to 150 °C when P_{H_2O} was 0.56(5) mbar (controlled

at ~2.1 ± 0.2% *RH*, 23 ± 1 °C, and 1 bar), and it increased to 230 °C when P_{H_2O} was 24.2(5) mbar (controlled at 91.9 ± 0.1% *RH*, 23 ± 1 °C, and 1 bar). The extraframework cation order-disorder phase transition is indicated by the disappearance of $k \neq 3n$ diffraction peaks and continuous shifts of $k = 3n$ peaks to higher 2θ angles (the order-disorder phase transition is marked by black dashed lines in Figs. 3.2c-l). One can consider the $k \neq 3n$ peaks as super-lattice reflections, appearing as a result of the ordering of Na^+ and Ca^{2+} extraframework cations in the mesolite channels. The extraframework cation order-disorder phase transition is 2nd-order in character with continuous changes in structure at the transition temperature, and the temperature at which the transition occurs is P_{H_2O}-dependent (Fig. 3.2). It is well known that reactions involving gas (e.g., $H_2O_{(g)}$) are influenced by the partial pressure of the gas involved, and a parallel example is the effect of CO_2 partial pressure on $CaCO_3$ decomposition. Hence, the comparatively moist environments employed on heating caused the initial dehydration temperatures to increase gradually. Because the $k \neq 3n$ reflections are most sensitive to the positions of Na^+ and Ca^{2+} cations and are less sensitive to the position and occupancy of Ow4 H_2O (confirmed by calculating XRD patterns with variations in Na, Ca, and Ow4 positions, and Ow4 occupancy), the P_{H_2O} dependence of the order-disorder phase transition temperature suggests that the triggering force causing the migration of Na^+ and Ca^{2+} cations to different channel sites is the dehydration process (primarily the loss of Ow4 H_2O molecules; see Rietveld refinements in Wang *et al.* 2010). If the formation of a random distribution of Na^+, Ca^{2+}, and vacancies is caused by a purely thermally induced process, the disappearance of $k \neq 3n$ reflections should be independent of P_{H_2O}. Moreover, exposure of Na/Ca-disordered metamesolite to moist air (Ståhl and Thomasson 1994) showed that disappearance of the $k \neq 3n$ reflections is irreversible, suggesting the existence

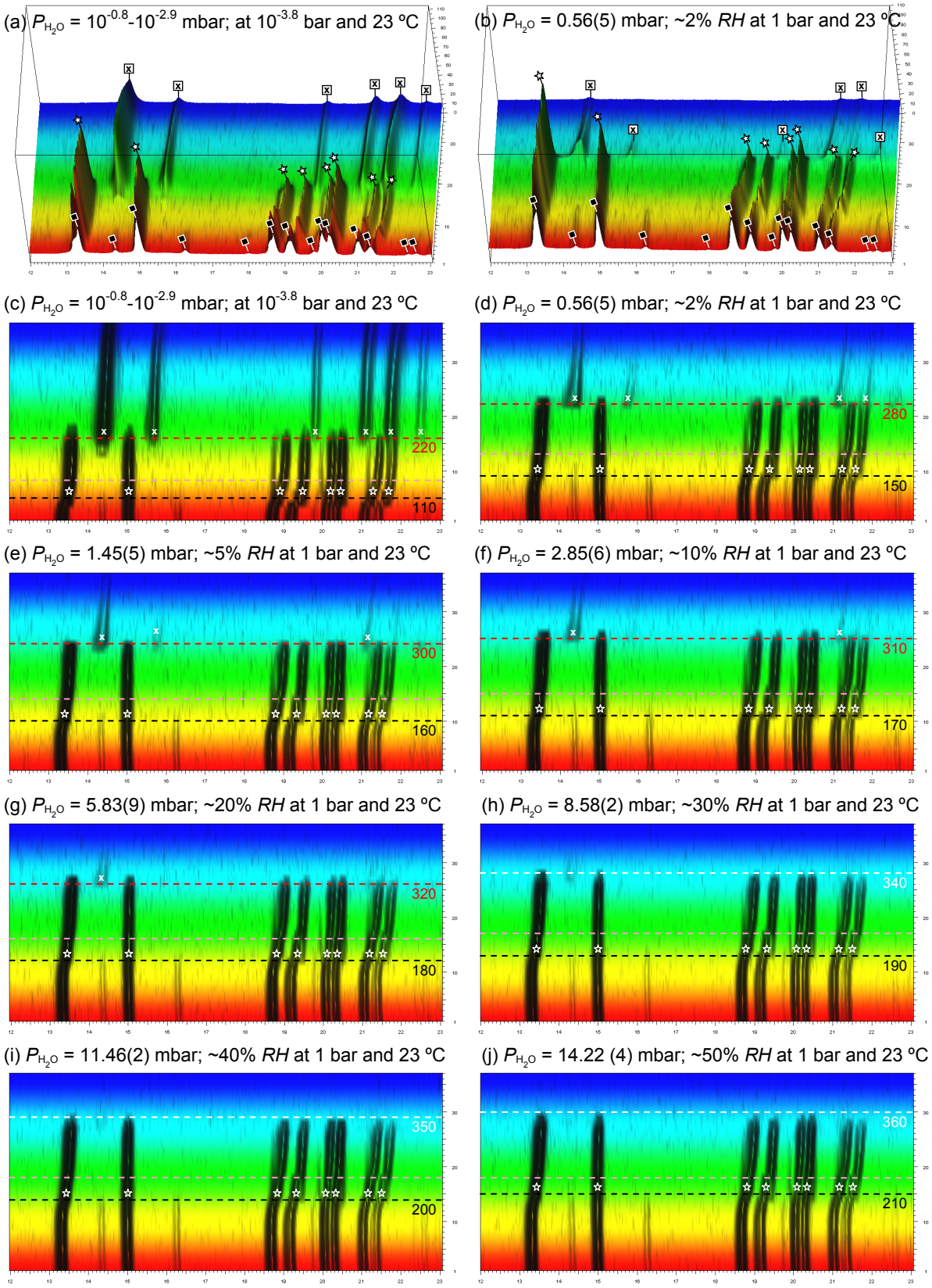

Figure 3.2. Continued on next page.

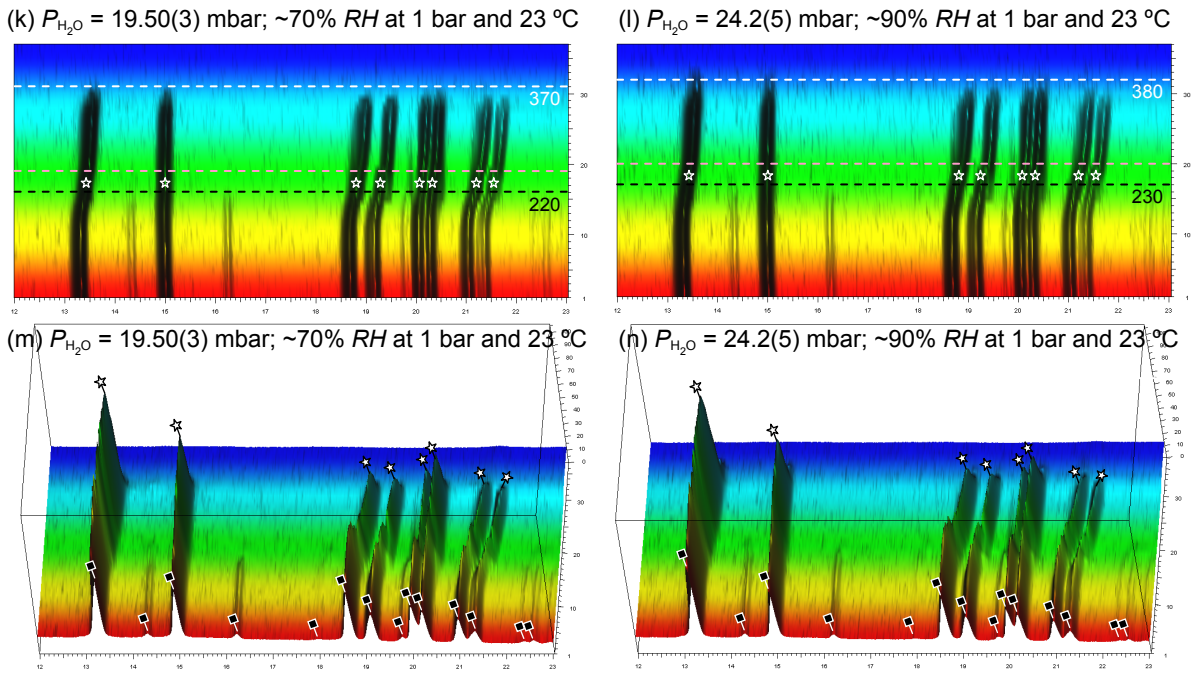

Figure 3.2. Temperature-resolved 3D-XRD patterns for mesolite measured under different P_{H_2O} conditions, illustrating the distinct changes as a function of temperature: *x*, *y* and *z* axes represent 12-23º *2θ*, intensity (cps), and temperature (#1-37, in sequence of 23, 50, 75, 100, 110, 120, 130, 140, 150, 160, 170, 180, 190, 200, 210, 220, 230, 240, 250, 260, 270, 280, 290, 300, 310, 320, 330, 340, 350, 360, 370, 380, 390, 400, 410, 420, and 430 ºC), respectively. The square, star, and x symbols represent diffraction peaks of mesolite, Na/Ca-disordered metamesolite, and x-metamesolite, respectively. The black dashed line represents the order-disorder phase transition **(c-l)**. The red dashed line represents the phase transition to x-metamesolite/amorphous T_5O_{10}, which only occurred under low-P_{H_2O} conditions **(c-g)**. The white dashed line represents the phase transition to amorphous T_5O_{10} **(h-l)**. At temperatures ~30-40 °C above the order-disordered phase transition, small but noticeable shifts occurred in the diffraction peaks, marked by the pink dashed line **(c-l)**. Plots **(a)**, **(b)**, **(m)** and **(n)** are orthogonal; Plots **(c)** to **(l)** are viewed down the *y* axis. Diffraction peaks that have no labels in the low-temperature region belong to mesolite. Note the increased background in plots **(b)**, **(m)** and **(n)**, which indicates formation of an amorphous T_5O_{10} phase upon dehydration.

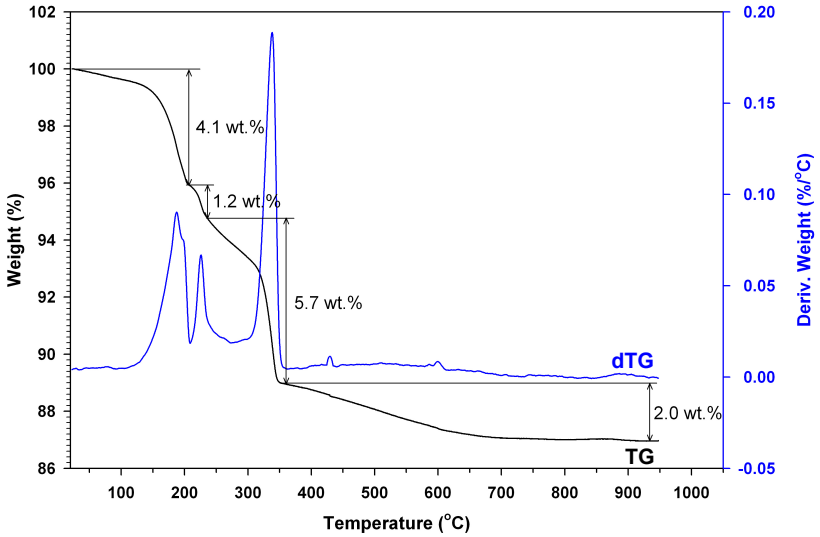

Figure 3.3. TG data for mesolite measured during dehydration (black curve). Sample mass was 11.5(2) mg. Measurement was made under ambient *RH* conditions (~20-30% *RH*) with 1 ºC/min heating rate. The first derivative of the black TG curve is given by the blue curve labeled dTG. The primary, secondary, and tertiary inflection temperatures (i.e., the maximum rate of weight change, representing a peak in the dTG plot) are at ~188, ~226, and ~338 ºC, respectively.

of a random distribution of Na^+, Ca^{2+}, and vacancies in the extraframework channel system even after rehydration. The corresponding TG weight loss curve (Fig. 3.3) measured under ~20-30% *RH* shows a primary inflection temperature (the maximum rate of weight change) of 188 °C, comparable with the order-disorder phase transition temperature observed under ~30% *RH* condition (Fig. 3.2h). This also supports the concept that the order-disorder phase transition in mesolite is trigged by the dehydration reaction. The weight loss based on TG measurement is 4.1 wt.% at ~210 °C, which is equivalent to the loss of 21 out of 64 H_2O molecules (i.e., 16 Ow4 H_2O + 5 Ow' H_2O, where Ow' = Ow1+Ow2+Ow3)[8]. The secondary inflection temperature in the TG curve is 226 °C (Fig. 3.3), which is ~38 °C higher than the prior inflection temperature. Consistently, at temperatures ~30-40 °C above the order-disorder phase transition, small but noticeable shifts in the XRD reflection peaks was observed (marked by pink dashed lines in Figs. 3.2c-l). This shift is associated with the continuous loss of Ow' H_2O molecules and represents the framework accommodation of Na/Ca-disordered metamesolite to changes in the hydration states. By ~240 °C, the total weight loss is 5.3 wt.%, which accounts for additional an 6 Ow' H_2O loss. Up to this stage (i.e., at temperatures ~50 °C above the order-disorder phase transition), the Ow' site occupancy in the Na/Ca-disordered metamesolite unit cell calculated from the TG weight loss curve is ~0.77 (i.e., $1-\frac{11}{48}$), corresponding well with Rietveld refinement results in Wang *et al.* (2010).

With further heating to higher temperatures, a continuous weight loss was seen in the TG curve (Fig. 3.3). As mentioned in the introduction, when the occupancy of the Ow' site decreased to <0.66 (equivalent to ~ 6.3 wt.% total weight loss), the local Ca configuration

[8] The Ow1+Ow2+Ow3 sites in the mesolite unit-cell setting are equivalent to the Ow' site in the Na/Ca-disordered metamesolite unit-cell setting.

could no longer statistically maintain a coordination number of six. The crystal structure of Na/Ca-disordered metamesolite then underwent a second phase transition. Surprisingly, this second phase transition that occurred on further heating not only showed P_{H_2O}-dependent transition temperature but also two distinct phase transition paths (see red and white dashed lines in Figs. 3.2c-l). When measurements were made at a low-P_{H_2O} (i.e. below ~6 mbar P_{H_2O}), Na/Ca-disordered metamesolite (Figs. 3.2a-g; star symbols) underwent a 1st-order displacive phase transition with a discontinuous change in unit-cell parameters to a newly discovered phase (Figs. 3.2a-g; x symbols). The structure of Na/Ca-disordered metamesolite "snapped" into this undetermined structure beginning at 220 °C when P_{H_2O} was ~$10^{-0.8}$-$10^{-2.9}$ mbar, increasing to 320 °C when P_{H_2O} was 5.83(9) mbar (controlled at ~20.04 ± 0.06% *RH*, 23 ± 1 °C, and 1 bar). This newly discovered phase (termed x-metamesolite) was clearly observed under low-P_{H_2O} conditions and coexisted with Na/Ca-disordered metamesolite over small temperature intervals (Figs. 3.2a-g). For instance, at temperatures between 220 and 250 °C (Figs. 3.2a and c), the x-metamesolite and Na/Ca-disordered metamesolite coexisted. At 250 °C, the diffraction intensities of the x-metamesolite phase reached a maximum and the intensities of the Na/Ca-disordered metamesolite phase decreased to zero (Figs. 3.2a and c). Above 290 °C, diffraction intensities of the x-metamesolite phase gradually decreased and diffraction peaks also broadened, together with an increase in the background (i.e., at this point the diffraction pattern is composed of a mixture of two phases, x-metamesolite and amorphous T_5O_{10}). By 430 °C, diffraction peaks of x-metamesolite remained although the intensities were weak. Conversely, when measurements were made at a high-P_{H_2O} (i.e. above ~8.5 mbar P_{H_2O}), Na/Ca-disordered metamesolite (Figs. 3.2h-n; star symbols) went through a phase transition directly to an amorphous phase without any evidence of a coexisting x-

metamesolite phase. The temperature of transition to the amorphous T_5O_{10} phase was also P_{H_2O}-dependent (as indicated by the white dashed lines in Figs. 3.2h-l), indicating that the high-temperature transformations in mesolite are trigged by the dehydration reaction. Once the amorphous T_5O_{10} phase was formed, the structure of mesolite lost its rehydration ability. The corresponding TG curve yields a third inflection temperature of 338 °C. In comparison with the previous two weight losses, this third weight loss has a sharper TG dehydration curve, and not all H_2O molecules were removed by 360 ºC (Fig. 3.3). The total weight loss is 11.0 wt.% at ~360 °C and the TG curve exhibited additional weight change at temperatures above 360 ºC, probably indicating the formation of OH groups. These hydroxyl groups gradually evolve upon further heating (see the gradual decreasing weight on TG curve at temperatures above 360 ºC; Fig. 3.3).

3.2.2 Phase transitions in mesolite analyzed by X-ray PDF

Based on qualitative observation, the temperature-resolved PDFs of mesolite (Fig. 3.4) measured in a dry air flow showed weak $G(r)$ variations from 25 to 250 °C and a clear phase transition to an amorphous phase at temperatures >250 °C. The PDF $G(r)$ signals were damped at about r >9 Å for 300, 350, and 400 °C PDFs (Fig. 3.4a), suggesting disappearance of long-range order in the structure. These data provided clear evidence of the phase transition to amorphous T_5O_{10} and these results correspond to XRD observations made when mesolite was heated under high-P_{H_2O} conditions. Apparently, when mesolite powder was packed into a small-volume glass capillary, the dry air flowing through the capillary was not sufficient to remove the build-up of P_{H_2O} in intercrystallite pore spaces, causing mesolite to behave in a manner similar to samples in XRD measurements made under high-P_{H_2O} conditions. In addition, the 50 °C temperature increments applied to PDF measurements may

also prohibit the chance of observing the x-metamesolite phase upon dehydration (relatively rapid heating rate may increase the opportunity to destroy the structure). Interestingly, the phase transition to Na/Ca-disordered metamesolite was difficult to observe in the PDFs. PDF $G(r)$ plots showed only gradual and weak changes with increasing temperature from 25 to 250 °C (Fig. 3.4). As the PDF $G(r)$ represents the probability of finding an atom at a distance r from any reference atom and is defined as the sum over all atomic pairs within the model crystal, the first $G(r)$ peak centered at 1.65 Å is the Si(Al)-O distances, the second peak in the r range of 2.4-2.8 Å is the overlap of Na(Ca)-O, Na(Ca)-Ow, and O-O distances, and the third peak at 3.1 Å is contributed by Na(Ca)-Si(Al) distances and the first shell of Si-Si(Al) distances (Fig. 3.4b). Peaks below 1.4 Å and centered at 1.9 and 2.1 Å (Fig. 3.4b) are termination ripples from the Fourier transform at a value of Q_{max} = 24 Å^{-1} (these termination ripples shifted when Q_{max} was dropped to 19 Å^{-1}). In the high-r region, the PDF $G(r)$ was difficult to interpret due to the complexity of the material. For example, the fourth peak at 3.8 Å is composed of the second shell of Si-Si, Si(Al)-O, Na(Ca)-Si(Al), and Na(Ca)-O distances and the first shell of Na-Na and Al-Al distances. Therefore, extracting structural information directly from PDF $G(r)$ without a fitted structure model is somewhat limited for complex materials. Some qualitative observations are described here, and detailed PDF refinement procedures using fitted structure models are presented in Wang *et al.* (2010). At temperatures ≤250 °C, the local structure below 4.8 Å remained almost unchanged, with minor variations (see Fig. 3.4b) such as: (i) the Si(Al)-O peaks (at 1.65 Å) and Na(Ca)-Si(Al)/Si-Si(Al) peaks (at 3.1 Å) broadened asymmetrically with increasing temperature; (ii) the peak centered at 2.45 Å gradually became resolved from the broad peak (2.4-2.8 Å) observed at 25 °C, and other peaks at ~3.6, ~4.3 and ~4.6 Å were also resolved in the low-temperature PDF $G(r)$

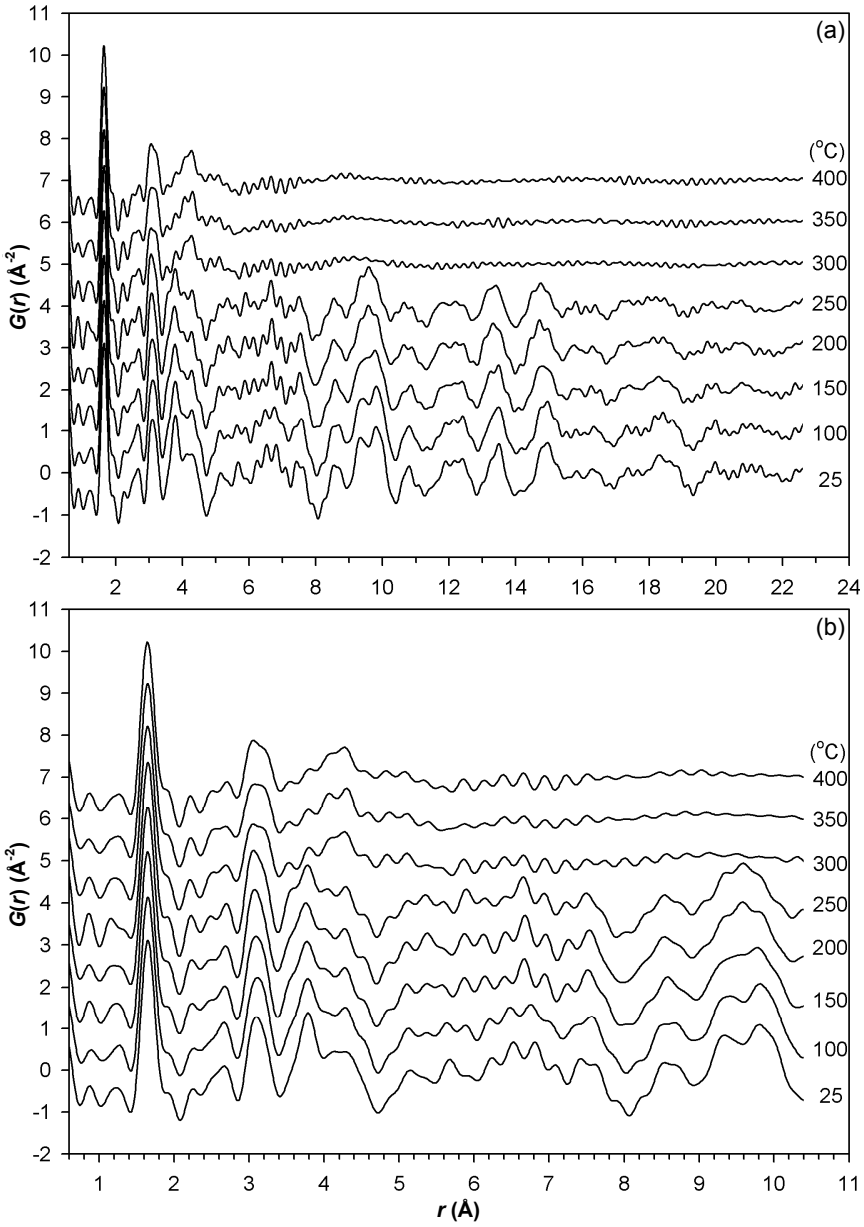

Figure 3.4. The reduced pair distribution functions, $G(r)$, obtained through direct Fourier transformation of the observed structure functions, $S(Q)$, are plotted and stacked in order of increasing temperature. Plot **(b)** is an expansion of the low-r region.

patterns; (iii) the intensity of the peak at ~3.8 Å decreased; (iv) peaks in the high-*r* region (> 4.8 Å) showed minor variations as well. All of these subtle changes are most likely related to the loss of the Ow4 H_2O molecules and to migration of the Na^+ and Ca^{2+} extraframework cations with temperature.

3.2.3 Average vs. local view of the structure: comparison of reciprocal-space vs. real-space determinations of crystal structures for mesolite and Na/Ca-disordered metamesolite

Briefly speaking, the difference between the average crystallographic structure and the local structure for a crystalline material is reflected in the *actual* bond lengths and/or bond angles. The number of atomic positions that deviate from the ideal crystallographic sites is usually small in the crystalline materials, and hence the concept of static deformations of the structure (i.e., lattice strains and thermal displacement factors) is often introduced in when discussing average structure models. In addition, if the deviations are smoothly varying in space they may be described by elasticity theory. To illustrate the difference between the average and local structures in mesolite and Na/Ca-disordered metamesolite, the fitted PDF $G(r)$ profiles (for 25 and 250 °C data) using the average structure models of mesolite and Na/Ca-disordered metamesolite are presented in Figures 3.5a and c, respectively. These two fits were achieved by constraining to the average structure models obtained with Rietveld (reciprocal-space) refinements (Wang *et al.* 2010). Only scale factor and peak sharpening parameters in the low-*r* range (i.e., δ_2 and *low-r α ratio*, attributed to correlated motion) were refined, and the starting average structure models gave sufficient matches with the exception of the low-*r* range (i.e., the difference curves were large at r <6.3 Å for the 25 °C PDF and at r <8.3 Å for the 250 °C PDF). Subsequent refinements varying unit-cell parameters, atomic positions, and thermal displacement parameters gave significantly improved fits for both

PDFs (Figs. 3.5b and d). Considering the complexity of the mesolite structure and the nature of real-space refinements, the final R_{wp} value of ~0.25 can be considered a reasonable result (many published PDF refinements have R_{wp} values varying from 0.1 to 0.4). As bond distances and angles were not constrained during the PDF refinements (i.e., the distributions of bond length and angle is naturally reflected in the PDF $G(r)$ function), the resulting models should provide better representations of the short- to medium-range structural features. For example, the refined atomic thermal displacement parameters were smaller in PDF refinements than in Rietveld refinements, and refined Si(Al)-O bond lengths showed a larger range of distributions. The distributions of bond distances likely arise from lattice deformations and contribute to the microstrain effects observed in XRD profiles. Figure 3.6 shows comparisons between the average (XRD) and local (PDF) structure models for mesolite and Na/Ca-disordered metamesolite. Noticeably, the precisions of refined unit-cell parameters for both mesolite and Na/Ca-disordered metamesolite are approximately one order of magnitude lower than those obtained with XRD Rietveld analyses. This is partly due to statistical noise and resolution limits in the data and partly arises from the difficulty of determining atomic pairs having a similar bond length within the model crystal.

As mentioned above, at temperatures above the order-disorder phase transition, Na^+ and Ca^{2+} extraframework cations randomly occupy the channel cation sites. The disappearance and irreversibility of super-lattice peaks observed in the room-temperature XRD pattern indicate a disordered distribution of Na^+, Ca^{2+}, and vacancies. As the PFD $G(r)$ plots only showed gradual and weak changes at temperatures up to 250 °C, it is doubtful that the Na^+/Ca^{2+} cations are forming truly random distributions in the channels. They may simply deviate from their room-temperature channel positions in a random fashion (but

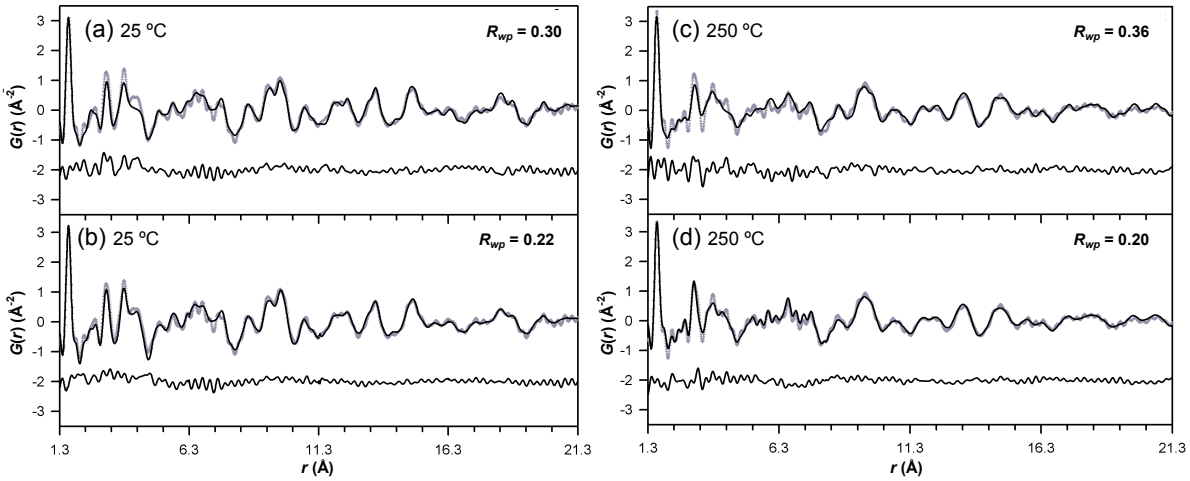

Figure 3.5. PDF refinements for mesolite **(a** and **b)** and Na/Ca-disordered metamesolite **(c** and **d)**. In plots **(a)** and **(c),** fits were achieved by constraining to the average structure models obtained with Rietveld refinements (this study), allowing only scale factor, δ_2, and *low-r α ratio* to vary. In plots **(b)** and **(d)**, fits were achieved by allowing scale factor, δ_2, *low-r α ratio*, unit-cell parameters, atomic positions, isotropic displacements, and occupancy factors to vary. For all plots, the observed PDF $G(r)$ function is shown with crosses and the calculated PDF $G(r)$ function is shown as a black solid line. The difference plot is at the bottom of each plot.

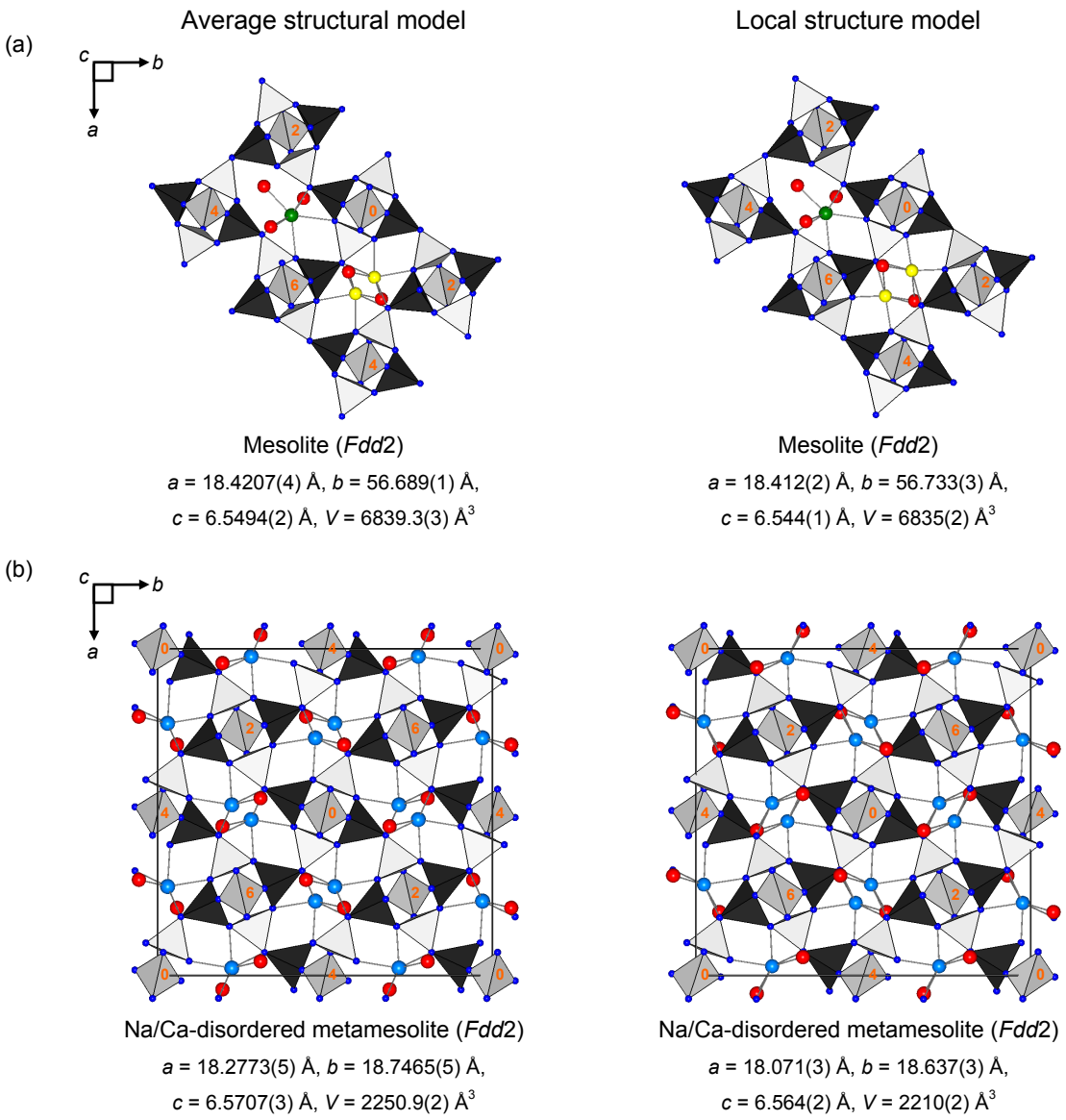

Figure 3.6. Average vs. local view of structure for mesolite **(a)** and Na/Ca-disordered metamesolite **(b)**. The average crystallographic structure was determined from XRD Rietveld refinements, whereas the local structure was determined from PDF real-space refinements. The large blue spheres in the Na/Ca-disordered metamesolite structure represent the extraframework sites for occupancy of (1/3 Ca +1/3 Na + 1/3 □). Other symbols are the same as in Figure 3.1.

remain localized in their room-temperature channels). In either case, XRD cannot "see" this feature, because it only provides average structural information. Thus, evaluation of the information concerning short-range order contained in the PDF is very valuable. Reverse Monte-Carlo refinement using high-quality data allows short-range order information to be extracted from a PDF (e.g., Proffen *et al.* 2002). However, in mesolite, the atomic pairs contributed by the aluminosilicate framework (e.g., Si-O, Al-O, O-O, Al-Al, and Si-Si) are much stronger than pairs contributed from the extraframework constituents (e.g., Na-Ow, Na-O, Ca-Ow, Ca-O, and Ca-Na), making it extremely difficult to discern any short-range Na/Ca ordering in the Na/Ca-disordered metamesolite phase. Further studies with better, higher-quality PDF data or diffuse scattering measurements should provide more insight into the nature of Na/Ca-disordered metamesolite.

3.2.4 Local structure of amorphous T_5O_{10} formed during mesolite dehydration

The disordered nature of amorphous T_5O_{10} does not lend itself to classical elastic powder diffraction methods, as the material does not give rise to Bragg diffraction peaks. However, the corresponding PDF $G(r)$ elucidates the residual local structure in the low-r region. By inspection, the amorphous T_5O_{10} phase formed during mesolite dehydration has a local structure very similar to the structure of the amorphous T_5O_{10} phase formed during scolecite dehydration (Fig. 3.7). In addition, the Si(Al)-O bonds (centered at ~1.65 Å) and the first coordination shell of Si-Si(Al) (centered at ~3.1 Å) were preserved, suggesting that the original long-range ordered aluminosilicate framework has distorted into randomly oriented domains. Domain sizes are roughly 7 Å, as indicated by sharp $G(r)$ features, showing that the intra-domain Si, Al, and O bonding correlations are preserved. The initial model for the amorphous T_5O_{10} domain structure was derived from the structure models of

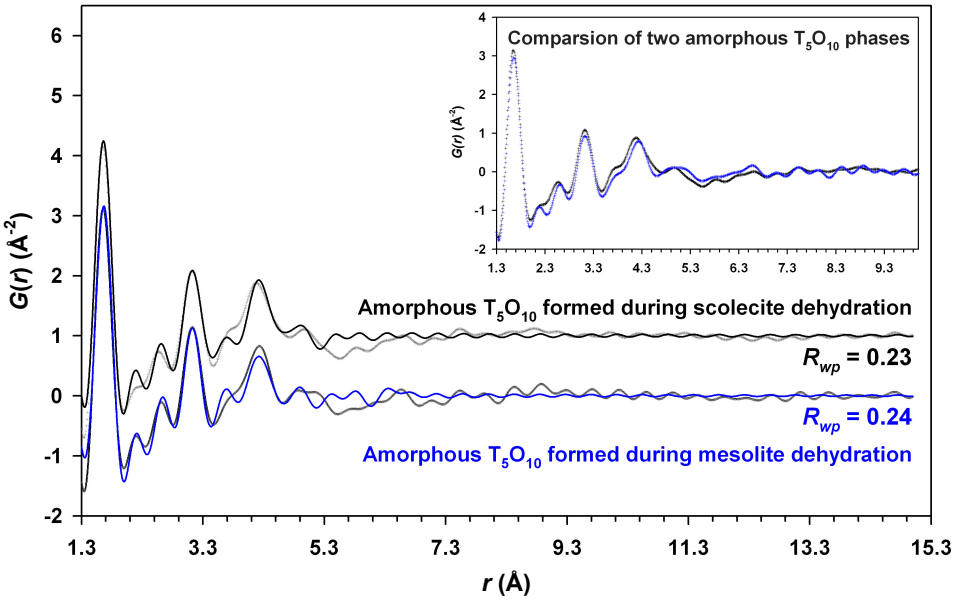

Figure 3.7. PDF refinements for amorphous T_5O_{10} phases formed during mesolite and scolecite dehydration (at 500 ºC). Fits were achieved by allowing scale factor, δ_2, *low-r α ratio*, unit-cell parameters, atomic positions, isotropic displacements, occupancy factors, and *spdiameter* to vary. The amorphous T_5O_{10} phase formed during mesolite dehydration (blue fit) has a local structure similar to that of the amorphous T_5O_{10} phase formed during scolecite dehydration (black fit), and their comparisons are shown in the insert. For all plots, the observed PDF $G(r)$ function is shown with gray crosses and the calculated PDF $G(r)$ function is shown as a black (or blue) solid line.

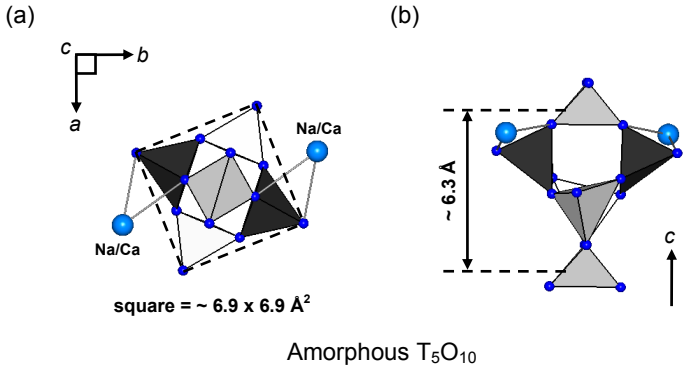

Figure 3.8. A twisted T_5O_{10} chain with dimensions (LWH) of ~6.9 x 6.9 x 6.3 Å. Amorphous T_5O_{10} comprises a collection of many of these twisted chains randomly oriented with respect to each other. Na^+ or Ca^{2+} cations (large blue spheres) and/or relic-OH groups are attached close to Al tetrahedra (black tetrahedra). **(a)** Viewed down the chain; **(b)** Viewed along the chain. Other symbols are the same as in Figure 3.1.

amorphous phase determined during scolecite dehydration (see discussions in section 2.3.2). In order to model the effect of the finite domain size, a shape damping parameter, *spdiameter* (a spherical form factor) was added into the calculated PDF $G(r)$ function. The initial value of *spdiameter* was set to 7 Å (i.e., the initial estimate for domain diameter) and was allowed to refine. After several refinement cycles, a suitable local structural picture from the initial trial model was obtained. The refinement process was terminated when no more improvements were observed, after ensuring that the resulting model was crystal chemically reasonable. The fitted PDF $G(r)$ function is shown in Figure 3.7. The final *spdiameter* value of 8.1(2) Å is slightly larger than expected, as the dimensions (LWH) of an untwisted single T_5O_{10} chain are approximately 7 × 7 × 6.5 Å (Alberti and Vezzalini 1981). Twisted chains will have roughly the same length and width but a smaller height, depending on the degrees of the twisting (Alberti and Vezzalini 1983). Final refinement results showed a twisted T_5O_{10} chain with dimensions (LWH) of about 6.9 × 6.9 × 6.3 Å (Fig. 3.8), suggesting that each domain is composed of a single twisted nano-fiber formed from the breakage of the aluminosilicate framework. Hence, amorphous T_5O_{10} can be described as a collection of nano-fibers randomly oriented with respect to each other. The slightly larger domain diameter (i.e., *spdiameter* = 8.1 ± 0.2 Å) suggests the attachments of Na^+ or Ca^{2+} cations (and possibly hydroxyl groups) to the nano-fibers. The calculated average number of cations attached to a single nano-fiber is 1.3, suggesting that each nano-fiber has zero, one, or two cations attached to it. Figure 3.8 shows a representation of the attachment of two cations to a chain. In addition, the PDF $G(r)$ in the r-range between 5.3 to 8 Å did not fit very well because a spherical form factor was used as a damping parameter. The nano-fibers are not

spherical and fiber-fiber correlations are weak, adding to the difficulties in obtaining a good PDF fit in this region (Fig. 3.7).

3.2.5 Indexing of the x-metamesolite X-ray diffraction pattern

To begin solution of the structure of x-metamesolite, which forms when mesolite is heated under low-P_{H_2O} condition, a mesolite specimen was mounted in a cavity holder and heated to 425 °C under a P_{H_2O} of ~$10^{-0.8}$-$10^{-2.6}$ mbar. After waiting 120 min for equilibrium, XRD data were collected from 10º to 120º 2θ, counting for 0.66 sec at each 0.017º 2θ step, equivalent to a count time of 613.3 sec/step. Three repeated measurements were made with a one-hour interval between each data collection, and the three raw data sets were then summed to improve counting statistics. The final XRD pattern is shown in Figure 3.9. The measured diffraction pattern was first indexed using the software package TOPAS-Academic v.4.1 (Coelho 2007) to determine possible space groups and unit-cell parameters. Successful pattern indexing requires knowledge of whether the unknown material is a single phase or a mixture. XRD data measured at 425 ºC showed a slightly increased background, suggesting that x-metamesolite coexisted with an amorphous phase, amorphous T_5O_{10}. Fortunately, the amorphous phase does not contribute any diffraction signals, and all diffraction peaks in Figure 3.9 belong to the x-metamesolite phase. After indexing, the solution was evaluated graphically using the Le Bail profile-fitting algorithm (Le Bail *et al.* 1988). Indexing and Le Bail fitting yielded unit-cell parameters of a = 16.731(3) Å, b = 17.822(2) Å, c = 6.312(1) Å, V = 1882.5(5) Å^3, and space group *Fdd2* fit all diffraction peaks with the exception of a peak at ~26.6º 2θ (Fig. 3.9). These determined unit-cell parameters for x-metamesolite are smaller than those for α2-metanatrolite (*Fdd2*, a = 17.576(1) Å, b = 18.163(1) Å, c = 6.3704(4) Å, V = 2033.7(2) Å^3) but larger than those for α1-metanatrolite (*F112*, a = 16.177(1) Å, b =

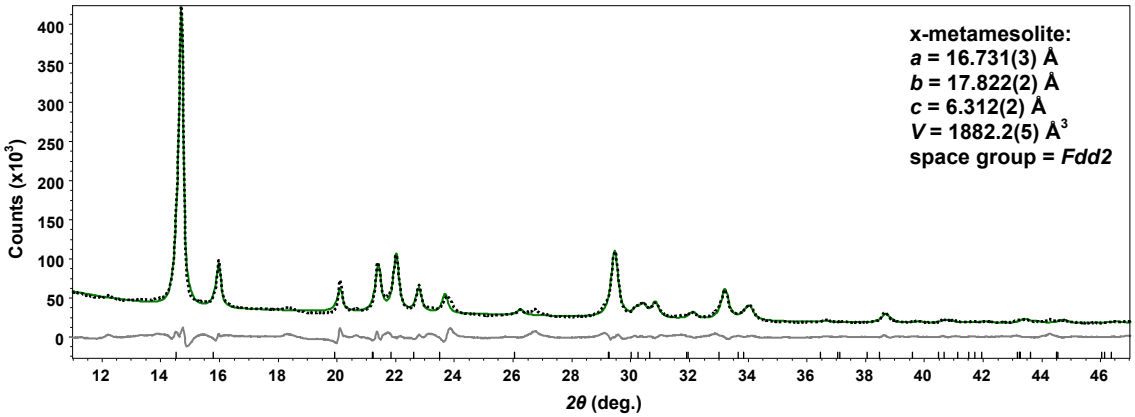

Figure 3.9. XRD pattern for x-metamesolite observed at 425 ºC and at a P_{H_2O} of $10^{-0.8}$-$10^{-2.6}$ mbar (roughing pump vacuum condition at pressure of $10^{-3.8}$ bar). The observed pattern is shown as a black dotted line, and a Le Bail fit profile is shown as a green line. Short vertical lines mark the positions of Bragg reflections (Kα1 and Kα2).

16.943(1) Å, c = 6.4370(4) Å, γ = 89.685(2)º, V = 1764.2(2) Å^3), indicating that the degree of NAT framework contraction and distortion of x-metamesolite falls between that found in these two metanatrolite phases. (for detailed descriptions of the structures of α1 and α2-metanatrolite, see discussions in Chapter 1 or in Wang and Bish 2008, 2010). Maintaining similar unit-cell dimensions but lowering the symmetry from space group *Fdd2* to its subgroups, such as *F112* (equivalent to *C121* in the standard setting) and *P121*, provided improved intensity fits for all reflections, including the missing peak at ~26.6º 2θ. However, the lower symmetry space group simply allows more reflections, which are forbidden for the higher symmetry space group, thereby giving a better intensity fit. As a consequence, the optimum intensity fit does not necessarily indicate the correct space group, which leads to ambiguity in determining the space group for further structure fitting. Complete determination of the atomic positions of the x-metamesolite phase with all possible space group settings is ongoing. In addition, based on the understanding of the phase transition behaviors in natrolite, the possibility of forming a small amount of a secondary phase (e.g., as a polymorph of x-metamesolite) that coexists with the x-metamesolite phase is also included (i.e., similar to the coexistence of α1- and α2-metanatrolite phases when natrolite is heated under low-P_{H_2O} conditions).

3.3 Chapter summary

This study reiterated the importance of considering the combined effects of temperature and P_{H_2O} in order to obtain a complete picture of structural phase transition behaviors for the zeolite mesolite, which showed P_{H_2O}-dependent phase transitions. The dehydration of mesolite occurred in two main steps, the first of which is the low-temperature

extraframework cation order-disorder phase transition, which is 2nd-order in character. During this reaction, Ow4 H_2O molecules are lost (i.e., 16 out of 64 H_2O molecules evolve) and the framework contracts along the *a* and *b* axes, associated with the loss of Ow4 H_2O molecules. Controlled-temperature and -P_{H_2O} XRD data showed that the transition temperature to Na/Ca-disordered metamesolite depends on the P_{H_2O} conditions. A comparatively moist environment employed on heating caused the initial dehydration temperature to increase. The $k \neq 3n$ reflections disappeared above the transition and did not reappear upon rehydration. The second main step, the high-temperature phase transition, is 1st-order in character and not only showed a P_{H_2O}-dependent transition temperature but also two different phase transition paths, namely a displacive phase transition to x-metamesolite (occurring at P_{H_2O} below ~6 mbar) and a phase transition to an amorphous T_5O_{10} phase (occurring at P_{H_2O} above ~8.5 mbar). During this reaction, 34% of the Ow' H_2O molecules were gradually lost (i.e., the Ow' occupancy gradually decreased to ~0.66, which is equivalent to the loss of ~16 of the remaining 48 H_2O molecules) and the reaction was followed instantly by either a displacive phase transition (as marked by changes in the unit-cell dimensions) or a phase transition to an amorphous phase (as marked by loss of long-range order in XRD and PDF data). The total amounts of H_2O lost during the dehydration reaction are also shown in TG data, with two relatively broad dehydration reactions followed by a sharper TG dehydration curve, and not all H_2O molecules were removed by 360 ºC. The TG curve exhibited additional weight loss at temperatures above 360 ºC, probably indicating the formation of relic-OH groups. The hydroxyl groups gradually evolved during further heating. Thus, the temperature of dehydration affects the nature of structural phase transitions in mesolite, and evidence for separate phase fields under low- and high-P_{H_2O} conditions was

found. When mesolite was heated under high-P_{H_2O} conditions, the newly observed x-metamesolite phase field was bypassed due to the enhanced stability of the hydrous phase, and mesolite transformed directly to Na/Ca-disordered metamesolite and then to amorphous T_5O_{10}. Lower P_{H_2O} conditions destabilized the hydrous phase at comparatively lower temperatures. Under these conditions, the aluminosilicate framework of Na/Ca-disordered metamesolite remained intact and the structure then underwent a displacive phase transition to the x-metamesolite structure. Hence, under low-P_{H_2O} conditions one sees the "hidden phase transition" to x-metamesolite that cannot be observed at higher P_{H_2O}.

The structure of Na/Ca-disordered metamesolite determined from XRD Rietveld analyses and PDF refinements showed a completely random distribution of Na^+, Ca^{2+}, and vacancies in the extraframework cation sites, in agreement with Ståhl and Thomasson's study (1994). However, the possibility of short-range order of extraframework cations in the Na/Ca-disordered metamesolite channels can not be excluded. Although the migration of extraframework cations and the distortions of the aluminosilicate framework are instigated by the dehydration reaction, the local arrangements of Na^+, Ca^{2+}, and vacancies in the framework channels may further influence whether or not the aluminosilicate framework is stabilized at higher temperatures. The exact physical process by which these two properties (i.e., thermal motions of the Na/Ca-H_2O complexes and the responses of the framework structures) combined to produce specific behaviors is still undetermined. However, the phase transition behaviors in mesolite should be very similar to natrolite and scolecite dehydration reactions, and the interactions of Na^+/Ca^{2+} cations and H_2O molecules with the framework oxygens have the potential to drive the mesolite phase transition behaviors. The structure of amorphous T_5O_{10} determined from PDF refinements is composed of a collection of randomly

oriented nano-fibers, each with a twisted T_5O_{10} structure with zero, one, or two Na^+/Ca^{2+} cations (and possibly relic-OH groups) attached to it. The determined unit-cell parameters and space group for x-metamesolite provide a clue that the framework structure of x-metamesolite is very similar to that of α1- or α2-metanatrolite.

CHAPTER 4

Infrared spectroscopic characterization of dehydration and accompanying phase transition behaviors in NAT-topology zeolites

Natural zeolites have open host frameworks composed of corner-shared (Al,SiO_4)-tetrahedra with cages and channels of molecular dimensions, occupied by various guest cations (mostly Na^+, K^+, Ca^{2+}, and Mg^{2+}) and H_2O molecules. Knowledge of interactions of H_2O molecules with the host Al-Si frameworks and the extraframework cations holds both fundamental interest and great importance for industrial applications. The behavior of H_2O molecules confined inside zeolite channels depends on many factors, including the connectivity of the host structure, the guest cation chemistry, and the hydration level, and is the result of a balance between host-guest and guest-guest interactions. van Reeuwijk (1974) studied the thermodynamic properties of several natural zeolites and he demonstrated a correlation between the entropy of H_2O molecules and the positions of cations inside the zeolite channels. Low-entropy (30-47 J/ºC/mole-H_2O) H_2O molecules in zeolites such as natrolite, mesolite, scolecite, thomsonite, stilbite and laumontite, generally result from the occurrence of distinct H_2O sites and a fixed H_2O coordination with guest cations occupying fixed positions in the room temperature structure. In contrast, high H_2O entropy (58-72 J/ºC /mole-H_2O) is found in the more open-structure zeolites, such as chabazite, heulandite, clinoptilolite and mordenite, and results from the coordination of H_2O molecules with cations that are not located at specific positions. As a consequence, H_2O molecules confined in the latter case are held by variable hydrogen bonding networks and ion-dipole attractions making up the complicated host-guest and the guest-guest interactions. Infrared (IR) spectroscopic

characterization of vibrational properties of H_2O molecules in the above two extreme cases (i.e., low vs. high H_2O entropy) has shown substantial differences in the H_2O O-H stretching modes. For instance, IR spectra for K-chabazite shown by Crupi *et al.* (2006) are complex, with multiple overlapping bands in the H_2O O-H stretching region, attributed to H_2O molecules engaged in different degrees of hydrogen bonding. In contrast, scolecite IR spectra have H_2O O-H stretching modes that are well-resolved into several distinct bands (Crupi *et al.* 2006). Because H_2O molecules in scolecite are only hydrogen bonded to the framework oxygens and are ion-dipole attracted to one extraframework Ca^{2+} cation (and not to other H_2O molecules), IR spectra for a case like scolecite have the potential to reveal the correlation between the O-H stretching frequency and hydrogen bond lengths (Å) as established by Libowitzky (1999). In this chapter, the results of an *in-situ* IR spectroscopic investigation focusing on the dehydration behavior of H_2O molecules in the channels of NAT-type zeolites are presented. As reported in the previous three chapters, X-ray diffraction (XRD) studies on the crystal structural evolution of natrolite, scolecite, and mesolite as a function of temperature showed the existence of different phase transition paths depending on the partial pressure of H_2O (i.e., P_{H_2O} or relative humidity, *RH*), with discoveries of new anhydrous phases under low-P_{H_2O} conditions (i.e., α2-metanatrolite, x1- metascolecite, x2-metascolecite, and x-metamesolite)[9]. These results indicated that the small-pore NAT-type channels provide an extreme case of confined H_2O molecules, and the P_{H_2O} level and the dynamics of H_2O molecules in NAT-type channels exert strong influence in determining which anhydrous phases ultimately form during dehydration. Accordingly, in addition to XRD studies, parallel measurements with an environmental cell on a diffuse-reflectance

[9] Please also refer to Wang and Bish (2008, 2010), and Bish and Wang (2010) for natrolite, and Wang *et al.* (2010) for mesolite.

infrared Fourier-transform spectroscopy (DRIFTS) allowed investigation of the thermal evolution of cation-H_2O-Al-Si framework interactions in NAT-type zeolites. As P_{H_2O} is a crucial variable in causing NAT-type zeolites to experience different phase transition paths, it is important to investigate the vibrational, energetic, and bonding properties of H_2O under controlled-temperature and -P_{H_2O} conditions and to evaluate the results in light of the corresponding static crystal structures obtained from XRD measurements. Such investigations are necessary to extend the current understanding of the dynamics of confined H_2O molecules and the nature of host-guest interactions in NAT-type zeolites.

4.1 Previous work

4.1.1 Spectroscopic investigations in NAT-topology zeolites

There have been several spectroscopic studies done previously on NAT-type zeolites. In the case of natrolite, Thompson *et al.* (1974) presented single-crystal NMR data on molecular motions of H_2O molecules as a function of temperature (from 4 to 545 K). They showed that before the phase transition to the anhydrous phase, H_2O molecules exhibit greater reorientational motion about one of the Ow-H···O hydrogen bonds, which involves breaking hydrogen bonds on further heating. Pechar and Rykl (1983) and Pechar (1983) presented powder IR and Raman spectra of natrolite and mesolite and made simple mode assignments based on their lattice dynamic calculations. Gottardi and Galli (1985) presented powder IR spectra for natrolite, scolecite, and mesolite, but little spectral interpretation was given. Goryainov and Smirnov (2001) reported a better lattice dynamic calculation than the one made by Pechar and Rykl (1983) for natrolite. About 40 additional bands were added, and they also pointed out some errors made in earlier calculations (e.g., Pechar and Rykl

1983). Wopenka *et al.* (1998) demonstrated the usefulness of Raman spectroscopy for identification of NAT-type zeolites on the basis of their strikingly different H_2O O-H stretching bands. Line and Kearley (1998, 2000) presented powder IR spectra and measured inelastic incoherent neutron scattering spectra for natrolite and scolecite, and they compared these experimental results with *ab-initio* calculations to understand the vibrational and librational behaviors involving Na^+/Ca^{2+} cations and H_2O molecules in NAT-type channels.

More recent studies began to consider the behavior of H_2O vibrational modes at different temperatures or hydration levels. For example, Kolesov and Geiger (2006) showed IR and Raman spectroscopic data clarifying the behavior of H_2O molecules as a function of temperature in the channels of natrolite and scolecite (using both powder and single-crystal samples). Prasad *et al.* (2006) presented powder IR spectra for scolecite during dehydration and rehydration. The same group (Prasad and Prasad 2007) also presented similar data for mesolite. Crupi *et al.* (2006) published low-temperature powder IR spectra (-10 to 80 ºC) for scolecite. Bougeard and Smirnov (2007; and references therein) reviewed the mobility of H_2O in different type of zeolites. For natrolite, they reported a very small self-diffusion coefficient of H_2O molecules whose diffusion is mainly induced by jumps of the Na^+ cations as temperature increases. All published H_2O vibrational spectra relating to the dehydration of NAT-type zeolites showed no major frequency shifts in the H_2O O-H stretching and H-O-H bending modes (although absorption bands become broader and weaker during the process of dehydration), indicating no major changes in the local H_2O bonding environment before dehydration, consistent with current XRD results. These data also suggest that the phase transition(s) observed in NAT-type zeolites are triggered by the dehydration reaction.

However, spectroscopic investigations that combined temperature and P_{H_2O} effects have not been done previously.

4.1.2 H_2O coordination in NAT-topology zeolites

The basic building blocks of the NAT-type framework are T_5O_{10} chains of (Al,SiO_4)-tetrahedra running parallel to the *c* axis (see Fig. 1.1a or Figs. 0.2B and 1.1A in Gottardi and Galli 1985). Natrolite (*Fdd*2), mesolite (*Fdd*2), and scolecite (*F*1*d*1 or *C*1*c*1 with half Z) have an ordered tetrahedral (Al,Si)-distribution and share the same aluminosilicate framework configuration. The major differences among these three zeolites are the numbers and arrangements of extraframework cations (Na^+ or Ca^{2+}) and H_2O molecules in their channel systems. Here, the aluminosilicate framework of mesolite is used (Fig. 4.1a) as an example to illustrate the local bonding environment of H_2O molecules in natrolite, mesolite, and scolecite. There are two distinct types of channels in mesolite, one with two Na^+ cations and two H_2O molecules (i.e., the same configuration as channels in natrolite), and the other containing one Ca^{2+} cation and three H_2O molecules (i.e., the same configuration as channels in scolecite). The cation environments of H_2O in natrolite and of H_2O in the Na portion of mesolite channels consist of two nearest-neighbor Na^+ cations, with a plane of H_2O molecules at approximately right angles to the plane containing the Na^+ cations (Fig. 4.1b), whereas the three H_2O molecules in scolecite and in the Ca portion of mesolite channels are bonded to only one Ca^{2+} cation (Fig. 4.1c). Notably, H_2O molecules in all three zeolite channels are relatively "far" apart (i.e., there are no H_2O-H_2O interactions in the first hydration shell), and they occupy general crystallographic positions. Each H_2O molecule forms hydrogen bonds of different strengths with its local surrounding framework oxygens, and each has reduced C_s symmetry (i.e., the two protons in an H_2O molecule are not

symmetrically equivalent; see Figs. 4.1b and c). Strictly speaking, the lower C_s symmetry of an H_2O molecule indicates that the H_2O does not show coupled IR-active vibrations of two symmetrically equivalent O-H bonds (i.e., υ_1 and υ_3) but rather independent O-H stretching modes. Each O-H bond vibrates independently with a frequency related to the local strength of hydrogen bonding. In general, increasing the strength of hydrogen bonding shifts the H_2O O-H stretching bands to lower frequencies and the band width can increase up to several hundred cm^{-1} as mentioned in Libowitzky and Beran (2004; this is related to resonance phenomena and increasing anharmonicity of strong hydrogen bonds). In addition, the H_2O H-O-H bending modes are also very sensitive to the local confined geometry. Factors including the strength and direction of hydrogen bonds (i.e., the O···H-Ow-H···O angles) and the number and chemistry of cations (with different electronegativities) in proximity to H_2O molecules will influence the band positions.

The representative structure models plotted in Figure 4.1 are from the neutron diffraction studies of Stuckenschmidt and Kirfel (2000) for mesolite (*Fdd*2), Artioli *et al.* (1984) for natrolite (*Fdd*2), and Joswig *et al.* (1984) for scolecite (*F*1*d*1). Among all the published structure models, the hydrogen bonds of (Ow4-H41···O10) and (Ow4-H42···O5) in mesolite, and of (Ow3-H31···O10) and (Ow3-H32···O5) in scolecite have bent angles consistently less than ~145° in contrast to other (Ow-H···O) angles (ranging from ~177° to 155°) found in natrolite, mesolite, and scolecite (Fig. 4.1). The mean value of the bent (Ow-H···O) angle found in hydrated crystals is ~166 ± 9° (as discussed in Chidambaram and Sikka 1968). Shorter hydrogen bonds are less bent on average than longer bonds because hydrogen bonds favor a linear Ow-H···O configuration. The small (Ow-H···O) angles for Ow4 H_2O in mesolite and Ow3 H_2O in scolecite indicate that they should form longer hydrogen bonds and

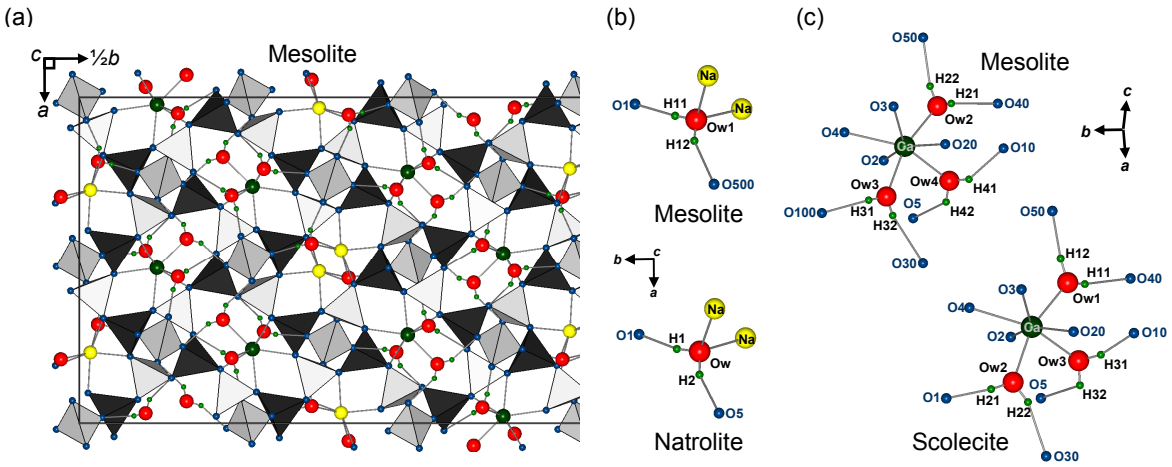

Figure 4.1. (a) Crystal structure model of mesolite viewed down the cross-linked T_5O_{10} chains. Si tetrahedra = grey; Al = tetrahedra = black; O atoms = blue spheres; Na^+ cations = yellow spheres; Ca^{2+} cations = dark green spheres; H_2O molecules = red Ow and light green H spheres; Bonds = solid gray lines. **(b)** and **(c)** local bonding environment of H_2O molecules in the channel system of mesolite, natrolite, and scolecite. The three zeolite structure models are taken from the neutron diffraction results of Stuckenschmidt and Kirfel (2000) for mesolite (*Fdd*2), Artioli *et al.* (1984) for natrolite (*Fdd*2), and Joswig *et al.* (1984) for scolecite (*F*1*d*1). The H_2O Ow and H atoms are relabeled in mesolite and scolecite for easy comparison.

should be the first H_2O molecules to leave the framework during dehydration. Many dehydration studies for mesolite and scolecite, including ours (e.g., Adiwidjaja 1972; van Reeuwijk 1974; Ståhl and Thomasson 1994; Ståhl and Hanson 1994; Kolesov and Geiger 2006; Prasad *et al.* 2006; Prasad and Prasad 2007; Wang *et al.* 2010) indeed showed two-step dehydration behaviors, with the loss of mesolite Ow4 and scolecite Ow3 H_2O molecules as the first step of dehydration. Unfortunately, hydrogen bond lengths determined from various diffraction results (e.g., Joswig *et al.* 1984; Artioli *et al.* 1986; Kvick *et al.* 1985; Stuckenschmidt *et al.* 1997; Kuntzinger *et al.* 1998; Stuckenschmidt and Kirfel 2000) are quite variable, probably due to the difficulty in determining accurate proton positions in a complex three-dimensional structure. In addition, the Ca-Ow4 bonds in mesolite and the Ca-Ow3 bonds in scolecite showed a tendency to be slightly longer (by ~0.03 Å) than the other Ca-Ow distances found in mesolite (i.e., Ca-Ow2 and Ca-Ow3) and scolecite (i.e., Ca-Ow1 and Ca-Ow2), which is also consistent with their dehydration behaviors. However, the emphasis here is that not all structure models show longer Ca-Ow4 (in mesolite) and Ca-Ow3 (in scolecite) bond distances (e.g., Artioli *et al.* 1986; Fälth and Hansen 1979; Stuckenschmidt and Kirfel 2000). This discrepancy may be due to the effects of thermal motion and positional disorder on the different Ca-Ow bond distances.

4.2 Samples and experimental methods

The three zeolites used for this study were from San Benito, California, USA (natrolite, $Na_{14.72}Al_{15.52}Si_{24.80}O_{80} \bullet 16.32H_2O$), Maharashtra, India (scolecite, $Ca_{7.81}Al_{15.62}Si_{24.30}O_{80} \bullet 24.51H_2O$), and Berufjőrdur, Iceland (mesolite, $Na_{15.76}Ca_{16.18}Al_{48.28}Si_{71.76}O_{240} \bullet 63.50H_2O$). The crystal chemistry of all three zeolites was

characterized by electron microprobe analysis of crystals in several thin sections, and their averaged chemical compositions are very close to ideal end-member stoichiometric formulae. Zeolite samples were dry ground into powders to maximize spectral quality in the DRIFTS analysis. For each measurement, a mix of 15 wt.% zeolite with 75 wt.% KBr matrix was placed into the sample cup of the DRIFTS environmental cell (Thermo Electron product 0031-902). The DRIFTS environmental cell allows diffuse-reflectance experiments to be conducted *in-situ* from 25 to 460 °C at monitored P_{H_2O} (*RH*) conditions. Two different P_{H_2O} conditions were used, ~10^{-1}-$10^{-2.7}$ mbar P_{H_2O} via roughing pump vacuum (~10^{-4} bar) and ~14-20 mbar P_{H_2O} at ambient conditions (corresponding to ~65 ± 5% *RH* at 23 ± 1 °C and 1 bar). The lower limit of P_{H_2O} ($10^{-2.7}$ mbar) under vacuum conditions was estimated based on the ambient *RH* at the time of measurement (i.e., ~65% *RH* at 23 °C; scaled by a factor of 10^{-4}). On the other hand, the upper limit of P_{H_2O} (10^{-1} mbar) under vacuum conditions was estimated based on the assumption that all the residual gas remaining in the cell was H_2O vapor. The ZnSe window in the DRIFTS environmental cell allows IR transmission within the 650-4000cm^{-1} range. Infrared spectra were collected with a Thermo-Nicolet Nexus 670 FTIR instrument. Spectra were collected with 100 co-added scans at a resolution of 4 cm^{-1} and an optical velocity of 0.1581 cm/sec using a deuterated triglycine sulfate detector (the total time for each collection at the set-point temperature was ~6.4 min). A stepwise heating procedure with a constant P_{H_2O} value for each measurement was applied (temperature was increased to the set-point temperature in 20 °C increments) and the sample was allowed to equilibrate (40 min) at a given temperature prior to data collection. Background spectra were collected using the same P_{H_2O} and temperature ramp, duplicating the assembly with pure KBr powder. Companion powder XRD experiments (Cu Kα radiation) were conducted using

thin-slurry mounts. Measurements were performed with environmental parameters (including temperature increments and P_{H_2O} conditions) similar to those used in DRIFTS, which facilitated comparison between XRD and DRIFTS results. Descriptions of the XRD instrument can be found in the section 1.1 or in Wang and Bish (2008, 2010), Bish and Wang (2010), and Wang *et al.* (2010). The advantage of using diffuse-reflectance geometry rather than the traditional transmission powder pellet or single-crystal method is that the effects of the build-up of P_{H_2O} within the sample were minimized, thereby providing a better control of P_{H_2O} and more accurate picture of the dehydration and accompanying phase transition behaviors.

4.3 Results and discussions

4.3.1 Spectral analysis

Figure 4.2 shows representative DRIFTS spectra for natrolite, scolecite, and mesolite measured at ambient conditions prior to heating (23 °C). All three samples have absorption band positions similar to published IR spectra. The spectra of NAT-type zeolites are characterized by: (i) several strong and weak bands below 1200 cm^{-1} assigned to antisymmetric Si-O-Si and Si-O-(Al) stretching vibrations (950-1200 cm^{-1}; as discussed in Moenke 1974) and deformation modes of the polymerized T_5O_{10} structure (550-850 cm^{-1}; as assigned by Mozgawa 2001); (ii) one or three absorption bands in the ~1650 cm^{-1} region caused by H_2O H-O-H bending; (iii) multiple strong absorption bands in the 3000-3700 cm^{-1} region caused by H_2O O-H stretching; (iv) several bands of very weak intensity lying on the low-wavenumber shoulder of the O-H stretching region (labeled with dot symbols in Fig. 4.2) that are either attributed to combination ($\upsilon_{O\text{-}H} \pm T_{H_2O}$) modes or associated with ($\upsilon_{O\text{-}H} \pm$

$C_{cation\text{-}H_2O}$) modes[10]; and (v) one or two broad absorption bands with weak intensity located in the ~2200 cm^{-1} region, bands that have not been previously mentioned (labeled with star symbols in Fig. 4.2). The band assignments described by Kolesov and Geiger (2006) are followed for H_2O O-H stretching and H-O-H bending in natrolite (Fig. 4.2a) and scolecite (Fig. 4.2b). In the case of mesolite, there are no available polarized IR or Raman spectra or theoretical lattice dynamical calculations. The Ow-H stretching bands were alternatively assigned based on the (Ow···O) distance-frequency correlation function established by Libowitzky (1999). The (Ow···O) distances (insert Table in Fig. 4.2c) were obtained from the mesolite structure determined using Rietveld refinements with XRD data collected under similar conditions. There are four crystallographically distinct H_2O molecules in the mesolite channels (i.e., Ow1, Ow2, Ow3 and Ow4; see Figs. 4.1b and c). Thus, in theory, one should observe eight Ow-H stretching bands and four H-Ow-H bending bands in the mesolite H_2O vibrational spectrum. However, the similar local hydrogen bonding environments among Ow1, Ow2, and Ow3 give rise to significant band overlap, complicating interpretation of the observed Ow-H stretching and H-Ow-H bending bands. Three major sub-bands near ~3550, ~3350 and ~3250 cm^{-1} (Fig. 4.2c) are roughly compatible with the spread of (Ow···O) distances from the determined mesolite structure model. In the H-Ow-H bending region, the band at 1592 cm^{-1} was assigned to the bending mode of (H41-Ow4-H42) because the local coordination of Ow4 is similar to Ow3 H_2O in scolecite (Fig. 4.1c). The two bands at 1661 and 1647 cm^{-1} were assigned to the (H-Ow-H) bending of Ow1, Ow2, and Ow3 H_2O molecules in mesolite (i.e., overlapping of three bending modes).

[10] T_{H_2O} is the external H_2O translational mode and $C_{cation\text{-}H_2O}$ is the cation-H_2O stretching mode. Both modes occur in roughly the same low-wavenumber region and it is easier to observe the combination bands for those H_2O molecules having stronger anharmonic hydrogen bonds; see discussions in Kolesov and Geiger (2006).

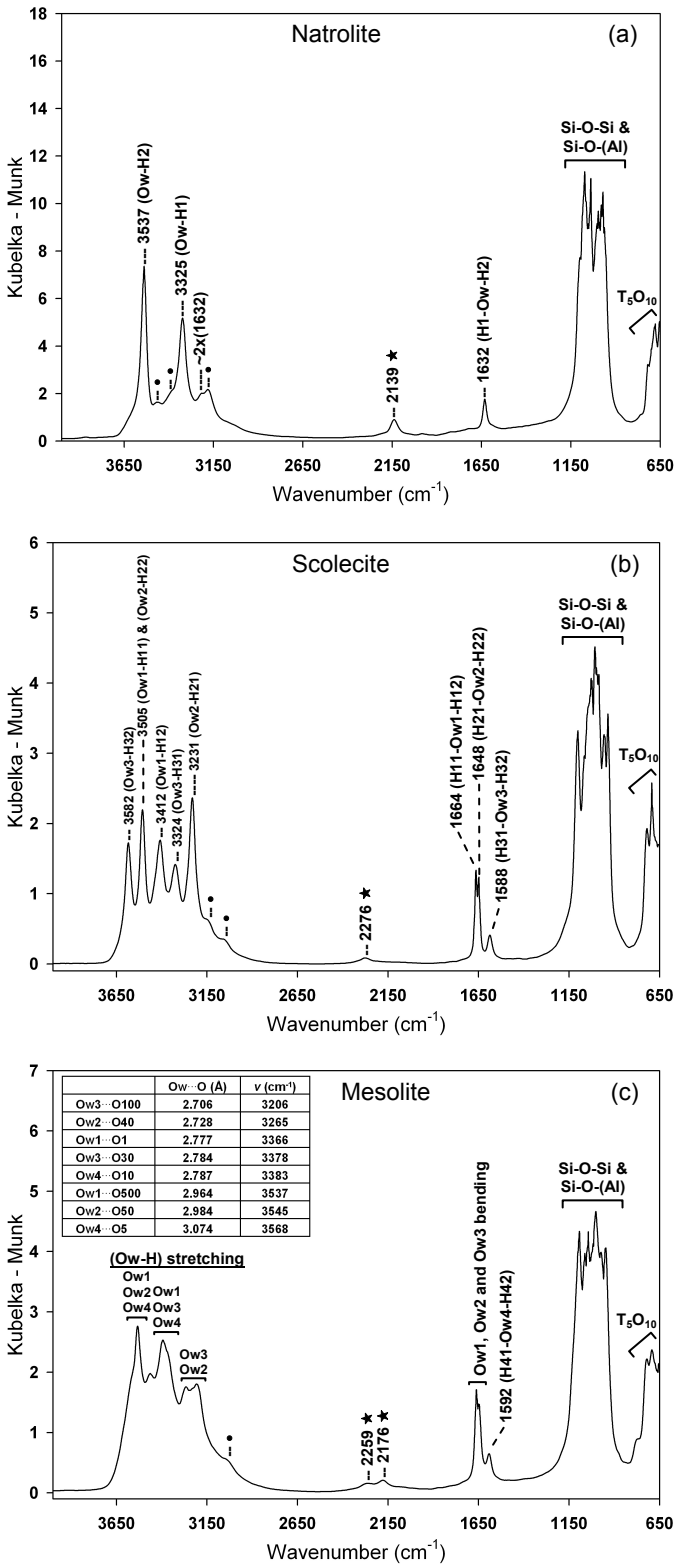

	Ow···O (Å)	ν (cm⁻¹)
Ow3···O100	2.706	3206
Ow2···O40	2.728	3265
Ow1···O1	2.777	3366
Ow3···O30	2.784	3378
Ow4···O10	2.787	3383
Ow1···O500	2.964	3537
Ow2···O50	2.984	3545
Ow4···O5	3.074	3568

Figure 4.2. DRIFTS spectra of **(a)** natrolite, **(b)** scolecite, and **(c)** mesolite. The (Ow-H) stretching bands in mesolite were assigned based on the (Ow···O) distance-frequency correlation function proposed by Libowitzky (1999).

Absorption bands observed at 2139 cm^{-1} in natrolite (Fig. 4.2a), at 2276 cm^{-1} in scolecite (Fig. 4.2b), and 2176 and at 2259 cm^{-1} in mesolite (Fig. 4.2c) were not caused by organic contaminations or CO_2 molecules trapped in NAT-type channels (e.g., cordierite contains CO_2 in its channels and shows a sharp IR absorption band at 2348 cm^{-1} as assigned by Armbruster and Bloss 1982). Carbon determination via the combustion method using a Costech Elemental Analyzer (up to 1020 °C) yielded <0.01 wt.% of CO_2 for all three zeolites. In addition, these ~2200 cm^{-1} absorption bands are not unique in this study. They were also apparent in published data where entire mid-IR spectra were presented (e.g., Fig. 5 in Line and Kearley 1998; Fig. 1a in Prasad *et al.* 2006; Fig. 1a in Parsad and Prasad 2007). In many previous studies, these ~2200 cm^{-1} absorption bands were either ignored or eliminated, probably due to their weak intensity and broad band width. Compared with other zeolites, natrolite, scolecite and mesolite are characterized by their relatively simple crystal structures, having only one, three, and four H_2O molecules in their asymmetric unit, respectively. They also have relatively simple hydrogen bonding and ion-dipole interactions with the framework oxygens and Na^+/Ca^{2+} cations. The simple channel constituents and the restricted host-guest interactions (i.e., cation-H_2O-Al-Si framework interactions) may explain the occurrence of absorption in the ~2200 cm^{-1} region. These absorption bands are most likely correlated with the coupling effects associating with the H_2O vibrational (and/or librational) modes, the local motions of Na^+/Ca^{2+} cations, and/or the Al-Si framework deformational modes. Depending on the type of extraframework cations, natrolite and scolecite can be considered as Na and Ca end-members, which give rise to a single absorption band observed at 2139 cm^{-1} in natrolite and at 2276 cm^{-1} in scolecite. Notably, the 2139 cm^{-1} band in natrolite is sharper than the 2276 cm^{-1} band in scolecite. Mesolite is the

intermediate material that has both natrolite and scolecite types of channels. Hence, two absorption bands are observed for mesolite at 2176 cm^{-1} and 2259 cm^{-1}. The 2176 cm^{-1} band is correlated with host-guest interactions in Na-containing channels and the 2259 cm^{-1} band is correlated with host-guest interactions in Ca-containing channels. The relative intensity and shape of both bands in mesolite follow the same trend observed in natrolite and scolecite.

If absorption in the ~2200 cm^{-1} region is a common feature for zeolites with strong host-guest interactions, one should observe similar features in other zeolite IR spectra, especially for those zeolites having reasonably fixed cation-H_2O-Al-Si framework coordinations and restricted interactions. DRIFTS spectra of thomsonite, stilbite, chabazite, and laumontite showed weak absorptions at ~2200 cm^{-1}, but the ~2200 cm^{-1} absorptions were absent from the spectra of clinoptilolite, heulandite, and mordenite (Fig. 4.3). Table 4-1 summarizes the channel system, size, and properties of guest cations and H_2O molecules for the above zeolites. Thomsonite, stilbite, and laumontite are generally classified as having small to medium size channels, and clinoptilolite, heulandite, and mordenite, on the other hand, have relatively larger channels. The smaller channel systems have more opportunities to form restricted cation-H_2O-Al-Si framework interactions and hence are more likely to have absorptions at ~2200 cm^{-1}. Chabazite is considered as one exception because it has medium to large channel systems with ellipsoidal cages. A DRIFTS spectrum of chabazite showed a weaker absorption at ~2200 cm^{-1}, probably associated with cation sites located near the wall of the cage where cation-H_2O-Al-Si framework interactions are relatively more confined. Additional evidence for the nature of host-guest interaction modes (at ~2200 cm^{-1}) comes from their P_{H_2O}-dependent behavior during dehydration (heating). When natrolite, scolecite and mesolite were heated under controlled P_{H_2O} conditions, the ~2200 cm^{-1} bands

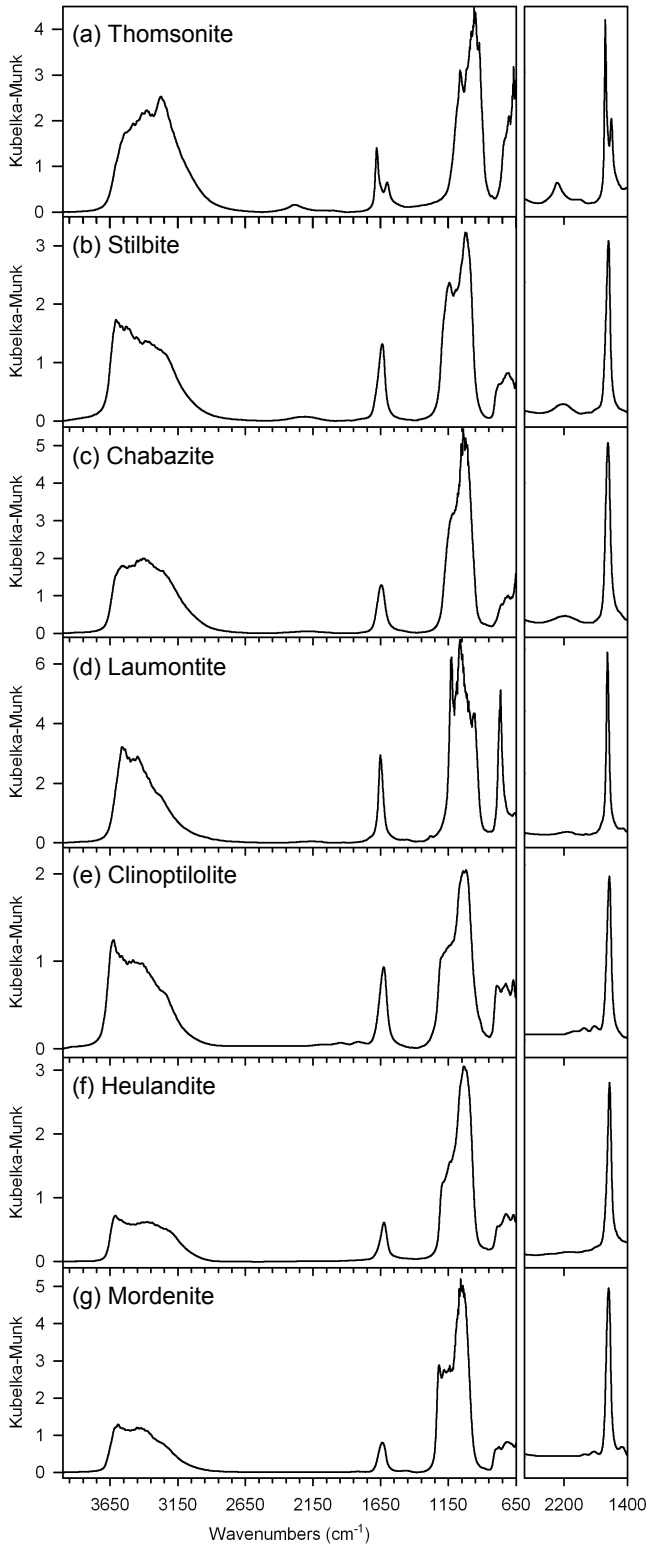

Figure 4.3. Representative DRIFTS spectra of several natural zeolites. The plots at right are the expansion in the 1400-2700 cm^{-1} region.

Table 4-1. Property of frameworks, channel cations, and H_2O molecules of several natural zeolites

Zeolites	Code	Channel system & Aperture size (Å)[1]	Representative aperture drawing[1]	Relative channel size	Channel cation and H_2O sites in zeolite frameworks[2]
Thomsonite	THO	3-D networks [100] **8** 2.3x3.9 ↔ [010] **8** 2.2x4 ↔ [001] **8** 2.2x3	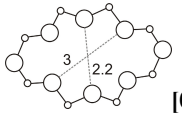 **[001]**	Small	The major 8-ring channels are along [001]. Four distinct H_2O sites and two channel cation sites reside in them. The cation is coordinated by framework oxygens at nearly opposite sides, plus some H_2O molecules (typical for narrow channels).
Stilbite	STI	2-D tabular plans [100] **10** 4.7x5 ↔ [001] **8** 2.7x5.6	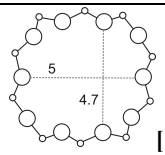 **[100]**	Medium	Two channel cation sites. One of the sites is general fully occupied by Ca^{2+} in the center of the main channel parallel to [100] and is completely surrounded by eight H_2O molecules without any contact with framework oxygens.
Chabazite	CHA	3-D ellipsoidal cages (~10x6x4) with access through aperture (3.8x3.8)	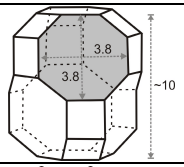	Medium	Small pore opening with a relatively large cage and inner surfaces. Three of four channel cation sites are located near the wall of the cage.
Laumontite	LAU	1-D channels [001] **10** 4x5.3	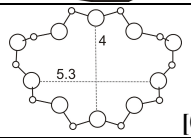 **[001]**	Medium	Medium size channels run parallel to [001]. Ca^{2+} is coordinated to four framework oxygens on one side only and bound to three H_2O molecules on the other side. Some other H_2O molecules are in the center of the channels bonded to other H_2O molecules and to the channel wall.
Heulandite & Clinoptilolite	HEU	2-D tabular plans {[001] **10** 3.1x7.5 + **8** 3.6x4.6} ↔ [100] **8** 2.8x4.7	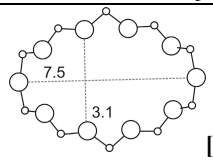 **[001]**	Large	Large channel systems contain different amounts of H_2O as a function of their extraframework cation chemistry and hydration state.
Mordenite	MOR	1-D channels [001] **12** 6.5x7.6 ↔ [001] **8** 2.6x5.7	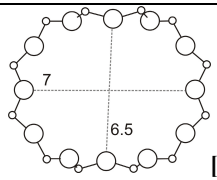 **[001]**	Large	

[1] Channel system and representative drawing are from Baerlocher and McCusker; Database of Zeolite Structures: http://www.iza-structure.org/databases/.
[2] Summarized from Gottardi and Galli (1985) and Armbruster and Gunter (2001).

disappeared as a function of P_{H_2O} (i.e., the ~2200 cm^{-1} bands disappeared at higher temperatures under comparatively moist environments), indicating that they in some way reflect the energetic interactions of H_2O molecules and Na^+/Ca^{2+} cations with the host structure during dehydration (see discussion below).

4.3.2 Natrolite dehydration behavior

Temperature-resolved DRIFTS spectra of natrolite showed clear single-step dehydration beginning >280 °C when natrolite was heated in a high-P_{H_2O} atmosphere (Fig. 4.4a) and >180 °C when natrolite was heated in a low-P_{H_2O} atmosphere (Fig. 4.4b). The difference in dehydration temperature is a reflection of the strong dependence on the surrounding P_{H_2O} during the measurements (i.e., a comparatively moist environment employed on heating caused initial dehydration temperatures to increase). Dehydration was evidenced by a large decrease in absorption intensities in the Ow-H stretching and H-Ow-H bending region and disappearance of the natrolite 2139 cm^{-1} band. Dehydration behavior reflected in the spectra was also consistent with thermogravimetric (TG) analysis result given in Figure 1.3. In addition, results of parallel XRD measurements performed under similar environmental conditions were also consistent with the spectral results. The XRD pattern measured at a high-P_{H_2O} (Fig. 4.5a) showed that dehydration began at ~300 °C, as indicated by the appearance of α1-metanatrolite reflections (circle symbols), and it was complete at ~340°C as indicated by the disappearance of natrolite reflections (square symbols). At temperatures between 300 and 340 °C, a discontinuous change in the XRD peak positions was observed (Fig. 4.5a; 320 °C line), which corresponds to a sharp H_2O loss at 320 °C in the IR spectra (Fig. 4.4a; bold line). Similarly, XRD data measured at a low-P_{H_2O} (Fig. 4.5b) showed that dehydration began at ~180 °C and was complete above 220 °C as evidenced by

the appearance of α2- and α1-metanatrolite reflections (star and circle symbols) and disappearance of natrolite reflections (square symbols), respectively. Consistently, an abrupt H_2O loss was seen at 220 °C in the IR spectra (Fig. 4.4b; bold line). Before dehydration, all observed IR bands became broad, likely due to an increase in the range of bond distances brought on by thermal motion as temperature increased. Notably, there was no detectable indication of the formation of OH groups after dehydration. With the exception of dehydration temperatures, there were no major differences (based on qualitative inspection) in the H_2O vibrational spectra collected under high- and low-P_{H_2O} conditions. However, the selected band positions (fitted with a Voigt profile) plotted as a function of temperature displayed some variations with P_{H_2O} (Fig. 4.6).

When natrolite was heated at a high-P_{H_2O} atmosphere, both the (Ow-H2) and (Ow-H1) stretching bands remained at roughly the same wavenumber for temperatures ≤280 °C (Figs. 4.6a and b; black lines). Above 280 °C, the (Ow-H2) band shifted to the high-wavenumber side (i.e., became a weaker hydrogen bond) and the (Ow-H1) band shifted to the low-wavenumber side (i.e., became a stronger hydrogen bond), suggesting that H_2O molecules evolve from the natrolite framework by first breaking the weakest hydrogen bond (i.e., Ow-H2···O5). The O5 atom in natrolite is the only framework oxygen that bridges two Si atoms (all other oxygens are bonded to one Si and one Al each), and hence, it will act as a poor hydrogen bond acceptor, which is consistent with the Ow-H2···O5 hydrogen bond becoming weaker during dehydration. This observation is also consistent with the NMR study of Thompson *et al.* (1974), who found that H_2O molecules exhibit a significant reorientation about one of the Ow-H···O bonds before dehydration. Moreover, the lack of significant wavenumber shifts for both Ow-H stretching bands before dehydration indicates

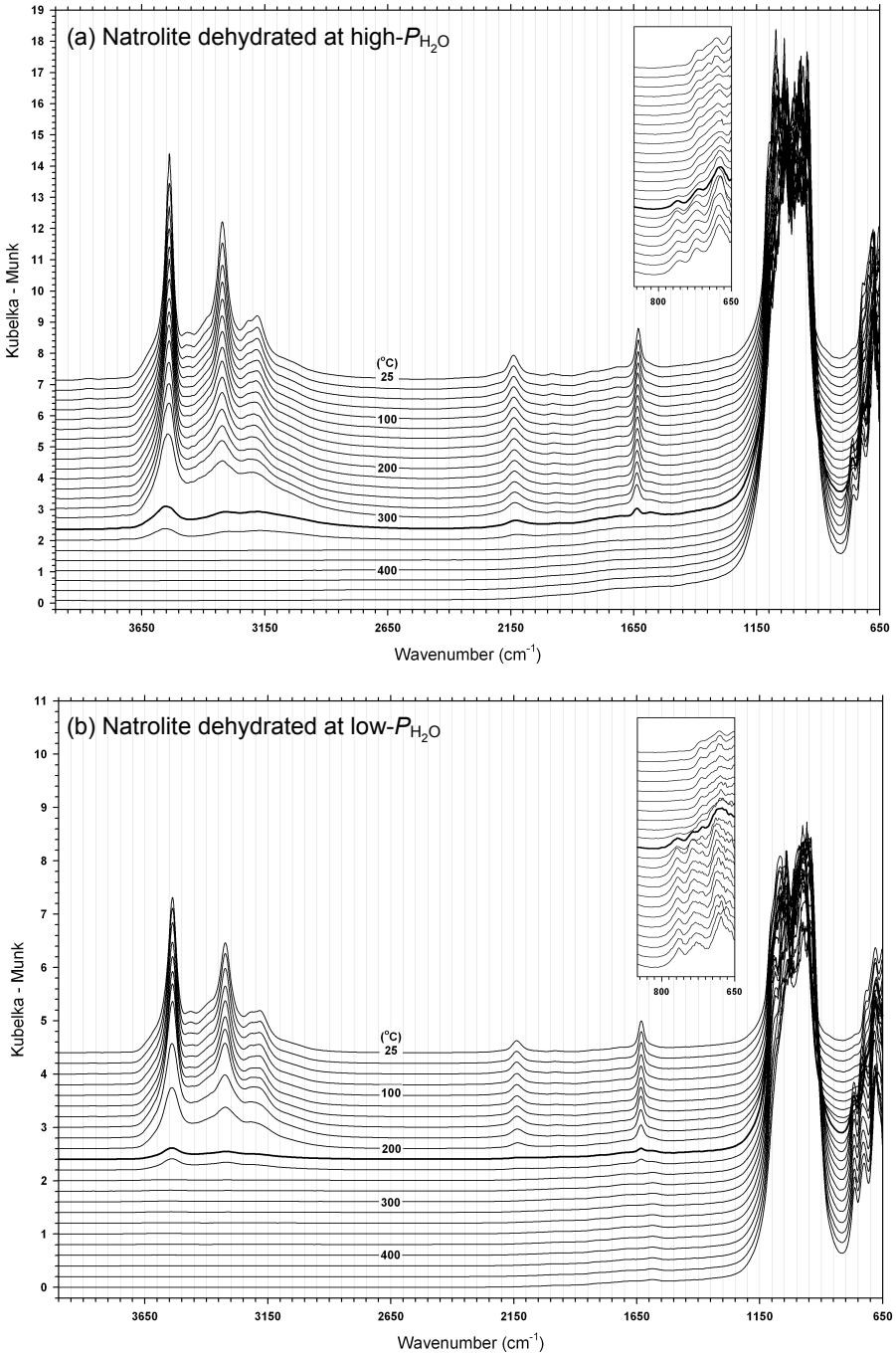

Figure 4.4. Temperature-resolved DRIFTS spectra of natrolite measured under different P_{H_2O} conditions. The temperature range from top to bottom is in the sequence of 25, 40, 60, 80, 100, 120, 140, 160, 180, 200, 220, 240, 260, 280, 300, 320, 340, 360, 380, 400, 420, 440 and 460 ºC. Bold spectra are at 320 ºC in plot **(a)** and at 220 ºC in plot **(b)**. The insert plots are the expansion in the region of T_5O_{10} structure deformational modes.

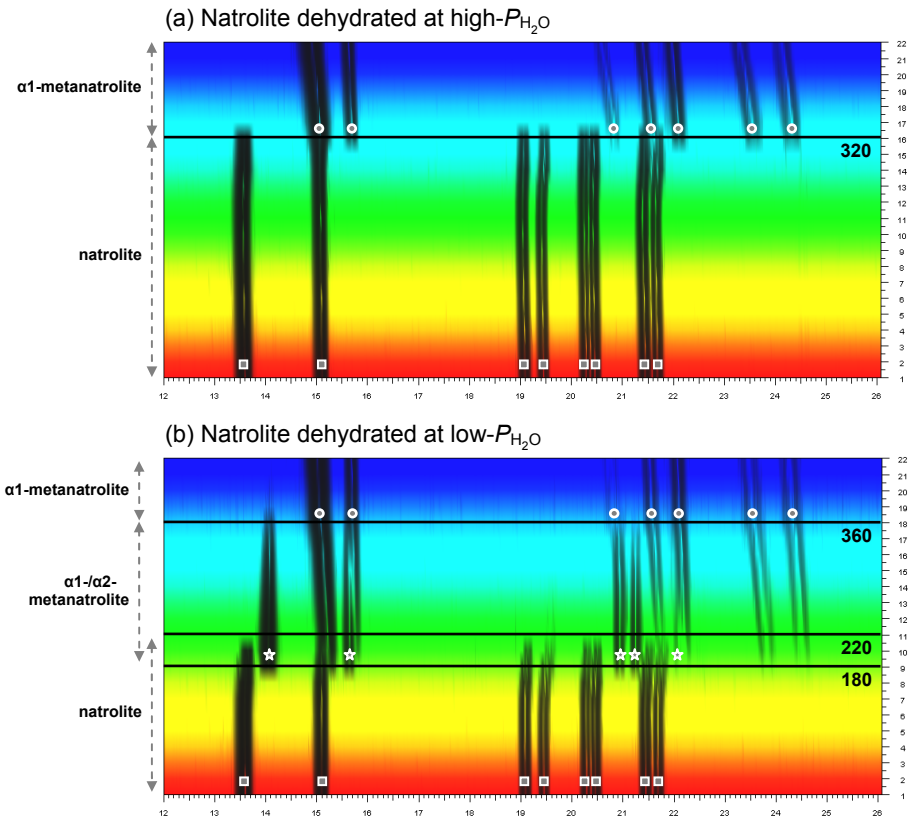

Figure 4.5. Temperature-resolved XRD patterns of natrolite measured under different P_{H_2O} conditions, illustrating the distinct changes as a function of temperature: *x* and *y* axes represent 12-26º *2θ* and temperature (#1-22, in sequence of 25, 40, 60, 80, 100, 120, 140, 160, 180, 200, 220, 240, 260, 280, 300, 320, 340, 360, 380, 400, 420, and 440 ºC). Plots are viewed down the intensity axis. The square, circle, and star symbols represent reflections of natrolite, α1-, and α2-metanatrolite phases, respectively.

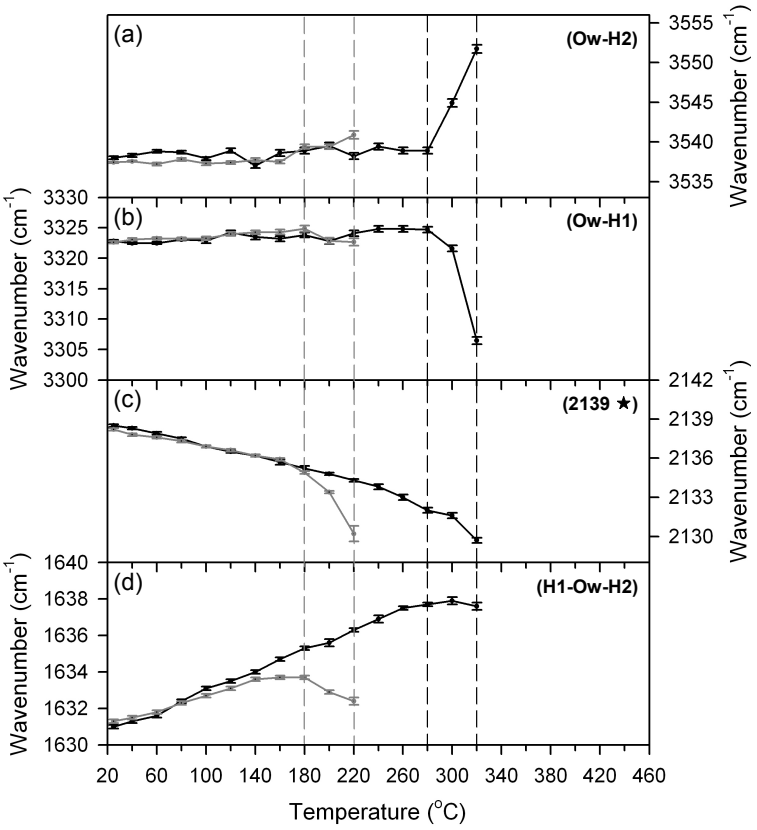

Figure 4.6. Frequency dependence of selected bands (with error bars) during natrolite dehydration as a function of temperature and P_{H_2O}: **(a)** (Ow-H2) stretching mode; **(b)** (Ow-H1) stretching mode; **(c)** combination modes of host-(Na-H_2O) at 2139 cm^{-1}; **(d)** (H1-Ow-H2) bending mode. Black lines are for a high-P_{H_2O} experiment and gray lines are for a low-P_{H_2O} experiment.

that no significant changes occurred in the bond strength or local hydrogen bonding environment of H_2O before dehydration. This observation is consistent with spectral results for the T_5O_{10} structural deformation region, which showed no changes in the 650-850 cm^{-1} region below 300 °C (see insert plot in Fig. 4.4a). XRD results also confirmed this observation with an unmodified XRD pattern below 300 °C (Fig. 4.5a)[11]. In contrast to Ow-H stretching bands, the (H1-Ow-H2) bending mode shifted to higher wavenumber as the temperature increased to ~280 °C and then the bending band moved slightly to lower wavenumbers at 320 °C (Fig. 4.6d; black line). Based on simple molecular dynamic considerations, the H_2O bending mode should migrate to the low-frequency side as temperature increased (i.e., decrease in the strength of hydrogen bond and shift to ~1595 cm^{-1} for free H_2O bending). Instead, an inverse relationship was observed during heating, and this trend was mentioned in Crupi *et al.* (2006) for scolecite (but no explanations were given). By comparing the thermal behavior of the (Ow-H2) and (Ow-H1) stretching bands with the behavior of the (H1-Ow-H2) bending band before dehydration (i.e., ≤280 °C), it is concluded that an increase in wavenumber of the (H1-Ow-H2) bending with temperature is not caused by any increase (or decrease) in the strength of hydrogen bonds. With no major changes in the natrolite framework and the local H_2O hydrogen bonding environment, the inverse temperature behavior of the (H1-Ow-H2) bending possibly relates to the effects of thermal motion of the Na^+ cations, which are located in close proximity to the H_2O molecules. Kolesov and Geiger (2006) discussed the H_2O bending behaviors in natrolite and scolecite and compared them with the case in beryl and cordierite. They concluded that when an H_2O molecule is bonded to a cation (such as Type II H_2O in beryl and cordierite), the existence of

[11] There still existed a minor framework modification characterized by <0.5% changes in the natrolite *a*, *b* and *c* unit-cell parameters immediately before dehydration; see discussions in Wang and Bish (2008).

the cation can cause an increase in wavenumber of the H_2O bending mode. Hence, an increase in wavenumber of the (H1-Ow-H2) bending mode with temperature can be related to the Na^+ cations thermally migrating toward H_2O molecules before dehydration. The increase in strength of interactions between Na^+ and H_2O with temperature not only led to an increase in wavenumber of the (H1-Ow-H2) bending mode, but it also caused a decrease in wavenumber of the natrolite 2139 cm^{-1} band (Fig. 4.6c; black line). The (H1-Ow-H2) bending band reached its maximum frequency just before dehydration and it then decreased as H_2O molecules began to leave the structure (i.e., >280 °C; Fig. 4.6d; black line).

When natrolite was heated in a low-P_{H_2O} atmosphere, the (Ow-H2) and (Ow-H1) stretching bands behaved in a manner similar to that observed at a high-P_{H_2O} (Figs. 4.6a and b; gray lines). The T_5O_{10} structural deformations (650-850 cm^{-1}) showed no changes < 180 °C (see the insert plot in Fig. 4.4b). The natrolite 2139 cm^{-1} band displayed a similar change in slope at temperatures <180 °C (Fig. 4.6c; gray line), and the wavenumber of the (H1-Ow-H2) bending band decreased more obviously at temperatures >180 °C (Fig. 4.6d; gray line). The thermal evolution of H_2O and the 2139 cm^{-1} band behaviors were very similar for natrolite dehydration under high- and low-P_{H_2O} conditions, i.e., all the gray lines appear to be extended proportionally and roughly match with all the black lines in Figure 4.6. However, under high-P_{H_2O} conditions, the absolute wavenumber for the H_2O bending and the natrolite 2139 cm^{-1} band observed at the dehydration temperature are different from that observed under low-P_{H_2O} conditions. These frequency differences immediately before dehydration illustrate the different local bonding interactions of the H_2O molecules and Na^+ cations with the host frameworks, which may provide a clue as to why the host framework of natrolite responds differently (i.e., experiences different phase transition paths) to P_{H_2O} conditions and

to the migration of its extraframework Na^+ cations. The existence of different energetic interactions of H_2O molecules and Na^+ cations with the natrolite Al-Si framework immediately before dehydration may induce deformational strains in the framework associated with the local Na-H_2O configurations. This local strain effect would be transmitted by flexing of the T-O-T bonds (T = Si or Al) to the entire framework, which further influences the range of energetically feasible T-O-T angles and results in different phase transition behaviors upon dehydration. The temperature of dehydration, the extent of Na^+ cation migration, the flexibility of the framework, and the developed subtle strain fields are strongly dependent on the P_{H_2O}.

4.3.3 Scolecite dehydration behavior

Dehydration of scolecite occurs in two main steps, with the loss of Ow3 H_2O molecules as the first dehydration step and the loss of Ow1 and Ow2 as the second dehydration step. Temperature-resolved DRIFTS spectra (Fig. 4.7a) and the corresponding XRD patterns (Fig. 4.8a) measured under high-P_{H_2O} conditions illustrated clear two-step dehydration behavior. The first dehydration occurred at 220 °C and is indicated by disappearance of the (H31-Ow3-H32) bending and the (Ow3-H31) and (Ow3-H32) stretching bands (Fig. 4.7a). The loss of Ow3 H_2O molecules caused changes in the local bonding environment of the remaining Ow1 and Ow2 H_2O molecules and gave rise to distinct modifications of the spectra in the Ow-H stretching region (Fig. 4.7a). The resulting structure, after the loss of Ow3 H_2O molecules, is metascolecite and is observed by shifts of XRD peaks to higher 2θ angles (Fig. 4.8a; above 220 °C line; the metascolecite phase is labeled with star symbols). In addition, at temperatures ≥220 °C, the (H11-Ow1-H12) and (H21-Ow2-H22) bending bands began to merge into one broad absorption band (see the

insert plot in Fig. 4.7a), likely caused by the increased variation of bond distances due to thermal motion and/or by the formation of similar local H_2O bonding configurations in metascolecite channels. Upon heating to 400 °C, the second dehydration occurred and was evidenced by a large decrease in absorptions in the (Ow-H) stretching and (H-Ow-H) bending regions and disappearance of the scolecite 2276 cm^{-1} band (Fig. 4.7a and the insert plot). Above 360 °C, X-ray diffraction intensities of the metascolecite phase gradually decreased, together with an increase in the background. By 400 °C, most metascolecite peaks were absent in the XRD pattern, the crystal structure was destroyed, and metascolecite became X-ray amorphous (Fig. 4.8a). At temperatures between 220 and 400°C, there exists a small continuous decrease in intensity of the (Ow-H) stretching and (H-Ow-H) bending bands due to the partial loss of remaining H_2O molecules as temperature increased (i.e., as a prelude to the transition to the amorphous phase). Observations in a high-P_{H_2O} atmosphere are alsoconsistent with previous dehydration studies and TG results of van Reeuwijk (1974) and Ståhl and Hanson (1994). Above 400 °C, weak (Ow-H) stretching and (H-Ow-H) bending absorptions were still seen in the IR spectra (Fig. 4.7a). These probably relate to the residual metascolecite phase that had not yet completely transformed to the amorphous phase (we also do not exclude the possible formation of OH groups).

Surprisingly, heating scolecite under a low-P_{H_2O} atmosphere yielded three different phase transitions (Fig. 4.8b). The first was a phase transition to the metascolecite phase (Fig. 4.8b; 120 °C line), which is the same as that observed at high-P_{H_2O} but it occurred at lower temperatures than for high-P_{H_2O} conditions (i.e., the transition temperature of scolecite-to-metascolecite is P_{H_2O}-dependent). The second and the third transitions occurred as two separate phase transitions to two unknown structures, referred to here as x2- and x1-

metascolecite (Fig. 4.8b; 240 and 300 °C lines). The intensity of x2-metascolecite reflections decreased progressively as temperature increased and the sample completely transformed to x1-metascolecite ≥340 °C (Fig. 4.8b). The phase transition phenomena observed in XRD patterns correspond well with the DRIFTS spectra (Fig. 4.7b). At temperatures <120 °C, no significant changes were seen in the spectra, except for the (H31-Ow3-H32) bending band shown in Figure 4.7b. Between 120 and 240°C, the IR bands relating to Ow3 H_2O internal vibrations disappeared and the resulting spectra in the (Ow-H) stretching region had features distinctly different from those observed in a high-P_{H_2O} atmosphere (Fig. 4.7). In other words, when the metascolecite phase formed under different temperature and P_{H_2O} conditions, IR spectra illustrate the energetic differences in local H_2O bonding interactions, which XRD data did not show (i.e., compare the 220-400 °C regions in Figs. 4.7a and 4.8a with the 120-240 °C regions in Figs. 4.7b and 4.8b). Upon further heating to 300 °C, diffraction peaks of the metascolecite phase completely disappeared (Fig. 4.8b), and this transition was also indicated by disappearance of the scolecite 2276 cm^{-1} band (see the insert plot in Fig. 4.7b). From 300 to 340 °C, both x2- and x1-metascolecite phases coexisted, and above 340 °C, x1-metascolecite was the only phase remaining (Fig. 4.8b). It is believed that x2-metascolecite is a partially dehydrated phase because the (H-Ow-H) bending absorption was still strong in the IR spectra at 300-340 °C. In addition, XRD data measured as a function of P_{H_2O} indicated that the transition temperature of x2-metascolecite-to-x1-metascolecite is P_{H_2O}-dependent, strongly suggesting that the transition involves H_2O (as discussed in the section 2.2.1). x1-metascolecite, on the other hand, is a nearly completely dehydrated phase. Although weak (Ow-H) stretching and (H-Ow-H) bending absorptions were still seen in the IR spectra >340 °C (Fig. 4.7b), these H_2O absorptions may be due to H_2O molecules trapped inside the

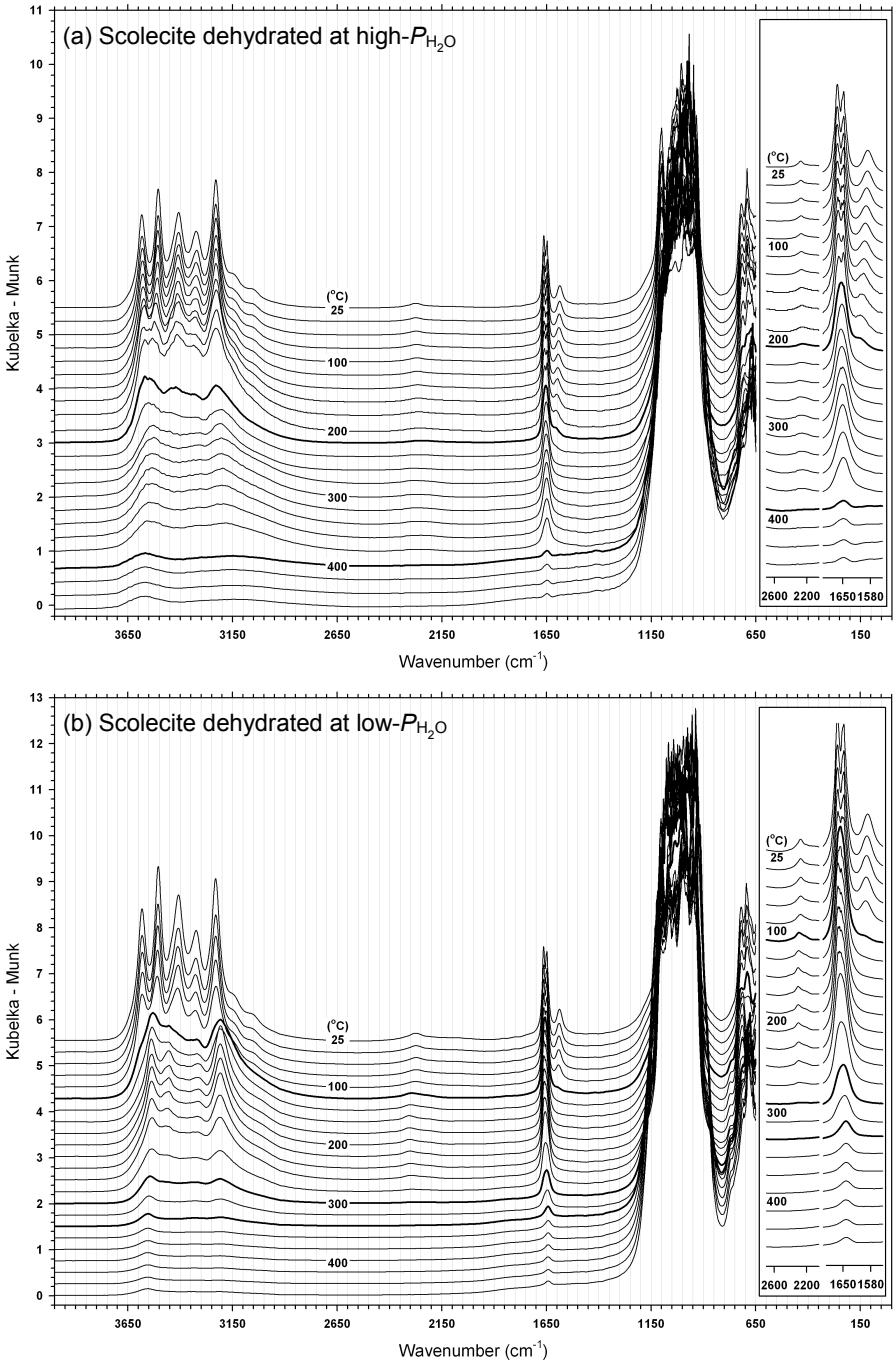

Figure 4.7. Temperature-resolved DRIFTS spectra of scolecite measured under different P_{H_2O} conditions. The temperature sequence is the same as in Figure 4.4. Bold spectra are at 220 and 400 ºC in plot **(a)** and at 120, 300 and 340 ºC in plot **(b)**. The insert plots are the expansions of H_2O bending and combination modes of host-(Ca-H_2O) at 2276 cm^{-1}.

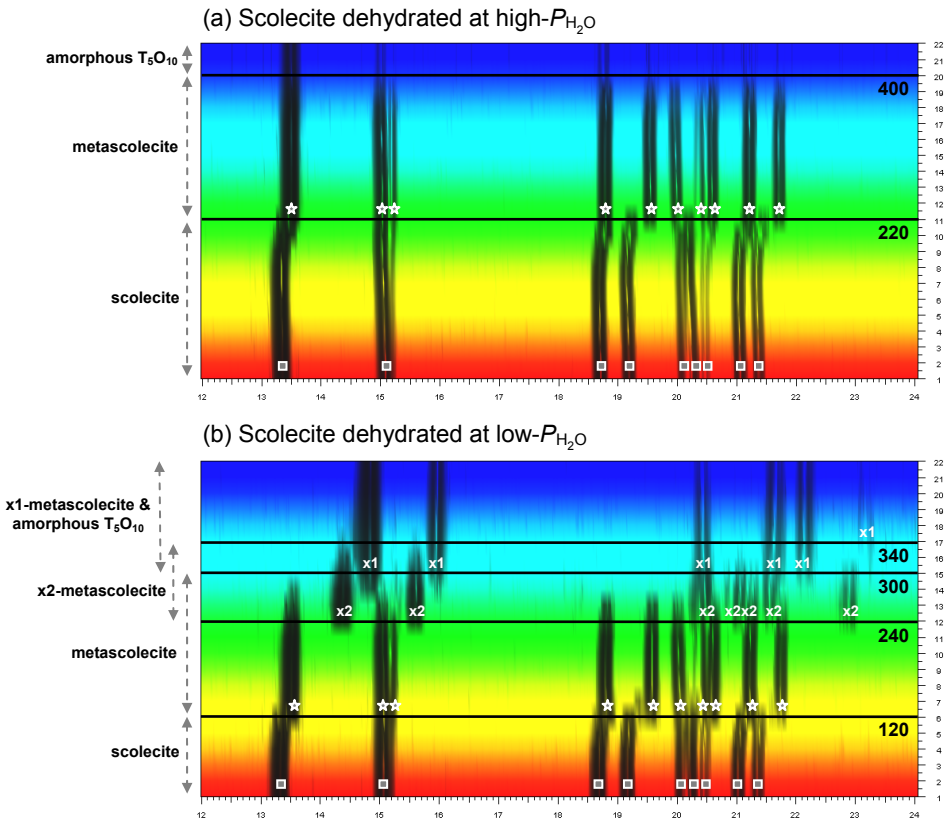

Figure 4.8. Temperature-resolved XRD patterns of scolecite measured under different P_{H_2O} conditions, illustrating the distinct changes as a function of temperature: *x* and *y* axes represent 12-24º *2θ* and temperature (#1-22, in the same sequence as in Fig. 4.5). Plots are viewed down the intensity axis. The square, star, x2, and x1 symbols represent reflections of scolecite, metascolecite, x1-, and x2-metascolecite phases, respectively. Note that amorphous phase does not contribute any diffraction signal.

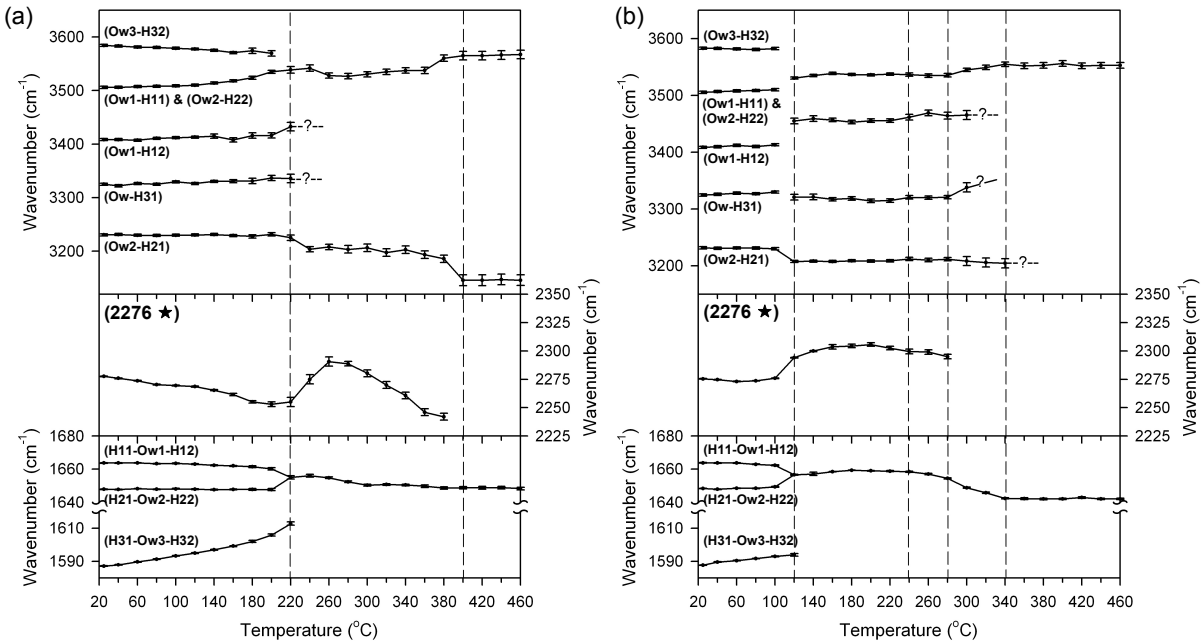

Figure 4.9. Frequency dependence of selected bands (with error bars) during scolecite dehydration as a function of temperature and P_{H_2O}: **(a)** a high-P_{H_2O} experiment; **(b)** a low-P_{H_2O} experiment.

contracted x1-metascolecite channels. The diffusion rate of H_2O molecules in x1-metascolecite is likely slower than for α1-metanatrolite because of the higher hydration energy of Ca^{2+} cations. After holding the specimen at 440 °C for 10 hours, all IR absorptions from internal H_2O bending vibrations were absent.

Figure 4.9 shows a plot of selected IR bands as a function of temperature and P_{H_2O}. Frequency dependence of selected bands (depicted either by abrupt shifts or changes in slope) is consistent with the dehydration/phase transition phenomena discussed above, and vertical dashed lines were used to outline these changes (Fig. 4.9). Question marks associated with certain bands indicate that their precise positions were not located due to band broadening and overlap as temperature increased. Gaps in the plot of the (Ow-H) stretching region reflect difficulties in tracking the dynamic evolution of certain (Ow-H) stretching bands during the scolecite-to-metascolecite transformation, e.g., the (Ow3-H32), (Ow1-H11) and (Ow2-H22) stretching bands. As seen for natrolite, the position of the (H31-Ow3-H32) bending band shifted progressively to higher frequencies until the first dehydration occurred (Fig. 4.9). The increase in frequency of the (H31-Ow3-H32) bending band with temperature was likely caused by pre-dehydration interaction between Ca^{2+} cations and the Ow3 H_2O molecules. Under high-P_{H_2O} conditions, the (H31-Ow3-H32) bending band migrated to even higher frequencies than for the specimen heated under low-P_{H_2O} conditions. The scolecite 2276 cm^{-1} band, on the other hand, consistently shifted to lower frequency before dehydration, especially for the specimen heated under high-P_{H_2O} conditions (Fig. 4.9a). The 220-400 °C interval in Figure 4.9a represents the metascolecite phase field (formed when scolecite was heated under high-P_{H_2O} conditions) and is comparable to the 120-240 °C interval in Figure 4.9b (the metascolecite phase field formed when scolecite was heated

under low-P_{H_2O} conditions). The behavior of scolecite over these two temperature intervals is significantly different, particularly the thermal evolution of the (Ow-H) stretching band and the scolecite 2276 cm^{-1} band (Fig. 4.9). These differences in thermal evolution of H_2O and migration of Ca^{2+} cations in the scolecite and metascolecite phase fields reflect the different local bonding interactions of H_2O molecules and Ca^{2+} cations with the host Al-Si frameworks, which may later influence the Al-Si framework flexibility as the transition temperature is approached during further heating. Different thermal evolutions of H_2O molecules and Ca^{2+} cations observed in DRIFTS spectra may provide evidence as to why metascolecite became amorphous when it was heated at high-P_{H_2O} whereas the framework exhibited two different structural transformations when heated at low-P_{H_2O}. The physical process behind the observed behavior can be imagined as follows: before dehydration, thermal migration of extraframework Ca^{2+} cations will influence the internal energy of T-O tetrahedra and the bond strength and angles within and between tetrahedra (i.e., causing small spontaneous lattice distortions). At dehydration, the loss of H_2O molecules will also cause a lattice distortion but this will be modified according to the lattice symmetry, bonding energy, and the manner in which the lattice is already distorted. The way the structure behaves on heating, hence, depends strongly on the interactions of H_2O molecules and Ca^{2+} cations with the host Al-Si frameworks.

4.3.4 Mesolite dehydration behavior

The dehydration of mesolite occurs in two main steps, the first of which is generally considered to be the low-temperature extraframework cation order-disorder phase transition. During this reaction, Ow4 H_2O molecules are lost and the framework contracts along the *a* and *b* axes, associated with the loss of Ow4 H_2O molecules. The resulting structure, namely

Na/Ca-disordered metamesolite, is considered to have a random distribution of Na^+ and Ca^{2+} in its channel cation site (primarily based on XRD results). The second step, the high-temperature phase transition, occurs via the loss of the remaining Ow1, Ow2, and Ow3 H_2O molecules. This transition shows two different transition paths depending on the P_{H_2O}, with a structural transition from Na/Ca-disordered metamesolite to x-metamesolite/amorphous T_5O_{10} at low-P_{H_2O} environments and a phase transition from Na/Ca-disordered metamesolite to amorphous T_5O_{10} at high-P_{H_2O} environments. Transition temperatures for the first and second dehydration reactions depend on the P_{H_2O} (i.e., similar to the case for natrolite and scolecite). Consistent with XRD studies, temperature-resolved DRIFTS spectra measured under high- and low-P_{H_2O} conditions revealed P_{H_2O}-dependent phenomena (Fig. 4.10). When mesolite was heated at a high-P_{H_2O} atmosphere, the mesolite-to-Na/Ca-disordered metamesolite reaction was seen at 220 °C, indicated by the disappearance of the Ow4 H_2O stretching and bending modes in IR spectra (Fig. 4.10a) and by the disappearance of $k \neq 3n$ super-lattice reflections in XRD patterns (Fig. 4.11a; Na/Ca-disordered metamesolite is labeled with star symbols). Upon further heating to 380 °C, the framework of Na/Ca-disordered metamesolite collapsed and became X-ray amorphous (Fig. 4.11a). This high-temperature phase transition was also apparent in the IR spectra, indicated by an abrupt decrease in absorptions in the (Ow-H) stretching and (H-Ow-H) bending region and also by disappearance of the mesolite 2176 cm^{-1} and 2259 cm^{-1} bands (Fig. 4.10a and the insert plot). Above 380 °C, weak (H-Ow-H) bending and (Ow-H) stretching absorptions remained, likely due to impaired H_2O diffusion as discussed in the case of scolecite. When mesolite was heated at a low-P_{H_2O} atmosphere, the mesolite-to-Na/Ca-disordered metamesolite reaction occurred at a lower temperature (i.e., 140 °C; see Figs. 4.10b and 4.11b). The second

dehydration reaction, Na/Ca-disordered metamesolite-to-x-metamesolite/amorphous T_5O_{10}, began at 240 °C. By 340 °C, Na/Ca-disordered metamesolite completely transformed to x-metamesolite (indicated by circle symbols in Fig. 4.11b) and amorphous T_5O_{10} (as evidenced by increased XRD background; see Fig. 3.2 or discussions in Wang *et al.* 2010). Between 140 and 340 °C, a continuous decrease in intensity of the (Ow-H) stretching and (H-Ow-H) bending absorptions was observed, associated with the gradual loss of remaining Ow1, Ow2, and Ow3 H_2O molecules as shown in the TG curve given in Figure 3.3 and as determined from Rietveld refinements with XRD data (Wang *et al.* 2010). From 360 to 400 °C, a small (H-Ow-H) bending absorption remained, and by 420 °C this (H-Ow-H) bending absorption had virtually disappeared (Fig. 4.10b).

Selected IR absorption bands plotted as a function of temperature and P_{H_2O} reflect the different thermal evolution of H_2O bonding and Na^+/Ca^{2+} migrations during dehydration (Fig. 4.12). For instance, at a high-P_{H_2O} atmosphere, the mesolite 2259 cm^{-1} band showed a minor decrease in frequency from 25 to 220 °C, and this band abruptly shifted to higher frequency ≥240 °C. In contrast, the mesolite 2176 cm^{-1} band was essentially invariant <160 °C and began to shift to lower frequency as temperature increased (Fig. 4.12a). These changes were caused by the loss of Ow4 H_2O molecules and can be used as an indicator of the mesolite to Na/Ca-disordered metamesolite transformation. By 300 °C, the two bands (i.e., 2176 cm^{-1} and 2259 cm^{-1}) merged into a single broad band at 2202 cm^{-1} (see Fig. 4.12a and insert plot in Fig. 4.10a). As mentioned above, the disappearance of super-lattice peaks that are observed in the room-temperature XRD pattern indicates the loss of the super-cell, due to the presence of a non-ordered distribution of Na^+ and Ca^{2+} cations in the distorted metamesolite channels. However, XRD methods only provide an average structural picture,

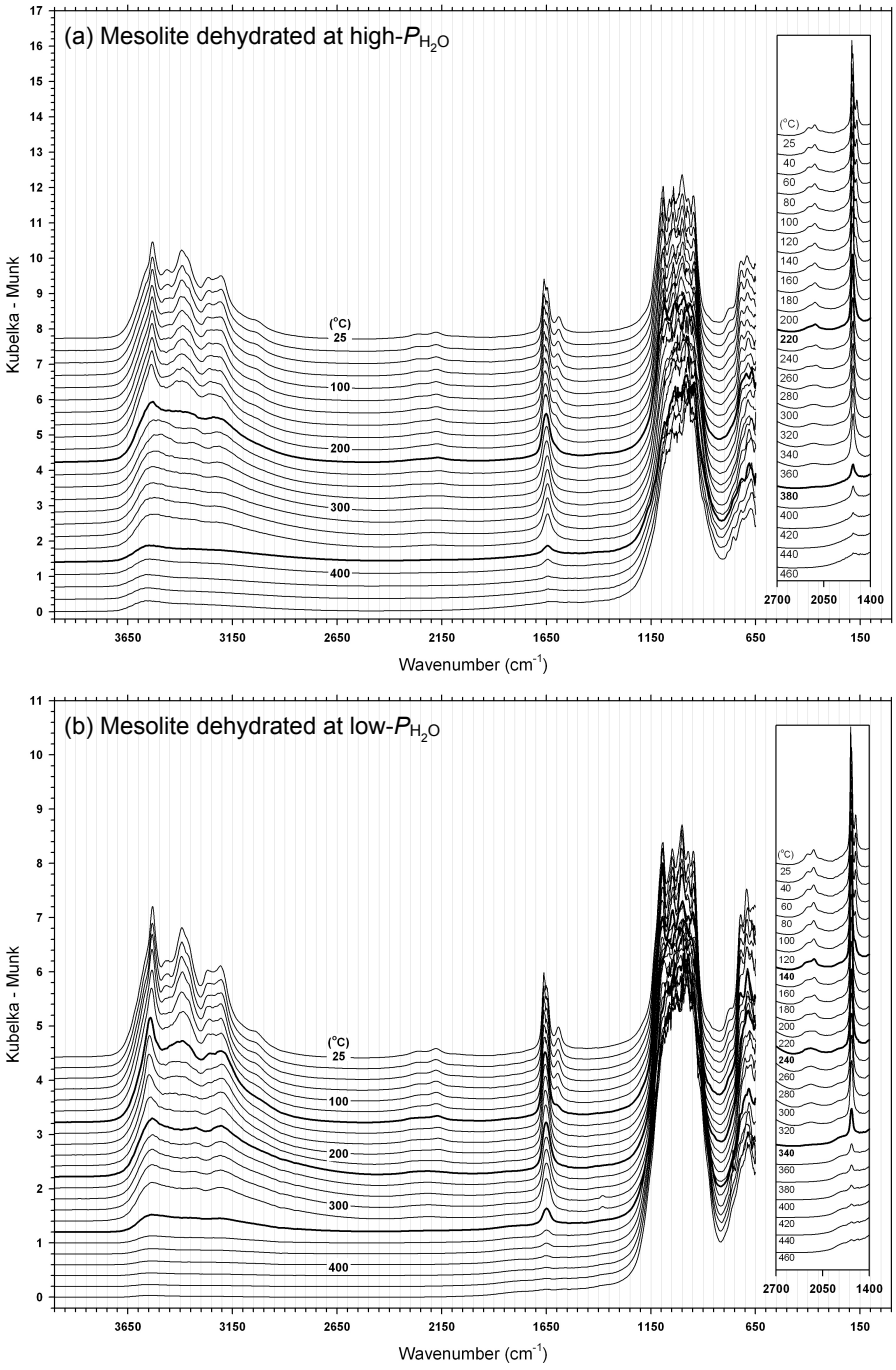

Figure 4.10. Temperature-resolved DRIFTS spectra of mesolite measured under different P_{H_2O} conditions. Temperature sequence is the same as in Figure 4.4. Bold spectra are at 220 and 380 ºC in plot **(a)**, and at 140, 240 and 340 ºC in plot **(b)**. The insert plots are the expansions of the H_2O bending mode and two combination modes at 2259 and 2176 cm^{-1}.

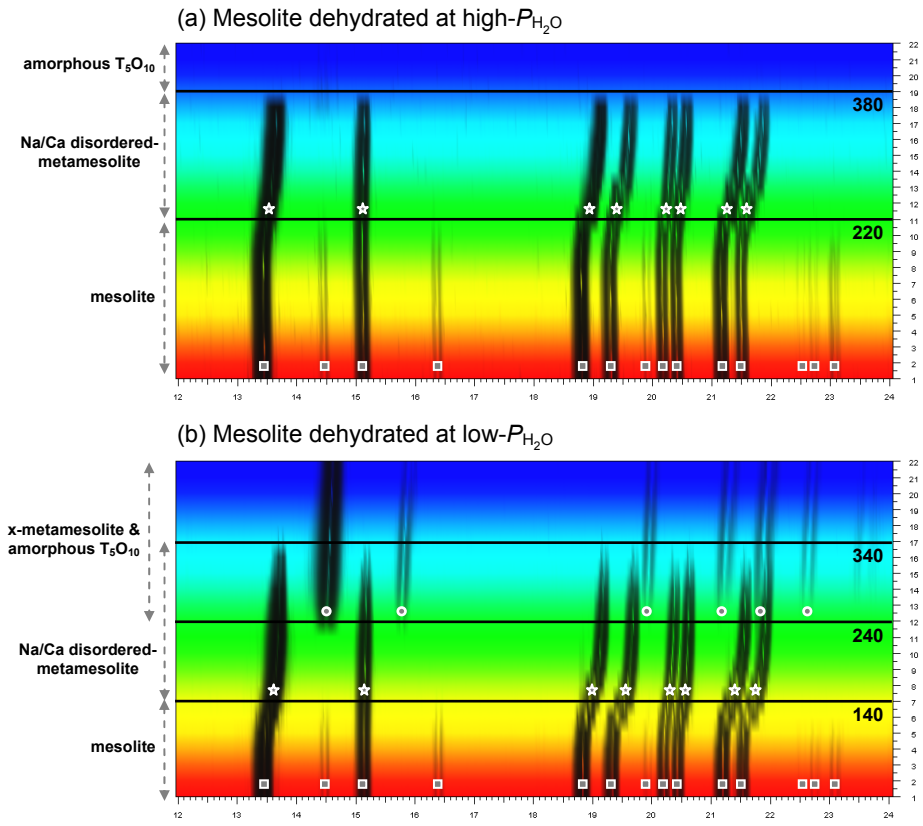

Figure 4.11. Temperature-resolved XRD patterns of mesolite measured under different P_{H_2O} conditions, illustrating the distinct changes as a function of temperature: *x* and *y* axes represent 12-24º *2θ* and temperature (#1-22, in the same sequence as in Fig. 4.5). Plots are viewed down the intensity axis. The square, star, and circle symbols represent reflections of mesolite, Na/Ca-disordered metamesolite, and x-metamesolite, respectively. Note that the amorphous T_5O_{10} phase does not contribute any diffraction signal.

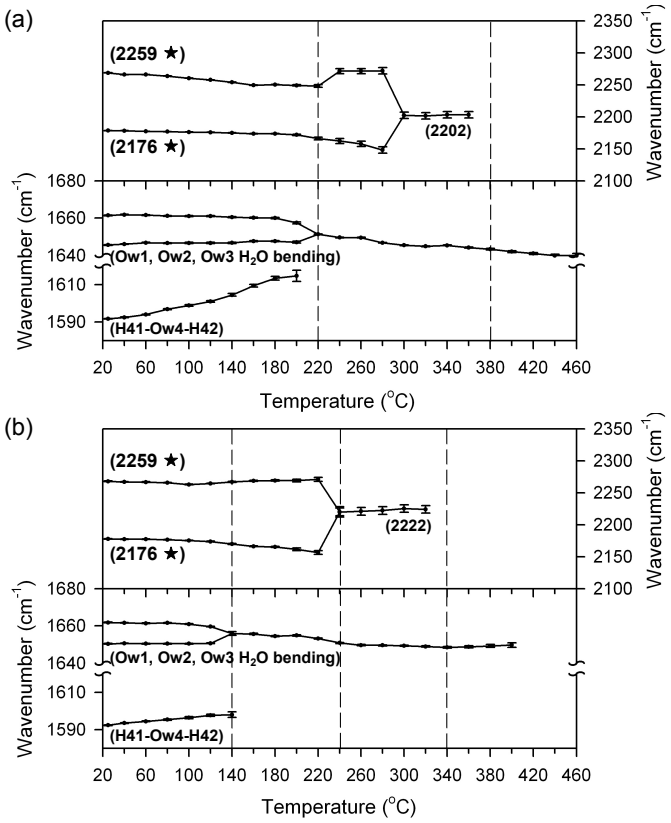

Figure 4.12. Frequency dependence of selected bands (with error bars) during mesolite dehydration as a function of temperature and P_{H_2O}: **(a)** a high-P_{H_2O} experiment; **(b)** a low-P_{H_2O} experiment.

whereas IR spectroscopy can provide information about more-local bonding interactions. Therefore, the 2176 cm^{-1} and 2259 cm^{-1} bands in mesolite can be used as local probes to indicate the degree of Na/Ca ordering. At temperatures between 220 and 280 °C (Fig. 4.12a and insert plot in Fig. 4.10a), two separate bands were observed, indicating that Na^{+} and Ca^{2+} cations are probably still localized near their room-temperature positions but with increased positional disordering (i.e., with Na^{+} and Ca^{2+} cations shifted randomly by thermal displacement, and XRD thus does not "see" this feature). A "truly" disordered Na/Ca distribution did not occur probably until a temperature of ~300 °C (as indicated by merging of the 2176 cm^{-1} and 2259 cm^{-1} bands at 300 °C). Upon further heating to higher temperatures, the structure of "true" Na/Ca-disordered metamesolite lost its three-dimensional order and the framework collapsed to amorphous T_5O_{10}. In contrast to results at a high-P_{H_2O} experiment, when mesolite was heated in low-P_{H_2O} conditions, the 2259 cm^{-1} and 2176 cm^{-1} bands increased and decreased, respectively, in frequency from 140 to 220 °C (Fig. 4.12b). Below 140 °C, no significant changes were observed, and by 240 °C, the 2259 cm^{-1} and 2176 cm^{-1} bands merged into one single band at 2222 cm^{-1} (see Fig. 4.12b and insert plot in Fig. 4.10b). Thus, the combination of IR and XRD results suggests that the metamesolite phase that formed at lower temperatures (i.e., the phase that occurs at 140-220°C and has Na^{+} and Ca^{2+} cations shifted randomly but still in the localized room-temperature channels) further transformed to x-metamesolite ≥240 °C. The "true" Na/Ca-disordered metamesolite phase (i.e., the phase that occurs ≥300 °C) formed at higher temperatures and continuously transformed to amorphous T_5O_{10} as temperature was increased. The difference in the temperature evolution of Na^{+}/Ca^{2+} cations and the nature of their order-disorder reactions observed from IR spectra may provide the evidence to clarify

the manner in which the mesolite framework responds to the migration of its Na^{+}/Ca^{2+}cations.

In addition, the dynamic evolution of H_2O hydrogen bonding as a function of temperature also exhibited different thermal behaviors under high- and low-P_{H_2O} conditions. This is reflected in the different spectral features in the (Ow-H) stretching region from 220 to 380°C in Figure 4.10a (high-P_{H_2O}) and from 140 to 340 °C in Figure 4.10b (low-P_{H_2O}). Moreover, under high-P_{H_2O} conditions, the (H41-Ow4-H42) bending absorption experienced greater shift to higher frequencies compared with the specimen heated under low-P_{H_2O} conditions. Unfortunately it was not possible to evaluate the detailed changes in H_2O local bonding environments (especially before and after the mesolite-to-Na/Ca-disordered metamesolite phase transition), due to the presence of multiple overlapping sub-bands in the (Ow-H) stretching and (H-Ow-H) bending region. The causes of different transition paths for mesolite heated under high- and low-P_{H_2O} conditions should be similar to those for natrolite and scolecite. Understanding the thermal evolution of H_2O and migration of Na^{+}/Ca^{2+}cations in the mesolite channels and how their behaviors affect the mesolite framework flexibility are key to pinpointing the transition mechanism(s).

4.4 Chapter summary

IR spectroscopic characterization of the vibrational properties of H_2O molecules and Na^{+}/Ca^{2+}cations in NAT-type zeolites is particularly useful for detection and characterization of their phase transitions. The results of IR studies not only confirmed the results of XRD analyses, but they also clarified the different energetic evolutions of H_2O molecules and Na^{+}/Ca^{2+}cations under high- and low-P_{H_2O} conditions. In addition, IR studies also provided

evidence for localized Na/Ca-configurations at lower temperatures, somewhat in conflict with diffraction data that provide a longer-range view of Na/Ca-disordering in metamesolite channels. The temperature- and P_{H_2O}-dependent phase transitions observed based on XRD and IR results underscore the importance of the combined effects of temperature and P_{H_2O} on zeolite phase transitions. These two environmental parameters (i.e., temperature and P_{H_2O}) are coupled and do not operate independently of one another. Their coupled effects influence the cation-H_2O-Al-Si framework interactions and result in different phase transition behaviors in the NAT system.

The "soft" behavior of the zeolite channels and the more rigid behaviors of their tetrahedral frameworks lead to displacive phase transitions, and the temperature at which the H_2O evolves and the structure distorts increases gradually as the environment moves from low- to high-P_{H_2O} conditions. The manner in which the tetrahedral framework can distort depends largely on its symmetry, i.e., it is constrained by the symmetry of the original high-symmetry phase. However, the nature of guest cations and H_2O molecules and their ability to induce displacive processes in a zeolite framework must also be considered. A general feature of aluminosilicate minerals is that the range of energetically feasible T-O-T angles and the flexibility of the structure are reduced when increasing the coordination of bridging oxygens by Na^+, K^+, or Ca^{2+} extraframework cations (e.g., the case in feldspars) and/or by H^+ from H_2O. Thus, the thermal behavior of the guest cation-H_2O complexes will generate local strain forces that may be coupled with the displacive process through framework strain fields.

Before dehydration, subtle thermal migration of guest cations will influence the internal energy of T-O tetrahedra and the bond strength and angles within and between tetrahedra (causing small spontaneous lattice distortions). At dehydration, the loss of H_2O

molecules will also cause a lattice distortion but this will be modified according to the lattice symmetry, bonding energy, and the manner in which the lattice is already distorted. These two processes are coupled, and the way the structure behaves on heating depends on the way in which these two component parts of the behavior interact. The discoveries of several new phases in low-P_{H_2O} environments (i.e., α2-metanatrolite, x2-metascolecite, x1-metascolecite and x-metamesolite) imply the existence of more than one transition mechanism. The observed transition behaviors can be, in general, rationalized in terms of two cooperating factors, namely thermally induced and dehydration-induced phase transition mechanisms. The dehydration-induced process is the primary one in determining the temperature at which the dehydration occurs. The thermally induced process appears to be a secondary mechanism in determining the phase transition path. The temperature at which dehydration occurs defines the energetic evolution of guest cation-H_2O complexes in the channel system and the accommodation of NAT-type frameworks around the local guest complexes. Both mechanisms together determine the dehydration temperatures, reaction paths, and which metaphases ultimately form.

CHAPTER 5

Hysteresis and thermodynamics in NAT-topology zeolites

The unique temperature- and P_{H_2O}-dependent structural phase transitions in NAT-type zeolites (natrolite, scolecite, and mesolite) suggest a need to evaluate the heat (enthalpy) evolved during these reactions and to develop suitable thermodynamic descriptions of these systems. One of the central themes in thermodynamics is that no matter what the response of a mineral structure to a change in the physical or chemical environments, the direction of change is always in the direction towards a free energy minimum (either to the absolute global minimum or to a local minimum). Additionally, it is also possible to associate particular macroscopic behaviors with certain general microscopic change. For instance, a discontinuity in molar volume may result from a change of structure from one polymorph to another, and an anomaly in heat capacity may result from a change in atomic ordering in a crystal. During dehydration of NAT-type zeolites, the characteristic features found through X-ray diffraction (XRD) and infrared (IR) experiments allowed the development of a general unified thermodynamic function in terms of an energy balance, which not only considers equilibrium but also includes possible energy contributions from irreversible and hysteretic process. One of the major difficulties in dealing with H_2O vapor sorption and desorption in zeolites is that the zeolite framework and its extraframework cations are potentially highly responsive to the sorption or desorption of H_2O molecules in the structure. In such a system, one does not deal with simple gas sorption and desorption on an inert physical surface, but with the entire polymorph network that is penetrated by H_2O molecules. In addition, the channel structure may be subjected to irreversible collapse upon dehydration (due to the

removal of H_2O molecules). Hence, the observed dehydration and rehydration phenomena are coupled to two features, namely the sorption/desorption of H_2O molecules and the corresponding extraframework cation mobility and framework modification. Both the structural changes and the nature of H_2O sorption/desorption contribute to the "thermodynamic" properties. For highly thermally stable zeolites (related mainly to the Al/Si ratio in the framework; see reviews in Cruciani 2006), such as clinoptilolite, mordenite, and chabazite, a small change in temperature or P_{H_2O} leads to nearly reversible changes in H_2O content with little or no modifications to the framework. The criteria for thermodynamic equilibrium (i.e., the process must be quasistatic and there must be no hysteresis) are approximately satisfied in such systems. Carey and Bish (1996) developed a thermodynamic formulation by equating the chemical potential of H_2O in the vapor phase to the chemical potential of the H_2O component in the zeolite structure (i.e., $\mu_{H_2O}^{vapor} = \mu_{H_2O}^{zeolite}$). This elegant approach, however, is limited to reversible and non-hysteretic processes. As particularly mentioned by Bish and Carey (2001), once the thermal or dehydration condition has exceeded the certain limits, zeolites no longer rehydrate or dehydrate according to the same physical process. Thermal or P_{H_2O} hysteresis is very common in zeolites, and the area of the hysteresis loop itself gives a measure of the amount of energy that has been dissipated or absorbed during the transformation. Hysteresis also represents a consequence of the macroscopic manifestation of entropy production in the system. To my knowledge, there are no suitable thermodynamic formulations available to deal with hysteretic behaviors commonly observed in zeolite systems. Accordingly, this final discussion is oriented towards a thermodynamic description of dehydration and rehydration in NAT-type zeolites. The discussion is organized into four sections. The first section gives an overview of hysteretic

behaviors when the sample temperature is changed in a cyclic way through the dehydration and rehydration. Section two introduces the general framework of equilibrium thermodynamics and moves on to thermodynamic treatments of the irreversible process. Concepts relating to the entropy production and its thermodynamic arguments will be emphasized. Many of the ideas discussed in this section were inspired from the hysteresis found in the shape-memory alloys and in the metal-hydride systems[12]. Section three derives a way to determine the heat (enthalpy) evolved during the process of dehydration and/or rehydration through the construction of a quasistatic reaction phase diagram in which data are plotted as (log P_{H_2O}) vs. (1000/T). Finally, a conclusive summary is given in the last section.

5.1 Thermal hysteresis in NAT-topology zeolites

A convenient way to observe thermal hysteresis in zeolites is through thermogravimetric (TG) analysis, where the weight changes due to dehydration (heating) and rehydration (cooling) reactions are recorded through a complete heating/cooling cycle. By applying a constant heating rate, the dynamic weight changes of a specimen under ambient or controlled-P_{H_2O} conditions were monitored. The major limitation of such TG analyses is that only a limited amount of information on structural transformations and mechanisms can be extracted. However, when combined with parallel XRD measurements, TG analyses can provide significant amounts of important information. A series of TG experiments was performed using a TA Instruments 2960 TG analyzer. All measurements were conventional isobaric experiments done at 1 bar and under an ambient atmosphere (~15-50% *RH*,

[12] Shape-memory alloys show a strongly temperature-dependent hysteresis to load- or temperature-induced deformation. In metal-hydride systems, pressure hysteresis is usually seen during the isothermal hydriding and dehydriding cycle.

corresponding to ~4-13 mbar P_{H_2O} at 22 ± 1 ºC) or a N_2 gas flow (100 cm^3/min) condition, which ensured at least two different humidity environments in the sample chamber. The results of these two measurements will be compared. Purging with N_2 gas reduces the atmospheric $H_2O_{(g)}$ to a large extent but does not effectively remove all H_2O within intercrystallite pore spaces. The predicted effective *RH* with an N_2 gas flow through the system is ~5-10% *RH* (at 22 ± 1 °C). Kinetic effects certainly exist in such dynamic measurements. In general, the shape of a hysteresis loop, i.e., the branches in the forward (heating) and reverse (cooling) paths, depends on the relation between two time scales, namely the intrinsic time scale of reaction/transformation within the zeolites (i.e., how fast a zeolite responds to changes in temperature and P_{H_2O}) and the time scale at which the system is driven externally (i.e., the heating/cooling rate or the atmospheric *RH* surrounding the sample). In order to reduce the influence of heating/cooling rate on the shape of a hysteresis loop, a slow heating/cooling rate (1 ºC/min) and a small amount of sample (11.5 ± 0.2 mg) were used for all measurements. The true behavior, however, is probably somewhere between these two time scales and the resulting hysteresis may be influenced by both kinetic effects. This represents an additional difficulty in the description of hysteresis, but for qualitative purposes, this should not pose a great problem as long as the extrinsic variations (e.g., temperature rate, P_{H_2O} condition, and amount of sample used) remained the same for each individual measurement. The experiments were mainly designed to measure: (i) the H_2O content of NAT-type zeolites as a function of temperature; (ii) the effect of *RH* (or P_{H_2O}) on the thermal hysteresis loop in NAT-type zeolites; (iii) variations in the hysteresis loop when heating was switched to cooling at some point through dehydration but before completion.

5.1.1 Natrolite

Upon dehydration, natrolite yielded an abrupt and single-stage weight loss in the TG curve. The inflection temperature was close to the end of weight loss (i.e., the maximum rate of weight change) and was 285 ºC when measurements were made under ambient conditions (~40-50% *RH*, corresponding to ~11-13 mbar P_{H_2O} at 22 ± 1 ºC), decreasing to 253 ºC when measurements were made under a flow of N_2 gas (Figs. 5.1 and 5.2). Based on the measured *RH* before and after each experiment and the measured inflection temperature, one can estimate that the TG measurement made under an ambient environment is approximately comparable to the observed XRD data measured at ~50% *RH* (see Fig. 1.2k). The corresponding sequence of dehydration reaction for these conditions is natrolite-to-α1/α2-metanatrolite. During rehydration, a hysteretic effect was apparent, especially near the completion of dehydration where most of the starting material was transformed to the α1-metanatrolite phase (Fig. 5.1; heating to >300 ºC). In Figure 5.1, the observed TG rehydration curve (a) is horizontal (no weight change) at the beginning of rehydration and then makes an upward trace as the temperature cools to ~220 ºC. When heating was switched to cooling partway through the dehydration reaction, such as curves (b-f) in Figure 5.1, smaller hysteretic effects were observed, with the TG rehydration curves showing some further weight loss and then rehydrating back to natrolite. Thus, "instant" rehydration is only possible as long as the framework of natrolite does not distort. When heating was switched to cooling somewhere partway along the dehydration path, some of the channels had contracted already, forming the α1-metanatrolite phase, whereas other channels remained intact. Thus the degree of hysteresis depends on the advancement of the natrolite-to-α1-metanatrolite reaction. The greater the proportion of the anhydrous phase produced on dehydration, the

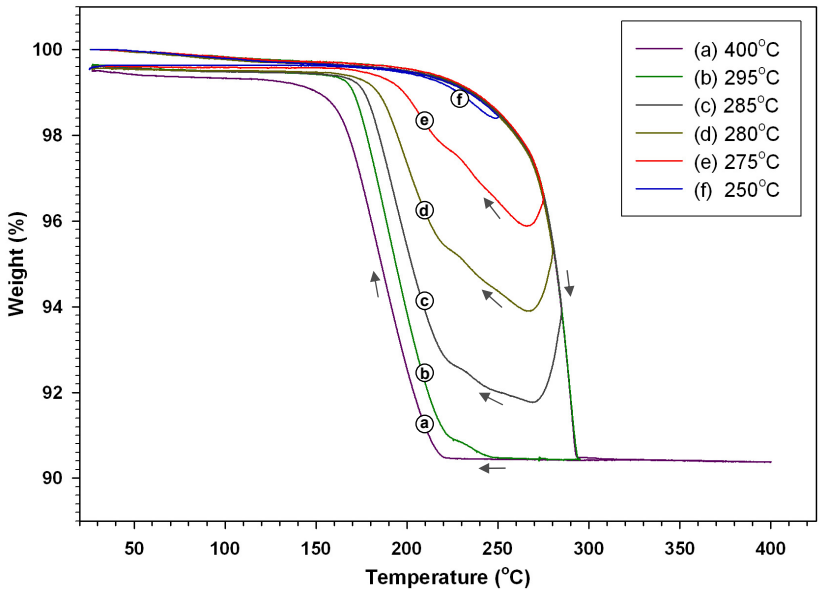

Figure 5.1. TG data for natrolite measured during dehydration (heating) and rehydration (cooling). Sample mass was 11.5(2) mg. Measurement was made under ambient *RH* conditions (~40-50% *RH*) with 1 ºC/min temperature rate. Thermal hysteretic behaviors were tested when the natrolite temperature was changed in a cyclic way through dehydration and rehydration.

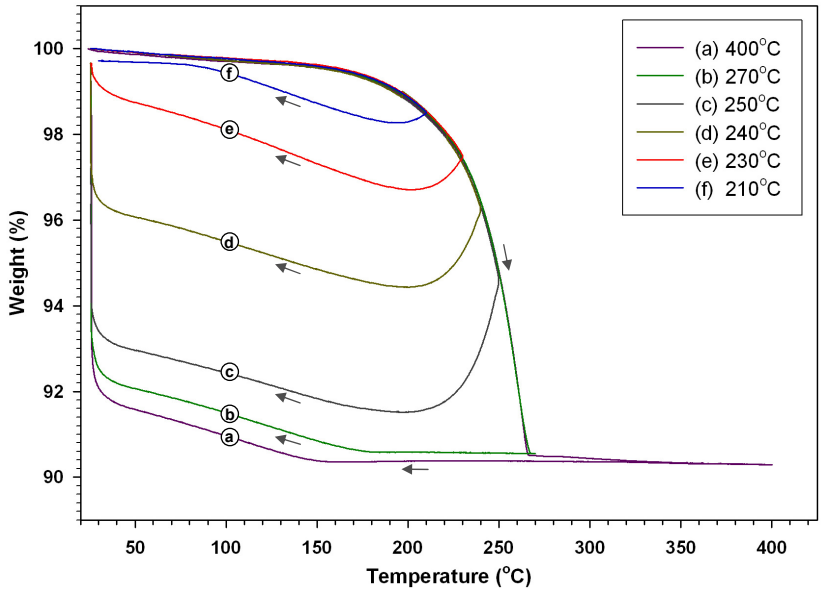

Figure 5.2. TG data for natrolite measured during dehydration (heating) and rehydration (cooling). Measurement was made under a flow of N_2 gas, which effectively lowers the system humidity to ~5-10% *RH*. Note that the dehydration reaction was promoted by decreased *RH* and a larger area of the hysteresis loop was found compared with Figure 5.1. The temperature rate and sample mass were the same as used in Figure 5.1.

stronger were the hysteretic effects observed on rehydration. After a complete heating/cooling cycle, the sample weight reverted back to 99.6(2) wt.% within the experimental time (~1500 min) and nearly closed hysteresis loops were seen in the TG curves. A certain amount of irreversible defects was perhaps generated during the transformation cycle, which may contribute to a small opening in the hysteresis loop.

A different aspect of dehydration/rehydration behavior and reversibility was measured by performing the same TG measurement but in a lower *RH* with a flow of N_2 gas purging the sample chamber. The decrease in inflection temperature to 253 ºC indicated that the transformation approximately corresponded to the XRD data measured under ~10% *RH* conditions (see Fig. 1.2g). Compared with results obtained under ambient *RH* conditions, the rehydration branch of the hysteresis loop yielded a very different shape (Fig. 5.2). Detailed features along the rehydration path were smoothed out and rehydration was more gradual and did not occur until the very end of the cooling cycle.

5.1.2 Scolecite

Upon heating to 425 ºC, scolecite underwent two main steps of dehydration, which resulted in an abrupt, two-stage weight loss in the TG curve. The TG dehydration course was virtually horizontal between the two main dehydration steps (Figs. 5.3 and 5.4). When measurements were made under ambient conditions (~15-20% *RH* condition, corresponding to ~4-6 mbar P_{H_2O} at 22 ± 1 ºC), the inflection temperatures were 188 and 356 ºC for each dehydration step (Fig. 5.3), approximately comparable to the XRD data measured at ~20% *RH* (see Fig. 2.2i). The corresponding sequence of dehydration reaction is scolecite-to-metascolecite-to-amorphous T_5O_{10}. During rehydration, a strong hysteretic effect was apparent, especially near the completion of dehydration where most of the starting materials

were transformed to the amorphous T_5O_{10} phase (Fig. 5.3; heating to >375 ºC). Once the amorphous T_5O_{10} phase had formed, the framework of metascolecite was subjected to irreversible distortion and lost its rehydration ability. The observed TG rehydration curves (a-b) were horizontal during the entire cooling process, which resulted in an open hysteresis loop after a complete heating/cooling cycle (Fig. 5.3). When heating was switching to cooling somewhere at lower temperatures, such as curves (c-d) in Figure 5.3, the degrees of rehydration depended on the extent of the metascolecite-to-amorphous T_5O_{10} reaction and the observed hysteresis was proportional to the amounts of the remaining metascolecite phase (i.e., the greater the proportion of the amorphous T_5O_{10} phase produced on dehydration, the stronger the hysteretic effects observed on rehydration). When temperature was increased only up to the completion of the scolecite-to-metascolecite reaction, a smaller hysteresis loop was obtained (Fig. 5.3; curves e-f). Finally, when heating was switched to cooling partway along the scolecite-to-metascolecite reaction, an even smaller hysteresis loop was found (Fig. 5.3; curve g). On average, the metascolecite phase adsorbed H_2O and converted 99.7(1) wt.% to scolecite within the experimental time (~1500 min). A nearly closed hysteresis loop was found in the TG curves (e-g) in Figure 5.3 and a small amount of irreversible defects may have been generated in the transformation cycle. Moreover, it is apparent that rehydration in scolecite (and also in natrolite) depends not only on the current driving value of temperature but also on the previous temperature path (i.e., hysteresis is also a manifestation of memory in the system). When measurements were made under a flow of N_2 gas, similar two-stage dehydration behaviors were observed during dehydration (Fig. 5.4). The major differences along the dehydration path were decreases in the inflection temperatures to 169 and 333 ºC in each dehydration step, which approximately corresponds to ~5-10% *RH* conditions in the

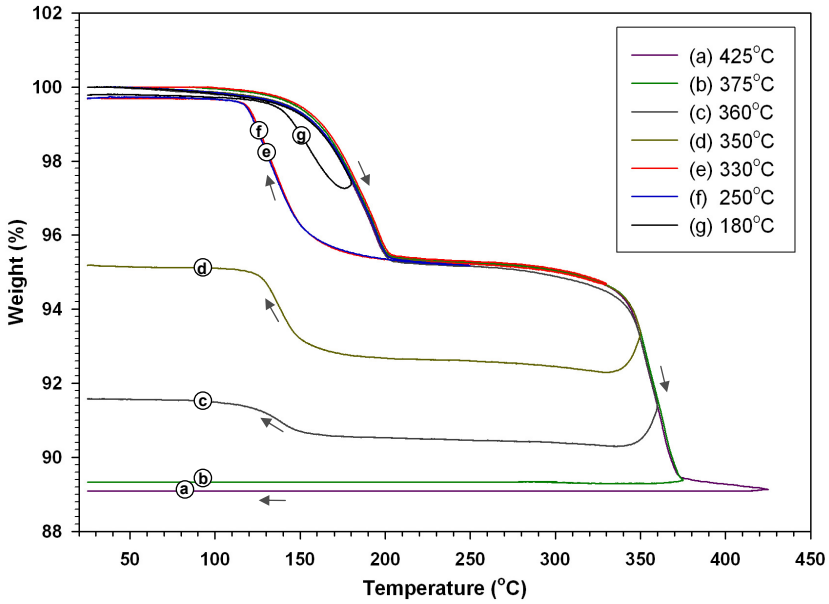

Figure 5.3. TG data for scolecite measured during dehydration (heating) and rehydration (cooling). Sample mass was 11.5(2) mg. Measurements were made under ambient *RH* conditions (~15-20% *RH*) with 1 ºC/min temperature rate. Thermal hysteretic behaviors were tested when the natrolite temperature was changed in a cyclic way through dehydration and rehydration.

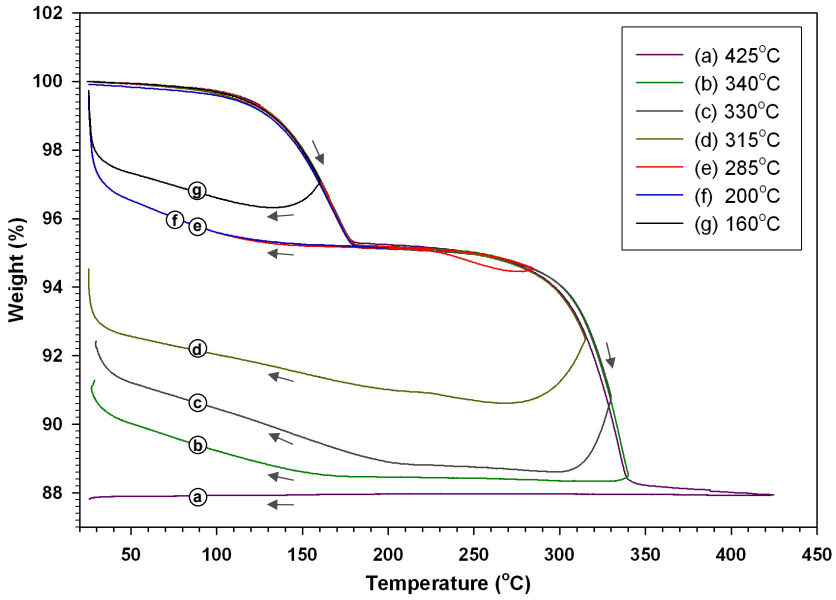

Figure 5.4. TG data for scolecite measured during dehydration (heating) and rehydration (cooling). Measurement was made under a flow of N_2 gas, which effectively lowers the system humidity to ~5-10% *RH*. Note that the dehydration reaction was promoted by decreased *RH* and a larger area of the hysteresis loop was found compared with Figure 5.3. The temperature rate and sample mass were the same as used in Figure 5.3.

XRD measurements (see Figs. 2.2f and g). Again, the reverse branch of a hysteresis loop along the rehydration path was very different from that obtained under ambient *RH* conditions. Detailed features along the rehydration path were smoothed out, and rehydration was prolonged to the very end of the cooling cycle (Fig. 5.4).

5.1.3 Mesolite

Thermal hysteresis in mesolite is conceptually similar to natrolite and scolecite with additional complexity due to the presence of two distinct types of channels in its structure (one is a natrolite-type channel and the other is a scolecite-type channel). The observed thermal hysteresis measured under ambient *RH* conditions (~20-30% *RH* condition, corresponding to ~6-8 mbar P_{H_2O} at 22 ± 1 ºC) yielded three main inflection temperatures, 188, 226, and 338 ºC, along the dehydration path (Fig. 5.5), which are approximately comparable to the observed XRD data measured at ~30% *RH* (see Fig. 3.2h). Inflection temperatures shifted to 165, 199, and 309 ºC when measurements were made under an N_2 gas flow, which approximately corresponds to ~5-10% *RH* conditions in the XRD measurements (see Figs. 3.2e and f). Thus, TG measurements made under ambient conditions correspond to the mesolite-to-Na/Ca-disordered metamesolite-to-amorphous T_5O_{10} reaction, whereas measurements made under an N_2 gas flow correspond to the mesolite-to-Na/Ca-disordered metamesolite-to-x-metamesolite/amorphous T_5O_{10} reaction. In addition, because of the existence of a small-step weight loss and gradual weight change in between the two abrupt dehydration steps, the rehydration behaviors along the reverse process showed two inflections in the TG curve measured under ambient conditions (each with its own hysteresis; see Fig. 5.5; curves c-g). Once the Na/Ca-disordered metamesolite phase began to transform to the amorphous T_5O_{10} phase, either completely or partially (depending on the extent of

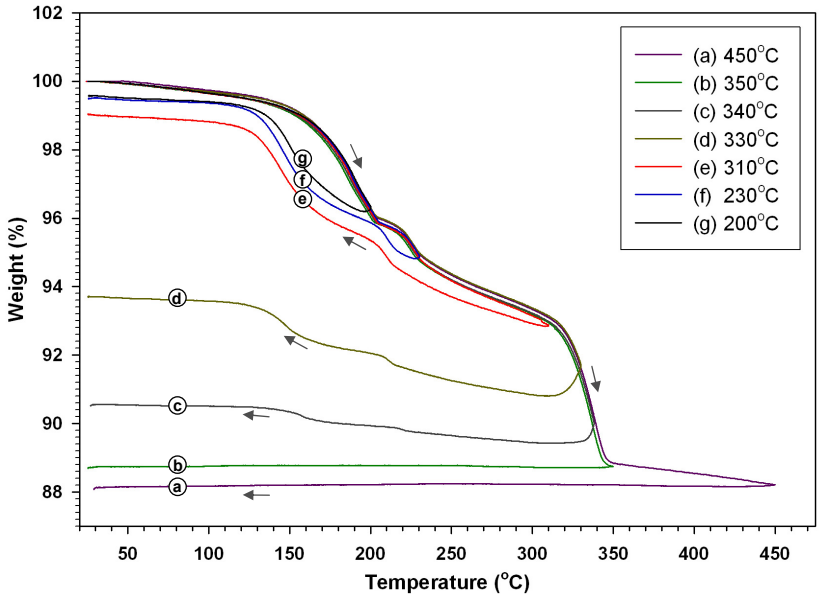

Figure 5.5. TG data for mesolite measured during dehydration (heating) and rehydration (cooling). Sample mass was 11.5(2) mg. Measurement was made under ambient *RH* conditions (~20-30% *RH*) with 1 ºC/min temperature rate. Thermal hysteretic behaviors were tested when the natrolite temperature was changed in a cyclic way through dehydration and rehydration.

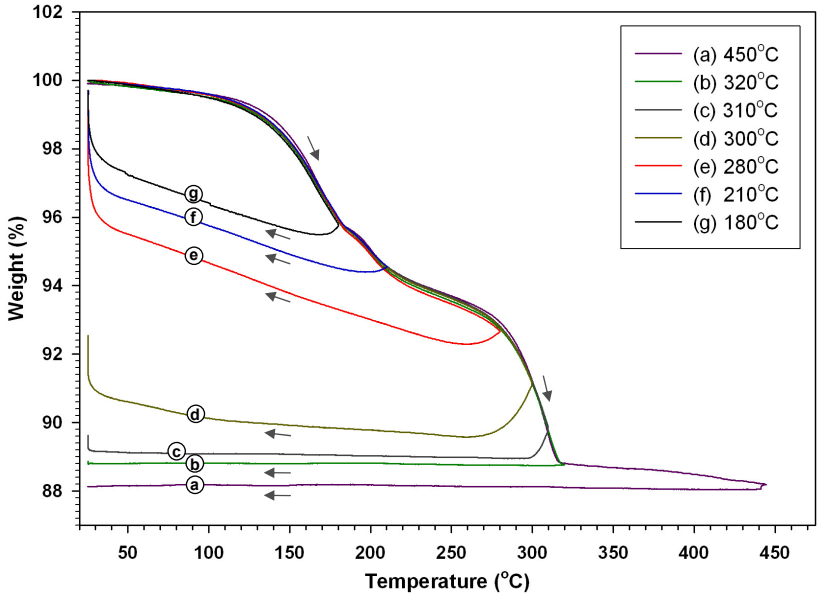

Figure 5.6. TG data for mesolite measured during dehydration (heating) and rehydration (cooling). Measurement was made under a flow of N_2 gas, which effectively lowers the system humidity to ~5-10% *RH*. Note that the dehydration reaction was promoted by decreased *RH* and a larger area of the hysteresis loop was found compared with Figure 5.5. The temperature rate and sample mass were the same as used in Figure 5.5.

reaction), the thermal hysteresis loop became an opened loop (Figs. 5.5 and 5.6; curves a-e). When temperature was increased only up to the formation of the Na/Ca-disordered metamesolite phase (i.e., ≤230 ºC at ambient conditions and ≤210 ºC under a N_2 gas flow), the sample weight reconverted back to 99.6(1) wt.% within the experimental time (~1500 min). However, the degrees of Na/Ca ordering in mesolite channels did not revert back to the original state as shown by XRD measurements. When experiments were made under an N_2 gas flow, rehydration was more gradual and did not occur until the very end of the cooling cycle (Fig. 5.6).

5.1.4 General explanations for thermal hysteresis in natrolite, scolecite, and mesolite

When the atmospheric *RH* was lower, delayed rehydration in the reverse branches of the hysteresis loop was apparent in all three zeolites. Similar kinetic mechanisms must apply to these three zeolite systems, and possible explanations are as follows. The intrinsic time scale of H_2O sorption and re-expansion of the distorted frameworks during rehydration are much longer than the extrinsic time scale of driving temperature rate. Therefore, the larger amount of undercooling, ΔT, is apparent for this dynamic phenomenon. However, this does not mean that the same measurements made under ambient conditions have no dynamic effects involved. In fact, it only means that at the given cooling rate (1 ºC/min), changes in the shape of the reverse branch are a result of non-quasistatic processes due mainly to the external conditions, including cooling rate and a low-*RH* environment. In contrast with the rehydration branching, the dehydration branching is very similar in shape with or without purging N_2 gas through the sample chamber, indicating that the time scale of H_2O desorption and framework distortion is negligible in comparison with the time scale of driving heating rate (i.e., a more static situation can be assumed). The temperature ramp rate has only a small

influence on the slope of dehydration branching, and the shifts in the inflection temperatures are merely a response of the system to the surrounding *RH* conditions (i.e., the comparatively moist environments employed on heating caused the initial dehydration temperatures to increase). These observations demonstrate that under a quasistatic heating rate (i.e., a process carried out reasonably slowly, but not necessarily reversible), the amount of superheating, ΔT, should be smaller than the amount of undercooling, and a state of quasistatic equilibrium is easier to achieve during the dehydration process. The actual position of the thermodynamically defined equilibrium pathway must be within the area enclosed by the hysteresis loop. In the NAT system, the equilibrium path is assumed to be located asymmetrically near the dehydration branching for several reasons. First, the mobility of extraframework cations and H_2O molecules and their diffusion rates are higher in the undistorted channels and they increase as temperature is increased. Second, it is energetically easier to shrink the aluminosilicate framework (through tetrahedral rotations) during heating than to re-expand it during the cooling process. Thus, the activation energy barrier required to re-expand the collapsed frameworks during rehydration is likely larger than the energy required for the opposite process (i.e., an asymmetric activation energy barrier along the forward and reverse paths of transformation can be imaged). Therefore, thermal hysteresis in NAT-type zeolites originates mainly within a reverse transformation process and results from: (i) the intrinsically non-equilibrium H_2O sorption/desorption process (chemical type reaction); (ii) the intrinsic irreversibility arising from aluminosilicate framework modifications (non-chemical type reaction); and (iii) if the time scale of external driving forces, such as *RH* conditions and temperature rates, is faster than the time scales of intrinsic processes, additional dynamic processes introduced by external forces must be considered.

5.2 Thermodynamics of dehydration/rehydration reactions and accompanying structural phase transitions in NAT-topology zeolites

Hysteretic systems are not in thermodynamic equilibrium and hence special attention must be paid to the origin of hysteresis and its associated entropy production when formulating any thermodynamic relations. The origin of hysteresis discussed in the previous section illustrates the difficulties involved when attempting to deal with or separate these origins into their individual energy contribution, due to their heterogeneous characters. For instance, it is difficult to judge the amount of entropy production only from the intrinsic non-equilibrium H_2O sorption/desorption process without considering the effects of aluminosilicate framework modifications (i.e., in the form of non-chemical type contributions such as variation in local bonding configurations, creation of defects, or elastic strain accommodations). To begin with, the thermodynamic variables considered here and the foundations of equilibrium thermodynamics will be introduced first. Concepts relating to different entropy production terms and their evolution along the transition paths will be discussed at the end of this section.

5.2.1 Thermodynamic variables

When dealing with an equilibrium reaction that involves both solid and gaseous substances at constant temperature and total pressure, the equilibrium condition ($dG = 0$) applies whether or not all species are in the same phases. A hypothetical description of a simple dehydration/rehydration reaction in zeolites can be written as

$$A_{(s)} \leftrightarrow B_{(s)} + nH_2O_{(g)} \qquad \text{at } T, P, \text{ and } P_{H_2O},$$

where A is the parent hydrous phase, B is either the hydrous or anhydrous daughter phase with the loss of n moles of $H_2O_{(g)}$ upon dehydration. Three independent variables,

temperature (T), total pressure (P), and partial pressure of H_2O (P_{H_2O}) are considered at equilibrium. Strictly specking, P_{H_2O} is not an independent variable and the range of P_{H_2O} that one can control depends on the T and P conditions. For instance, when the gas phase is in the gas mixture (e.g., $H_2O_{(g)}$ in air), P_{H_2O} is commonly known as relative humidity (RH) , and the maximum amount of $H_2O_{(g)}$ that the air is able to hold without condensation depends on the T and P conditions. Conversely, at constant T and P, there is a limited range of P_{H_2O} that can be independently controlled through the correlation between RH and dew point temperatures. Furthermore, P_{H_2O} (either pure or in gas mixture) for a reaction equilibrium involving solid and gaseous substances at constant T is also affected by P (if changing) through the volume changes of the solids that contribute to the free energy of the reaction (see derivation below).

5.2.2 Thermodynamic relations for hypothetical equilibrium processes

If the above hypothetical reaction occurs under equilibrium conditions (i.e., quasistatic and no hysteresis), the thermodynamic derivation can be treated as a simple chemical reaction whether or not there is a change in the structure between the parent and daughter phases. In order to express the changes of state function in terms of interesting quantities, enthalpy and volume, Orville and Greenwood's (1965) derivation was followed and with the following modifications[13]. The total derivative of the molar Gibbs free energy of ideal H_2O gas is given by

$$\mathrm{d}\left(\frac{g_{H_2O}}{T}\right) = h_{H_2O}\mathrm{d}\left(\frac{1}{T}\right) + \frac{1}{T}\mathrm{d}h_{H_2O} - \mathrm{d}s_{H_2O} = h_{H_2O}\mathrm{d}\left(\frac{1}{T}\right) + R\mathrm{d}\ln P_{H_2O} \quad . \tag{1}$$

[13] Fisher and Zen (1971) also derived thermodynamic relations for this hypothetical reaction but through different approaches. They were more interested in calculation of the standard free energy of formation (at 298.15 K and 1 bar) of solid phases from hydrothermal equilibrium data.

The $R\mathrm{d}\ln P_{H_2O}$ term in equation (1) is from the ideal gas law and the total derivative of enthalpy. In a similar way, the total derivative of the molar Gibbs free energy of any pure solid phase is given by

$$\mathrm{d}(\frac{g_{solid}}{T}) = h_{solid}\mathrm{d}(\frac{1}{T}) + \frac{1}{T}\mathrm{d}h_{solid} - \mathrm{d}s_{solid} = h_{solid}\mathrm{d}(\frac{1}{T}) + \frac{v_{solid}}{T}\mathrm{d}P \quad . \tag{2}$$

As the Gibbs free energy of a reaction is zero at equilibrium T and P, one obtains

$$(\Delta G_r)_{T,P} = (\Delta G_{f,B})_{T,P} - (\Delta G_{f,A})_{T,P} + n(\Delta G_{f,H_2O})_{T,P} = 0 \quad , \tag{3a}$$

where $\Delta G_r =$ Gibbs free energy of reaction, $A_{(s)} \leftrightarrow B_{(s)} + nH_2O_{(g)}$, and

$\Delta G_{f,i} =$ Gibbs free energy of formation of pure substance i.

Expressed in terms of intensive properties, equation (3a) becomes

$$(\Delta g_r)_{T,P} = (\Delta g_{f,B})_{T,P} - (\Delta g_{f,A})_{T,P} + (\Delta g_{f,H_2O})_{T,P} = (\Delta g_{solid})_{T,P} + (g_{H_2O})_{T,P} \quad , \tag{3b}$$

where $\Delta g_r =$ molar Gibbs free energy of reaction (per molecule of H_2O),

$\Delta g_{solid} =$ molar Gibbs free energy change of reaction involving solid phases only (per molecule of H_2O), and

$g_{H_2O} =$ molar Gibbs free energy of H_2O.

In analogy with equation (3b), combining equations (1) and (2) gives

$$\mathrm{d}(\frac{\Delta g_r}{T}) = \mathrm{d}(\frac{\Delta g_{solid}}{T}) + \mathrm{d}(\frac{g_{H_2O}}{T}) = \Delta h_r \mathrm{d}(\frac{1}{T}) + \frac{\Delta v_{solid}}{T}\mathrm{d}P + R\mathrm{d}\ln P_{H_2O} \quad , \tag{4a}$$

where $\Delta h_r =$ molar enthalpy of reaction (per molecule of H_2O), and

$\Delta v_{solid} =$ molar volume change of reactants to products in solid phases only (per molecule of H_2O).

At equilibrium T, P, and P_{H_2O}, $\Delta g_r = 0$ and to maintain equilibrium $\mathrm{d}(\Delta g_r) = 0$. Hence, equation (4a) becomes

$$\frac{\mathrm{d}(\Delta g_r)}{T} + \Delta g_r \mathrm{d}(\frac{1}{T}) = 0 = \Delta h_r \mathrm{d}(\frac{1}{T}) + \frac{\Delta v_{solid}}{T}\mathrm{d}P + R\mathrm{d}\ln P_{H_2O} \quad . \tag{4b}$$

Rearranging (4b)

$$\frac{\mathrm{d}\ln P_{H_2O}}{\mathrm{d}(\frac{1}{T})} = -\frac{\Delta h_r}{R} - \frac{\Delta v_{solid}}{RT}\frac{\mathrm{d}P}{\mathrm{d}(\frac{1}{T})} \qquad \text{or}$$

$$\frac{\mathrm{d}\log P_{H_2O}}{\mathrm{d}(\frac{1}{T})} = -\frac{\Delta h_r}{2.303R} - \frac{\Delta v_{solid}}{2.303RT}\frac{\mathrm{d}P}{\mathrm{d}(\frac{1}{T})} \quad . \tag{4c}$$

Equation (4c) relates the sets of controllable quantities (i.e., P_{H_2O}, and T) to the other sets of measureable quantities (i.e., Δh_r, and Δv_{solid}), and it contains important information. For instance, if P is constant, equation (4c) reduces to the familiar van't Hoff equation

$$\left(\frac{\partial \log P_{H_2O}}{\partial(\frac{1}{T})}\right)_P = -\frac{\Delta h_r}{2.303R} \qquad \text{at any } T \text{ and constant } P. \tag{5}$$

Δh_r is a function of both T and P and will be equal to the usual molar standard enthalpy of reaction Δh_r^o only when P is equal to 1 bar and T is equal to 298.15 K. When P is fixed, a plot of ($\log P_{H_2O}$) vs. ($1/T$) will be a straight line only if the heat capacity of a reaction (ΔC_P) does not vary with temperature, i.e., $\Delta C_P = \left(\frac{\mathrm{d}(\Delta h_r)}{\mathrm{d}T}\right)_P$. The variation of ΔC_P with temperature is likely to be small within a few hundred degrees (usually amounts to only a few percent), and depending on the uncertainty of experimental results, changes in $\mathrm{d}(\Delta h_r)$

with temperature may or may not be observed from the equilibrium curve in the (log P_{H_2O}) vs. (1/T) plot.

Applying Maxwell's relation (i.e., the second derivatives with respective to P and *1/T*) to equation (4b) gives the cross differentiation identity

$$\frac{\mathrm{d}(\Delta h_r)}{\mathrm{d}P} = \frac{\mathrm{d}(\frac{\Delta v_{solid}}{T})}{\mathrm{d}(\frac{1}{T})} \quad . \tag{6a}$$

If the thermal expansion and the compressibility are known for all solids involved, the volume change with T and P may be evaluated precisely. When this is not the case, estimates based on refined unit-cell parameters using XRD data at room T or at the transition T can be used. Consider that the molar volume of each solid is a very slowly varying function of pressure (i.e., solids are rather incompressible) and the thermal expansion and the compressibility tend to cancel. Therefore, the volumes of solid phases on two sides of a reaction (i.e., Δv_{solid}) are nearly constant. Hence, Δv_{solid} is assumed to be independent of T and P and equation (6a) becomes

$$\mathrm{d}(\Delta h_r) \approx \Delta v_{solid}\mathrm{d}P \qquad \text{at any } T \text{ and } P. \tag{6b}$$

Integration from 1 bar to any P while keeping T constant gives

$$(\Delta h_r)_{T,P} \approx (\Delta h_r)_{T,1} + \Delta v_{solid}(P-1) \quad . \tag{6c}$$

The changes of Δh_r with T and P, therefore, can be approximately expressed as

$$(\Delta h_r)_{T,P} \approx (\Delta h_r^o)_{298.15,1} + \int_{298.15}^{T} \Delta C_P \mathrm{d}T + \Delta v_{solid}(P-1) \quad , \tag{7}$$

where the temperature integral is at P = 1 bar.

If P is not constant, the plot of (log P_{H_2O}) vs. (1/T) changes due to the $\frac{-\Delta v_{solid}}{2.303RT}\frac{dP}{d(\frac{1}{T})}$ correction term in equation (4c), which means that the effect of changing P from 1 bar while keeping T constant is to displace the point of log P_{H_2O} (i.e., equilibrium boundary) by $\sim\frac{-\Delta v_{solid}(P-1)}{2.303RT}$ amounts (Eugster and Wones 1962), i.e.,

$$(\log P_{H_2O})_P = (\log P_{H_2O})_1 - \frac{\Delta v_{solid}(P-1)}{2.303RT} \quad . \tag{8}$$

An equivalent way of stating this effect is that it changes the slope (or curvature) of the equilibrium boundary via $\sim\frac{-\Delta v_{solid}(P-1)}{2.303R}$ amounts. To illustrate how a change in P displaces and varies the slope (or curvature) of an equilibrium boundary, schematic diagrams of (log P_{H_2O}) vs. (1000/T) for two dummy reactions are shown in Figure 5.7. Solid straight lines in Figure 5.7 represent the isobaric equilibrium boundaries for a dummy dehydration reaction ($A_{(s)} \leftrightarrow B_{(s)} + H_2O_{(g)}$) under different P conditions (at $P = 10^{-4}$, 1, 2 and 3 bar). Similarly, dashed curved lines represent the isobaric equilibrium boundaries for another dummy dehydration reaction ($C_{(s)} \leftrightarrow D_{(s)} + H_2O_{(g)}$) under different P conditions (Fig. 5.7). The slope in the (log P_{H_2O}) vs. (1000/T) plot is the molar enthalpy of a reaction and is set to be larger for reaction A↔B ($\Delta h_{A\leftrightarrow B}$). The molar heat capacity for reaction A↔B ($\Delta C_{P,A\leftrightarrow B}$) is assumed to be constant (i.e., the change of $\Delta h_{A\leftrightarrow B}$ with temperature is constant). For both dehydration reactions, the molar volume change (Δv_{solid}) is set to be negative (e.g., most zeolites undergo dehydration-induced reductions in volume to accommodate the loss of H_2O), and three different quantities were assigned, i.e., Δv_{solid} = -100, -50, and -20 (cm^3/mole-H_2O). To convert the units of cm^3/mole-H_2O to kJ/bar/mole-H_2O the conversion 1

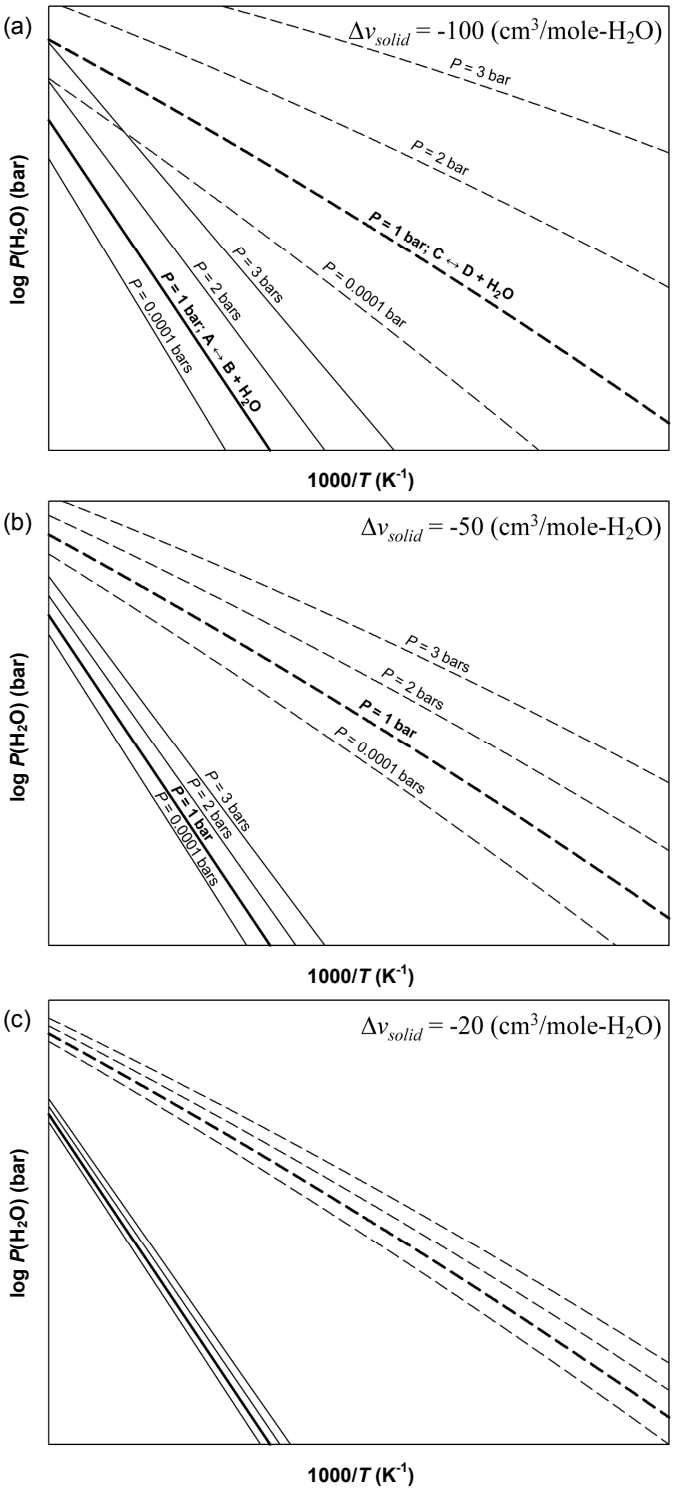

Figure 5.7. Schematic diagrams for two dummy dehydration reactions (A↔B: a set of solid lines; and C↔D: a set of dashed lines), illustrating the effects of changing total pressure (P) on the changes in the slope and position of the equilibrium boundary. In **(a)**, **(b)** and **(c)**, the molar volume change (Δv_{solid}) was set to -100, -50, and -20 cm^3/mole-H_2O (i.e., reduction in volume upon dehydration), respectively.

cm^3 = 0.1 kJ/bar was used. When Δv_{solid} is negative and large (e.g., Fig. 5.7a), equilibrium boundaries of A↔B and C↔D are displaced according to the signs of the $\Delta v_{solid}(P-1)$ term in equation (8). The amount of shifts relates not only to the absolute $\Delta v_{solid}(P-1)$ value but also depends on the Δh_r value. The effect of changing *P* has a greater influence for a reaction having a small Δh_r value (Fig. 5.7a). Note that each individual boundary in Figure 5.7a has its own slope (or curvature). Furthermore, the maximum amount of displacements for *P* <<1 bar is limited to the value of $\sim\frac{\Delta v_{solid}}{2.303RT}$, and in principle, there are no limits for *P* above 1 bar. Similar trends are seen in Figures 5.7b and c where the Δv_{solid} values are relatively small. Hence, the $\frac{-\Delta v_{solid}(P-1)}{2.303RT}$ correction term in equation (8) or the $\frac{\Delta v_{solid}}{T}\mathrm{d}P$ term in equation (4b) is not negligible even for a small change in Δv_{solid}, particularly at high pressures, although the effect will be almost negligible below two or three hundred bars (similar discussions are also emphasized by Orville and Greenwood 1965).

5.2.3 Thermodynamic treatments for hysteretic and/or irreversible processes

In reality, no macroscopic process is perfectly reversible. When a reaction and/or a transformation occurs as a result of temperature excursions, the observed macroscopic changes do not occur at the thermodynamically defined equilibrium *T*, because at equilibrium *T* the free energy is the same on either sides of the equilibrium boundary. Only when there is a reduction in free energy will there be a driving force to drive the transitions. Therefore, some degree of hysteresis on the heating and cooling path will be observed (i.e., superheating, undercooling, and exhibit of metastability will be required), and the amount of hysteresis (or irreversibility) depends on the nature of transitions in the system. Because a

perfectly reversible path never exists, equilibrium conditions are frequently obtained within a small area of a hysteresis loop or within the limits of experimental precisions. However, if hysteresis far exceeds the experimental precisions, irreversible thermodynamics must be considered for entropy production that occurs during the irreversible process. From the second law of thermodynamics, Prigogine (1961) rewrote the Clausius inequality for the change in entropy ($\mathrm{d}S$) during any transformations as a sum of two parts:

$$\mathrm{d}S = \mathrm{d}S_e + \delta S_i \quad . \tag{9a}$$

Here $\mathrm{d}S_e$ arises from the exchange of entropy (due to exchange of energy and matter) between the system (e.g., zeolite) and its exterior. δS_i is entropy created within the system due only to irreversible (non-equilibrium) processes, and it is always greater than zero during such processes and equal to zero at equilibrium. The symbol δ is used to express the infinitesimal entropy production along the path of transformation, and the variation of δS_i depends on the path (i.e., similar to the heat (Q) and work (W) in the first law of thermodynamics). The advantage of describing irreversibility in terms of δS_i rather than by the entropy change of the exterior (or more generally the 'universe") is that with this treatment the origin of the irreversibility is clearly identified within the system. In practice, the thermodynamic system for dehydration and/or rehydration of a zeolite consists of two open sub-systems, the zeolite and its exterior. The state of the exterior is considered so large that its T, P, and $P_{\mathrm{H_2O}}$ do not change noticeably when heat and matter enter or leave. Entropy production, δS_i, within a zeolite is related to two different types of irreversible paths, chemical (δS_{ch}) and non-chemical (δS_{nch}) reactions. Entropy production of the chemical type

is related to the rate differences between H_2O sorption and desorption and it can be expressed as

$$\delta S_{ch} = -(\frac{\mu_{H_2O}^{zeolite}}{T_{zeolite}} - \frac{\mu_{H_2O}^{exterior}}{T_{exterior}})\mathrm{d}n_{H_2O} = -\Delta(\frac{\mu_{H_2O}}{T})\mathrm{d}n_{H_2O} \quad . \tag{9b}$$

Entropy production of the non-chemical type is from irreversible aluminosilicate framework modifications and can be expressed as

$$\delta S_{nch} = \frac{\delta Q_{nch}^{zeolite}}{T_{zeolite}} + \frac{\delta W_{nch.fr}^{zeolite}}{T_{zeolite}} \quad , \tag{9c}$$

where $\frac{\delta Q_{nch}^{zeolite}}{T_{zeolite}}$ is the entropy production accounting for internal work as an irreversible heat, such as the energy loss as acoustic waves. $\frac{\delta W_{nch.fr}^{zeolite}}{T_{zeolite}}$ is an irreversible frictional energy accounting for energy forms other than heat. One can think of this second term as related to several frictional works during the transformation, including the creation of defects, the formation of strain-induced mosaicity, and the breakdown of the initial crystallites into smaller sizes. The so-called "uncompensated heat" as introduced by Clausius (1865) is obtained when δS_i is multiplied by the transformation temperature *T*, i.e.,

$$T\delta S_i = T(\delta S_{ch} + \delta S_{nch}) = \delta Q_i \quad . \tag{9d}$$

This "uncompensated heat (δQ_i)" is a virtual heat (i.e., contains both heat and work forms) reflecting entropy production from irreversible changes in a zeolite during its transformation. Now the fundamental thermodynamic equations become

$$\mathrm{d}H^{\dagger} = (\mathrm{d}H + \mathrm{d}E_s + \delta Q_i) = T\mathrm{d}S + V\mathrm{d}P \qquad \text{and} \tag{10a}$$

$$(\mathrm{d}G + \mathrm{d}E_s + \delta Q_i) = -S\mathrm{d}T + V\mathrm{d}P \quad . \tag{10b}$$

Equations (10a) and (10b) are from the combination of the first and second laws of thermodynamics. Strain energy term ($\mathrm{d}E_s$) is added to the derivation to account for lattice distortive strains, including interfacial energy (i.e., the energy due to creation of interface between the parent and the daughter phases) and elastic stored energy (i.e., the energy necessary to accommodate residual strains stored within and between tetrahedral frameworks). Strains are commonly seen in framework silicates and they result from changes in atom positions, bond angles, and symmetry of the original parent structure during transformations. In addition, the strain energy term should be, in a sense, counter balanced by the frictional energy term. For instance, if the initial crystallites did not break down upon dehydration, the interfacial energy between the parent and the daughter phases will accumulate. From equation (10b), one can deduce that at constant T and P, the driving force is determined by

$$\mathrm{d}G = -\mathrm{d}E_s - \delta Q_i \qquad \text{where } \delta Q_i \geq 0 . \tag{10c}$$

Applying the above concepts into the derivation of equation (4a) and expressed in terms of molar quantity, equation (4a) can be rewritten to a suitable equation for a hysteretic system, i.e.,

$$\mathrm{d}\left(\frac{\Delta g_r + \Delta e_s + q_i}{T}\right) = (\Delta h_r^{\dagger})\mathrm{d}\left(\frac{1}{T}\right) + \frac{\Delta v_{solid}}{T}\mathrm{d}P + R\mathrm{d}\ln P_{H_2O} \quad . \tag{10d}$$

The $\mathrm{d}H^{\dagger}$ term in equation (10a) is called the *apparent* enthalpy for a fundamental thermodynamic relation and was first introduced by Everett and Whitton (1955) for their study of the adsorption of benzene vapor by active charcoals. The $\Delta h_r^{\dagger}$ term in equation (10d) is the corresponding result of the *apparent* molar enthalpy for a reaction that exhibits a hysteresis. $\Delta h_r^{\dagger}$ contains a contribution from the theoretical enthalpy change of a reversible

reaction including a strain energy contribution ($\Delta h_r + \Delta e_s$) and the "uncompensated heat (q_i)" arising from irreversible processes, i.e.,

$$\Delta h_r^{\dagger} = (\Delta h_r + \Delta e_s) + q_i \quad . \tag{10e}$$

In light of equation (10d), a delicate energy balance among the reaction free energy change (Δg_r), the accumulation or release of strain energy (Δe_s), and the magnitude of "uncompensated heat (q_i)" is established. One can image that as a transition proceeds, the strain energy and the "uncompensated heat" will introduce variations to the free energy change, which make the system behave as if it has a rugged free energy landscape. Under the influence of driving forces (e.g., T, P, and P_{H_2O} in this study), the system will pass from one relative minimum to another and give a sequence of metastability until the absolute minimum is approached. Therefore, different structures and transition paths may be observed depending on the external driving variables. In NAT-type zeolites, the behavior of structural phase transitions showed strong temperature- and P_{H_2O}-dependence.

According to equation (10d), when using the van't Hoff-type operation (e.g., equations (4c) and (5)) to compute enthalpy changes with data from either the forward (dehydration) or reverse (rehydration) branches of a hysteresis loop, the computed thermal results contain the contributions of strain energy and "uncompensated heat". Because the "uncompensated heat" and strain energy may or may not be detected from the heat changes in the surroundings, their magnitude cannot be evaluated exactly without knowledge of the position of equilibrium pathways within the area enclosed by a hysteresis loop (i.e., a Carnot-like cycle can be imagined to be connected to the system showing hysteresis). Hence, assumptions of equilibrium conditions must be made. Such assumptions necessarily cause problems because the thermal results are biased by the assumptions; this issue has been

discussed by La Mer (1967) and Adamson (1963). For instance, the equilibrium pathway is commonly assumed to lie half way between the forward and reverse branches for martensitic transformations (e.g., Planes *et al.* 1988; Flanagan *et. al.* 1995; Palumbo 2008). Occasionally, use of just one branch of the hysteresis loop has been considered (e.g., Ehrlich and Bettelheim 1963; van Olphen 1965), and comparisons between the determined *apparent* thermal results and the results from independent calorimetric measurements are usually made to justify the equilibrium assumptions. No matter what assumptions are made, the *apparent* thermodynamic quantities, such as enthalpy, have no practical meaning without assumed equilibrium criteria and may only serve as approximations to the true equilibrium functions of state.

5.3 Examples

Up to this point, the thermodynamic formulations suitable for computing the heat evolved during dehydration and rehydration in NAT-type zeolites have been described.The situation becomes difficult because different contributions to the free energy change inside the "uncompensated heat" and strain energy terms are still not well defined, but their roles have been discussed. In the following three examples, the van't Hoff-type reaction phase diagram using data obtained from the XRD measurements (where *T, P*, and P_{H_2O} were better controlled) is presented. Through the construction of quasistatic reaction phase diagrams in which data are plotted as (log P_{H_2O}) vs. (1000/*T*) at *P* = 1 bar, the *apparent* enthalpy of dehydration ($\Delta h^{\dagger}_{dehy}$) and/or rehydration ($\Delta h^{\dagger}_{rehy}$) can be extracted graphically from the best fit of available data by a least-squares method. On some occasions, roughing pump vacuum (*P* = $10^{-3.8}$ bar) was applied to the system in order to extend the range of P_{H_2O} down to ~10^{-4}-10^{-6}

bar. In this case, the $\Delta h^{\dagger}_{dehy}$ and/or $\Delta h^{\dagger}_{rehy}$ values were affected by P through the $\Delta v_{solid}(P-1)$ correction term as discussed earlier.

5.3.1 P_{H_2O}-T reaction phase diagram during natrolite dehydration and rehydration

The P_{H_2O} and T conditions in which dehydration and rehydration occur in natrolite were determined from sudden peak shifts in the temperature-resolved XRD patterns. Consideration of these data yielded a number of P_{H_2O}-T pairs (with error bars) presented in Figure 5.8a, as (log P_{H_2O}) vs. (1000/T). All data were obtained at P = 1 bar except for the last data point at the bottom of the plot where the reaction temperatures were determined under P = $10^{-3.8}$ bar and P_{H_2O} = ~10^{-4}-10^{-6} bar conditions (Fig. 5.8a). van Reeuwijk's data (1974) are also included (circle symbols) in the plot. van Reeuwijk's measurements focused mainly on the high-P_{H_2O} range under P = 1 bar conditions and were based on results of the differential thermal analysis (DTA) inhibited diffusion method under a range of sub-ambient to 1 bar P_{H_2O} conditions. As his dehydration data are based on the DTA onset temperature, they differ by a small amount from the actual phase transition temperatures, as discussed by van Reeuwijk (1974).

Two distinct P_{H_2O}-dependent phase transitions were observed during the process of natrolite dehydration, namely, the transformation of natrolite-to-α1-metanatrolite and the transformation of natrolite-to-α1/α2-metanatrolite. In theory, the trace (i.e., $\Delta h^{\dagger}_{dehy}$) of dehydration data in the P_{H_2O}-T plot should change as low-P_{H_2O} conditions were approached, in a manner reflecting the finite difference in the lattice distortion, frictional work, and stored stain energy during and between the formation of these two anhydrous polymorphs. Unfortunately, the uncertainty in P_{H_2O} increases as P_{H_2O} goes to its lower limits. With the

current experimental precisions, there was no obvious variation in the $\Delta h^{\dagger}_{dehy}$ for these two P_{H_2O}-dependent transformations. A linear regression fit was applied to the P_{H_2O}-T pairs obtained at P = 1 bar and was extrapolated to the ~10^{-4}-10^{-6} bar P_{H_2O} region. The $\Delta h^{\dagger}_{dehy}$ value is 105.6 ± 5.5 kJ/mole-H_2O as obtained from the slope of the regression line. Correction for $\Delta h^{\dagger}_{dehy}$ when $P = 10^{-3.8}$ bar should also be considered for the molar volume change of the natrolite-to-α1/α2-metanatrolite reaction. The molar volumes of natrolite (Δv_{nat} = 84.33), α1-metanatrolite ($\Delta v_{\alpha 1}$ = 65.99) and α2-metanatrolite ($\Delta v_{\alpha 2}$ = 76.54) were determined from refined unit-cell parameters using XRD data measured at room T or at the transition T, and these values were converted to a per molecule of H_2O basis (cm^3/mole-H_2O). The molar volume change of the natrolite-to-α1-metanatrolite reaction is thus $\Delta v_{nat \rightarrow \alpha 1}$ = -18.34 (cm^3/mole-H_2O) = -1.834 (kJ/bar/mole-H_2O), and the molar volume change for the natrolite-to-α2-metanatrolite reaction is $\Delta v_{nat \rightarrow \alpha 2}$ = -7.79 (cm^3/mole-H_2O) = -0.779 (kJ/bar/mole-H_2O). Hence, the molar volume change for the natrolite-to-α1/α2-metanatrolite reaction ($\Delta v_{nat \rightarrow \alpha 1/\alpha 2}$) is between these two volume change limits, and the actual value depends on the proportions of α1- and α2-metanatrolite formed during dehydration. Therefore, the maximum and minimum changes in $\Delta h^{\dagger}_{dehy}$ with P (when $P = 10^{-3.8}$ bar) are ~1.834 and ~0.779 kJ/mole-H_2O, which are within error of the regression line.

Transformation during rehydration involves a reaction directly from α1-metanatrolite-to-natrolite, because α2-metanatrolite is a metastable phase and it further transformed to α1-metanatrolite at temperatures above 350 ºC during heating. The effect of hysteresis can be seen in Figure 5.8b, where slightly different slopes of the van't Hoff plots were found from

data obtained during dehydration and rehydration. The $\Delta h^{\dagger}_{rehy}$ value is -88.9 ± 4.5 kJ/mole-H_2O determined from the slope of the linear regression line using only P_{H_2O}-T pairs obtained at P = 1 bar. As discussed above, correction for $\Delta h^{\dagger}_{rehy}$ when $P = 10^{-3.8}$ bar was still within error of the regression line. The gap between these two regression lines during dehydration and rehydration is the "uncompensated heat" due to hysteresis, and the amount of the "uncompensated heat" can be approximately computed in two ways. One is from the difference in temperature at a given P_{H_2O} condition (equation 11a) and another is from the difference in P_{H_2O} at a given temperature (equation 11b). Assume that after a complete heating/cooling cycle, the hydration state and the framework of natrolite perfectly return to their initial states and that no frictional works and/or strain-induced mosaicity remained in the structure. This assumption is necessary due to the fact that, after a complete cycle, the system has come back to the same thermodynamic state from which the cycle started, and hence all state functions return to their original value. From equation (10d), one obtains

$$\mathrm{d}(\frac{q_i}{T}) = (\Delta h_r{}^{\dagger})\mathrm{d}(\frac{1}{T}) \qquad \text{at a given } P_{H_2O} \text{ (after a complete cycle with fixed } P\text{),} \tag{11a}$$

and

$$\mathrm{d}(\frac{q_i}{T}) = R\mathrm{d}\ln P_{H_2O} \qquad \text{at a given } T \text{ (after a complete cycle with fixed } P\text{).} \tag{11b}$$

Integrating and rearranging above equations, (11a) and (11b) become

$$q_i = \oint \delta q_i = \oint (\Delta h_r{}^{\dagger} - q_i) T\mathrm{d}(\frac{1}{T}) \approx |\Delta h_r| \frac{|\Delta T|}{T_{eq}} \qquad \text{and} \tag{11c}$$

$$q_i = \oint \delta q_i = RT \ln(\frac{P_{H_2O;rehy}}{P_{H_2O;dehy}}) \quad , \tag{11d}$$

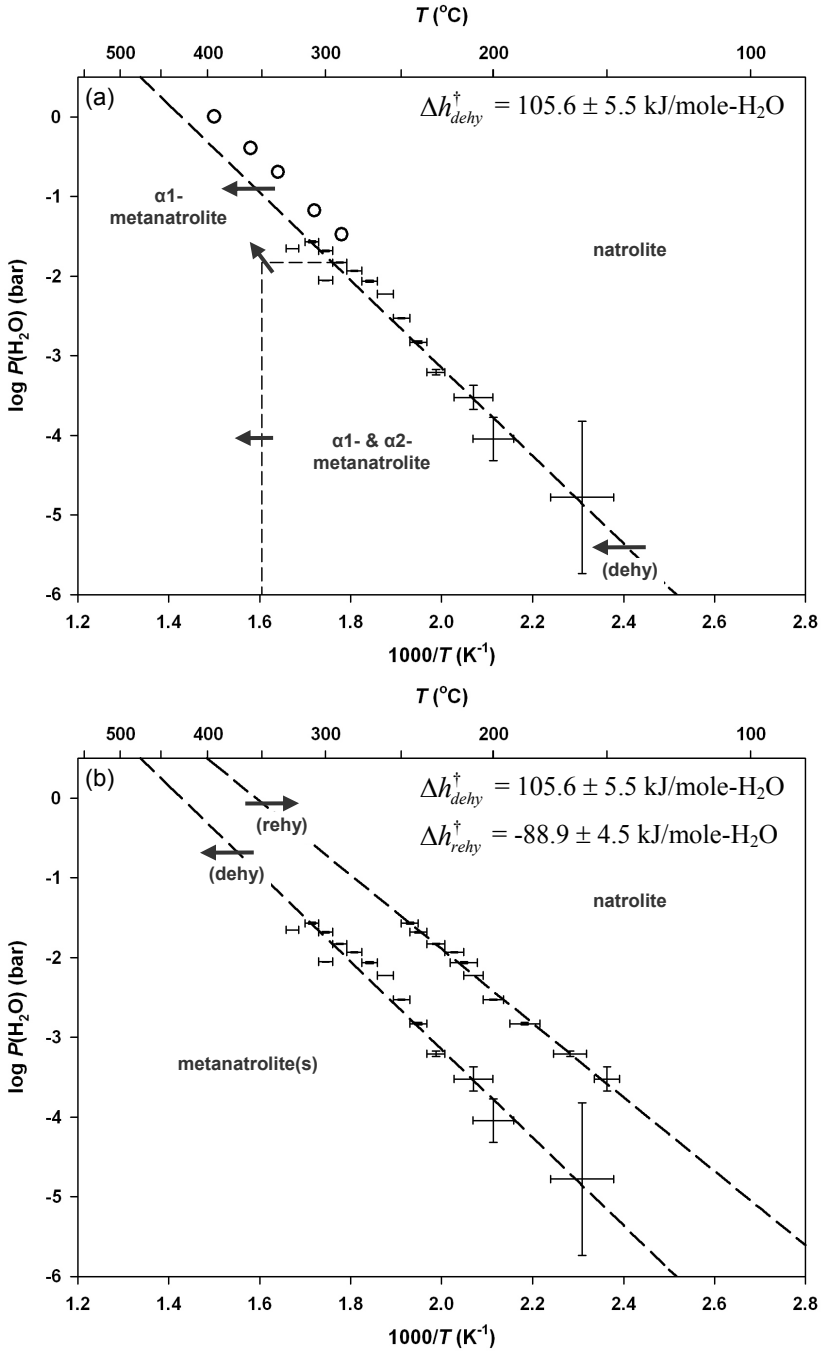

Figure 5.8. P_{H_2O}-T reaction phase diagram during natrolite dehydration and rehydration. Temperature errors are in units of 1000/T and P_{H_2O} errors are in log units. The dashed line represents the best fit using all available data points, excluding van Reeuwijk (1974)'s data (circle symbols) and the last data point where the uncertainty of P_{H_2O} is large. In **(a)**, the horizontal and vertical dashed lines outline the maximum P_{H_2O} and T conditions where α2-metanatrolite exists and irreversibly transforms to α1-metanatrolite. In **(b)**, thermal hysteresis during natrolite dehydration and rehydration is illustrated. Arrows in both diagrams indicate the direction of reaction.

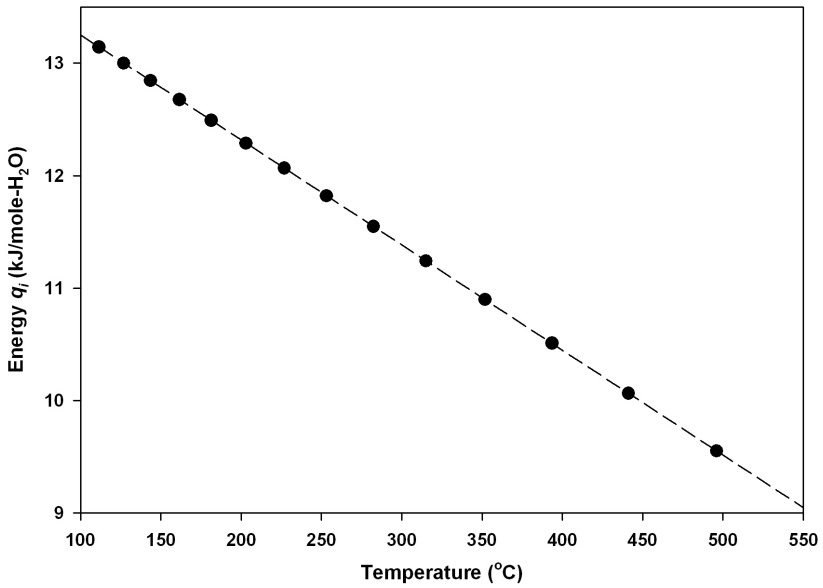

Figure 5.9. The associated evolution of uncompensated energy as a function of temperature (black circles) obtained from Figure 5.8b. Higher-temperature data on this figure were obtained from reactions occurring under higher-P_{H_2O} conditions.

where Δh_r is the enthalpy change for a transition unaffected by hysteresis and any possible strains, and $T_{eq} \approx \sqrt{T_{dehy} T_{rehy}}$. It is apparent that equation (11d) is easier to calculate than (11c) because Δh_r and T_{eq} are not known very accurately. Calculation of q_i at a given T via the equation (11d) is illustrated in Figure 5.9. The amount of "uncompensated heat (q_i)" determined during natrolite dehydration and rehydration ranges from 9 to 13 kJ/mole-H_2O. The amount of q_i decreases as environments move from low- to high-P_{H_2O}.

5.3.2 P_{H_2O}-T reaction phase diagram during scolecite dehydration

In the study of scolecite, only the determinations of *apparent* enthalpies during dehydration ($\Delta h^{\dagger}_{dehy}$) are shown for the two steps of the dehydration reactions (Fig. 5.10). Analyses followed the same procedures as in natrolite. The first dehydration step in scolecite is the low-temperature scolecite-to-metascolecite transition, and the determined $\Delta h^{\dagger}_{dehy(1)}$ for this reaction is 97.6 ± 3.3 kJ/mole-H_2O. The molar volume change of the scolecite-to-metascolecite transition is $\Delta v_{sco \rightarrow metasco}$ = -3.75 (cm^3/mole-H_2O) = -0.375 (kJ/bar/mole-H_2O). Thus, correction for $\Delta h^{\dagger}_{dehy(1)}$ when $P = 10^{-3.8}$ bar is a very small quantity (i.e., ~0.375 kJ/mole-H_2O) and is within the data error. The second dehydration step, the high-temperature phase transition, shows two distinct P_{H_2O}-dependent transitions paths. One is the transformation from metascolecite to the amorphous T_5O_{10} phase and the other is the transformation from metascolecite to x2-metascolecite. Similar to natrolite, no observe apparent changes in the trace of dehydration data for these two P_{H_2O}-dependent transformations were observed, due mainly to the large P_{H_2O} errors in the low-P_{H_2O} region (Fig. 5.10). The obtained $\Delta h^{\dagger}_{dehy(2)}$ for this second high-temperature dehydration reaction is

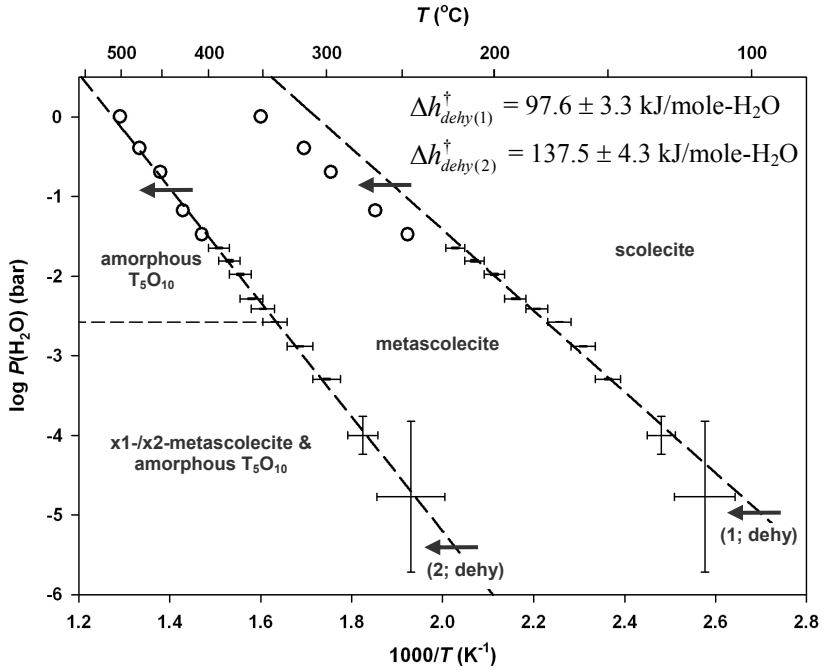

Figure 5.10. P_{H_2O}-T reaction phase diagram during scolecite dehydration only. Temperature errors are in units of 1000/T and P_{H_2O} errors are in log units. The dashed line represents the best fit using all available data points, excluding van Reeuwijk (1974)'s data (circle symbols) and the two last data points where the uncertainty of P_{H_2O} is large. The horizontal dashed lines outline the maximum P_{H_2O} conditions where x1- and x2-metascolecite phases exist. Arrows in the diagrams indicate the direction of reaction.

137.5 ± 4.3 kJ/mole-H_2O. The molar volume change for the metascolecite-to-x2-metascolecite reaction is $\Delta v_{metasco \rightarrow x2}$ = -10.49 (cm^3/mole-H_2O) = -1.049 (kJ/bar/mole-H_2O). Correction for $\Delta h^{\dagger}_{dehy(2)}$ when $P = 10^{-3.8}$ bar was ~1.049 kJ/mole-H_2O and was still smaller than the experimental errors. Strictly speaking, there is a third dehydration reaction under low-P_{H_2O} conditions, i.e., the transformation from x2-metascolecite to x1-metascolecite/amorphous T_5O_{10} phase. The *apparent* enthalpy of this third dehydration reaction was not determined due to the limited amount of data available in the low-P_{H_2O} region.

5.3.3 P_{H_2O}-T reaction phase diagram during mesolite dehydration

Dehydration of mesolite occurred in two main steps, the first of which is the low-temperature extraframework cation order-disorder phase transition, and $\Delta h^{\dagger}_{dehy(1)}$ for this reaction is 87.2 ± 4.1 kJ/mole-H_2O (Fig. 5.11). The second step of dehydration shows two different phase transition paths depending on P_{H_2O}, namely the transformation to amorphous T_5O_{10} and the transformation to x-metamesolite/amorphous T_5O_{10}. There were no noticeable changes in the trace of dehydration data for these two P_{H_2O}-dependent transformations. The $\Delta h^{\dagger}_{dehy(2)}$ for the second step of dehydration is 120.4 ± 4.7 kJ/mole-H_2O (Fig. 5.11). The molar volume change for the mesolite-to-Na/Ca-disordered metamesolite reaction is $\Delta v_{mes \rightarrow dis.metames}$ = -1.09 (cm^3/mole-H_2O) = -0.109 (kJ/bar/mole-H_2O), and the volume change for the Na/Ca-disordered metamesolite-to-x-metamesolite reaction is $\Delta v_{dis.metames \rightarrow x}$ = -13.87 (cm^3/mole-H_2O) = -1.387 (kJ/bar/mole-H_2O). The molar volume change for transformation to the amorphous T_5O_{10} phase was indeterminate. Corrections for $\Delta h^{\dagger}_{dehy(1)}$ and $\Delta h^{\dagger}_{dehy(2)}$ when

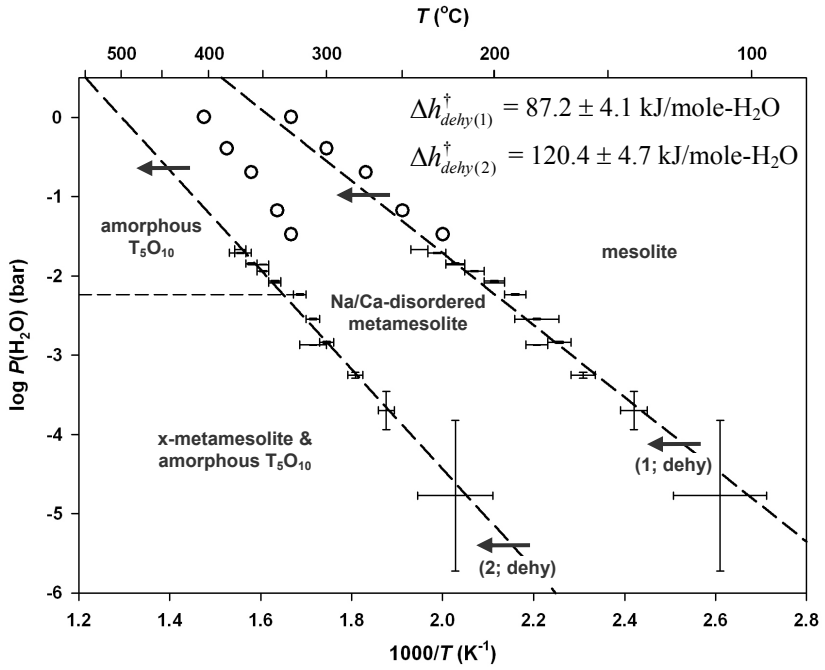

Figure 5.11. P_{H_2O}-T reaction phase diagram during mesolite dehydration only. Temperature errors are in units of 1000/T and P_{H_2O} errors are in log units. The dashed line represents the best fit using all available data points, excluding van Reeuwijk (1974)'s data (circle symbols) and the two last data points where the uncertainty of P_{H_2O} is large. The horizontal dashed lines outline the maximum P_{H_2O} conditions where the x-metamesolite phase exists. Arrows in the diagrams indicate the direction of reaction.

$P = 10^{-3.8}$ bar were within the data error for the first dehydration reaction and should also be within error of the regression line for the second dehydration reaction.

5.3.4 Summary of thermodynamic results for natrolite, scolecite, and mesolite

All of the determined *apparent* enthalpies of dehydration ($\Delta h^{\dagger}_{dehy}$) in NAT-type zeolites agree within error with those of van Reeuwijk's data (1974). Several other calorimetric measurements for studies of rehydration in natrolite (e.g., Guliev *et al.* 1989a; Kiseleva *et al.* 1997; Neuhoff and Wang 2007) also showed small to negligible inconsistencies between the measured enthalpies and the *apparent* enthalpies determined in this study. However, larger inconsistencies were found for scolecite and mesolite (e.g., Guliev *et al.* 1989a, 1989b). These discrepancies result from only a few studies made previously, and may also be attributed, in part, to different reference conditions for defining the amount of H_2O in the sample before, during, and after experiments. Direct knowledge of the sample hydration/dehydration states and the advancement of a reaction during a change in temperature or P_{H_2O} is usually not available for many calorimetric measurements. Such information is an inherent criterion in any thermodynamic analysis, because the extent of a reaction governs the integral results. Sample dehydration states are typically assumed based on other experimental results (e.g., XRD and TG), and often fully hydrated or dehydrated states are assumed at the end of an experiment. This may be erroneous, especially for slowly reacting systems or for system existing in multiple hydration/dehydration stages (e.g., scolecite and mesolite). The single-step hydration/dehydration behavior in natrolite is the simplest, whereas scolecite and mesolite have more complex behaviors that added additional complexity in predicting accurate hydration/dehydration states. Furthermore, hysteresis, the potential for irreversible changes in the zeolite structure, and the P_{H_2O}-dependent reaction

behaviors found in this study further complicate the picture provided by calorimetrically measured thermodynamic data. Although extraction of thermodynamic data from a reaction phase diagram is not a direct measurement of the enthalpy of a reaction, the obtained thermal results are better defined in terms of the transition temperatures (which are influenced by P_{H_2O} conditions), the hydration/dehydration states, any irreversible changes in the structure, and sample hysteretic behaviors.

The summary of *apparent* enthalpy of dehydration data in Table 5-1 shows that at the same Al:H_2O ratio (i.e., 1:1), the $\Delta h^{\dagger}_{dehy}$ becomes more endothermic in the order of increasing hydration energy of extraframework cations (i.e., $Ca^{2+} > Ca^{2+}/Na^{+} > Na^{+}$). This general relation has been observed by Carey and Navrotsky (1992) and discussed later by Bish and Carey (2001) for several other cation-exchanged zeolites (e.g., clinoptilolite, chabazite, mordenite, laumontite, and synthetic zeolites). However, in NAT-type zeolites, the value of $\Delta h^{\dagger}_{dehy}$ does not correlate only with guest cation type and the ratio of the framework charge to the number of H_2O molecules. It also relates to the local hydrogen bonding configurations. For instance, the first dehydration step in mesolite and scolecite is easier (smaller $\Delta h^{\dagger}_{dehy}$) because the H_2O molecules that leave the structure have longer hydrogen bonds resulting from the smaller (Ow-H···O) angles in their bonding configurations (see discussions in the section 4.1.2). The distortion of the framework and decrease in the unit-cell volume after the first dehydration further alter the bond strength and configuration of remaining H_2O molecules, which also plays a part in the increase of $\Delta h^{\dagger}_{dehy}$ during the second dehydration step in mesolite and scolecite. Among the three NAT-type zeolites, affinities for H_2O are associated with local H_2O bonding configuration, the Al:H_2O ratio, and type of extraframework cations. Generally speaking, the enthalpy of dehydration reflects the amount

Table 5-1. *Apparent* enthalpy of dehydration ($\Delta h^{\dagger}_{dehy}$) of NAT-type zeolites

Reaction[1]	$\Delta h^{\dagger}_{dehy}$ **(kJ/mole-H_2O)**[2]	**Al:H_2O ratio in the parent phase**
Natrolite* dehydration		
$Na_2Al_2Si_3O_{10} \bullet 2H_2O \rightarrow Na_2Al_2Si_3O_{10} + 2H_2O_{(g)}$	105.6 ± 5.5**	1:1
Scolecite* dehydration		
the first step		
$CaAl_2Si_3O_{10} \bullet 3H_2O \rightarrow CaAl_2Si_3O_{10} \bullet 2H_2O + H_2O_{(g)}$	97.6 ± 3.3	2:3
the second step (n <1.5; estimated based on TG curve)		
$CaAl_2Si_3O_{10} \bullet 2H_2O \rightarrow CaAl_2Si_3O_{10} \bullet (2-n)H_2O + nH_2O_{(g)}$	137.5 ± 4.3	1:1
Mesolite* dehydration		
the first step		
$Na_2Ca_2Al_6Si_9O_{30} \bullet 8H_2O \rightarrow Na_2Ca_2Al_6Si_9O_{30} \bullet 6H_2O + 2H_2O_{(g)}$	87.2 ± 4.1	3:4
the second step		
$Na_2Ca_2Al_6Si_9O_{30} \bullet 6H_2O \rightarrow Na_2Ca_2Al_6Si_9O_{30} + 6H_2O_{(g)}$	120.4 ± 4.7	1:1

[1] The formation of relic-OH groups is not included in the expressions.
[2] The *T* and *P* conditions valid for $\Delta h^{\dagger}_{dehy}$ values are from ambient *T* to < ~500 ºC and from *P* ~$10^{-3.8}$ to 1 bar.

* The measured crystal chemistry for natrolite, scolecite and mesolite samples are $Na_{1.84}Al_{1.94}Si_{3.10}O_{10} \bullet 2.04H_2O$ (Z = 8), $Ca_{0.98}Al_{1.95}Si_{3.04}O_{10} \bullet 3.06H_2O$ (Z = 4 or 8) and $Na_{1.97}Ca_{2.02}Al_{6.04}Si_{8.97}O_{30} \bullet 7.94H_2O$ (Z =8), respectively.
** The *apparent* enthalpy of rehydration ($\Delta h^{\dagger}_{rehy}$) in natrolite is -88.9 ± 4.5 (kJ/mole-H_2O).

of H_2O lost for a given change in temperature. Bish and Carey (2001) mentioned that zeolites with high enthalpy of dehydration dehydrate over narrow temperature intervals, and this phenomenon can be qualitatively seen the slope of the TG weight loss curve. The first weight loss in scolecite and mesolite has a more gradual slope than its second weight loss curve. Furthermore, in comparison with a smooth TG weight loss curve, such as those exhibited by clinoptilolite, chabazite and mordenite, a smaller enthalpy of dehydration was found (Bish and Carey 2001), indicating that clinoptilolite, chabazite, and mordenite retain their H_2O molecules less effectively than do natrolite, scolecite and mesolite.

The amount of "uncompensated heat (q_i)" determined in natrolite gives an approximate idea of the order of entropy production in mesolite and scolecite (after a complete transformation cycle). The entropy production is contributed, in part, by the lattice volume changes accompanying the dehydration/rehydration reaction. Hence, the first dehydration step in mesolite and scolecite should have a smaller amount of "uncompensated heat" than that in natrolite due to their smaller volume changes upon the first dehydration. A small area of hysteresis loop in the corresponding TG experiments (curves e-f in Fig. 5.3 and curves f-g in Fig. 5.5) also indicated that upon first dehydration, mesolite and scolecite should have smaller degrees of entropy production. The second dehydration step in mesolite and scolecite is, however, opposite, and it should give a larger amount of "uncompensated heat" consistent with the opened hysteresis loop observed in the TG experiments.

5.4. Chapter summary

A study of thermodynamics of dehydration and rehydration reactions in NAT-type zeolites must consider a number of important characteristic features such as: (i) the structural

phase transformations associated with dehydration and rehydration reactions and their temperature- and P_{H_2O}-dependent behaviors; (ii) interfacial and strain energy contributions to the accommodation of hydrous/anhydrous phase domains and induced elastic strains within and between tetrahedral frameworks during transformations; (iii) the difference in the rate of H_2O diffusion in open vs. distorted frameworks; and (iv) the irreversible processes important for understanding the hysteresis cycle. The primary difficulty in dealing with these contributions to the free energy change is their heterogeneous characters, and the situation is even more complex for a hysteric system because the precise operative mechanisms in these zeolites are still not well understood. The method used to determine the amount of "uncompensated heat (q_i)" in natrolite provides qualitative information about the order of "uncompensated heat" during the cyclic transformations in scolecite and mesolite. Together with contributions from the enthalpy changes (Δh_r; unaffected by hysteresis), the "uncompensated heat (q_i)" and the reversible elastic strain energy (Δe_s) contribute to the heats evolved during the chemical dehydration/rehydration reactions and to the accompanying non-chemical structural transformations. Quantities such as q_i, Δe_s, and even the energy contribution of the molar volume changes, i.e. $\Delta v_{solid}(P-1)$, are negligibly small (should be no more than a few hundred J/mole-H_2O) in comparison with the "chemical bond energy Δh_r" (about a few hundred kJ/mole-H_2O). This somewhat justifies the usual procedure of measuring the calorimetric heat no matter whether or not one is aware of the existence of hysteresis and the presence of temperature- and P_{H_2O}-dependent variations in structural transformations.

CHAPTER 6

Conclusions

Nanoporous solids, particularly zeolites, are important in a variety of natural and industrial settings due to their unique chemical and structural properties. The wide variety of applications for natural and synthetic zeolites depends largely on their open frameworks, which provide internal flexibility to interact with a variety of guest cations and molecules. In geology, natural zeolites are of interest due to their high molar volumes, open crystal structures, and high H_2O contents (>10 wt.% H_2O), which make them important in low-temperature geological systems. Additionally, these properties make zeolites stable only at low temperatures, pressures, and in water-saturated environments (which has led to the recognition of the so-called zeolite facies by geologists). Many zeolites exhibit a range of compositions with respect to both their aluminosilicate frameworks (host) and to their non-framework cations and H_2O molecules (guests). In addition, many framework configurations can occur, and these play important roles not only in defining the structural symmetry but also in determining physical and chemical properties. In many industrial applications, zeolites must be activated by heating. This involves dehydration of the minerals and consequently often causes drastic changes (either reversible or irreversible) in the host structures. Hence, the knowledge of the thermal properties of zeolites is crucial and this aspect has been studied for many years. However, studies of zeolite structural behaviors, particularly under carefully controlled humidity conditions (*RH*; also known as partial pressure of water, P_{H_2O}), have only recently begun in the scientific community. Investigations of the combined temperature and P_{H_2O} (or *RH*) effects on zeolite dehydration and

accompanying structural displacive phase transitions[14] are still not well understood. An interesting question, which is the primary focus of this research, is whether displacive processes (constrained by symmetry) in the host structure of zeolites interact with host-guest interactions. If so, it should be possible to determine under what environmental conditions (i.e., temperature, P_{H_2O}, and guest composition) the symmetry-constrained force fields can defy the predicted host-guest interactions and, hence, vary structural phase transition phenomena. The answer to this question is important because these structural interactions may affect catalytic properties at high temperatures or the adsorption behaviors at lower temperatures. Exploration of the detailed interactions between the host structure and the guest cations and H_2O molecules can enhance our understanding of the physical process(es) by which these two properties (i.e., host symmetry and guest chemistry) combined to produce specific behaviors that vary with temperature, P_{H_2O}, and guest compositions.

This research consists of systematic explorations of the effects of host-guest interactions on structural changes in NAT-topology zeolites (natrolite, scolecite, and mesolite). These zeolites were chosen for their framework configurations that provide nanometer-sized local pore structures. The bonding configurations among guest cations, H_2O, and aluminosilicate frameworks are less complex and better defined than in many other more-complex zeolites. In addition, the strength of hydrogen bonding and ion-dipole attraction of hydrogen atoms and guest cations with the host framework are strong in such confined environments. Investigation of dehydration reactions and accompanying structural phase transitions under *in-situ* controlled temperature- and P_{H_2O}-environments revealed

[14] Displacive phase transitions are based on the phenomena that the soft behavior of the zeolite channels and the more rigid behavior of their tetrahedral frameworks lead to easy rotation of any two adjacent tetrahedra around an oxygen hinge, resulting in a so-called displacive transformation (i.e., no breaking of bonds). This displacive process can be driven by changing temperature, pressure, humidity, or substitution with different guest components.

remarkably different transformation behaviors. For instance, dehydration (on heating) of the zeolite natrolite ($Na_{16}Al_{16}Si_{24}O_{80} \bullet 16H_2O$; *Fdd*2) showed different displacive phase transition paths depending on the P_{H_2O} and temperature of transformation. In natrolite, the anhydrous α1-metanatrolite phase ($Na_{16}Al_{16}Si_{24}O_{80}$; *F*112) occurred at elevated P_{H_2O}, whereas a new anhydrous phase, α2-metanatrolite ($Na_{16}Al_{16}Si_{24}O_{80}$; *Fdd*2) was found at low-P_{H_2O}. A low-P_{H_2O} atmosphere allowed access to a phase space that was not accessible at higher P_{H_2O}, because dehydration in the former was suppressed, thereby destabilizing hydrated natrolite to lower temperatures. The increase in the temperature of the *Fdd*2 → *F*112 transition at elevated P_{H_2O} illustrates the existence of different energetic interactions among the host natrolite structure and the guest Na-H_2O complexes. The occurrence of different dynamic interactions among the H_2O molecules, Na^+ cations, and the natrolite Al-Si frameworks immediately before dehydration was observed through infrared spectroscopic studies. Crystal structural analyses reconciled these data and showed that the different structural evolutions found under different P_{H_2O} and temperature conditions resulted from specific host-guest interactions. Before dehydration, the subtle thermal behavior of the guest Na-H_2O complexes will generate local strain forces. This local strain effect will be transmitted by flexing of the T-O-T bonds and angles (T = Si or Al) to the entire framework. However, the manner in which the host framework can distort is also constrained by the symmetry of the original phase. These two interacting forces, i.e., the displacive process induced by the thermal motion of guests vs. constraint by the original symmetry, may be coupled (combined), which further determines the range of energetically feasible T-O-T angles and results in different phase transition behaviors upon dehydration.

Similar transition mechanism(s) and temperature-/P_{H_2O}-dependent phase transition phenomena were also observed in scolecite ($Ca_4Al_8Si_{12}O_{40} \bullet 12H_2O$; $C1c1$) and mesolite ($Na_{16}Ca_{16}Al_{48}Si_{72}O_{240} \bullet 64H_2O$; $Fdd2$). Both zeolites share the same aluminosilicate framework configuration as natrolite[15]. However, in the mesolite or scolecite channels, half (in mesolite) or all (in scolecite) of the guest cations sites are occupied by Ca^{2+}, which largely restricts the flexibility of the host structure due to the presence of an insufficient number of cations to stabilize the small T-O-T angles formed in the distorted/dehydrated frameworks. During scolecite dehydration, the transformation to an amorphous T_5O_{10} phase was observed over a wide P_{H_2O} range, indicating the difficulty in maintaining the framework rigidity in the Ca-bearing zeolites. Only at low-P_{H_2O} conditions did the scolecite structure have the opportunity to undergo displacive transformations to x1-/x2-metascolecite phases. Mesolite dehydration and its accompanying structural changes are conceptually similar to those observed with natrolite and scolecite. The response of the mesolite crystal structure to dehydration also shows two different phase transition paths, depending on the P_{H_2O} and temperature conditions, with a transition to an amorphous T_5O_{10} phase at elevated P_{H_2O}, and a displacive phase transition to the x-metamesolite phase at low-P_{H_2O}. The observation of different phase transition paths under high- and low-P_{H_2O} conditions, once again, reiterates the coupling process by which the thermal behaviors of guest cation-H_2O complexes are coupled with the framework symmetry constraints through direct bonding interactions. This coupling among host-guest interactions and symmetry constraints in the host structures under

[15] The standard space group setting in scolecite is $C1c1$ (monoclinic; Z = 4), which has a unit-cell volume half that in the non-standard space group setting, $F1d1$ (monoclinic; Z = 8). The $F1d1$ cell setting in scolecite is structurally easier to compare with natrolite (orthorhombic; $Fdd2$; Z = 8). Mesolite has the same space group setting as natrolite ($Fdd2$). However, due to guest cation Na^+/Ca^{2+} ordering in the mesolite channel system, mesolite has a tripled *b* unit-cell length and a tripled unit-cell volume.

specific temperature and P_{H_2O} conditions controls the phase transition behaviors and it ultimately determines which metaphases form. In addition, in order to compensate for the lack of guest cations and to stabilize the small T-O-T angles found in the x1-/x2-metascolecite and x-metamesolite frameworks, the frameworks of scolecite and mesolite appear to have a strong ability to retain H_2O protons and therefore relic-OH groups form in dehydrated Ca-bearing zeolite frameworks.

The determined bulk thermodynamic behaviors in the NAT system were consistent with the observed structural behaviors. The computed *apparent* enthalpies of dehydration ($\Delta h^{\dagger}_{dehy}$) in all three zeolites reflect strong dependence not only on guest cation chemistry but also on the local hydrogen bonding configurations. Unfortunately, the finite energy differences for a zeolite undergoing different polymorphic phase transitions have been shown to be small in comparison with the "chemical bond energy" upon dehydration, and calculations for these finite energy differences were unable to resolve with the current experimental precisions. The dehydration/rehydration hysteresis effect that occurs in the NAT system is mainly caused by the intrinsic irreversibility of the lattice transformation, but the difference in the rate of H_2O diffusion in the open vs. distorted frameworks must also be considered. The presently incomplete thermodynamic treatment of the displacive structural changes and accompanying hysteresis effect in the NAT system can be further analyzed in the future based on the Landau theory of phase transitions using the changes of observable macroscopic properties through the phase transition (e.g., changes in unit-cell parameters, rotation angles in the framework tetrahedra, and appearance/disappearance of certain diffraction peaks or absorption bands upon transformation).

These fundamental structure-based studies and *in-situ* experimental results illustrate the key features of the atomistic mechanisms by which the structures respond. Further studies of the relations between the thermal motion of guests and their elastic/anelastic interactions with the host lattice are essential to determining and predicting host structural stabilities and the structural breakdown mechanisms in the NAT system. Fundamental concepts obtained from this study can be readily applied to other zeolites and many other zeolite-like systems. For example, anelastic properties of analcime ($NaAlSi_2O_6 \bullet H_2O$) and lawsonite ($CaAl_2Si_2O_7(OH)_2 \bullet H_2O$) are being used to test whether the dynamics of interactions between H_2O protons and a host structure could cause attenuation of seismic waves when they are present in abundance at depth in the Earth (McKnight *et al.* 2007). Methane hydrate, a clathrate compound with a large amount of methane trapped within its ice-like structural cages, is abundant in some oceanic sediments. It has been suggested that global warming may ultimately cause these materials to become unstable, producing potentially catastrophic effects on global climate. Their structural breakdown likely involves some of the concepts developed in this study. Epsomite phases ($MgSO_4 \bullet nH_2O$), a series of hydrated species, bear similar clathrate behaviors. These hydrous sulfate minerals and their wide structural stabilities are believed to have some control on cycling of H_2O near the martian surface. The nature of internal host-guest interactions in these materials (zeolites or zeolite-like systems) largely influences and defines their chemical and physical properties, and exploitation of host-guest interactions in these systems is extremely important in Nature and technology.

References cited

Adamson, A.W. (1963) Discussion. In S.H. Ehrlich and F.A. Bettelheim, Infrared spectroscopy of the water vapor sorption process of mucopolysaccharides, p. 1959-1960. The Journal of Physical Chemistry, 67, 1954-1959.

Adiwidjaja, G. (1972) Struturbeziehungen in der Natrolithgruppe und das Entwässerungsverhalten des Skolezits. Dissertation, Universität Hamburg, Hamburg, Germany.

Alberti, A. and Gottardi, G. (1988) The determination of the Al-content in the tetrahedra of framework silicates. Zeitschrift für Kristallographie, 184, 49-61.

Alberti, A. and Vezzalini, G. (1981) A partially disordered natrolite: Relationships between cell parameters and Si-Al distribution. Acta Crystallographica, B37, 781-788.

Alberti, A. and Vezzalini, G. (1983) How the structure of natrolite is modified through the heating-induced dehydration. Neues Jahrbuch für Mineralogie-Monatshefte, H3, 135-144.

Armbruster, T. and Bloss, F.D. (1982) Orientation and effects of channel H_2O and CO_2 in cordierite. American Mineralogist, 67, 284-291.

Armbruster, T. and Gunter, M.E. (2001) Crystal structures of natural zeolites. In D.L. Bish and D.W. Ming, Eds., Natural Zeolites: Occurrence, Properties, Applications, p. 1-68. Mineralogical Society of America, vol. 45, Washington, DC.

Artioli, G. (1997) In situ powder diffraction studies of temperature induced transformations in minerals. Nuclear Instruments and Methods in Physics Research, B133, 45-49.

Artioli, G. (1999a) Dehydration processes in natural zeolites. Plinius: Supplemento italiano all'European Journal of Mineralogy, 21, 253-257.

Artioli, G. (1999b) In situ structural and kinetic powder diffraction studies of aluminosilicates. In K. Wright and R. Catlow, Eds., Microscopic Properties and Processes in Minerals, p. 177-187. NATO Science Series C, Kluwer, Dordrecht.

Artioli, G., Smith, J.V., and Kvick, Å. (1984) Neutron diffraction study of natrolite, $Na_2Al_2Si_3O_{10} \cdot 2H_2O$, at 20 K. Acta Crystallographica, C40, 1658-1662.

Artioli, G., Smith, J.V., and Pluth, J.J. (1986) X-ray structure refinement of mesolite. Acta Crystallographica, C42, 937-942.

Baerlocher, Ch. and McCusker, L.B., Database of Zeolite Structures: http://www.iza-structure.org/databases/

Baur, W.H. (1980) Straight Si-O-Si bridging bonds do exist in silicates and silicon dioxide polymorphs. Acta Crystallographica, B36, 2198-2202.

Baur, W.H. and Joswig, W. (1996) The phase of natrolite occurring during dehydration and rehydration studied by single crystal X-ray diffraction methods between room temperature and 923 K. Neues Jahrbuch für Mineralogie-Monatshefte, H4, 171-187.

Belitsky, I.A., Fursenko, B.A., Gabuda, S.P., Kholdeev, O.V., and Seryotkin, Yu.V. (1992) Structural transformations in natrolite and edingtonite. Physics and Chemistry of Minerals, 18, 497-505.

Bish, D.L. and Carey, J.W. (2001) Thermal behavior of natural zeolite. In D.L. Bish and D.W. Ming, Eds., Natural Zeolites: Occurrence, Properties, Applications, p. 403-452. Mineralogical Society of America, vol. 45, Washington, DC.

Bish, D.L. and Wang, H.-W. (2010) Phase transitions in natural zeolites and the importance of P_{H_2O}. Philosophical Magazine, 90, 2425-2441.

Bougeard, D. and Smirnov, K.S. (2007) Modeling studies of water in crystalline nanoporous aluminosilicates. Physical Chemistry Chemical Physics, 9, 226-245.

Buerger, M.J. (1951) Crystallographic aspects of phase transformation. In R. Smoluchowski, J.E. Mayer, and W.A. Weyl, Eds., Phase Transformations in Solids, p. 183-209. John Wiley & Sons, New York.

Buerger, M.J. (1972) Phase transformations. Soviet Physics-Crystallography, 16, 959-968.

Carey, J.W. and Bish, D.L. (1996) Equilibrium in the clinoptilolite-H_2O system. American Mineralogist, 81, 952-962.

Carey, J.W. and Navrotsky, A. (1992) The molar enthalpy of dehydration of cordierite. American Mineralogist, 77, 930-936.

Chidambaram, R. and Sikka, S.K. (1968) Bent O-H···O hydrogen bonds in crystals. Chemical Physics Letters, 2, 162-165.

Chupas, P.J., Chapman, K.W., Kurtz, C., Hanson, J.C., Lee, P.L., and Grey, C.P. (2008) A versatile sample-environment cell for non-ambient X-ray scattering experiments. Journal of Applied Crystallography, 41, 822-824.

Chupas, P.J., Qiu, X., Hanson, J.C., Lee, P.L., Grey, C.P., and Billinge, S.J.L. (2003) Rapid-acquisition pair distribution function (RA-PDF) analysis. Journal of Applied Crystallography, 36, 1342-1347.

Clausius, R. (1865) The Mechanical Theory of Heat – with its Applications to the Steam Engine and to Physical Properties of Bodies, reprint in 2008, 394 p. BiblioBazaar.

Coelho, A.A. (2007) TOPAS-Academic v.4.1, http://www.topas-academic.net. Coelho Software, Brisbane, Australia.

Comodi, P., Gatta, G.D., and Zanazzi, P.F. (2002) High-pressure structural behavior of scolecite. European Journal of Mineralogy, 14, 567-574.

Coombs, D.S., Alberti A., Armbruster, T., Artioli, G., Colella, C., Galli, E., Grice, J.D., Liebau, F., Mandarino, J.A., Minato, H., Nickel, E.H., Passaglia, E., Peacor, D.R., Quartieri, S., Rinaldi, R., Ross, M., Sheppard, R.A., Tillmanns, E., and Vezzalini, G. (1998) Recommended nomenclature for zeolite minerals; report of the Subcommittee on Zeolites of the International Mineralogical Association, Commission on New Minerals and Mineral Names. Mineralogical Magazine, 62, 533-571.

Cruciani, G. (2006) Zeolites upon heating: Factors governing their thermal stability and structural changes. Journal of Physics and Chemistry of Solids, 67, 1973-1994.

Cruciani, G., Martucci, A., and Meneghini, C. (2003) Dehydration dynamics of epistilbite by *in situ* time resolved synchrotron powder diffraction. European Journal of Mineralogy, 15, 257-266.

Crupi, V., Longo, F., Majolino, D., and Venuti, V. (2006) Vibrational properties of water molecules adsorbed in different zeolitic frameworks. Journal of Physics: Condensed Matter, 18, 3563-3580.

Dove, M.T. (1997) Theory of displacive phase transitions in minerals. American Mineralogist, 88, 213-244.

Egami, T. and Billinge, S.J.L. (2003) Underneath the Bragg peaks: Structural analysis of complex materials, 1st edition, 404 p. Pergamon Materials Series vol. 7, Oxford.

Ehrlich, S.H. and Bettelheim, F.A. (1963) Infrared spectroscopy of the water vapor sorption process of mucopolysaccharides. The Journal of Physical Chemistry, 67, 1954-1959.

Eugster, H.P. and Wones, D.R. (1962) Stability relations of the ferruginous biotite, annite. Journal of Petrology, 3, 82-125.

Everett, D.H. and Whitton, W.I. (1955) A thermodynamic study of the adsorption of benzene vapor by active charcoals. Proceedings of the Royal Society of London. Series A, Mathematical and Physical Sciences, 203, 91-110.

Fälth, L. and Hansen, S. (1979) Structure of scolecite from Poona, India. Acta Crystallographica, B35, 1877-1880.

Farrow, C.L., Juhás, P., Liu, J.W., Bryndin, D., Božin, E.S., Bloch, J., Proffen, Th., and Billinge, S.J.L. (2007) PDFfit2 and PDFgui: computer programs for studying nanostructure in crystals. Journal of Physics: Condensed Matter, 19, 335219.

Farrow, C.L., Juhás, P., Liu, J.W., Bryndin, D., Božin, E.S., Bloch, J., Proffen, Th., and Billinge, S.J.L. (2009) PDFgui user guide, http://www.diffpy.org/documentation.shtml.

Fisher, J.R. and Zen, E.-AN. (1971) Thermochemical calculations from hydrothermal phase equilibrium data and the free energy of H_2O. American Journal of Science, 270, 297-314.

Flanagan, T.B., Park, C.-N., and Oates, W.A. (1995) Hysteresis in solid state reactions. Progress in Solid State Chemistry, 23, 291-363.

Geisinger, K.L., Gibbs, G.V., and Navrotsky, A. (1985) A molecular orbital study of bond length and angle variations in framework structures. Physics and Chemistry of Minerals, 11, 266-283.

Goryainov, S.V. and Smirnov, M.B. (2001) Raman spectra and lattice-dynamical calculations of natrolite. European Journal of Mineralogy, 13, 507-519.

Gottardi, G. and Galli, E. (1985) Natural zeolites, 409 p. Minerals and Rocks, vol. 18, Springer-Verlag, Heidelberg.

Guliev, T.M., Isirikyan, A.A., Mirzai, D.I., and Serpinskii, V.V. (1989a) Energy of rehydration of natrolite and scolecite. Bulletin of the Academy of Sciences of the USSR Division of Chemical Science, 37, 1308-1310.

Guliev, T.M., Isirikyan, A.A., Mirzai, D.I., and Serpinskii, V.V. (1989b) Rehydration energy of mesolite and thomsonite. Bulletin of the Academy of Sciences of the USSR Division of Chemical Science, 37, 1497-1499.

Hammersley, A.P., Svensson, S.O., Hanfland, M., Fitch, A.N., and Häusermann, D. (1996) Two-dimensional detector software: From real detector to idealized image or two-theta scan. High Pressure Research, 14, 235-248.

Hey, M.H. (1932) Studies on the zeolites. Part III: Natrolite and metanatrolite. Mineralogical Magazine, 23, 243-289.

Joswig, W. and Baur, W.H. (1995) The extreme collapse of a framework of NAT topology: the crystal structure of metanatrolite (dehydrated natrolite) at 548 K. Neues Jahrbuch für Mineralogie-Monatshefte, H1, 26-38.

Joswig, W., Bartl, H., and Fuess, H. (1984) Structure refinement of scolecite by neutron diffraction. Zeitschrift für Kristallographie, 166, 219-223.

Kisekeva, I., Ogorodova, L.P., Melchakova, L.V., Belitsky, I.A., and Fursenko, B.A. (1997) Thermochemical investigation of natural fibrous zeolites. European Journal of Mineralogy, 9, 327-332.

Kolesov, B.A. and Geiger, C.A. (2006) Behavior of H_2O molecules in the channels of natrolite and scolecite: A Raman and IR spectroscopic investigation of hydrous microporous silicates. American Mineralogist, 91, 1039-1048.

Kuntzinger, S., Ghermani, N.E., Dusausoy, Y., and Lecomte, C. (1998) Distribution and topology of the electron density in an aluminosilicate compound from high-resolution X-ray diffraction data: the case of scolecite. Acta Crystallographica, B54, 819-833.

Kvick, Å., Ståhl, K., and Smith, J.V. (1985) A neutron diffraction study of the bonding of zeolitic water in scolecite at 20 K. Zeitschrift für Kristallographie, 171, 141-154.

La Mer, V.K. (1967) The calculation of thermodynamic quantities from hysteresis data. Journal of Colloid and Interface Science, 23, 297-301.

Le Bail, A., Duroy, H., and Fourquet, J.L. (1988) Ab-initio structure determination of $LiSbWO_6$ by X-ray powder diffraction. Materials Research Bulletin, 23, 447-452.

Libowitzky, E. (1999) Correlation of O-H stretching frequencies and O-H···O hydrogen bond lengths in minerals. Monatshefte für Chemie, 130, 1047-1059.

Libowitzky, E. and Beran, A. (2004) IR spectroscopic characterization of hydrous species in minerals. In A. Beran and E. Libowitzky, Eds., Spectroscopic Methods in Mineralogy, p. 227-279. EMU Notes in Mineralogy, vol. 6, Budapest.

Line, C.M.B. and Kearley, G.J. (1998) The librational and vibrational spectra of water in natrolite, $Na_2Al_2Si_3O_{10} \cdot 2H_2O$ compared with ab-initio calculations. Chemical Physics, 234, 207-222.

Line, C.M.B. and Kearley, G.J. (2000) An inelastic incoherent neutron scattering study of water in small-pored zeolites and other water-bearing minerals. Journal of Chemical Physics, 112, 9058-9067.

Martínez-Iñesta, M. and Lobo, R.F. (2005) Investigation of the negative thermal expansion mechanism of zeolite chabazite using the pair distribution function method. Journal of Physical Chemistry B, 109, 9389-9396.

Martínez-Iñesta, M. and Lobo, R.F. (2007) Investigation of the structure of platinum clusters supported in zeolite beta using the pair distribution function. Journal of Physical Chemistry C, 111, 8573-8579.

Martínez-Iñesta, M., Peral, I., Proffen, Th., and Lobo, R.F. (2005) A pair distribution function analysis of zeolite beta. Microporous and Mesoporous Materials, 77, 55-66.

McKnight, R.E.A., Carpenter, M.A., Darling, T.W., Buckley, A., and Taylor P.A. (2007) Acustic dissipation associated with phase transitions in lawsonite, $CaAl_2Si_2O_7(OH)_2 \cdot H_2O$. American Mineralogist, 92, 1665-1672.

Meier, W.M. (1960). The crystal structure of natrolite. Zeitschrift für Kristallographie, 113, 430-444.

Mirzai, D.I. (1985) The mechanism of dehydration of natural calcium zeolite-scolecite. Doklady Akademii Nauk SSSR, 2, 420-424.

Mirzai, D.I., Guliev, T.M., Pribylov, A.A., and Barash, A.B. (1989) Hydroxyl group formation in the dehydration of scolecite. Bulletin of the Academy of Sciences of the USSR Division of Chemical Science, 38, 654-655.

Moenke, H.H.W. (1974) Silica, the three-dimensional silicates, borosilicates and beryllium silicates. In V.C. Farmer, Ed., The Infrared Spectra of Minerals, p. 365-382. Mineralogical Society, vol. 4, London.

Mozgawa, W. (2001) The relation between structure and vibrational spectra of natural zeolites. Journal of Molecular Structure, 596, 129-137.

Neuhoff, P.S. and Wang, J. (2007) Isothermal measurement of heats of hydration in zeolites by simultaneous thermogravimetry and differential scanning calorimeter. Clay and Clay Minerals, 55, 239-252.

Orville, P.M. and Greenwood, H.J. (1965) Determination of ΔH of reaction from experimental pressure-temperature curves. American Journal of Science, 263, 678-683.

Oszlanyi, G. and Suto, A. (2004) Ab initio structure solution by charge flipping. Acta Crystallographica, A60, 134-141.

Oszlanyi, G. and Suto, A. (2005) Ab initio structure solution by charge flipping. II. Use of weak reflections. Acta Crystallographica, A61, 147-152.

Palumbo, M. (2008) Thermodynamics of martensitic transformations in the framework of the CALPHAD approach. Calphad Computer Coupling of Phase Diagrams and Thermochemistry, 32, 693-708.

Passaglia, E. and Sheppard, R.A. (2001). The crystal chemistry of zeolites. In D.L. Bish and, D.W. Ming, Eds., Natural Zeolites: Occurrence, Properties, Applications, p. 69-116. Mineralogical Society of America, vol. 45, Washington, DC.

Pauling, L. (1930) The structure of some sodium and calcium aluminosilicates. Proceedings of the National Academy of Sciences, USA, 16, 453-459.

Pechar, F. (1983) Study of complex vibrational spectra of natural mesolite. Crystal Research and Technology, 18, 1045-1052.

Pechar, F. and Rykl, D. (1983) Study of the vibrational spectra of natural natrolite. Canadian Mineralogist, 21, 689-695.

Planes, A., Macqueron, J.L., and Ortin, J. (1988) Energy contributions in the martensitic transformation of shape-memory alloys. Philosophical Magazine Letters, 57, 291-298.

Prasad, P.S.R. and Prasad, K.S. (2007) Dehydration and rehydration of mesolite: An *in situ* FTIR study. Microporous and Mesoporous Minerals, 100, 287-294.

Prasad, P.S.R., Prasad, K.S., Sreedhar, B., and Murthy, S.R. (2006) *In-situ* FTIR study of dehydration and rehydration mechanisms of natural scolecite. European Journal of Mineralogy, 18, 265-272.

Prigogine, I. (1961) Introduction to thermodynamics of irreversible processes, 2nd edition, 119 p. John Wiley & Sons, New York.

Proffen, Th., Petkov, V., Billinge, S.J.L., and Vogt, T. (2002) Chemical short range order obtained from the atomic pair distribution function. Zeitschrift für Kristallographie, 217, 47-50.

Qiu, X., Thompson, J.W., and Billinge, S.J.L. (2004) PDFgetX2: A GUI-driven program to obtain the pair distribution function from X-ray powder diffraction data. Journal of Applied Crystallography, 37, 678-678.

Rinne, F. (1890) Über die umänderungen welche die zeolithe durch erwärmen bei und nach dem trübwerden erfahren. Sitzungsberichte der Preussischen Akademie der Wissenschaften, Physikalisch-Mathematische Klasse, 46, 1163-1207.

Rinne, F. (1923) Über die umänderungen welche die zeolithe durch erwärmen bei und nach dem trübwerden erfahren. Neues Jahrbuch für Mineralogie, Geologie und Paläontologie, 48, 240-249.

Ståhl, K. and Hanson, J. (1994) Real-time X-ray synchrotron powder diffraction studies of the dehydration processes in scolecite and mesolite. Journal of Applied Crystallography, 27, 543-550.

Ståhl, K. and Thomasson, R. (1994) The dehydration and rehydration processes in the natural zeolite mesolite studied by conventional and synchrotron X-ray powder diffraction. Zeolites: The International Journal of Molecular Sieves, 14, 12-17.

Stuckenschmidt, E. and Kirfel, A. (2000) Zeolites of NAT topology: Structure refinement of mesolite from single crystal X-ray data and comparison with the structures of natrolite and scolecite. European Journal of Mineralogy, 12, 571-579.

Stuckenschmidt, E., Joswig, W., Baur, W.H., and Hofmeister, W. (1997) Scolecite, Part I: Refinement of high-order data, separation of internal and external vibrational amplitudes from displacement parameters. Physics and Chemistry of Minerals, 24, 403-410.

Taylor, W.H., Meek, C.A., and Jackson, W.W. (1933) The structures of the fibrous zeolites. Zeitschrift für Kristallographie, 84, 373-398.

Thompson, R.T., Knispel, R.R., and Petch, H.E. (1974) NMR study of the molecular motion of water in natrolite. Canadian Journal of Physics, 52, 2164-2173.

van Olphen, H. (1965) Thermodynamics of interlayer adsorption of water in clays I.- Sodium vermiculite. Journal of Colloid Science, 20, 822-837.

van Reeuwijk, L.P. (1974) The thermal dehydration of natural zeolites. Ph.D. thesis, Communications Agricultural University, Wageningen, Netherlands.

Wang, H.-W. and Bish, D.L. (2008) A P_{H_2O}-dependent structural phase transition in the zeolite natrolite. American Mineralogist, 93, 1191-1194.

Wang, H.-W. and Bish, D.L. (2010) X-ray diffraction study of the zeolite natrolite: T-P_{H_2O} phase diagram and phase transitions during dehydration/rehydration. European Journal of Mineralogy, 22, 271-284.

Wang, H.-W., Bish, D.L., and Ma, H. (2010) P_{H_2O}-dependent structural phase transitions in the zeolite mesolite: Real- and reciprocal-space crystal structure refinements. American Mineralogist, 95, 686-698.

Wopenka, B., Freeman, J.J., and Nikischer, T. (1998) Raman spectroscopic identification of fibrous natural zeolites. Applied Spectroscopy, 52, 54-63.

Wu, J.S., Leinenweber, K., Spence, J.C.H., and O'Keefe, M. (2006) Ab initio phasing of X-ray powder diffraction patterns by charge flipping. Nature Materials, 5, 647-652.

Hsiu-Wen Wang
Dept. of Geological Sciences
Indiana University
1001 E. 10th Street
Bloomington, IN 47405
Tel: 812-606-5701
hw7@indiana.edu
mypage.iu.edu/~hw7

EDUCATION

Indiana University Bloomington (IUB), Geological Sciences — Ph.D., Sep. 2007- May. 2011
Minor in spectroscopy; Overall GPA 3.9/4.0

Ph.D. thesis title: Investigation of phase transition behaviors and transition mechanisms of NAT-topology zeolites.

Indiana University Bloomington (IUB), Geological Sciences — M.S., Sep. 2005-Aug. 2007
Overall GPA 3.9/4.0

M.S. thesis title: Dehydration/rehydration-induced structural phase transitions in natrolite.

National Cheng Kung University (NCKU), Earth Sciences — B.S., Sep. 1999-Jun. 2003
Overall GPA 3.9/4.0; Accumulated GPA in the last two years 4.0/4.0

B.S. thesis title: Inverted trend of muscovite crystallinity in Plio-Pleistocene sediments from coastal range, eastern Taiwan: diagenetic alternation vs. orogenic lifting of metamorphosed source rocks.

WORKING AND TEACHING EXPERIENCE

Teaching Assistant in Geological Sciences, IUB

H205 Gas Prices & Petroleum Geology — Spring 2009, Fall 2009.

G103 Earth Science - Materials and Processes — Fall 2008, Fall 2009, Spring 2010.

G427 Introduction to X-ray Mineralogy — Spring 2006, Spring 2009.

G105 Earth: Our Habitable Planet — Fall 2006.

Research Assistant, National Sun Yat-Sen University, Taiwan — 2004-2005
Determination of physical and chemical properties of lateritic strata using powder X-ray diffraction, petrographic microscope and scanning electron microscope (SEM) techniques.

Earth Science Teacher, National Shan-Hua Senior High School, Taiwan — 2003-2004
Fundamental Earth science education, including astronomy, meteorology, oceanography and geology. Advisor of student scientific research competition in 2004.

COMPETITIVE AWARDS AND HONORS

Estwing award for the best graduate student in the Department of Geological Sciences, IUB (Recognition is based on GPA and research achievements) — 2010.

Grassmann fellowship for Ph.D. in Clay and/or Zeolite Mineralogy — 2007-2008 & 2010-2011.

Winner of excellence in student poster presentation contest at the Clay Mineral Society annual meeting, Santa Fe, New Mexico — June, 2007.

Associate Instructor award for excellence in teaching introduction of geology labs, Dept. of Geological Sciences, Indiana University — 2007.

Bruker AXS excellence in X-ray diffraction scholarship for unique applications in the category of Geology and Chemistry — 2006, international competition for one ($5,000) of two grants.

Winner of honorable student poster contest at the Annual Meeting of Geological Society of China — 2003.

The President's Award (top 5% in class) of the College of Science, Dept. of Earth Sciences, NCKU — 2002, 2001, 2000.

GRANTS

Edward H. Kraus Crystallographic Research Grant awarded by the Mineralogy Society of America — 2010, international competition for a $5,000 grant.

Student travel grants awarded by the American Crystallographic Association — 2011; the Women in Science Program, Indiana University — 2010; the Geological Society of America — 2009; the Geochemical Society and the College of Arts & Sciences, Indiana University — 2008.

EXTERNAL INTERACTIONS

Diffuse Scattering and Structure Simulation Workshop, University of Erlangen-Nürnberg, Erlangen, Germany — August 2010; State University of New York, Stony Brook, New York, USA — May 2010.

General beamline user of the Advanced Photon Source at Argonne National Laboratory — 2008-cycle-2, 2010-cycle-2, 2011-cycle-1.

LANSCE Neutron Scattering School: Phase transformations, Los Alamos National Laboratory — July 2009.

Vice President of Student Advisory Committee in the Dept. of Geological Sciences, IUB — 2008 to 2009.

National School on Neutron and X-ray Scattering at Argonne National Laboratory — August, 2007.

Visiting scientist in Dept. of Earth Sciences, University of Cambridge — July, 2007.